Structure and dynamics of artificial lipid membranes containing the glycosphingolipid Gb$_3$

Ole Mathis Schütte

from Bremen

Göttingen 2015

Structure and dynamics
of artificial lipid membranes
containing the glycosphingolipid Gb$_3$

Dissertation

for the award of the degree

Doctor rerum naturalium

of the Georg-August-Universität Göttingen

within the doctoral program
Physics of Biological and Complex Systems
of the Georg-August University School of Science (GAUSS)

submitted by

Ole Mathis Schütte

from Bremen

Göttingen 2015

Members of the Thesis Committee:

Prof. Dr. Claudia Steinem,
Institut für Organische und Biomolekulare Chemie,
Georg-August-Universität Göttingen

Prof. Dr. Jörg Enderlein,
Drittes Physikalisches Institut,
Georg-August-Universität Göttingen

Prof. Dr. Ulf Diederichsen,
Institut für Organische und Biomolekulare Chemie,
Georg-August-Universität Göttingen

Members of the Examination Board:

Referee: Prof. Dr. Claudia Steinem,
Institut für Organische und Biomolekulare Chemie,
Georg-August-Universität Göttingen

2nd Referee: Prof. Dr. Ulf Diederichsen,
Institut für Organische und Biomolekulare Chemie,
Georg-August-Universität Göttingen

Further members of the Examination Board:

Prof. Dr. Jörg Enderlein,
Drittes Physikalisches Institut,
Georg-August-Universität Göttingen

Prof. Dr. Burkhard Geil,
Institut für Physikalische Chemie,
Georg-August-Universität Göttingen

Prof. Dr. Michael Meinecke,
Zentrum für Biochemie und Molekulare Zellbiologie,
Georg-August-Universität Göttingen

Prof. Dr. Tim Salditt,
Drittes Physikalisches Institut,
Georg-August-Universität Göttingen

Date of oral examination:

16 July 2015

Declaration

I, Ole Mathis Schütte, hereby certify that my doctoral thesis entitled "Structure and dynamics of artificial lipid membranes containing the glycosphingolipid Gb_3" has been written independently and with no other sources and aids than quoted.

Göttingen, 2015

<div style="text-align:right">

_____

Ole Mathis Schütte

</div>

„*Ein Loch ist da, wo etwas nicht ist.*“
Kaspar Hauser

Abstract The lateral structure of the plasma membrane of mammalian cells is governed by the underlying actin cytoskeleton and the complex composition of the membrane. Using phase-separated membranes of the raft-like mixture DOPC/ Sphingomyelin/Cholesterol 40:40:20 allows to study the membrane structure in a chemically well defined model system.

Solid supported membranes were prepared and the phase separation into an ordered a disordered phase was investigated by fluorescence and atomic force microscopy.

The membranes contained $5\,\text{mol}\%$ of one of the naturally occurring derivatives of the receptor glycosphingolipid Gb_3 of the Shiga Toxin B-subunit (STxB) with either a saturated, an unsaturated, a α-hydroxylated or one of the diastereoisomers of the α-hydroxylated and unsaturated fatty acid bound to its ceramide backbone. Depending on the Gb_3 species in the membrane the lipid distribution between the phases varies. STxB binds only to the ordered phase and its lateral organization vastly differs. Protein cluster formation leads to an interphase lipid rearrangement and sterically more demanding Gb_3 derivatives induce a homogeneous coverage of the ordered phase with STxB. In giant unilamellar vesicles, containing a α-hydroxylated and unsaturated Gb_3 derivative, STxB binding induced the formation of tubular membrane invaginations which are the toxin's mechanism of endocytosis. The results show that the fatty acid of Gb_3 strongly influences the lateral membrane organization and STxB binding, indicating distinct biological functions of the molecules.

To mimic the role of the cytoskeleton, phase-separated membranes were prepared on porous substrates with different pore diameters and porosities. The combination of solid supported and freestanding membrane areas induces the formation of small lipid domains. Contact to the solid support immobilizes them, while domains fully located in the freestanding membrane area are moving. To describe the diffusion of the domains, a theoretical model was developed. Analysis of the movement in conjunction with topographic data, gathered by scanning ion-conductance microscopy, identifies a curved membrane region at the pore border as a major determinant of domain diffusion. STxB binding to the membranes leads to lipid redistribution between the solid supported and freestanding membrane areas, resulting in an altered morphology of the domains. The dynamics of lipid domains and protein clusters show that porous substrates compartmentalize the membrane in a similar way as proposed for the cytoskeleton underlying the plasma membrane.

Zusammenfassung Die laterale Struktur der Plasmamembran von Säugetierzellen wird durch das Zytoskelett und die komplexe Zusammensetzung der Membran bestimmt. Phasenseparierte Membranen der *raft*-ähnlichen Lipidmischung DOPC/ Sphingomyelin/Cholesterin 40:40:20 erlauben es die Membranorganisation in einem chemisch definierten Modellsystem zu untersuchen.

Festkörperunterstützte Membranen wurden mit $5\,mol\%$ eines natürlich vorkommenden Derivates des Rezeptorglykosphingolipids Gb_3 der Shiga Toxin Untereinheit B (STxB) dotiert, das eine gesättigte, ungesättigte, α-hydroxylierte oder α-hydroxyliert und ungesättigte Fettsäure am Ceramidgrundgerüst trägt. Die Phasenseparation der Membran in eine geordnete und eine ungeordnete Phase wurde mittels Fluoreszenz- und Rasterkraftmikroskopie untersucht. Die Verteilung der Lipide in und zwischen den beiden Phasen ist abhängig von der Gb_3-Spezies in der Membran. Die laterale Organisation von STxB gebunden an Gb_3-haltige Membranen variiert stark. Die Bildung von Proteinclustern führt zu einer Umverteilung von Lipiden zwischen den Phasen, während sterisch anspruchsvollere Gb_3-Spezies eine homogene Belegung mit Protein erzeugen. Die Bindung von STxB an unilamellare Riesenvesikel dotiert mit einer der Gb_3-Spezies mit α-hydroxylierter und ungesättigter Fettsäure führt zur Bildung von Membraninvaginationen, welche der Endozytosemechanismus des Toxins sind. Die Ergebnisse zeigen, dass die an Gb_3 gebundene Fettsäure einen Einfluss auf die laterale Organisation der Membran und die Anbindung von STxB hat. Dies deutet auf unterschiedliche biologische Funktionen der Moleküle hin.

Porenüberspannende Membranen präpariert auf porösen Substraten mit unterschiedlichen Porendurchmessern und Porositäten erlauben es den Einfluss des Zytoskeletts auf die Plasmamembran nachzubilden. Festkörperunterstützte Membranbereiche induzieren die Bildung kleiner Lipiddomänen und direkter Kontakt zum Festkörper immobilisiert diese, wohingegen Domänen in den freitragenden Membranen beweglich sind. Um die Bewegung der Domänen zu beschreiben wurde ein theoretisches Model entwickelt. Die Diffusion ist durch einen gekrümmten Bereich am Rand der porenüberspannenden Membran gehindert, welcher durch Rasterionenleitfähigkeitsmikroskopie bestätigt werden konnte. Die Bindung von STxB an die Membranen führt zu einer Umverteilung der Lipide zwischen festkörperunterstützten und freistehenden Bereichen und verändert die Domänenmorphologie. Die Dynamik von Proteinclustern und der Lipiddomänen zeigt, dass das poröse Substrat, ähnlich wie das Zytoskelett, die Membran in Kompartimente unterteilt.

Contents

1 Introduction

Biological membranes are abundant in living cells. They shield the cell from its exterior, compartmentalize organelles and form a platform for controlled exchange of metabolites.

Artificial lipid membranes offer the possibility to study complex biological processes in a chemically well defined manner. Changing the composition of the membranes and employing various biophysical techniques, enables to monitor how small changes on the molecular level lead to large scale changes in the membrane. Systematically studying these alterations allows to rationalize and understand the membrane's influence on important biological phenomenons.

1.1 Structure of biological membranes

In recent years the picture of the biological lipid membrane has complexified. Membranes are built up of a mixture of amphiphilic lipids and embedded and anchored proteins.[1] The amphiphilic structure of the lipids induces a self-organization in aqueous solution, resulting in the formation of a lipid bilayer composed of two leaflets. The early model of the plasma membrane, developed by Singer and Nicolson in the 1970s, was based on the idea that the lipids form a 2D fluidic structure that serves the purpose of compartmentalizing cell organelles and shielding the cell from the exterior.[2] Additionally the membranes serves as a matrix for embedded and bound proteins which form a 'fluid mosaic' structure. They allow for the controlled exchange of metabolites between the compartments, form areas of distinct chemical environments and allow the cell to build up (electro)chemical gradients, which serve important roles in energy production.[1] Apart from the barrier role of the membrane, other processes occurring were nearly exclusively linked to the activity of the membrane proteins.

New experimental approaches allowed to study the lipid matrix in more detail.[3] Techniques like shotgun mass spectrometry quantified the lipid diversity and the

sheer number of up to 100000 different lipids species in eukaryotes, hints to a more functional role of the lipid membrane.[4] Different organelles are enriched in specific lipids.[1] Lipids differ in their hydrophobic moiety which is usually one or more hydrocarbon chains with different degrees of saturation, methylation and hydroxylation. They are linked to different backbones bearing a hydrophilic headgroup which shows an even broader range of chemical structures ranging from simple carboxylic acids and (phosphorylated) alkylamines to highly complex, chemically modified polysaccharides.[1] Additionally, sterols like cholesterol are located in the membrane, serving specific functions.

The plasma membrane shielding the cell from its environment has a highly complex structure. Its inner leaflet, facing the cytosol, is mainly enriched in phosphatidylethanolamine, phosphatidylserin and phosphatidylinositides.[1] These specific lipids play a role in anchoring membrane proteins,[5] forming protein-lipid clusters[6] and act as precursors for second messengers.[7] The outer leaflet is the direct interface of the cell to its environment. It is enriched in cholesterol, saturated lipids like sphingomyelin and glycolipids. The higher content of saturated lipids forms a tight structure fulfilling the barrier function of the plasma membrane. Simons and coworkers found that the lateral structure of the outer leaflet of the membrane is not homogeneous but domains enriched in cholesterol and sphingolipids are formed. They termed these areas 'lipid rafts'.[8]

Heterogeneity of the plasma membrane and lipid rafts

The outer leaflet of the plasma membrane contains elevated fractions of sphingolipids.[8] Cholesterol forms stronger interactions with saturated sphingolipids leading to a clustering of the lipids in distinct membrane domains termed rafts.[9] They are nanoscale assemblies which are highly dynamic.[3] The enrichment of saturated lipids and cholesterol thickens the membrane resulting in an increased affinity of certain transmembrane proteins and lipid-linked receptors to the rafts.[3,10] Figure 1.1 shows a schematic model of the plasma membrane organization.
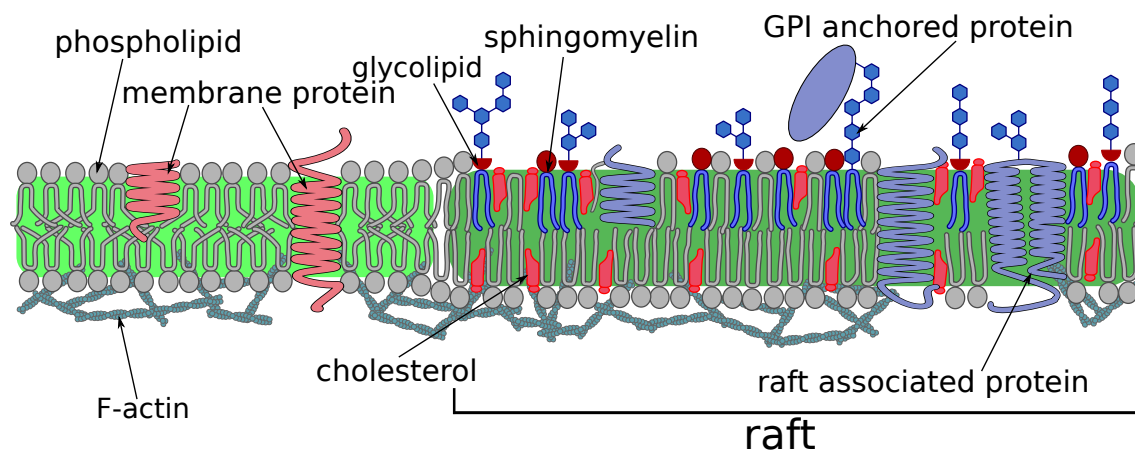
Figure 1.1: Lateral organization of the plasma membrane. Lipid rafts are formed by the interaction of cholesterol (red) and sphingolipids (blue) in the upper (outer) leaflet of the membrane. Image adapted from Lingwood and Simons.[11]

The rafts differ in both its lipid and protein content from the surrounding membrane areas, which contain an increased amount of unsaturated phospholipids.[11] Whether the raft exists only in the outer leaflet of the membrane is unknown. Long chain sphingolipids might interdigitate into the bottom layer, coupling the leaflets. The local clustering of receptors and proteins enhances their density allowing them to act as a beacon in signaling and transport processes.[10] Rafts are believed to have a size of 20 to 200 nm in diameter depending on external stimuli.[11] Their direct study is complicated by their small size and their highly fluctuating structure deprives them of being studied with classical microscopy.[11] Whether rafts truly exist or the plasma membrane inhomogeneity is caused by other factors like specific lipid/protein clustering or the actin cytoskeleton is still under debate.[12]

The development of super-resolution optical stimulated-emission-depletion (STED) microscopy allowed to study the nanoscale dynamics of lipids in the membrane.[13] Eggeling and coworkers used STED based fluorescence correlation spectroscopy (FCS) and found that the raft component sphingomyelin indeed partitions into small domains, slowing its diffusion in the membrane.[14] Non-raft lipids do not show this behavior. The lipid diffusion was not only influenced by a partitioning into lipid domains but also an entrapment in compartments was found.[15] The idea of compartmentalization of plasma membrane was first developed by Kusumi *et al.*.[16,17] He proposed the picket-fence model. It is based on the idea that the F-actin network below the plasma membrane can compartmentalize the membrane into distinct areas. Cross-linking of actin filaments forms a two dimensional mesh below

the plasma membrane. Using-high speed single particle tracking, the diffusion of lipids was found to be compartmentalized in regions defined by this actin mesh. Depolymerizing the F-actin by e.g. adding Latrunculin recovers free diffusion. A graphical representation based on the work by Kusumi is given on in Figure 5.3 on page 150.

The concept of the actin cytoskeleton regulating the plasma membrane organization is compelling. Rafts as an organizing principle rely on the lipid composition. Modulating it requires the relocalization of lipids from and to the plasma membrane by vesicle fusion. On the other hand the cytoskeleton allows dynamic rearrangement affecting the plasma membrane.

Microtubuli facilitate intracellular transport and intermediate filaments give the cell its mechanical stability.[1] The filamentous actin (F-actin) network is mostly localized in proximity to the plasma membrane. It is a polymer of the globular protein actin. The formation of these filaments is ATP dependent and the cell uses a variety of proteins to control the length and degree of cross-linking of the filaments. The F-actin network allows the cell to perform active processes like vesicle scission and movement.[1] Certain transmembrane proteins can directly bind to actin,[16] and the plasma membrane can be connected by proteins of the Ezrin/Radixin/Moesin family, acting as dynamic linkers, to the cytoskeleton.[18] This linkage influences the organization of the membrane and the diffusion of lipids and proteins. Immobilized proteins can act as a picket-like seed for domain formation. Close contact to the actin filaments forms areas in the membrane which are surrounded by the actin in a fence like manner.[16] The size of these meshes is highly variable and depends on the number of adhesion sites and cross-linking proteins. It varies between different cell type and typically in in the range of 40 to 300 nm.[19,20]

The small size of rafts and complex protein machinery involved in controlling the lateral structure of the plasma membrane complicates direct survey of their properties.

Linking the biological membrane to artificial models

The first evidences of the existence of rafts in the plasma membrane were gained by solubilizing the membrane using cold non-ionic detergent.[3] Parts of the membrane formed detergent-resistant-membranes (DRMs) enriched in cholesterol,

sphingolipids and certain proteins. However, a direct linkage to the postulated rafts was difficult because the harsh conditions might disrupt the preorganized membrane and lead to artifacts.[3, 21]

Using milder chemicals it is possible to stimulate cells into growing giant plasma membrane vesicles (GPMVs).[22–27] These vesicles contain all lipids of the plasma membrane. Studying these natural extracts led to the conclusion that the nanoscopic rafts are lost. However, GPMVs still form domains enriched in cholesterol and sphingomyelin below room temperature, indicating that the lipids in the plasma membrane also have a tendency to phase separate. GPMVs link the raft hypothesis to the phase separation observed in artificial lipid membranes.

1.2 Membrane model systems

It is possible to use natural lipid extracts to study the properties of lipid membranes *in vitro*. In a bottom up approach the membrane can also be built up by mixing chemically defined lipid species, allowing for full control of the membrane composition. Changing the compositions allows to rationalize how a single lipid species and its interplay with other lipids changes the properties of the membrane. The phase behavior of lipids is complex. They are able to adopt a variety of different thermodynamical phases depending on their environment. In cells most membranes are in a lamellar phase.[1] Figure 1.2 shows the general phase behavior within the lamellar phase.[28] The hydrophilic headgroup of the lipids are shown as circles, the hydrocarbon chains as sticks. At low temperature the chains adopt a all-*trans* conformation leading to a tight packing of the chains which are tilted by 30° compared to the membrane normal. In this gel (l_{β}'), or solid like (S_{o}), state the lipids are packed tightly and the diffusivity is small.[28] Increasing the temperature above the main transition temperature, which is dependent on the chemical structure of the lipid, leads to the formation of a liquid-crystalline (l_{α}) or liquid-disordered (l_{d}) state. The hydrocarbon chains partially adopt *gauche* conformation resulting in a thinner membrane,[28] weakened lipid-lipid interactions and higher diffusivity. The transitions between the gel and liquid state can also occur via a pretransition to the ripple phase (p_{β}') where the membrane adopts a wavy structure and first defects in the tight packing of the hydrocarbon chains appear.
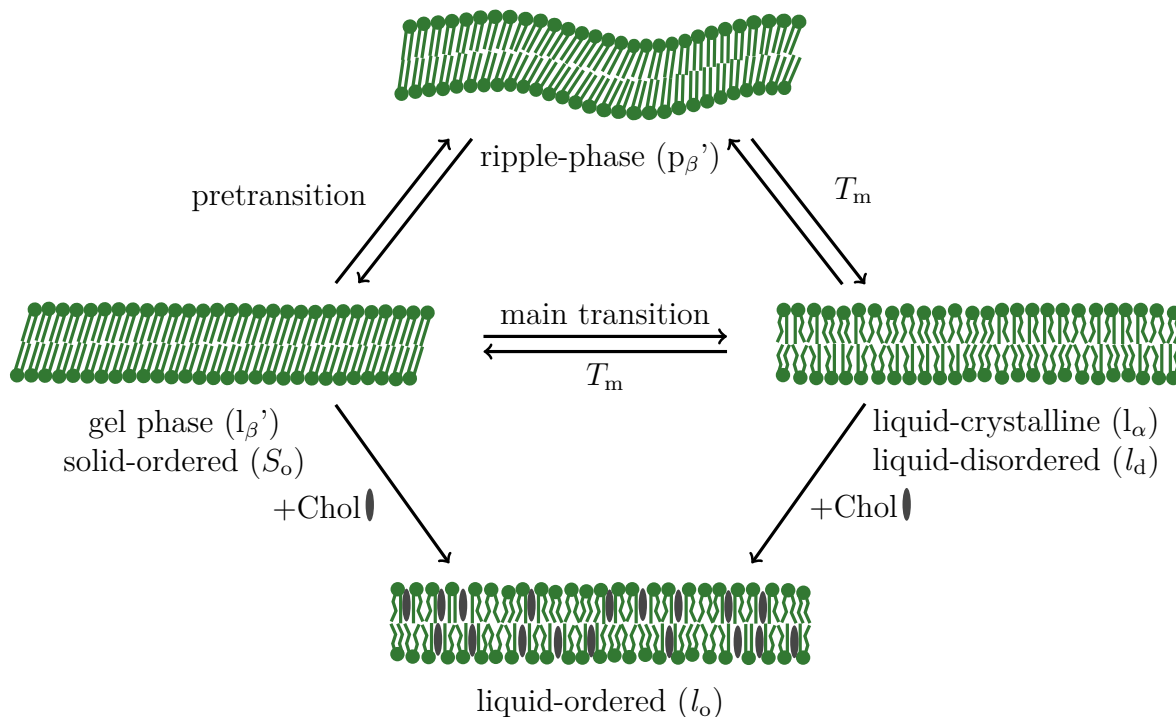
Figure 1.2: Different physical states of membranes in aqueous solution. Depending on the temperature and cholesterol content the membrane adapts different lamellar phases.[28]

The main transition temperature mainly depends on the lengths of the hydrocarbon chains and the degree of saturation. Saturated lipids have a high melting temperature, unsaturated lower.[1] This already hints to a relation of these thermodynamic phases with lipids rafts, where the mostly saturated sphingomyelin segregates from unsaturated phospholipids.

Introducing cholesterol into lipid mixtures leads to an intermediate state of the membrane termed 'liquid-ordered', or l_o. The high density packing of the gel phase is disrupted by cholesterol but it induces order in loosely packed aggregates.[28]

To model the raft forming composition of the outer leaflet of the plasma membrane, cholesterol (Chol) can be mixed to a fluid phospholipid like 1,2-dioleoyl-*sn*-glycero-3-phosphocholine (DOPC) or 1-palmitoyl-2-oleoyl-*sn*-glycero-3-phosphocholine (POPC) and a high melting, saturated lipid like 1,2-dipalmitoyl-*sn*-glycero-3-phosphocholine (DPPC) or sphingomyelin (SM) in various ratios.[29–32] The phase behavior of this lipid mixture at different temperatures has been extensively studied by a variety of techniques including calorimetry,[33] NMR[33] and EPR spectroscopy,[31] x-ray scattering[34] and fluorescence microscopy.[29] A ternary phase diagram of

DOPC/SM/Chol is given in Figure 1.3. One at room temperature including tie lines is given in 4.24 on page 108. More detailed phase diagrams with varying lipids and temperatures can be found in the compendium of phase diagrams of Derek Marsh.[31, 32]
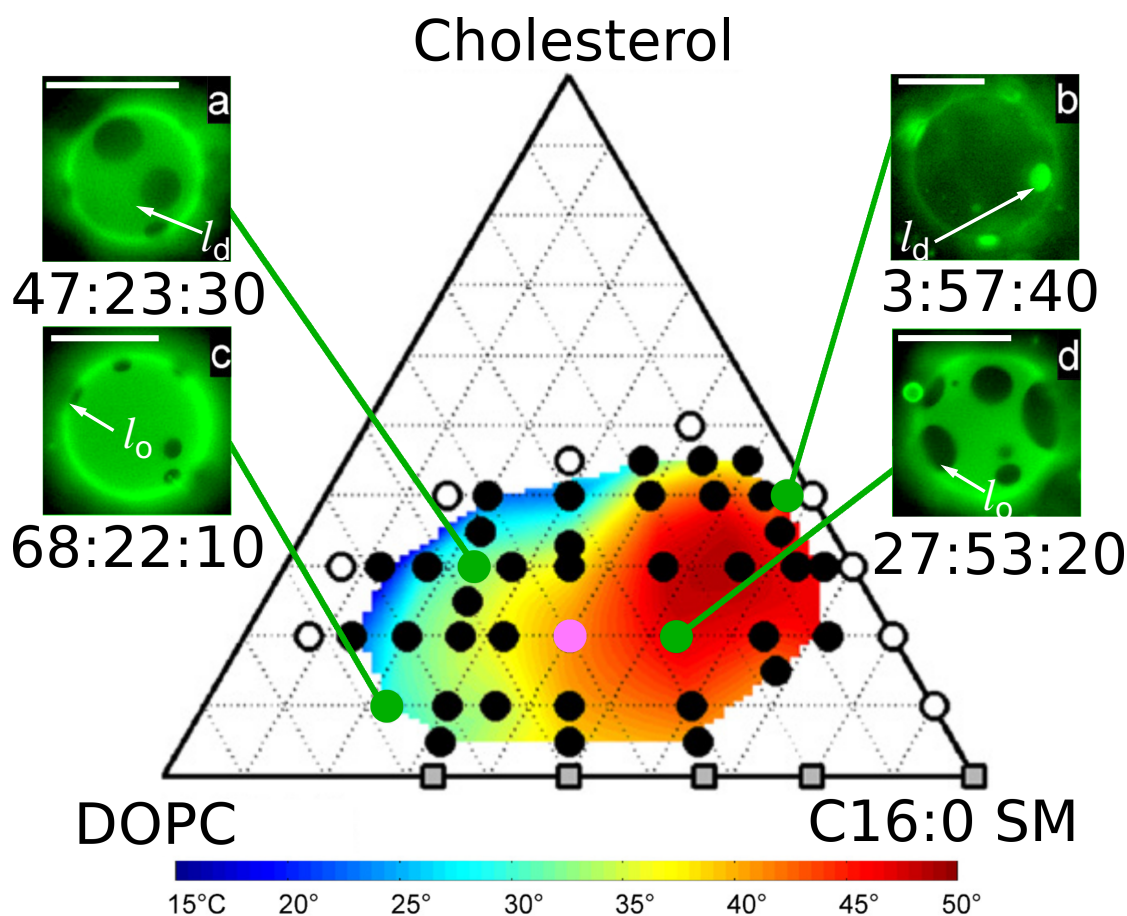
Figure 1.3: Phase diagram of DOPC/SM/Chol at different temperatures. The membrane segregates into domains identified by the partition of a fluorescent dye. Filled circles show compositions with coexisting l_o and l_d phase. The insets shows fluorescence micrographs of GUVs stained with a l_d selective dye. Scale bars: 20 µm. The magenta dot marks the lipid composition DOPC/SM/Chol 40:40:20 used as the matrix in this work. Image modified from Veatch and Keller.[30]

Below the phase transition temperature the membrane segregates into lipid phases.[29, 30] Using a bulky lipid coupled fluorescent dye the phases can be observed using fluorescence microscopy.[35] The steric demand, and in most cases the charge, prevent the tight packing of the dye in the more ordered phases, excluding them

to the disordered phase. This results in an enrichment in the l_d phase and brighter fluorescence.[35,36]

Veatch and Keller used confocal fluorescence microscopy to study the phase behavior of giant unilamellar vesicles (GUVs) and found micrometer sized dark l_o domains on the surface of GUVs.[29,30] Bezlyepkina determined the tie lines in the ternary mixture allowing to calculate the lipids compositions of the phases.[37] Indeed, the more ordered phase is enriched in cholesterol and sphingomyelin and resembles the composition of lipid rafts. Comparing their results to GPMVs reveals that GUVs exaggerate the properties of the ordered phase, resulting a large difference of diffusivity and membrane order between the two phases.[27]

Studying the phase separation into liquid-disordered and liquid-ordered domains therefore allows to study the properties of the putative rafts in an easy and controlled way. Classically, two different artificial model systems are employed.
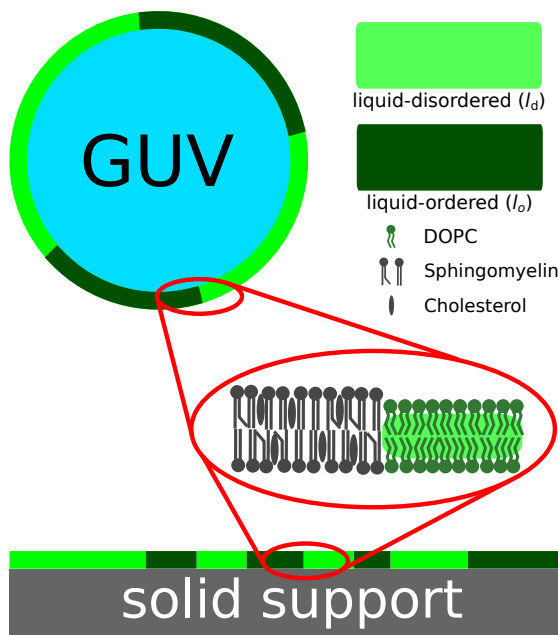
Figure 1.4: Schematic drawing of a phase-separated GUV and solid support membrane. The l_d phase enriched in DOPC can be identified by the bright green fluorescence. The l_o phase composed of SM and Chol appears dark.

Studying lipid vesicles of various sizes provides a system in which lipid diffusion and overall dynamics of the system are fast. Small and large vesicles with sizes between 20 and 1000 nm cannot be studied individually but only in bulk experiments. Using GUVs with diameters of 10 to 100 µm allows to visualize the phase separation with single vesicles by fluorescence microscopy. Figure 1.4 shows a schematic view of an equatorial slice through a giant vesicle. The ordered phase is identified by the exclusion of the fluorescent dye and lower diffusivity. Giant vesicles have the advantages that the membrane is freestanding and proteins can be added to bind to the outside of the vesicle. Furthermore, using more sophisticated techniques like micropipette aspiration and tether pulling, allows to adjust mechanical properties like tension and curvature of the membrane.[38,39]

However, they cannot be studied using by high resolutions techniques like atomic force microscopy (AFM).By spreading of vesicles, the membrane can be transfered to a solid support. The strong contact to the support leads to the formation of smaller lipid domains and the lateral movement of lipids and domains is strongly lowered.[40] Using techniques like surface plasmon resonance (SPR) and AFM allows to quantify the interaction of proteins with the membrane. AFM provides information about the topography of the samples and confirms the elevated height of the l_o phase ($\Delta h = 0.5$-$1\,$nm) which is caused by the assembly of saturated lipids and cholesterol.[41, 42] Biosensing techniques allow to extract binding affinities and capacities of proteins binding the (phase-separated) membrane.

In this thesis both solid supported membranes and giant unilamellar vesicles were used. Additionally pore-spanning lipid bilayers were employed. In this model system the membrane is suspended over several pores in a solid support. It has the advantage to combine the stability of solid supported membranes with the high lipid dynamics of GUVs in the freestanding membrane areas. They have previously been used to study membrane mechanics,[43–45] fission and fusion processes,,[46–50] the lateral organization of membranes[51, 52] and transmembrane transport.[49, 53] Their preparation is presented in Section 3.2.3.

1.3 Shiga toxin binding to its receptor Gb$_3$

Shiga toxin (STx) is a noxious protein produced by *Shigella dysenteriae.* Structurally the protein (70.5 kDa) is, like Cholera and Pertussis toxin, a member of AB$_5$ protein family.[54, 55] Enterohemorrhagic strains of *Escherichia coli* (EHEC) produce structurally highly related isoforms called shiga like toxin or verotoxins. The protein is of high clinical importance because infections with EHEC oder Shigella frequently lead to minor epidemics.[56] In 2011, contaminated fenugreek seed led to an outbreak of a hybrid culture of enteroaggegative *E. coli* and EHEC, infecting more than 4000 people. Symptoms include diarrhea and the hemolytic uremic syndrome which led to the death of 50 patients in Germany.[57]

Structure of Shiga toxin
Different isoforms of the protein are known. They are termed STx1 and STx2 with different variants STx2a-h.[58] STx1 differs in only one amino acid from STx but STx2 variants only share approx. 60 % sequence identity. They differ in their glycolipid

binding preference and cellular toxicity. In general, the protein can be divided into two parts. Figure 1.5A shows the crystal structure of the full length Shiga toxin. Panel B shows a schematic drawing of the protein structure. The A-subunit (STxA, 287 amino acids, 32 kDa, blue) has catalytic N-glycosidase activity, cleaving an adenine base at position 4324 of the 28S rRNA of mammalian cells. This obstructs protein biosynthesis and leads to cell death.[59] The A-subunit consists of two parts A1 and A2, additionally connected by a disulfide bond and is linked non-covalently to the 5 B-subunits. Each of the B-units consists of 69 amino acids (7.7 kDa) and forms a α-helical section and six β-sheets. The sheets of the different B-subunits interact forming a pentameric structure with the five α-helices creating a pore like structure which binds to one α-helix of the A-subunit. The B-subunits forms a pentagonal structure with an edge length of approximately 2.5 nm and a height of 2 nm.[60]
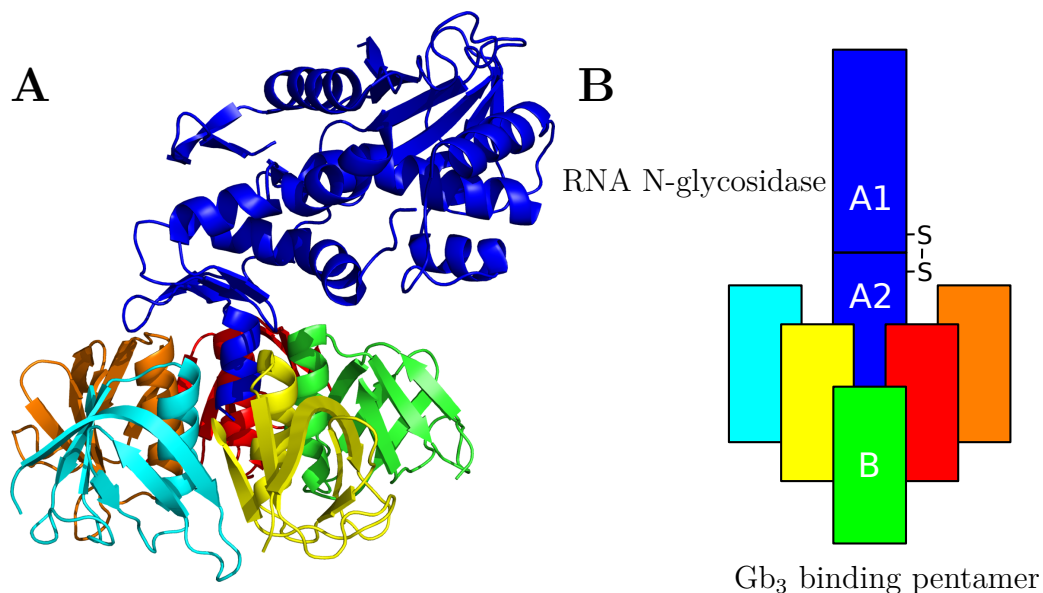
Figure 1.5: A Crystal structure of Shiga toxin (PDB 1DM0).[61] Gb$_3$ binding sites are located at the bottom of the colored pentameric B-subunit. **B** Schematic drawing showing the structure of the protein. The cell toxic A-subunit is colored blue.[62]

While the A-subunit has a toxic effect, the B-subunits facilitate the endocytosis of the protein. The amino acid sequence of STxB is given in Section 7.1.

Interaction of Shiga toxin with cellular membranes

The STx complex and the isolated B-subunits (STxB) interact with membrane via the binding to the glycosphingolipid globotriaosylceramide Gb$_3$ (CD77, Pk antigen).

As a glycoreceptor, Gb$_3$ is found in the extracellular leaflet of mammalian cells. It consists of trisaccharide headgroup (α-galactose(1-4)-β-galactose(1-4)-β-glucose) linked to a sphingosine backbone bearing different fatty acids (Figure 1.6). Ling *et al.* were able to crystallize the B-subunits of STx1 in presence of a water soluble analogue of Gb$_3$. They found that each of the subunits has three bindings sites for Gb$_3$, resulting in a total of 15 receptors bound to a single protein (Figure 1.7A).[60]
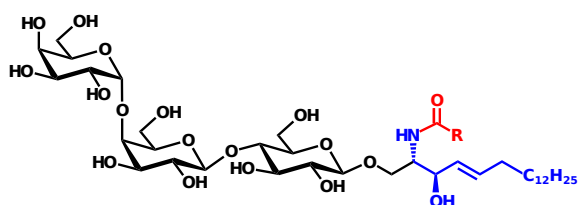
Figure 1.6: Structure of Gb$_3$. The sugar headgroup (black) is connected to the ceramide backbone (blue) which is linked to different fatty acids via an amide bond (red).

Using solution NMR Sihimizu *et al.* only found 5 bindings sites.[63] Pina *et al.* used UV/vis and CD spectroscopy to study the binding of STxB to its receptor.[64] The different sites are occupied consecutively with differing affinity.[64,65] The strongest binding (site 2) is mediated by hydrogen bonding. In site 1 hydrophobic interactions between the phenylalanine at position 30 and the terminal galactose are formed. Binding at the weakest site 3 is mediated by tryptophan 34.
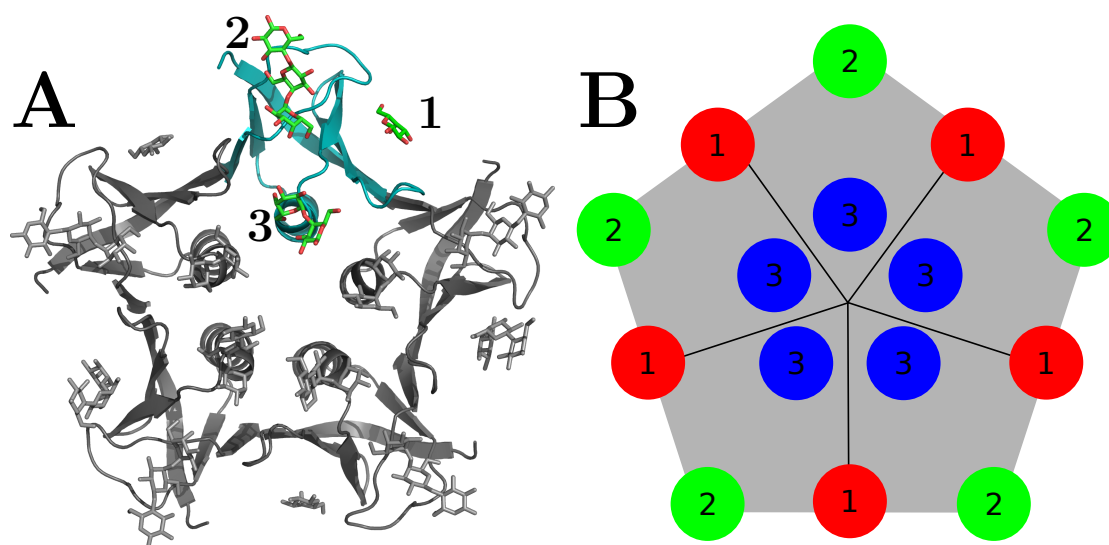
Figure 1.7: A Crystal structure of the STx1 B-subunit (PDB 1BOS) cocrystallized with a soluble Gb$_3$ receptor analogue.[60] The three different binding sites are numbered. **B** Schematic illustration of the binding sites of Gb$_3$. Sizes are drawn to scale.[60,66]

The binding induces minor changes in the protein structure which can be resolved in the UV/vis and CD spectra and comparing the crystal structures

in absence and presence of the receptor.[59–61,64] Replacing the tryptophan 34 does not inhibit protein binding and cell toxicity,[67,68] but reduces the ability to enter into high avidity interactions with Gb_3.[69] Figure 1.7B shows schematic drawing of STxB (gray pentamer) and the three different binding sites. The areas of the lipids and the protein are drawn to scale.[60,66]

It is apparent that occupation of all 15 binding sites leads to a crowding of the receptor below the protein.[60,66] This crowding has been identified as one of the main factors in the mechanism of the B-subunits' endocytosis because it leads to a lipid compaction underneath the protein. The endocytosis can occur independent of the usual pathways involving clathrin. Figure 1.8 shows the currently accepted model.[70] STxB binds to Gb_3 (blue) in the planar plasma membrane. First the high affinity binding sites are occupied.[64] Additional binding of Gb_3 saturates the other binding sites. The lipids underneath the protein get compacted as found by Laurdan microscopy.[39,71] This compaction leads to a stretching of the mostly fatty acids of Gb_3 and induces a local thickening of the membrane which leads to an exposure of the hydrophobic chains of the lipids to the aqueous environment (hydrophobic mismatch).[41,70] To minimize the evolving line tension multiple STxB pentamers start to cluster and minimize the circumference of the aggregate.[72] The headgroup compaction, induced

Figure 1.8: Endocytosis of STxB. The protein binds to its receptor Gb_3 and the subsequent binding of more Gb_3 induces lipid compaction. The resulting line tension is decreased by the induction of curvature in the membrane.[70]

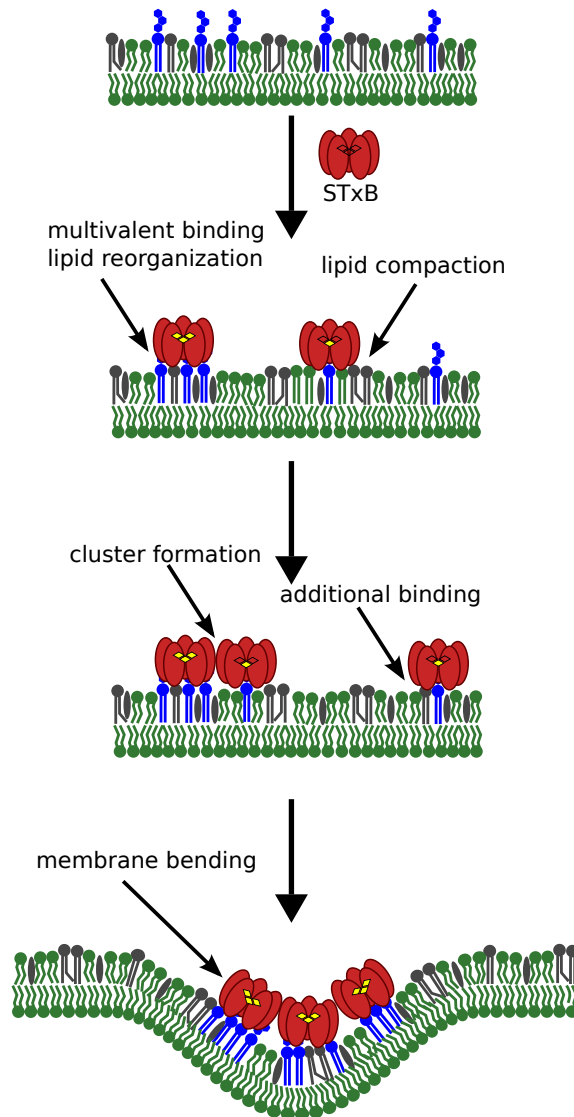by STxB binding, favors the emerging of negative curvature in the upper leaflet of the membrane. Given a sufficient cluster size and low membrane tension it is therefore energetically favorable to bend the membrane forming an invagination.[72] This minimizes line tension because the 3D invaginations has a lower contact line to the surrounding thinner membrane than the 2D STxB aggregate. Using GUVs composed of DOPC, cholesterol and Gb₃, Römer *et al.* could show that the interactions of Gb₃ with STxB is sufficient to induces the formation of membrane tubes in artificial membranes.[71] However, endocytosis of the protein requires scission of the tubes which was achieved by dynamic rearrangement by the underlying F-actin cytoskeleton in HeLa cells.[39]

Lingwood and coworkers determined the affinities of Shiga-like toxins to Gb₃ with different fatty acids. They found that long carbon chains, unsaturation and hydroxylations of the fatty acids increase binding capacity.[66,73,74] The affinities towards the protein are in the low nanomolar range.[75] Using GUVs, Römer assessed differences in the propensity to facilitate the formation of invaginations as a function of the fatty acids. Gb₃ bearing a saturated C22:0 chain bound to Gb₃ but no invaginations were found. Gb₃ with an unsaturated C22:1 chain readily induced invaginations. From the experiments no distinct reasons for this behavior could be extracted but a link to different capabilities in stabilizing negative curvature are hypothesized.[71,72]

Shiga toxin tranport in cells

STx's endocytosis and intramolecular fate have attracted wide spread interest, because the toxin's receptor lipid is overexpressed in certain cancers like gastric, intestinal or testicular cancer.[76] Additionally, cargo can be bound to STxB, allowing to insert it into cells bypassing the usual endocytosis pathways. A detailed overview is given by Johannes and Römer in their review.[59] Figure 1.9 shows the route of STx.
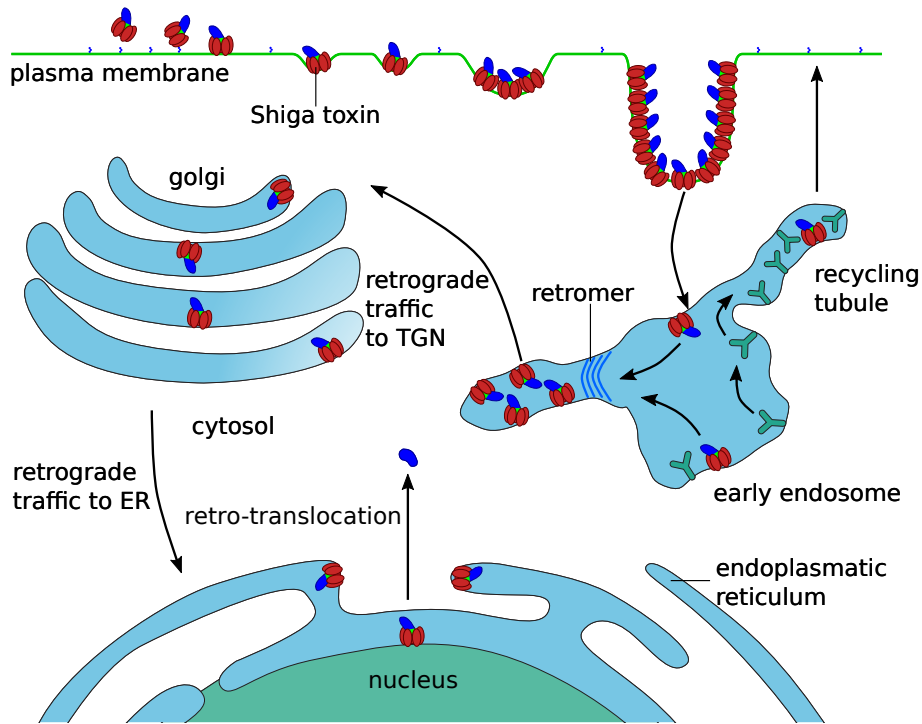
Figure 1.9: Cellular pathway of STx. After internalization the toxin is translocated to the ER via the retrograde pathway. The A-subunit is then released into the cytosol. Image modified from Johannes *et al.*.[59]

The protein binds to the plasma membrane (green) via Gb$_3$. Invaginations are formed resulting in vesicles after scission of invaginations. The protein follows the retrograde pathway to the early endosome. In the endosome it is selectively sorted into areas of high negative curvature like the recycling tubules. Different proteins involved in endocytosis like epsin, clathrin and the retromer complex form vesicles including STx. These are traveled to the endoplasmatic reticulum via the *trans*-golgi network. The A1-subunit is cleaved from the protein by proteases in the early endosome but remains bound to STxA2-STxB complex by the disulfide bridge which finally gets reduced in the lumen of the ER. The A1-subunit is translocated to the cytosol and catalytically inhibits protein biosynthesis.[59]

2 Scope of the thesis

The plasma membrane of mammalian cells is composed of different lipids and proteins. Their interaction and the underlying cytoskeleton lead to a complex lateral organization of the membrane, controlling important cellular processes. Artificial model systems can be used to study the phase behavior of lipid bilayers under chemically defined conditions.

The aim of this thesis is to understand how lipid-lipid interactions and the physical contact of the membrane to a support change the structure and the dynamics of phase-separated lipid bilayers including the Shiga toxin receptor lipid globotriaosylceramide (Gb_3).

Different cell lines show varying vulnerability towards infections with Shiga toxin producing bacteria and in these cells Gb_3 differs in the fatty acid bound to the ceramide backbone. To investigate a possible influence of the bound fatty acid on the binding of Shiga toxin, biosensing techniques are used to determine the affinities of the distinct Gb_3 species towards the toxin. The lateral organization of solid supported membranes doped with different Gb_3 derivatives is investigated using fluorescence and atomic force microscopy allowing to study how the lateral organization and binding of STxB influence each other in a mutual way. A special emphasis is put on the biologically most relevant Gb_3 species found in cancer cells.

Pore-spanning lipid bilayer (PSLBs) are employed as a minimal model system for the interaction of the plasma membrane with the cytoskeleton. Using porous substrates, with different pore diameters and surface porosities, enables to study how the compartmentalization of the membrane into freestanding and solid supported areas modulates the phase behavior of the artificial membrane. Employing fluorescence and scanning ion-conductance microscopy the interplay of membrane topography and lateral membrane organization on the dynamics of lipids domains and the binding of Shiga toxin are investigated. This allows to rationalize how the actin cytoskeleton in cells can control dynamic processes occurring at the plasma membrane.

3 Materials and methods

3.1 Used materials

3.1.1 Matrix lipids

In this thesis artificial lipid membranes composed of different lipids were used as a mimic of the plasma membrane. All membranes were composed of the fluid phospholipid 1,2-dioleoyl-*sn*-glycero-3-phosphocholine doped with the Shiga toxin receptor Gb_3. Additionally a 'raft-like' lipid mixture including cholesterol and sphingomyelin was used to mimic the presumed lateral organization of the outer leaflet of the plasma membrane more closely.

1,2-Dioleoyl-*sn*-glycero-3-phosphocholine (DOPC)
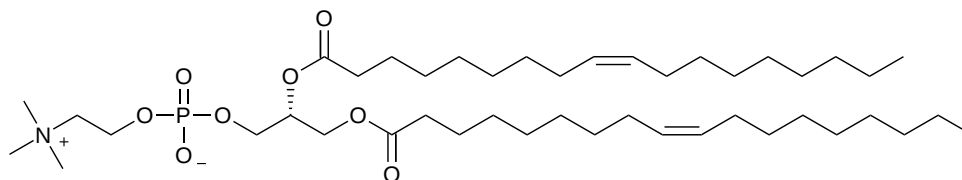
Scheme 3.1: Structure of 1,2-dioleoyl-*sn*-glycero-3-phosphocholine (DOPC).

DOPC (Scheme 3.1, $C_{44}H_{84}NO_8P$, $M = 786.15\,\mathrm{g\,mol^{-1}}$) is a synthetic phospholipid consisting of a zwitterionic choline headgroup, a glycerol backbone and two oleic acid moieties. The fatty acids consist of a linear carbon chain with an (*Z*) configurated double bond in position Δ^9. The double bonds form kinks in the membrane impairing tight lipid packing, leading to a low main transition temperature of –20 °C. It is frequently used in *in vitro* studies as a substitute for the naturally occurring 1-palmitoyl-2-oleoyl-*sn*-glycero-3-phosphocholine (POPC) because it forms soft, fluid membranes and has a lower tendency to form nanoscopic

lipid domains which impair the use of fluorescence microscopy.[77]

Sphingomyelin (SM)
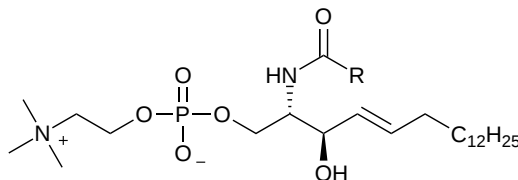
Scheme 3.2: Structure of sphingomyelin (SM). R corresponds to different fatty acids as listed in Table 3.1.

Sphingomyelin (SM, Scheme 3.2) is a major component of the outer leaf plasma membrane of animal cells,[78] where it constitutes up to 30 % of the total lipids. It occurs as a mixture of several molecules differing in their fatty acid. SM consists of a C18:1 sphingosine backbone with a choline headgroup. The fatty acid is attached via an amide linkage. In this thesis sphingomyelin from bovine or porcine brain was used. The main component of these mixtures is C18:0 SM ($C_{41}H_{83}N_2O_6P$, $M = 731.09\,\mathrm{g\,mol^{-1}}$). The fatty acids attached to the backbone are similar for both SMs used and proved to show identical phase behavior (Table 3.1). In lipid membranes, SM forms specific interactions with cholesterol leading to the formation of liquid-ordered phases in fluid phospholipids matrices.[78] The mostly saturated fatty acids lead to a high main transition temperature of $+41\,^\circ\mathrm{C}$.[29]

Table 3.1: Molecular species of bovine and porcine brain sphingomyelin. Data taken from Shaw *et al.*,[79] Ramstedt *et al.*[80] and Avanti Polar Lipids.[81]

Fatty Acid	% of bovine SM[79]	% of bovine SM[80]	% of porcine SM[81]
C16:0	2	2	2
C18:0	49	43	50
C20:0	5	6	5
C22:0	8	8	7
C22:1	-	4	-
C23:0	-	2	-
C23:1	-	2	-
C24:0	6	6	5
C24:1	20	27	21
Others	10	-	10

Cholesterol (Chol)
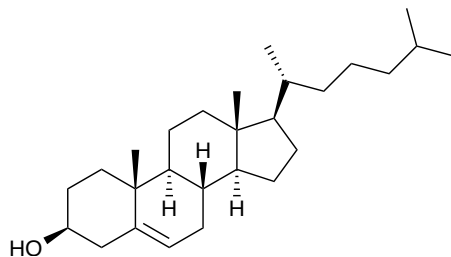
Scheme 3.3: Structure of cholesterol (Chol).

Cholesterol (Chol, Scheme 3.3, $C_{27}H_{46}O$, $M = 386.65\,\mathrm{g\,mol^{-1}}$) is a steroid that constitutes up to 20 to $40\,\%$ of mammalian cell membranes.[1] In membranes it acts as a regulator of fluidity. The rigid tetracyclic backbone increases the order of saturated fatty acid chains and stiffens the upper part of the hydrophobic membrane regions. Specific interactions with sphingomyelin and glycolipids alter the organization and function of these lipids.[75, 78]

3.1.2 Fluorescent probes

In this thesis fluorescence microscopy (Section 3.3.1) was used as the main tool to investigate the membrane organization. The techniques requires the use of lipid coupled dyes to visualize the membrane.

Dyes to label the l_d phase

To be able to observe the phase separation (Section 1.2) sterically demanding dyes can be used, that preferentially enrich in the disordered phase.[35] Even though their partition coefficient between the phases varies,[36] they offer sufficient contrast to unambiguously identify the disordered membrane phase and quantify its area. An overview of partitions coefficients between the disordered and ordered phases in GUVs and GPMVs is given by Sezgin *et. al.*.[36] In Scheme 3.4 the chemical structures of four different dyes to label the l_d phase are shown.
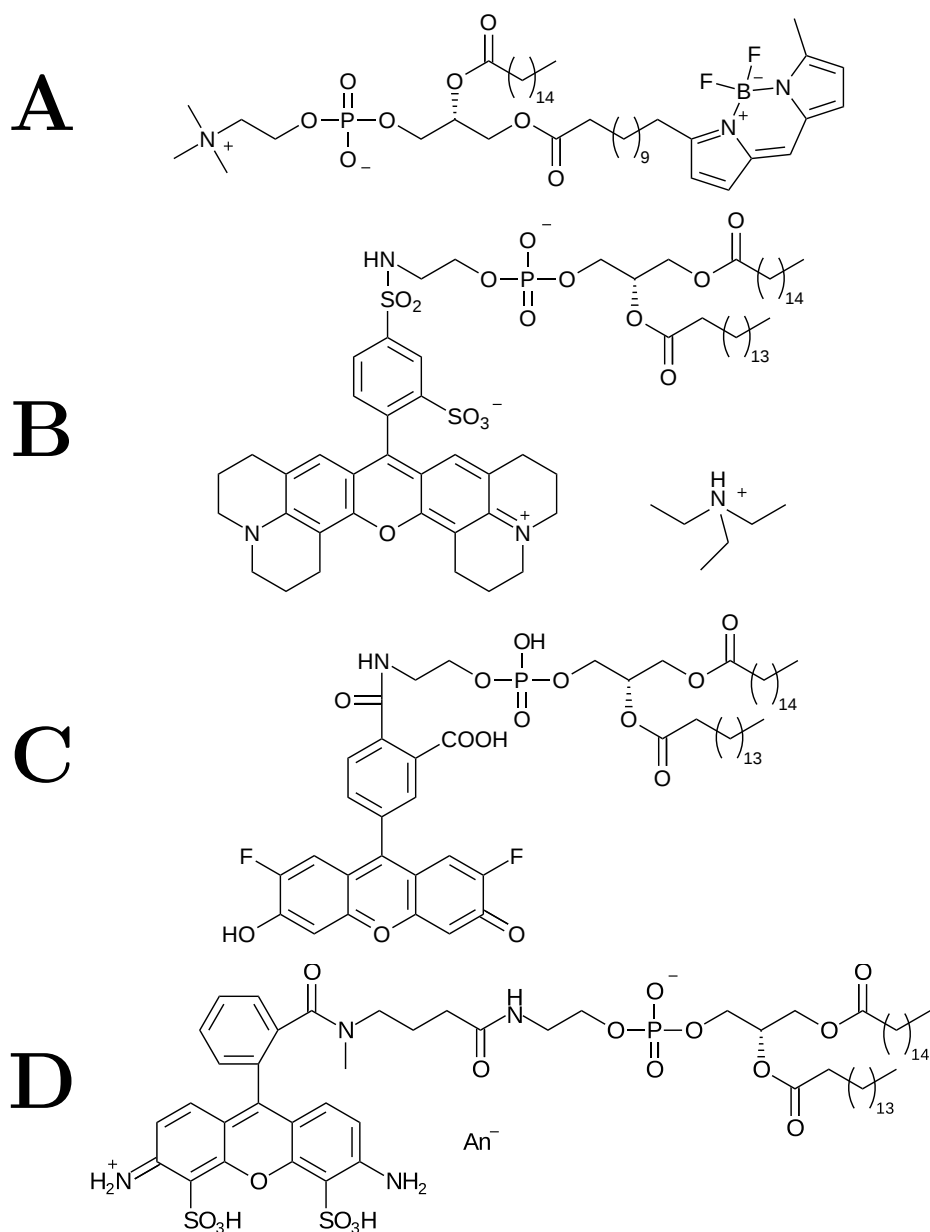
Scheme 3.4: Structures of the lipid coupled dyes used to label the l_d phase. **A** Bodipy-PC **B** TexasRed DHPE triethylammonium salt **C** OregonGreen DHPE **D** Atto488 DHPE.

Bodipy-PC is based on a phosphatidylcholine lipid (Scheme 3.4A). The fatty acid at position 1 is functionalized with a boron-dipyrromethene fluorophor. The steric demand of the fluorophor expels the dye from the ordered phase.

TexasRed DHPE, OregonGreen DHPE and Atto488 DHPE (Scheme 3.4B-D) are all based on a saturated phospholipid and a xanthen based fluorophor attached to the headgroup. The bulky polyaromatic structure and the charge expel the molecules

from the tightly packed l_o phase despite the saturated fatty acid.

All four dyes were used to label the l_d phase and the l_d area percentage was found to be independent of the dye used. Bodipy-PC, OregonGreen and Atto488 were used in combination with the more red shifted Cy3 labeling STxB. The spectral properties of the dyes are given in Table 3.2.

Perylene

In contrast to the dye that selectively label the l_d phase, perylene (Scheme 3.5, $C_{20}H_{12}$, $M = 252.32\,\mathrm{g\,mol^{-1}}$) is a small, uncharged non-polar polyaromatic molecule. It partitions in the membrane and shows no strong affinity for the l_d phase. Depending on the exact chemical composition of the membrane it preferentially partitions in the l_o or l_d phase but the partition coefficient is close to one.[35] Its photostability and spectral properties (Table 3.2) are rather poor but the low excitation and emission wavelength allow to combine perylene with the dyes to label the l_d phase. Perylene can thus be used to discriminate the l_o phase from non membrane covered regions.
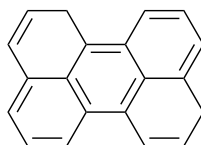
Scheme 3.5: Structure of perylene.

STxB-Cy3

STxB labeled with the fluorophor Cy3 (Scheme 3.6) was obtained from Prof. Dr. Winfried Römer (BIOSS an Institute of Biology II, Albert-Ludwigs University Freiburg). The protein was expressed in *E. Coli*, purified by ion exchange chromatography and fluorescently labeled at a lysine residue.[54] This construct allows to localize STxB by fluorescence microscopy after binding to Gb_3 in membranes. The spectral properties of the dye are given in Table 3.2.
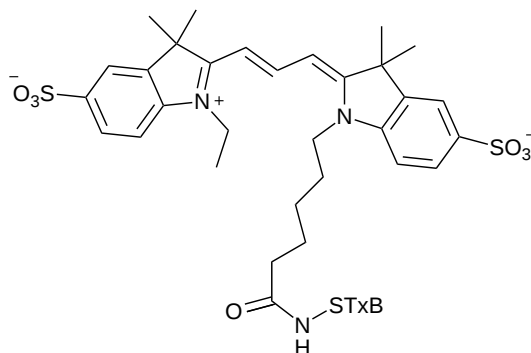
Scheme 3.6: Structure of the Cy3 STxB conjugate.

Table 3.2: Spectral properties of the fluorescent dyes used and excitation/emission wavelength used by the CLSM.

Dye	λ_{exc}^{max}/nm	λ_{em}^{max}/nm	ϵ/M^{-1} cm^{-1}	λ_{ex} CLSM	λ_{em} CLSM‡
Bodipy-PC[82]	500	510	>80000	488 nm	496-575 nm
TexasRed[82]	595	615	85000	561 nm	574-620 nm
OregonGreen[82]	501	526	85000	488 nm	496-575 nm
Atto488[83]	501	523	90000	488 nm	496-575 nm
perylene[84]	436	436	38500	405 nm	408-479 nm
Cy3[82]	550	570	136000	561 nm	574-620 nm

‡ Typical values. Detection was adjusted for maximum contrast.

3.1.3 Gb₃ glycosphingolipids

Globotriaosylceramide (Gb$_3$, CD77, Scheme 3.7) is the natural receptor lipid of Shiga toxin. It is located in the outer leaflet of mammalian plasma membranes. Its biological function is unknown and knockout mice show no altered phenotype.[85] The lipid consists of trisaccharide headgroup (α-galactose(1-4)-β-galactose(1-4)-β-glucose) linked to the sphingosine backbone bearing different fatty acids. In this work Gb$_3$ from porcine erythrocytes (Gb$_3$-Porc, Table 3.3) was used. Additionally, chemically pure Gb$_3$ derivatives bearing defined fatty acids were synthesized in the group of Prof. Dr. Daniel B. Werz (Institute of Organic Chemistry, Technical University Braunschweig) according to the retrosynthetic Scheme 3.7. Details of the syntheses are presented elsewhere.[86–88]
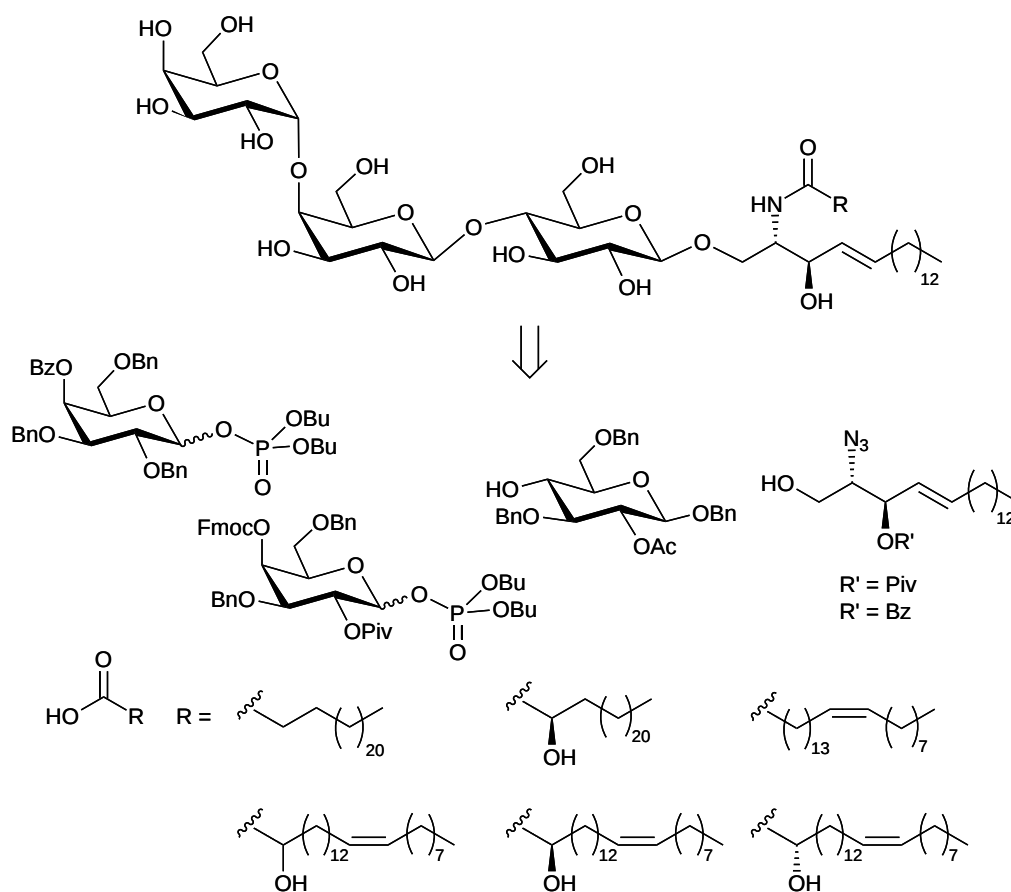
Scheme 3.7: Retrosynthetic pathway to Gb$_3$.

Even though the interaction with STxB is headgroup mediated the fatty acid was found to influence binding and cell toxicity.[54,66,73,74] Different cell lines express different Gb$_3$ species.

Table 3.3: Molecular species of Gb_3 in different cells. Data for erythrocytes and HeLa cells are taken from Figure S4 of Römer *et al.*.[39] Gb_3 derivatives investigated in Section 4.1 and 4.2 are printed in bold.

Fatty Acid	% of total Gb_3 in	
	Erythrocytes	HeLa
C16:0	3	3
C18:0	2	0
C18:1	2	0
C20:0	2	0
C22:0	17	3
C23:0	1	7
C24:0	**29**	**6**
C24:1	**5**	**1**
C22:0 2-OH	3	10
C23:0 2-OH	1	0
C24:0 2-OH	**19**	**29**
C24:1 2-OH	**10**	**41**
Others	6	0

3.2 Preparative methods

Artificial lipid membranes mimicking the outer leaflet of the mammalian plasma membrane were prepared on different supports.

3.2.1 Preparation of unilamellar vesicles

To create planar artificial membranes on solid or porous support, vesicles are spread above the phase-transition temperature of the lipid mixture. Small and large unilamellar vesicle can be used to form solid supported membranes. Spanning the micrometer sized pores of porous substrates requires to use giant unilamellar vesicles.[89]

Small and large unilamellar vesicles

Small and large unilamellar vesicles (SUV and LUVs) have a diameter of 20 to 1000 nm. They are used in bulk assays and to form planar solid supported membranes. Spreading of the vesicles on the support results in the full coverage of the support because upon spreading the individual vesicles fuse to form a homogeneous membrane.[89] SUVs were used for surface plasmon resonance spectroscopy (SPR) and

reflectometric interference spectroscopy (RIfS) experiments and LUVs were spread to form membrane for AFM and fluorescence microscopy experiments.

Experimental procedure

Stock solutions of DOPC, sphingomyelin and cholesterol where prepared in chloroform. Final concentration ($c \approx$ 1-2 mg mL^{-1}) was determined using a Langmuir film balance and the A_{20} value of the lipids. Gb$_3$ derivatives were dissolved in chloroform:methanol 3:1 (*v:v*) and used without further analysis. Stock solutions of lipid coupled fluorescent dyes were prepared in chloroform or mixtures of chloroform/methanol. To obtain lipid films, the stock solutions were mixed in the desired molar ratio with 250 µL chloroform:methanol 4:1 (*v:v*) in glass test tubes. The solvent was evaporated under a constant stream of nitrogen at 55 °C above the phase separation temperature of the lipid mixture. The film was further dried at 55 °C for 3-12 h under reduced pressure. Films were stored at 4 °C until use.

Lipid films were hydrated in 500 µL buffer (PBS - phosphate buffered saline, 2.7 mM KCl, 136 mM NaCl, 1.5 mM KH$_2$PO$_4$, 8.1 mM Na$_2$HPO$_4$, pH 7.4 for small vesicles, 20 mM TRIS/HCl, 100 mM NaCl, 1 mM CaCl$_2$, pH 7.4 for large vesicles) at 55 °C for 30 min. The resulting suspension was vortexed three times for 30 s in 5 min intervals to detach the lipid stacks from the glass and form multilamellar vesicles (nominal lipid concentration 0.2-0.3 mg mL^{-1}).

For large unilamellar vesicles the suspension was extruded at 55 °C through a 50 nm polycarbonate membrane using a miniextruder. The solution was diluted to 1000 µL and stored at 55 °C in a sealed tube. To obtain small unilamellar vesicles the suspension was diluted to 1000 µL and sonified using a Bandelin sonopuls bath sonifier for 30 min (4 Cycles, 80 % intensity). Prior to SPR experiments the suspension was further diluted by adding 5000 µL of buffer solution. The suspensions were stored at room temperature until used.

Giant unilamellar vesicles

Giant unilamellar vesicles (GUVs) have a diameter of 10 to 100 µm. Due to their size, the lipid membrane can be investigated by fluorescence microscopy. The standard technique to form the vesicles was introduced by Angelova and relies of the controlled detachment of lipid films from a conductive surface by applying an alternating current.[90] The electroformation method reproducibly forms unilamellar vesicles in good yields and can also be applied to lipid mixtures that exhibit phase separation at room temperature.[29]

Experimental procedure

Indium tin oxide (ITO) slides were cleaned with ethanol, water and chloroform and dried under a stream of nitrogen. Using the Agilent frequency generator the slides were prepared with a silicone spacer and adhesive copper electrodes. Slides were preheated to 55 °C in a heating oven. Stock solution of the lipids were mixed to give the desired lipid ratio. The mixture was slowly applied to the ITO slide using a hamilton syringe to avoid the formation of droplets. The lipid film was rehydrated using preheated sucrose solution ($c = 200\text{-}300\,\mathrm{mmol\,L^{-1}}$) to give a final lipid concentration of $c = 0.05\text{-}0.2\,\mathrm{mg\,mL^{-1}}$. The solution was kept at 55 °C for 15 min. A sinusoidal AC voltage of 1.6 V (12 Hz) was applied for 2 to 3 h. The frequency was subsequently lowered to 5 Hz and a square voltage was applied for 15 min. The samples were slowly cooled to room temperature in the heating oven (3-6 h) and stored at 4 °C or room temperature for up to three days. Using the Nanion VesiclePrep protocol, the voltage and frequency changes were applied gradually over 30 min and using the square wave was omitted.

Giant unilamellar vesicles were used to form pore-spanning lipid membranes as described in Section 3.2.3. The percentage of ordered phase lipids of the vesicles was determined as described in Section 3.4.1.

Experiments to quantify the propensity of Gb_3 derivatives to facilitate the formation STxB induced invaginations (Section 4.2.3.1) were performed as follows. The vesicles were prepared in sucrose solution. The osmolarity was measured and isoosmotic mixtures of PBS and glucose solution were prepared in a petri dish. STxB or STxB-Cy3 was added to give a final concentration of 60 nM. The GUVs were added and allowed to settle to the bottom of the petri dish for 10 min. Imaging was performed using the CLSM or SDCLM using both confocal slices and z-stack imaging. Measuring time was limited to ≈ 20 min to avoid an influence of buffer evaporation. The experiment was then repeated under identical conditions. The images were manually inspected using ImageJ and matlab to determine the fraction of vesicles showing invaginations and STxB clusters. Percentages are given as mean ± pooled standard deviation between the individual experiments.

3.2.2 Solid supported membranes

Spreading unilamellar vesicles on planar surfaces enables the creation of defect free two dimensional membranes.

Lipid bilayers on hydrophilic substrates

Solid supported membranes (SSMs) were created by spreading of large unilamellar vesicles on mica support ($KAl_2[(OH, F)_2/AlSi_3O_{10}]$). Atomically flat mica sheets were created by repeated removal of the upper mica layers using adhesive tape. Mica sheets (1.2 by 0.8 cm) were mounted in custom made PTFE chambers and heated to 55 °C. Vesicles were spread at elevated temperature (55 °C) above the phase-transition temperature ($T_M \approx 40$ °C).[30] 200 µL vesicles suspension was added to the substrate and the calcium concentration was increased to 10 mM by adding $CaCl_2$ to induce spreading. After 10 min Ca^{2+} concentration was lowered to 1 mM by adding buffer solution and spreading was continued for further 50 min. After cooling to room temperature, excess vesicles were removed by rinsing with 100 mL PBS. Membranes were incubated with STxB or STxB-Cy3 at a final concentration of 60 nM by adding a stock solution of the protein and vigorous mixing using a pipette. After 1 h samples were rinsed with PBS.

Hybrid bilayers

The preparation of hybrid bilayers used for SPR experiments is described in Section 3.3.4.1 and Figure 3.14.

3.2.3 Pore-spanning lipid bilayers

Different porous substrate with varying pore diameter and surface porosity were used (Figure 3.1). The porosity is defined as the ratio of pore area compared to the total area of the porous regions of the substrate.

$$P = \frac{A_{\text{pores}}}{A_{\text{total}}} \tag{3.1}$$
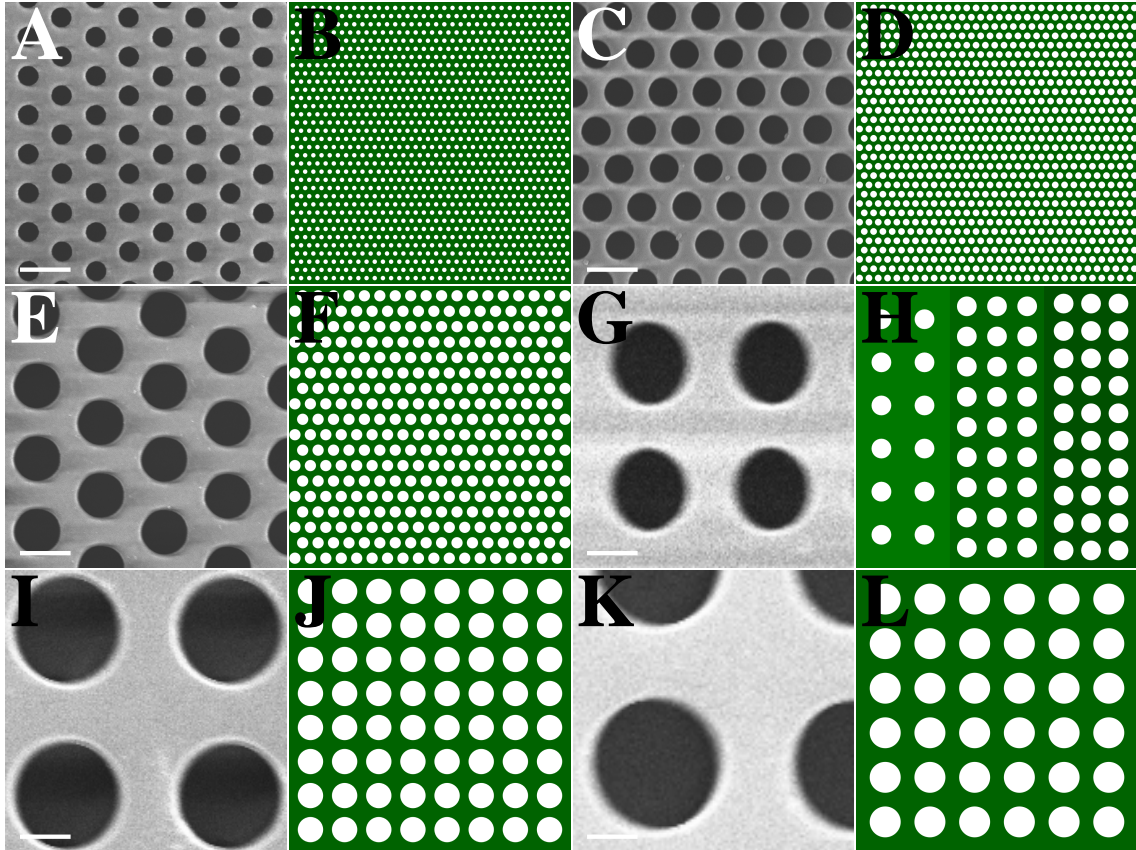
Figure 3.1: Scanning electron microscopic and schematic drawing of the substrates used. Scale for all SEM images is identical to allow for direct comparison of the pore sizes. For SEM imaging the samples were coated with gold. The schematic drawings illustrate the pore sizes and porosities at a smaller scaling. **A/B** Pore diameter 0.8 µm, porosity 23 %. **C/D** Pore diameter 1.2 µm, porosity 41 %. **E/F** Pore diameter 2.0 µm, porosity 41 %. **G/H** Pore diameter 3.5 µm, porosity 39, 28, 14 %. **I/J** Pore diameter 4.5 µm, porosity 38 %. **K/L** Pore diameter 5.5 µm, porosity 36 %. Scale bars: 2 µm. Panels **A**, **C** and **E** modified from Orth.[52]

All substrates used have the structure of a sieve or the cylindric pores that are linked at the bottom by over etching. Table 3.4 summarizes the properties of the porous substrates used.

Table 3.4: Properties of the porous substrates used.

pore diameter / µm	porosity / %	material	supplier
0.8	23	silicon nitride	fluXXion
1.2	41	silicon nitride	fluXXion
2.0	41	silicon nitride	fluXXion
3.5	39	silicon dioxide	CAESAR[53]
3.5	28	silicon dioxide	CAESAR
3.5	14	silicon dioxide	CAESAR
4.5	38	silicon dioxide	CAESAR
5.5	36	silicon dioxide	CAESAR

The substrate were rinsed with ethanol, dried under a stream of nitrogen and cleaned using argon plasma. The surface was sputter-coated with a thin layer of titanium (40 mA, 20 s, 0.7 mbar). Gold was evaporated atop with a thickness of 30 nm at a deposition rate of $\approx 0.3\,\mathrm{nm\,s^{-1}}$. The substrate were incubated overnight in a solution of 1-mercaptohexanol (1 mM in n-propanol) at room temperature.

Spreading of GUVs on hydrophilically functionalized gold surfaces
Figure 3.2 illustrates the preparation of pore-spanning lipid bilayers (PSLBs). GUVs were prepared as described in Section 3.2.1. The gold coated, hydrophilically functionalized substrates were rinsed with n-propanol to remove residual mercaptohexanol.
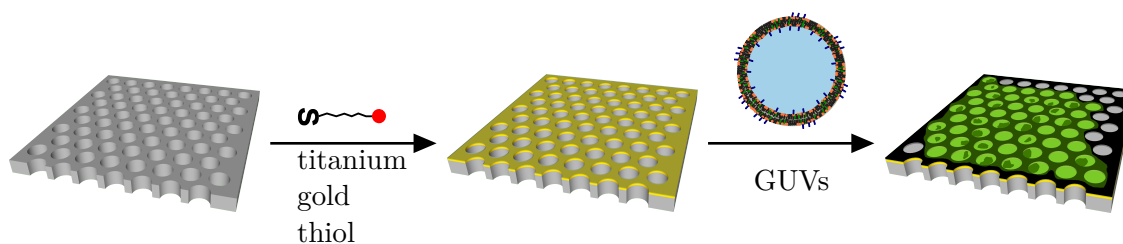

Figure 3.2: Scheme showing the preparation of pore-spanning lipid bilayers. The substrates are coated with an adhesive titanium layer and after evaporation of gold mercaptohexanol self assembles on the surface. Spreading of GUVs above the phase separation temperature and subsequent cooling leads to the formation of PSLBs.

The substrates were built into custom made, weighted PTFE chambers with a total volume of 2-3 mL and covered with a small volume of *n*-propanol. After 5 min, the chamber was filled with 1.5 mL spreading buffer (100 mM KCl, 10 mM CaCl$_2$, 10 mM HEPES, pH 7.4). It was rinsed carefully 17 times with buffer by exchanging 1 mL of the total volume to remove the organic solvent. After rising, the chamber was filled with buffer and put in a preheated oven at 55 °C. The GUV solution (2-4 µL) was carefully trickled into the solution and the GUVs were allowed to spread for 2 h at 55 °C. After cooling to room temperature (1 h) the samples were rinsed with PBS to remove residual GUVs.

The pore-spanning membranes were then imaged using SICM or fluorescence microscopy. Fluorescence images of the membrane organization were recorded using two color imaging (perylene and a l_d marker dye). Image settings were individually adjusted to enhance the image quality. The surface of the substrates was not fully covered by membrane, but isolated patches resulting from spreading of individual GUVs were found.

Incubation with STxB(-Cy3)

STxB was obtained from Prof. Dr. Winfried Römer (BIOSS an Institute of Biology II, Albert-Ludwigs University Freiburg). The protein was expressed in *E. Coli*, purified by ion exchange chromatography.[54]

The buffer volume in the sample chambers was reduced to $\approx$ 1.5 mL and determined using a balance. A defined volume of the STxB or STxB-Cy3 stock solution in PBS was added and the solution was vigorously mixed using a pipette to give a final concentration of 60 nM. The concentration refers to the pentameric B-subunit, not the B-monomer. After incubation for 1 h at room temperature in the dark, the samples were rinsed with 100 mL PBS to remove unbound protein. The membranes were reimaged using the fluorescence microscope.

All fluorescence data was evaluated using Zen, ImageJ or by a custom written matlab software (Sections 3.4.2 and 3.4.3).

Cholesterol extraction using methyl-βcyclodextrin (mβCD)

Methyl-β-cyclodextrin (mβCD, Scheme 3.8) allows to selectively extract cholesterol from lipid membranes. The molecule is built up of seven hexoses linked to a ring. The formed cavity is of suitable size to include one cholesterol molecule in a complex. To increase water solubility the sugars are partially methylated depriving the molecule

of intramolecular hydrogen bonds. By adding mβCD the cholesterol is extracted from the membrane into the aqueous phase.[91]

R = H, Me
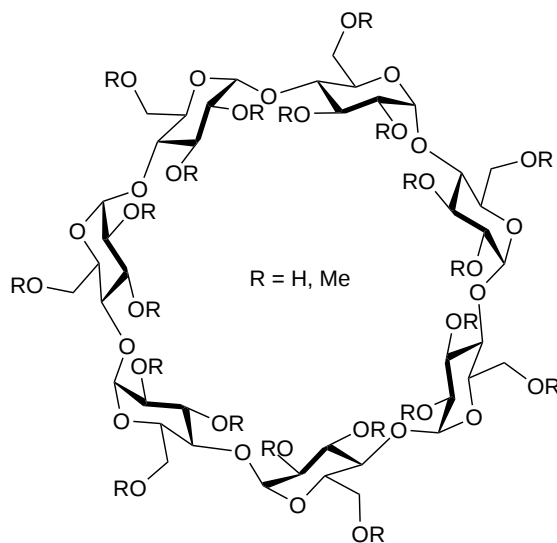
Scheme 3.8: Structure of mβCD.

Experimental procedure

The experimental procedure was adapted from Orth *et al.*.[51,52] A defined volume of a mβCD-stock solution in ultrapure water ($c = 38\,\text{mM}$) was added to the measuring chamber giving a final concentration of $1\,\text{mM}$. The membrane was then imaged over time and the area occupied by l_o area and bound STxB was quantified as described in Section 3.4.2.

3.3 Biophysical methods

Different biophysical techniques were used to study artificial membranes.

3.3.1 Fluorescence microscopy

Fluorescence microscopy was used as the main tool to visualize the organization of the lipid membranes by imaging the localization of fluorescently labeled lipids (Section 3.1.2). In this thesis three different types of microscopes were used. Epifluorescence allows to image the two dimensional organization of planar membranes. Confocal laser scanning microscopy uses a pinhole to allow for the directed investigation of confocal slices of the specimen, adding the possibility to extract

information about the three dimensional structure of the sample. Spinning disc confocal laser microscopy is an advanced version of the confocal microscope allowing high speed and high throughput imaging of three dimensional samples.

Fluorescence terms the emission of light after excitation of a molecule. The fluorophor is usually excited using monochromatic light, resulting in a vibronic transition of the molecule from the vibrational and electronic ground state an excited electronic and vibrational state. In the condensed phase, e.g. aqueous solution, the fluorophor rapidly relaxes into the vibrational ground state of the exited electronic state by collisions with surrounding molecules. The life time of this state is typically in the range of nanoseconds before the molecule will emit a photon isotropically and relax back to the electronic ground state. Due to the energy dissipation by collisions, the emitted photon will be red-shifted (Stokes-Shift). This allows for the simultaneous excitation of a specimen and the detection of the emitted light at lower wavelengths.

3.3.1.1 Epifluorescence and confocal laser scanning microscopy

Figure 3.3A shows a setup of an epifluorescence microscope. The light source used for excitation is a mercury lamp emitting white light. An adjustable emission filter blocks all light except the wavelengths needed for excitation (green). The light is directed onto the sample by a dichroic mirror and an objective, exciting the fluorescent molecules. The emitted light (red) can pass the mirror, is further filtered and detected on a camera. The microscope always illuminate the whole sample, making it possible to detect the fluorescence on the camera frame-by-frame, allowing for high time resolution and sensitivity. The lateral resolution achieved is limited by the Abbe's law. Using the definition to separate two objects by the full width at the half maximum of the intensity point spread function the resolution is

$$d_{\text{FWHM}} = \frac{0.51 \cdot \lambda_{em}}{n \sin \alpha} = \frac{0.51 \cdot \lambda_{em}}{NA} \tag{3.2}$$

with λ_{em}: emission wavelength, $NA = n \sin \alpha$: numerical aperture of the objective, n refractive index of the imaged medium and α the opening angle of the objective.[92] For for typical wavelengths and objectives used the resolution is in the range of 200-400 nm.
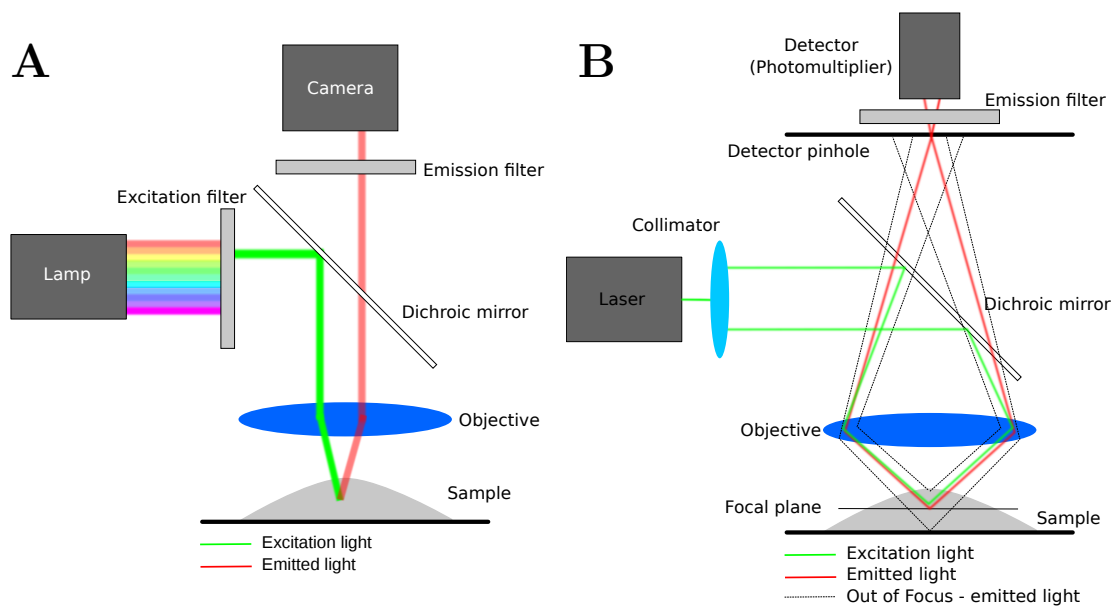
Figure 3.3: Schematic drawing of the setups of the epifluorescence microscope and CLSM.

An advanced version of the epifluorescence microscope is the confocal laser scanning microscope (CLSM) shown in Figure 3.3B. The sample is illuminated by a collimated laser beam. The monochromatic light (green) is directed onto the sample by a dichroic mirror and an objective. The sample is not fully illuminated but scanned spot-by-spot in the x-y plane using galvanometer mirrors modifying the light path. The advantage is that only a small focal volume of the sample is illuminated, minimizing photo damage and bleaching. However, this also results in a slower image acquisition rate. The emitted light passes the dichroic mirror. The central element of the microscope is the adjustable pinhole. It is integrated into the light path in such a way that only light from the focal plane can pass it. Light emitted from fluorophors above and below the plane (dotted lines) is blocked at the pinhole. The detector used is a photomultiplier, enabling for sensitive detection. The lateral resolution of the microscope depends on the width of the adjustable pinhole. At large pinhole diameters the lateral resolution is close to the one one epifluorescence microscopy but depends on the wavelength of the excitation light (λ_{ex}).[92]

$$d_{\mathrm{FWHM}} = \frac{0.51 \cdot \lambda_{ex}}{n \sin \alpha} = \frac{0.51 \cdot \lambda_{ex}}{NA} \qquad (3.3)$$

The pinhole can be narrowed down below the width of the first maximum of the airy pattern of the emitted light (1 airy unit) to increase the resolution by a factor

of ≈ 1.4 at the cost of light intensity. The axial resolution achieved is lower and in the range of one micrometer. A detailed overview over the resolution and optical slice thickness in given in the work of S. Wilhelm.[92]

3.3.1.2 Spinning disk confocal laser microscopy

The main advantage of the confocal microscope is to image the sample in three dimensions using a pinhole to exclude out of focus light. A drawback is the slower lateral recording time because the imaged in scanned in raster coordinates. To overcome this bias, the spinning disc confocal laser microscope (SDCLM) was developed. Figure 3.4 depicts the microscope.[93]
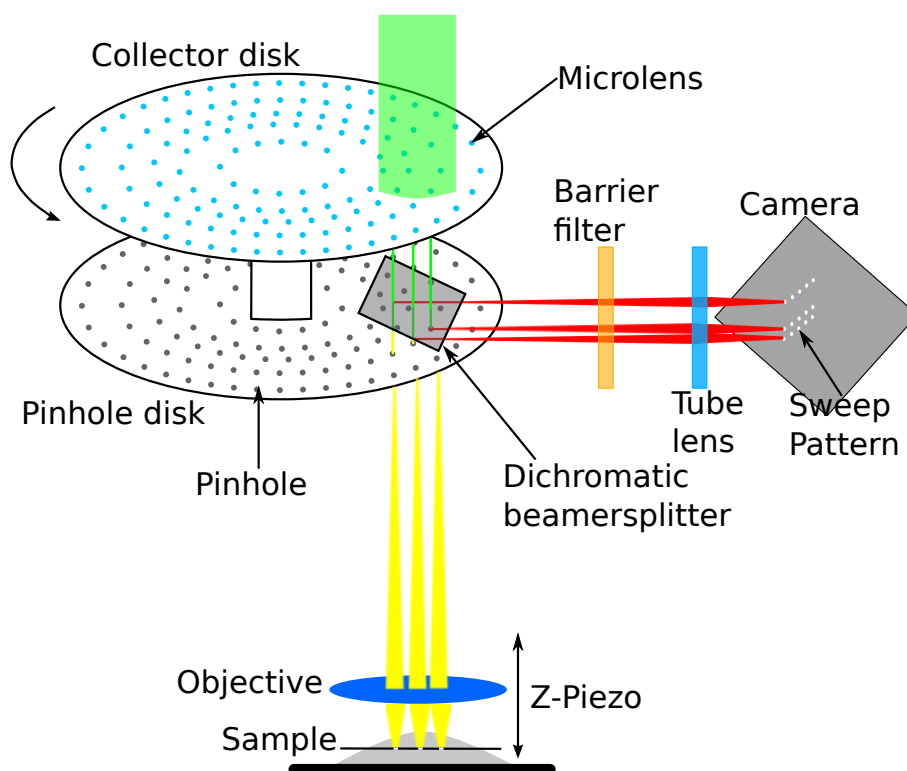
Figure 3.4: Schematic drawing of the setup of the spinning disc confocal laser microscopy.

To increase the speed of recording not a single pinhole but an array with tenth of thousands of pinholes is used. The pinholes are located on a disk in the pattern of an archimedian spiral. The disk used in this work rotates at $5000\,\mathrm{rpm}$, allowing to sweep every point of the sample with high speed. The light source is a collimated laser beam that illuminates a rotating micro lens array. Each lens focuses the excitation light to pass through one precisely positioned pinhole of the second disc.

An objective transmits the light to the focal plane of interest. Emitted light from out of focus planes is blocked at the pinhole disk as shown in Figure 3.3B. The emitted light passing the pinhole is reflected by a dichroic mirror, is filtered and transmitted onto a highly sensitive detector. Using a camera allows to measure the emitted light from all illuminated pinholes simultaneously, drastically increasing the recording speed compared to the point scanner of a conventional CLSM. In the setup used, the objective is coupled to a piezo, which can move it up and down. This allows to change the focal plane and enables high speed three dimensional imaging. A drawback of the setup is a low light efficiency, requiring photostable fluorophors, high intensity illumination and high numerical aperture objectives. In principle the resolution of the SDCLM is identical to the CLSM.[93] For practical reasons the pinholes are larger, lowering the resolution the axial and lateral resolution. Additionally, the close proximity of multiple pinholes decreases contrast ('pinhole crosstalk') if light erroneously passes through a neighboring pinhole. A detailed overview over the resolution, applications and techniques can be found at the Zeiss Campus.[93]

Experimental procedure

Two different epifluorescence microscopes, one CLSM and one SDCLM were used to image solid supported and pore-spanning lipid membranes. All setups were upright microscopes equipped with water immersion objectives. Details of the objectives and filter sets used are given in the Appendix (Section 7.9). The CLSM uses a spectral detector allowing to adjust the detected wavelengths. The values used for detection are given in Table 3.2. Detailed procedures used for fluorescence imaging are given in Section 3.2.3, 3.4.1 and 3.4.3.

The procedure for fluorescence recovery after photobleaching (FRAP) experiments to test the mobility of lipids in pore-spanning lipid bilayers was adapted from Orth *et al.*,[51,52] using the functions built in into the Zen software. The membrane with the initial intensity I_i was bleached in a circular region of interest (ROI), including one to seven pores, by a strong laser pulse to the level I_0. Recovery of the intensity by diffusion of lipid coupled fluorophors into the ROI was measured over time until the new equilibrium value I_{eq} was reached. The time course was fitted according to Equation 3.4.

$$I(t) = I_{eq} - I_1 \cdot \exp\frac{-t}{T_1} \qquad (3.4)$$

with $I_1 = I_{eq} - I_0$: intensity change caused by the mobile fraction and T_1 time constant. The time constant was used to calculate the characteristic diffusion time τ_D which can be used to calculate the diffusion coefficient D knowing the radius of the ROI ω.

$$\tau_D = \log 0.5 \cdot (-T_1) \text{ and } D = \frac{\omega^2}{4\tau_D} \tag{3.5}$$

The mobile fraction F_m of the lipids was calculated knowing the intensity after bleaching I_0.

$$F_m = \frac{I_1}{I_i - I_0} \tag{3.6}$$

Due to the simple diffusion model and the quenching of fluorescence on the pore rims the determined values are only a qualitative measure for the mobility.

3.3.2 Atomic force microscopy

Atomic force microscopy (AFM) is a raster scanning technique allowing to visualize the topography of a surface with subnanometer resolution. The principle and application were introduced by Binning, Quate and Gerber in the mid eighties of the last century.[94] It is based on the direct interaction between the scanning tip and the atoms of the scanned surface. AFM allows to map the topography of the samples in 3D and can, in contrast to other high resolution scanning techniques like electron microscopy, also be applied in water and is not limited to electrically conductive samples. Compared to recently developed high resolution fluorescence techniques like STED or localization microscopy it has a superior resolution in both axial and lateral dimension of up to 0.1 and 1 nm,[95,96] but requires direct interaction of the scanning tip to the surface of interest. These properties make it an excellent tool to study biological samples under native conditions.

Setup and working principle

The working principle of an atomic force microscope is shown in Figure 3.5.
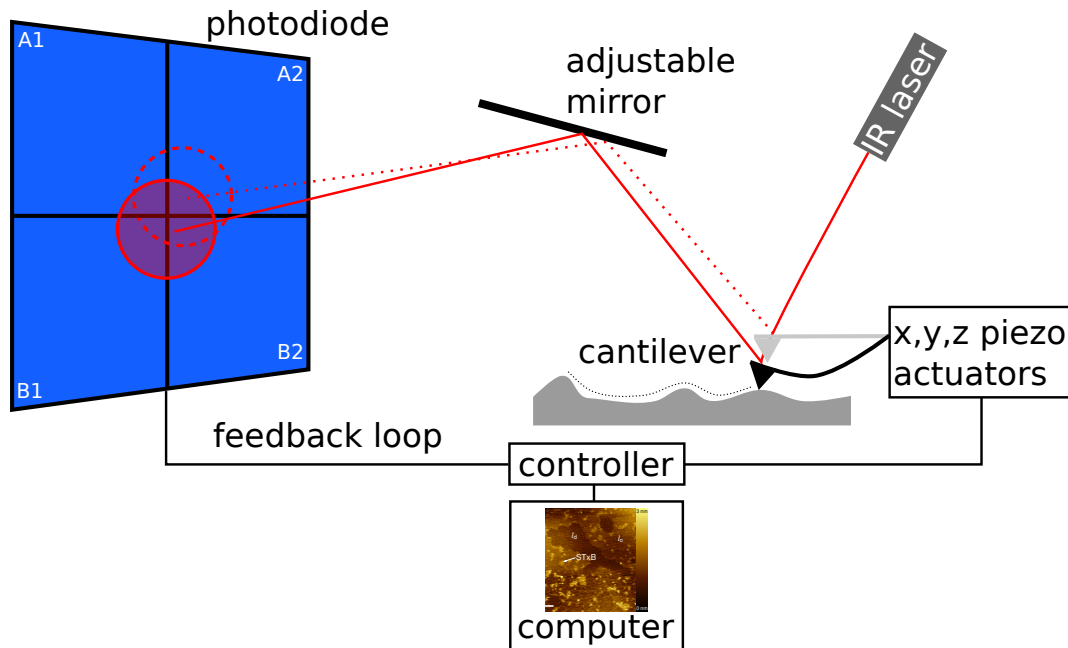

Figure 3.5: Setup of an AFM experiment. The cantilever is moved on the surface and reflects a light beam onto the photodiode. The position of the signal on the diode controls the movement of the piezo actuators by a feedback loop. Object sizes and the angles of the light beams are chosen arbitrary for clarity.

The scanning probe is a cantilever bearing a sharp tip on the bottom side. Using a z-piezo actuator the cantilever can be moved towards the surface until the tip interacts with the sample resulting in a bending of the lever. This bending can be detected using a light beam, usually emitted by a laser or super radiant diode, which is reflected from the top side of the cantilever. The beam gets directed onto a detector built of four photodiodes by an adjustable mirror. The long path of the light transfers small displacements of the cantilever into a larger measurable changes on the diodes. Bending of the cantilever upon contact to the surface changes to position of the reflected beam on the diode array. Using this principle, both the vertical and lateral deflection of the scanning tip can be calculated. The resulting signal is coupled into a feedback loop controlling the movement of the z-piezo actuator. It is amplified by proportional-integral-differential controller.

This element compares a given value for the cantilever deflection (setpoint) with the actual measured value and creates a signal to compensate for a possible difference.

The proportional gain creates a fast feedback proportional to the measured difference which can result in an overcompensation. The integral gain measures the temporal changes resulting in a precise but slow amplifier signal. The differential gain creates a spurious signal if a change in the input is detected.

These feedback loops allow to control the z-position and deflection of the cantilever. To obtain a map of the surface, additionally x-y piezo actuators are either integrated into the sample holder or the cantilever stage. They allow to position the scanning tip laterally with nanometer precision. Scanning the surface in x-y direction, while controlling the z-position of the cantilever, creates a 3D image of the sample. Images are usually scanned line by line. One dimension is scanned fast (fast scan axis) while the other is scanned subsequently (slow scan axis).

Modes and scanning

The AFM setup can be applied to investigate a variety of properties of surfaces. Using force spectroscopy, mechanical properties of the sample can be studied. A commonly used mode is the AC or tapping-mode. The cantilever is excited to oscillate in z-direction while scanning allows to minimize the interaction of the tip with the sample. In this thesis the contact mode was used. The cantilever is brought into contact with the sample, applying a defined force onto the surface. Two different modes are available using the contact mode. The cantilever can be moved at a constant height. The resulting image shows the forces acting on the lever as a function of the lateral coordinates. This mode allows fast scanning but has several disadvantages. A high force is applied which might deform a soft substrate and steep, high ascends might damage the scanning tip. To avoid these obstacles, the slower, more regulated constant force mode can be used. The applied force is set to the setpoint value and the feedback loop controls the z position of the cantilever to keep a constant force, changing the height of the probe. The sample shown in Figure 3.5 is scanned in constant force contact mode. If the applied force is low compared to the samples hardness the topography of the sample can be accurately scanned. However, if the feedback loop is too slow the image can still be distorted by the cantilever moving along the surface.

Imaging phase-separated lipid membranes allows to identify the l_o phase by its elevated height of $\Delta h \approx 0.5$-$1.0\,\mathrm{nm}$.[97] It is crucial to apply a low force to avoid

mechanical deformation of the l_o phase. Figure 3.6 shows a schematic trajectory of a cantilever scanning a phase-separated membrane with bound STxB.
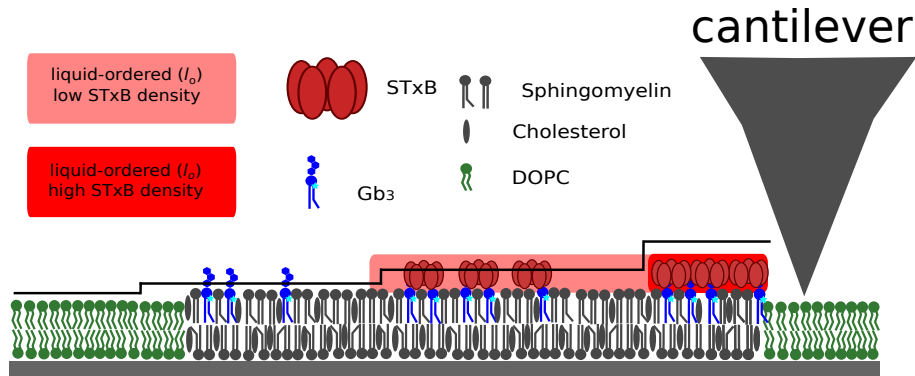

Figure 3.6: Schematic drawing of the cantilever substrate interaction in AFM. The lateral resolution of the AFM does not resolve individual proteins but measures an averaged height over the .

The black line shows the measured topography compared to the real sample. The x,y resolution of the AFM used for the measurements used in this thesis was set to 59×59 nm. At the border of the l_d and l_o phase no sharp increase in height is found but a smeared transition between the two phases due to the cantilever shape and scanning speed. This results in a broadening of the height distributions used for analysis (*vide infra*) but does not impair the analysis of the height differences because the imaged phases are in the size range of several micrometers. However, the pixel size is large compared to the crystallographic dimensions of STxB.[60] A single pentamer cannot be resolved. The height measured corresponds to the product of the protein height of approx. 2 nm and its surface density. Densely packed STxB results in a height close to 2 nm while areas with less protein have a lower height.

Experimental procedure

AFM topography maps were recorded using a JPK NanoWizard I. Membranes prepared on mica in custom made PTFE chambers were imaged in PBS at 20 °C using cantilevers with a nominal spring constant of $k = 0.03 \, \text{N} \, \text{m}^{-1}$ (Ultrasharp CSC38/no al). The cantilever was mounted and immersed into the solution to equilibrate. Images were recorded at a scan speed of 30 µm s^{-1} (fast scan axis) with a resolution of 512×512 pixels in contact mode using constant force. The setpoint was chosen manually and adjusted during measurements. One pixel corresponds to an

area of 59×59 nm. Using higher lateral resolution was found to deform the samples, resulting in lower apparent heights of the lipid phases and the bound protein. Images were analyzed using Gwyddion 2.26 or 2.34.[98] Binned height histograms were created from manually chosen regions in the images. The histogram was fitted in matlab using multiple Gaussian distributions. The height of the lowest phase (l_d) was set to 0. Values for individual histograms are given as $(h_2 - h_1) \pm (\sigma_2 + \sigma_1)$ (*note that the matlab2014 fitting toolbox parameter c for Gaussian distributions is $\sigma \cdot \sqrt{2}$*). Pooled values for the height differences are given as mean ± standard deviation. Images are visualized using the 'gold' color coding included in Gwyddion.

3.3.3 Scanning ion-conductance microscopy

Scanning ion-conductance microscopy (SICM) is a scanning probe technique which relies on the reduction of an ion current flowing into a nanopipette upon close tip-sample distances. Since its introduction in 1989,[99] it has been widely used to study biological and artificial samples. Compared to atomic force microscopy the resolution in both x,y and z direction is lower but the scanning tip is not brought into mechanical contact with the sample thus allowing to image the sample in a fully contact free manner. In this thesis hopping-mode SICM was used to map the topography of pore-spanning lipid membranes. A detailed description of the experimental setup based on a Ionscope ICNano2000 is given in Figure 3.7.

The electric flow of ions between two electrodes is measured. The bath electrode is submersed into the conductive buffer solution. The pipette electrode is located in the buffer filled nanopipette. The pipette has conical shape and its tip has an opening diameter of roughly 100 nm. The pipette is moved by three piezo actuators in x,y and z direction to scan the sample in a hopping fashion to be able to image step ascends. The pipette is moved downwards towards the surface until the close proximity to the surface restricts the ion flow to a chosen set point value of the maximum flow (typically > 99.4 %). An exemplary approach curve is shown in Figure 3.9. The z position at which the setpoint is reached is recorded. The pipette is then retracted, moved to the next scanning position and approached to the surface. In this manner a typographical map of the surface can be extracted with resolution of approximately 100 nm in lateral and 10 nm is axial direction.[100, 101]
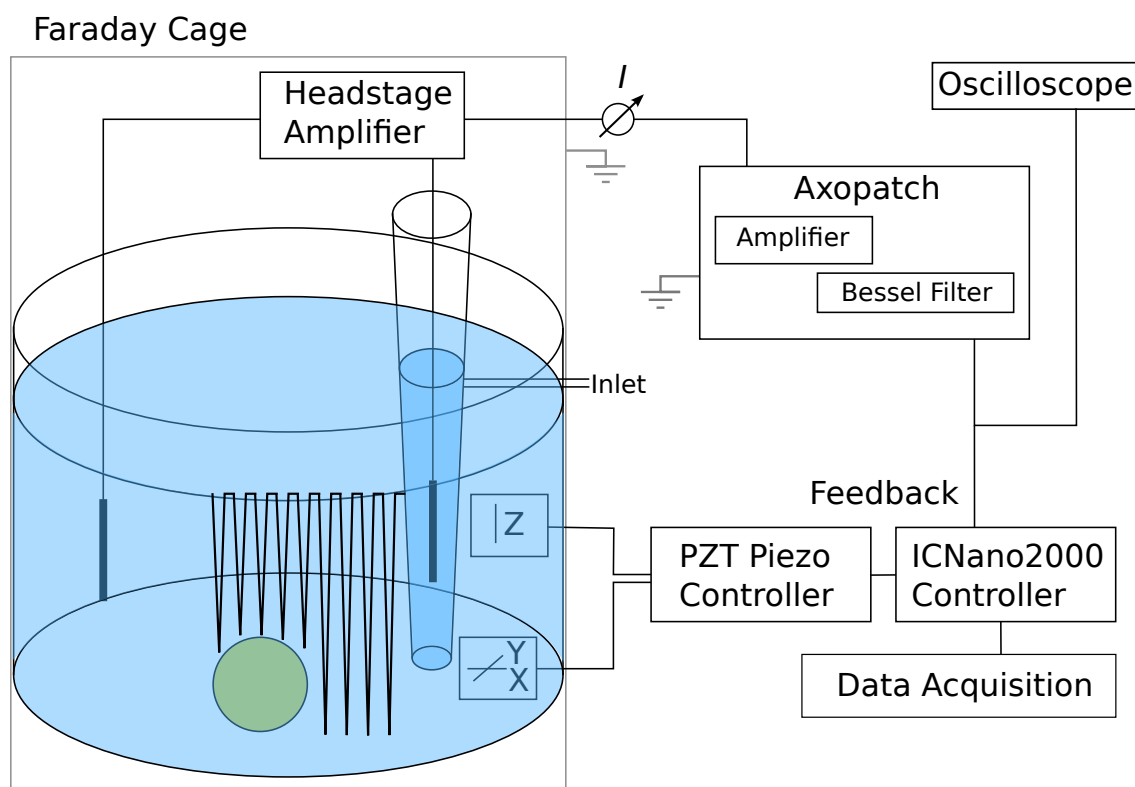
Figure 3.7: Experimental setup of an SICM experiment. The sample (yellow ball) is imaged by the pipette in a hopping movement in an electrolyte solution. The movement is controlled by an array of three piezos moving the pipette. The bath electrode is connected to the pipette electrode inside the nanopipette. The whole sample stage is in a faraday cage to shield electromagnetic noise. Current signal is amplified by the headstage and the Axopatch. The filtered signal is transfered to the ICNano2000 controller, further processed and used to control the piezo feedback loop.

The electric current is typically in the range of 0.5-3 nA. It is amplified by the headstage and the Axopatch. In the Axopatch the signal is filtered by a 1 kHz 4 pole bessel filter and transfered to the controller and the oscilloscope. In the ICNano controller the signal is further filtered and processed to feed the feedback loop controlling the piezo actuators.

The flowing ion current can be theoretically described by a theory published by Nitz *et al.*.[102] Figure 3.8 shows the geometrical considerations needed to describe the interaction between the pipette (blue) and the non ion-conductive surface (red). In close proximity to the surface the ion current is restricted by a resistance R_{tot} which can be divided into three individual contributions (Equation 3.7).
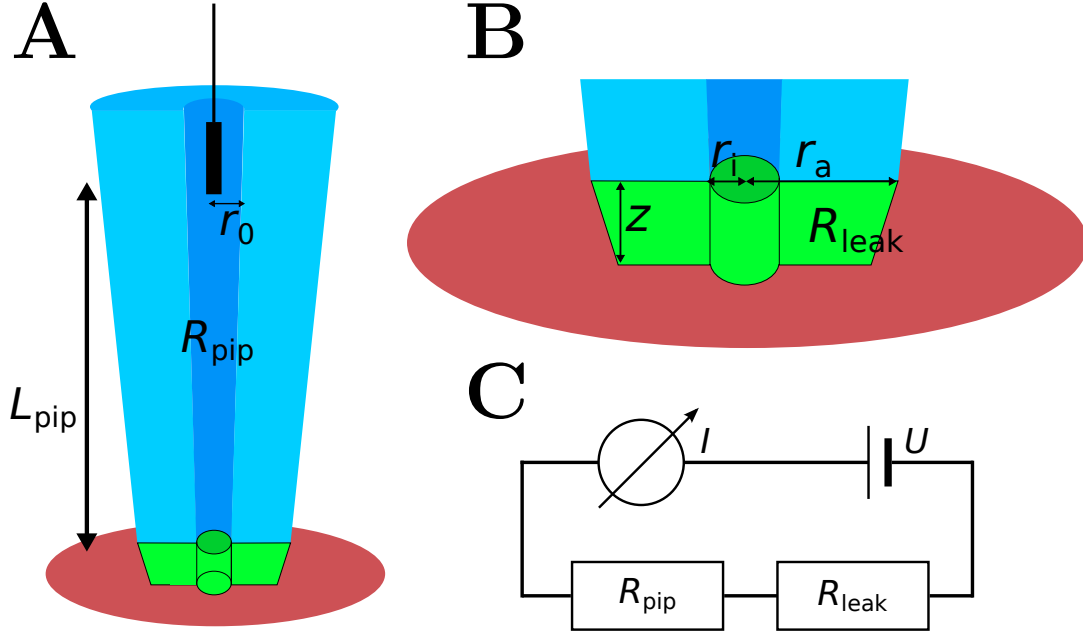
Figure 3.8: Schematic drawing of the SICM nanopipette and the physical properties relevant for the simplified model derived by Nitz *et al.*.[102] **A** The nanopipette has a conical shape. The electrode is located in the widening region. Ion flow through the pipette poses an electrical resistance R_{pip}. Sample surface is shown in red. **B** Zoom of contact region of **A**. Pipette approaches up to a distance z to the surface. Ion flow is restricted by the physical dimensions of the nanopipette resulting in a resistance R_{leak}. **C** Equivalent circuit for the situation shown in **A** and **B**.

The resistance of the bath solution R_{sol} depends on the solution's specific conductivity κ and is small compared to the other contributions and can be neglected.[100]

$$R_{\text{tot}} = R_{\text{pip}} + R_{\text{leak}} + R_{\text{sol}} \tag{3.7}$$

Ions flowing through the pipette to the electrode have to travel the distance L_{pip}. The geometry of the nanopipette can be approximated as a widening cylinder (cone) with a minimal opening radius r_{i} extending to the radius r_0 at the electrode. The resistance can be expressed as shown in Equation 3.8 and additionally depends on the specific conductivity of the solution κ.[102]

$$R_{\text{pip}} = \frac{1}{\pi\kappa} \int_0^{L_{\text{pip}}} \left[r_{\text{i}} + (r_0 - r_{\text{i}})\frac{L}{L_{\text{pip}}} \right]^{-2} dL = \frac{L_{\text{pip}}}{\pi\kappa r_0 r_{\text{i}}} \tag{3.8}$$

At pipette-samples distances in the range of tenth of nanometers the current flow is additionally restricted by the movement of the ions parallel to the surface from

the bulk to the pipette opening. The description of this leakage resistance R_leak is more complex. It can be divided into the resistance of ions flowing below the pipette opening and below the glass surface at the bottom the pipette. The latter depends on the flow through the electric field at the outer border of the pipette at r_a and the inner border at r_i. Assuming a distance from the surface $z \approx \frac{1}{2} r_\text{i}$ the leakage resistance can be approximated as:[102]

$$R_\text{leak} \approx \frac{3}{2\kappa\pi z} \ln\left(\frac{r_\text{a}}{r_\text{i}}\right). \tag{3.9}$$

At large pipette sample distances z the leakage resistance vanishes and the current at saturation (I_sat) can be obtained.

$$I_\text{sat} \approx \frac{U}{R_\text{pip}} = \frac{U}{\dfrac{L_\text{pip}}{\kappa\pi r_0 r_\text{i}}} \tag{3.10}$$

Close to the surface R_leak is growing and the total ion flow as a function of the tip-sample distance z is described by Equation 3.11.

$$I(z) = \frac{U}{R_\text{tot}} \approx \frac{U}{R_\text{pip} + R_\text{leak}} = I_\text{sat}\left[1 + \frac{r_0 r_\text{i}}{2z L_\text{pip}}\left[\ln\left(\frac{r_\text{a}}{r_\text{i}}\right) + \ln(2)\right] + \frac{r_0 r_\text{i}}{2 L_\text{pip} r_\text{i}^2}\right]^{-1} \tag{3.11}$$

A typical curve obtained for reasonable physical parameters ($r_0 = 0.3\,\text{mm}$, $r_\text{i} = 50\,\text{nm}$, $r_\text{i} = 85\,\text{nm}$, $L_\text{pip} = 10\,\text{mm}$, $\kappa = 0.92\,\text{S m}^{-1}$, $U = 100\,\text{mV}$) is shown in Figure 3.9. The current drastically drops as the tip-sample separation approaches zero. At the chosen set point the piezo movement towards the surface stops and the pipette is retracted.
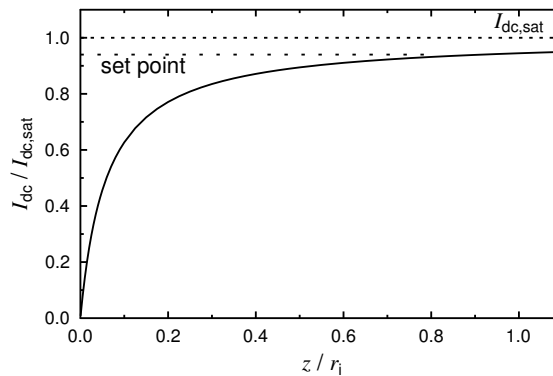
Figure 3.9: *I/z* curve based on the equation derived by *Nitz et al.* (Equation 3.11).[102] Set point 0.94, $r_0 = 0.3\,\text{mm}$, $r_\text{i} = 50\,\text{nm}$, $r_\text{i} = 85\,\text{nm}$, $L_\text{pip} = 10\,\text{mm}$, $\kappa = 0.92\,\text{S m}^{-1}$, $U = 100\,\text{mV}$.

Experimental procedure

Figure 3.10 shows a schematic example of the used settings. Typical values used in an experiment to image a pore-spanning membrane are given in Table 3.5.
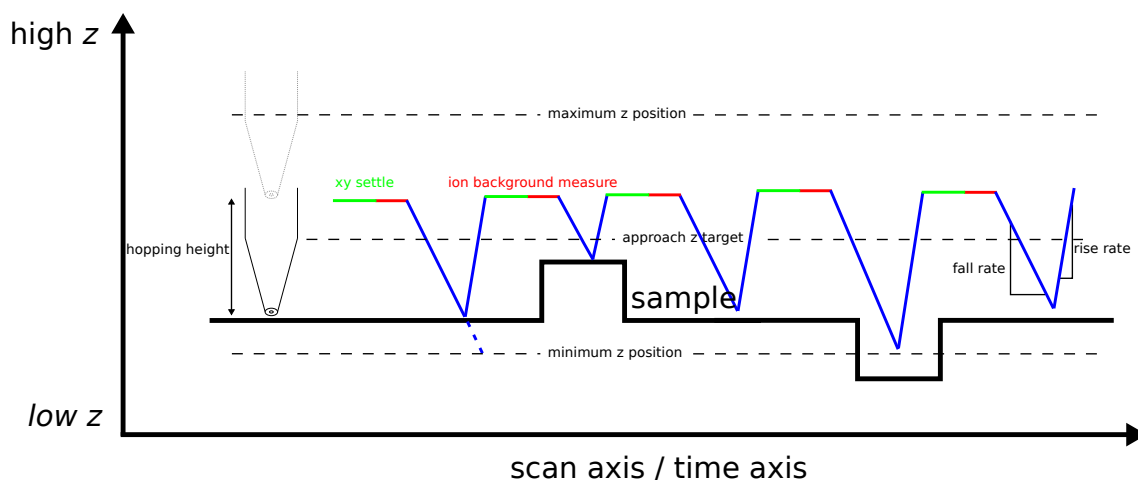

Figure 3.10: Schematic drawing of a SICM scan. Movement of the pipette along the sample (black) is illustrated as the black line.

All experiments were conducted at room temperature. Electrodes (Ag/AgCl) were prepared by oxidation of silver wire using sodium hypochlorite solution (1.6 M in water). The samples were immobilized in a custom made PTFE chamber or in a petri dish. Nanopipettes were freshly produced from glass capillaries (borosilicate with filament, outer diameter 1.00 mm, inner diameter 0.58 mm, length 80 mm) using a puller (Sutter Instruments P1000, settings: heat: ramp - 10, ramp 523, pull: 55, velocity: 110, delay: 80, pressure: 400, loops: 1, time 10.4-10.5 s). The pipette was filled with degased filtered PBS and the electrode was put into the capillary. The pipette was positioned above the substrate using the x,y motors and immersed into buffer solution. A voltage of 200 mV was applied and successful electric contact resulted in a current of around 1 nA. *Hopping height* was set to values between 1000 and 3000 nm to allow imaging of steep ascends. The surface was approached at *approach speeds* between 1 and 10 nm s^{-1} up to *approach z target* height. The height was usually chosen set to 12.5 μm allowing to image both high and low objects (z piezo range 25 μm). A successful approach was indicated by the typical approach curve visible in the oscilloscope. Imaging was performed at image sizes of 5 to 100 μm^2 with 10x10 up to 512x512 data points.

During hopping the pipette is allowed to come to rest for the time defined as *xy settle*. The current at saturation is measured for the time set by *ion background*

measure. The pipette is then moved towards the bottom by a speed of *fall rate* and retracted after the set point (typically 99.6 %) is reached, using the speed set in *rise rate*. The pipette is then moved to the next x,y position and the cycle is repeated. For imaging porous substrates the *minimum z position* was defined. It sets a lower limit for the z movement of the pipette avoiding a deep descend of the pipette into an open pore which might damage the nanopipette. Table 3.5 is giving typical settings used. Image analysis was performed using Gwyddion and matlab.[98] Small images and images of pores with a small diameter were typically used without any post processing steps. Images of larger pores required to flatten the image using a second order polynomial to correct for thermal drift. Height differences between pore and rim were read out using matlab. The height at the pore center was compared to the height of 4 rim positions surrounding the pore. Final values for the pore depth as given as mean $\pm$ standard deviation. Images are visualized using the 'gold' color coding included in Gwyddion.

Table 3.5: Typical values chosen for SICM experiments.

Parameter	value
U / mV	200
set point / 0.1 %	3-4
immerse speed / $\mu m\,s^{-1}$	200
approach speed / $\mu m\,s^{-1}$	1-10
hopping height / μm	1-3
fall rate / $nm\,ms^{-1}$	15
rise rate / $nm\,ms^{-1}$	250
xy settle / ms	15
background measurement time / ms	5
image size / μm	x: 5-100 y: 5-100
measurement points / μm	x: 10-512 y: 10-512
scan direction	unidirectional
max z position / μm	25
min z position / μm	9-12‡
approach z target / μm	12.5
ion immerse threshold / mV	200

‡ Chosen to fulfill hopping height > (approach z target - min z position)

3.3.4 Biosensing methods

Biosensing describes techniques used to analyze the interaction of an analyte, e.g. a protein, with a physiochemical detector. In this thesis surface plasmon resonance (SPR) spectroscopy was used to monitor the binding of Shiga toxin (Section 1.3) to its receptor lipid Gb_3 in artificial lipid membranes. The measurements enable to extract the dissociation constant (K_D) of the interaction. Reflectometric interference spectroscopy (RIfS) was used to determine the amount of STxB bound the membranes.

3.3.4.1 Surface plasmon resonance spectroscopy

SPR is a biosensing technique that is based on the excitation of surface plasmons at the interface of a gold surface to an analyte. It can be used to quantify the affinity of a ligand to a functionalized surface.

Physical background

Surface plasmons are charge oscillations that propagate parallel to the interface of a noble metal (usually gold or silver) to a dielectric medium. The plasmon decays exponentially in z direction, making the technique suitable to detect changes in close proximity ($\approx 200\,\text{nm}$) to the surface.[103]

To excite a surface plasmon a thin gold layer is illuminated at the angle of total internal reflection, resulting in an evanescent wave propagating into the gold, exciting a plasmon on the on averted site. The schematic drawings shown are based on the commonly used Kretschmann configuration.[104]
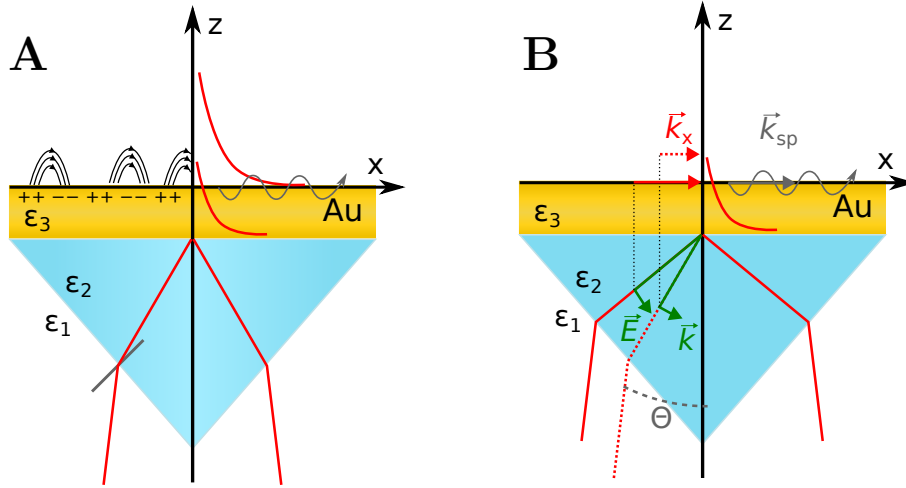
Figure 3.11: Excitation of surface plasmons in SPR. **A** Light (red) is illuminated to the backside of a gold layer via a prism. After total internal reflection an evanescent wave (red) can excite the plasmon (gray) which is propagating electronic density fluctuation. **B** To excite the plasmon, p-polarized light (red) has to couple its momentum $\vec{k}_x$ to the momentum of the plasmon $\vec{k}_{sp}$. ($\epsilon_3 > \epsilon_2 > \epsilon_1$).

Figure 3.11A shows light entering a prism (blue) from a medium with a lower dielectric constant ϵ_1. It is transmitted to the gold surface and can excite an evanescent wave in the gold which leads to electric density oscillations that can result in the excitation of a surface plasmon (gray wave). SPR must use p-polarized light to excite the plasmon resonance. The moment of the photon in x-direction ($\vec{k}_x$) has to match the one of the plasmon ($\vec{k}_{sp}$). Changing the incidence angle of the light modifies the photon's momentum in x direction by $\vec{k}_x = \vec{k} \cdot \sin\Theta$ (Figure 3.11B).[105] To excite a plasmon, the dispersion relation of the free photon and the excited plasmon must match. Dispersion of the plasmon is dependent on both the refractive index of the gold ϵ_3 and of the dielectric medium with ϵ_1.

$$\vec{k}_x = \frac{\omega}{c} \sqrt{\frac{\epsilon_3 \epsilon_1}{\epsilon_3 + \epsilon_1}} \tag{3.12}$$

The free photon in the dielectric disperses as $k_{photon} = \frac{\omega}{c}\sqrt{\epsilon}$. Under these conditions the photon will only fulfill the coupling conditions if a high refractive index prism and total internal reflection at the interface between the prism and the gold layer is used.

$$\vec{k}_x = \frac{\omega}{c}\sqrt{\epsilon_2}\sin\Theta = \vec{k}_{sp} \tag{3.13}$$

Combining both equations shows, that the condition to excite a surface plasmon depends on the dielectric close to the surface of the gold layer. Changing it by e.g. adsorption of molecules requires to adjust the angle Θ to excite the plasmon. Excitation of a plasmon results in an attenuation of the light that is reflected at the gold surface.
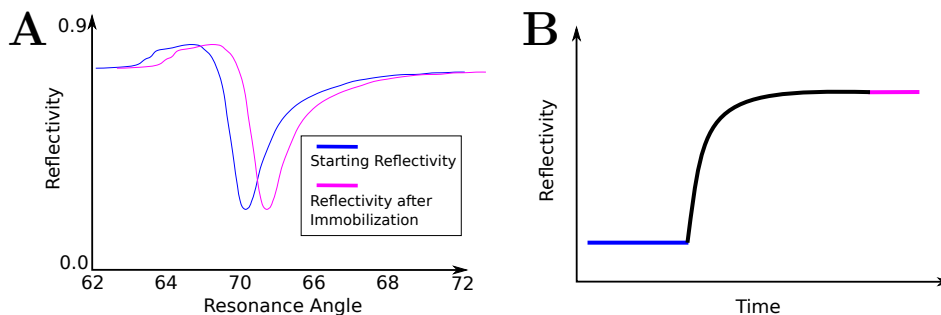

Figure 3.12: SPR spectrum and time course of an experiment. **A** SPR spectrum. The measured reflectivity drops when the resonance angle for exciting a plasmon is reached. Changing the adlayer on the gold layer changes the coupling conditions and resonance angle. **B** The angle shift can be measured over time. Plotting the reflectivity of an angle close to resonance vs. time allows to extract the kinetics of an adsorption process to the gold layer.

Figure 3.12A illustrates this process. The blue curve shows the reflectivity as a function of the angle Θ. A drop in reflectivity occurs at the resonance angle needed to excite the plasmon. Changing the properties of the dielectric medium in contact to the gold surface results in different coupling conditions and a change in resonance angle. Measuring the reflectivity over time (Figure 3.12B) at an angle close to resonance allows to extract a time course for kinetic measurements. A second mode tracks the angle of resonance to obtain the kinetics.

Experimental setup

In this thesis SPR was used to determine the dissociation constant K_D of the STxB-Gb$_3$-interaction in artificial membranes using a commercial SPR setup. The setup is depicted in Figure 3.13.
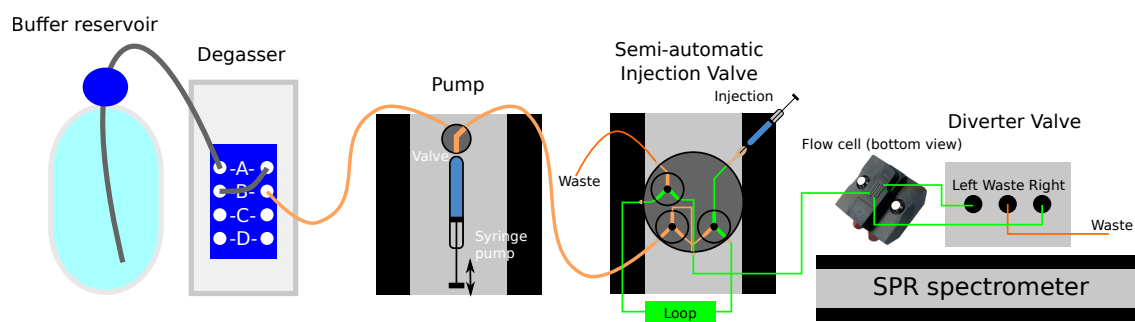
Figure 3.13: Experimental setup of the SPR experiment based on the Reichert SR700DC spectrometer. Buffer is degassed and injected into the spectrometer using a syringe pump. Analyte solution can be added via a second loop that can be triggered using the injection valve.[106]

The prism and gold layer are located in the flow cell. Freshly degassed buffer is inserted into the cell using a syringe pump. To inject vesicles and proteins a second loop is used. The loop is filled with the solution of interest by a syringe. The semi-automatic injection valve can divert the flow of the pump to the second loop, pushing the analyte solution into the measuring chamber. Thin tubings are used to avert unwanted mixing of buffer and analyte solution. The setup can only be used in an open loop configuration, meaning that substances that passed the measuring chamber are discarded. A special feature of the SPR setup is the divergent beam used to excite the plasmon. The beam hits the surface of the gold at different angles (55-85°) simultaneously and is reflected onto a linear detector array, allowing to detect the resonance angle Θ without the use of goniometer.

Experimental procedure

The experimental procedure was adapted from Nakajima *et al.*.[107] SPR sensor chips were coated with a thin chromium (2 nm) and gold (50 nm) layer using evaporation in high vacuum. Prior to experiments the chips were rinsed with ethanol, dried under a stream of nitrogen and cleaned using argon plasma. They were then incubated in a solution of 1-octanethiol ($c = 16$ mM) overnight at 4 °C.

Small unilamellar vesicles containing the STxB receptor lipids Gb_3 were prepared as described in Section 3.2.1. The SPR sensor chip was rinsed with ethanol, dried in a stream of nitrogen and then mounted into the spectrometer. High refractive index immersion oil was used to connect the chip and the spectrometer. The chip was then rinsed with buffer until a baseline in the reflectivity time course was reached. Figure 3.14 shows the experimental procedure.
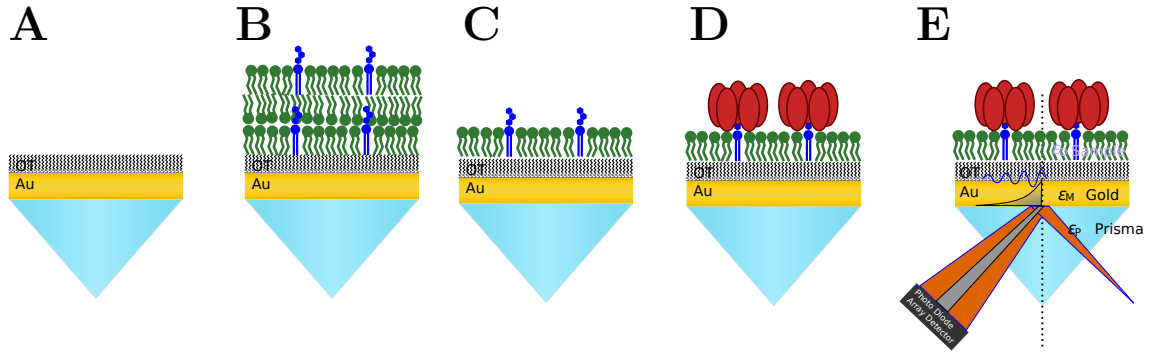
Figure 3.14: Schematic course of a SPR experiment. **A** The octanethiol functionalized sensor chip is mounted into the spectrometer. **B** Addition of vesicles leads to the formation of multilayers which are removed by rinsing with sodium hydroxide solution to give **C**. **D** Binding of STxB changes the thickness of the adsorbed layer. **E** The resonance conditions for plasmon formation are measured by a divergent beam that is reflected onto a photo diode array detector.

Vesicles (final lipid concentration $c = 0.03 \, \text{mg} \, \text{mL}^{-1}$) were added via the 5000 µL loop at a flow rate of 50 µL min^{-1} to the octanethiol monolayer (panel A). Spreading of the vesicles resulted in a high change in reflectivity which can be attributed to the formation of phospholipid multistacks (panel B). The flow rate was lowered to 25 µL min^{-1} and the stacks were removed by repeated (3-9×) addition of sodium hydroxide solution (50 mM in ultrapure water). Hydrophobic defects were blocked by the addition of bovine serum albumine solution (1 mg mL^{-1} in PBS). The hydrophobic surface functionalization results in the formation of a hybrid bilayer where the bottom layer consists of octanethiol. STxB at a defined concentration was added via the 250 or 500 µL loop resulting in addition times of 10 and 20 min (panel D). The concentrations given refer to the pentameric B-subunit, not the B-monomer. All addition steps were followed by rinsing with PBS. Data was analyzed using matlab. One of the two measuring channels was evaluated by first correcting for linear drift by subtracting a polynom of the first order that was fitted to a manually chosen region of time course. Changes in reflectivity were extracted with respect to the baseline before STxB addition. The obtained adsorption isotherms were fitted using the Langmuir model (Equation 3.14). The reflectivity R and R_{rel} are proportional to the surface coverage Θ.

$$\Theta = \frac{K_{\text{A}}\Theta_{\text{max}}c_{\text{eq}}}{1 + K_{\text{A}}c_{\text{eq}}} \tag{3.14}$$

The absolute changes in reflectivity were found to strongly vary among different preparations and all changes were normalized to the reflectivity change at a concentration near saturation giving Equation 3.15. Fitting the reflectivity vs. time data of isolated STxB additions to obtain kinetic parameters of the interaction was not successful using the Langmuir model and models suggested by Nakajima *et al.*.[107]

$$\Theta\text{rel} = \Theta_{\text{max,rel}} \frac{K_A c_{\text{eq}}}{1 + K_A c_{\text{eq}}} = \Theta_{\text{max,rel}} \frac{c_{\text{eq}}}{K_D + c_{\text{eq}}} \tag{3.15}$$

Values for the dissociation constant are given as the fitted value $\pm$ the error of the fit.

3.3.4.2 Reflectometric interference spectroscopy

Reflectometric interference spectroscopy (RIfS) is a noninvasive biosensing technique to determine the thicknesses of thin, transparent layers. White light is partially reflected at the interfaces of the layers or refracted and transmitted. The refracted light travels through the dielectric layer and is reflected at an interface to the next layer. This results in two different optical path lengths for both reflected beams, leading to a characteristic interference spectrum.[108] In this thesis RIfS was used to determine the thickness of the STxB layer bound to Gb$_3$ containing lipid membranes.

Physical background

RIfS is capable to determine changes in the optical thickness (OT) of thin films. OT is defined as the product of the film's thickness d and its refractive index n.

Refraction of a light beam at the interface between media with different refractive indices n_1 and n_2 is described by Snell's law assuming a homogeneous, isotropic non-magnetic conditions.[109]

$$n_1 \sin \delta_1 = n_2 \sin \delta_2 \tag{3.16}$$

Figure 3.15 illustrates the light path. The incident light hits the surface of in an angle δ_1 from the medium denoted n_1 by its refractive index and is either reflected (I_1) or gets refracted in an angle δ_2 into the medium with a different refractive index (n_2).
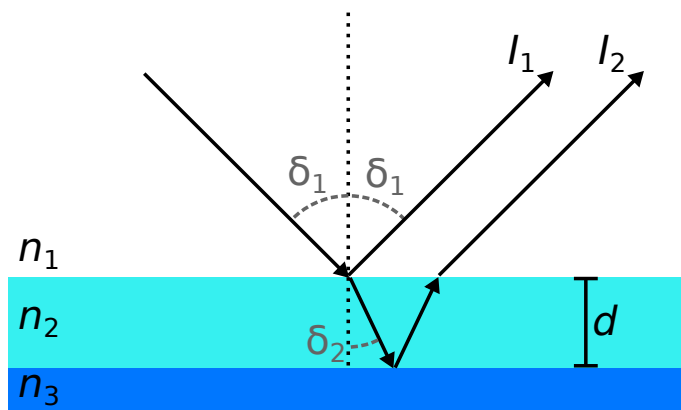
Figure 3.15: The light beams (black) travel through three different media denoted by their refractive index (n_x). The light is refracted at the phase border between n_1 and n_2. The transmitted light is reflected at the interface of n_2 and n_3, resulting in an optical path difference of the beams I_1 and I_2, which leads to interference.

Partially transmitted light travels an additional distance in the medium n_2, before being reflected at interface to the third medium (n_3, dark blue). Another refraction at the interface to the surrounding medium n_1 leads to an overlap of both rays I_1 and I_2. The passing of an additional layer results in a difference in optical path length (Δs) for both rays. For RIfS experiments the light is shone in perpendicular to the surface ($\delta_1 = \delta_2 = 0$). The difference in path length can be calculated as

$$\Delta s = \frac{2n_2 d}{\cos \delta_2} = 2n_2 d \tag{3.17}$$

and depends on the thickness of the medium (d). Constructive interference occurs when the difference in optical path length Δs is a multiple of the wavelength λ.[109] The different optical path lengths results in a phase shift $\Delta \phi$ of the two light beams with intensities I_1 and I_2 depending on the wavelength λ.

$$\Delta \phi(\lambda) = \frac{2\pi}{\lambda} d n_2 \cos \delta_2 = \frac{2\pi}{\lambda} d n_2 \tag{3.18}$$

To obtain the optical thickness of an adsorbed layer as in Figure 3.15 one can use the Fresnel coefficients r and t describing the reflection and transmission at the interface respectively. One can image the medium with the refractive index n_1 as the buffer solution, n_2 as the index of a silicon dioxide layer with the adsorbed analyte and n_3

as the index of silicon. Transmitted light exhibits full reflection at the phase border of the dioxide (n_2) to the silicon wafer (n_3). The reflection index is

$$r_{123} = \frac{r_{12} + r_{23}\exp\left(-2i\Delta\phi\right)}{1 - r_{21}r_{23}\exp\left(-2i\Delta\phi\right)}\text{with } r_{xy} = \frac{n_x - n_y}{n_x + n_y}. \tag{3.19}$$

The reflectivity is defined as $R \equiv |r|^2$ and at perpendicular illumination ($\cos\phi = 0$) the reflectivity R can be written as

$$R(\lambda, OT) = |r_{123}|^2 = \left(\frac{r_{12}^2 + r_{23}^2 + 2r_{12}r_{23}\cos\left(\frac{4\pi}{\lambda}OT\right)}{1 + r_{12}^2 r_{23}^2 + r_{12}r_{23}\cos\left(\frac{4\pi}{\lambda}OT\right)}\right). \tag{3.20}$$

The measured reflectivity spectrum can be fitted to Equation 3.20 to allow for the determination of the optical thickness, which can be converted to the height of the adsorbed layer.

Experimental setup

Figure 3.16 shows the experimental setup of the custom built RIfS setup.
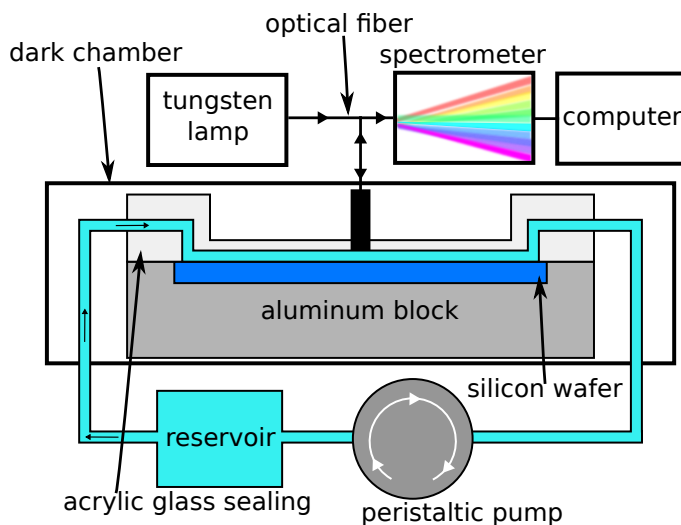
Figure 3.16: Experimental setup of the RIfS experiment. White light is transmitted to the measuring chamber using an optical fiber. The light is refracted and reflected at the silicon wafer resulting in the reflectivity spectrum measured. Analytes can be added using a peristaltic pump.

White light (350-950 nm) is transmitted to the sample chamber using an optical fiber which enters the perpendicular to the reflective surface. The reflected light is

gathered by a second strand integrated into the optical fiber and transmitted to a spectrometer which measures the reflectivity spectrum. Data analysis is done using a computer by fitting the reflectivity spectrum in the range of 500 to 700 nm.

The measuring chamber consists of a dark chamber surrounding the sample cell, built up of an aluminium stage and an acrylic glass sealing. The reflective surface used in the experiment is a silicon wafer covered with a 5 µm thick silicon dioxide layer. A peristaltic pump allows to inject substances to flow over the wafer. The refractive indices used are $n_1 = 1.331$, $n_3 = 3.8714$, and a wavelength depended value for n_2 for the buffer solution, the silicon layer and both the analyte adsorbed and the silicon dioxide layer.[110]

Experimental procedure

The experimental procedure was adapted from Krick *et al.*.[111] Prior to the measurements two reference reflectivity spectra were recorded. The first one was recorded using a highly reflective aluminium surface to obtain the intensity spectrum of the lamp. A dark spectrum was recorded without illumination. These reference spectra allow to calculate the reflectivity spectrum during the measurement. All measurements were conducted at room temperature using freshly degassed PBS. Small unilamellar vesicles containing the Shiga toxin receptor lipid Gb$_3$ were prepared as described in Section 3.2.1. The silicon wafers were hydrophilized by incubating them for 20 min at 70 °C in a mixture (*v*:*v*:*v* 5:1:1) of ultra pure water, hydrogen peroxide solution (30 %) and ammonium hydroxide solution (25 %). Substrates were stored in water for up to two days. The substrate was rinsed with ethanol, dried in a steam of nitrogen and treated with oxygen plasma. After mounting to the measurement chamber the substrate was rinsed with water and buffer at a high flow rate. The flow rate was lowered to 500 µL min^{-1} and the vesicles (final concentration 0.1 mg mL^{-1}) were added in a closed-loop configuration, resulting in a rapid increase in optical thickness, indicative of spreading to a bilayer membrane. After reaching constant baseline the sample was first rinsed with buffer, followed by the addition of bovine serum albumin solution (final concentration 1 mg mL^{-1}), to block hydrophobic defects, and rinsing with PBS. STxB solutions were added in via the closed-loop to determine the change ΔOT in equilibrium. The concentrations given refer to the pentameric B-subunit, not the B-monomer. Sample was rinsed with PBS to remove reversibly bound STxB.

Data analysis was performed in matlab. The measured changes in optical thickness were converted to the absolute heights of the layers by using a refractive index of 1.49

and 1.47 for membrane and protein respectively.[112,113] An exemplary measurement is presented in Figure 4.33 on page 125.

3.4 Data analysis methods

3.4.1 Phase percentage determination in giant vesicles

A prerequisite for the interpretation of data obtained on phase-separated pore-spanning lipid membranes is to quantify the phase behavior of the GUVs used to create them.

To determine the percentages of the liquid-ordered and liquid-disordered phase 3D fluorescence imaging the CLSM or SDCLM were used. Approaches published in literature are based on the 3D reconstruction of the vesicle surface and require full staining of the vesicle.[37,114,115] This approach was not used in this thesis because full staining of the l_o phase could only be produced by incubation with fluorescent labeled Shiga toxin.

Instead, orthographic azimuthal projections of the half spheres of the GUV were created.[116] The fluorescence from one half sphere is projected onto a plane perpendicular to the z-axis (Figure 3.17A).
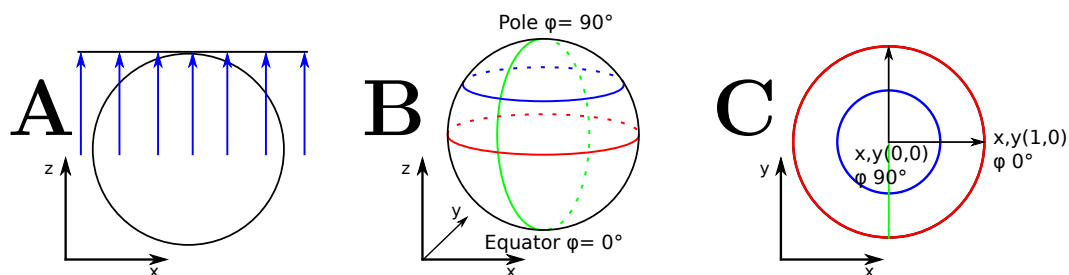

Figure 3.17: Orthographic azimuthal projection. **A** Half sphere is projected onto a plane orthogonal to the plane. **B** Spherical coordinates used. **C** Corresponding cartesian coordinates of the projection.

The process of image reconstruction is shown in more detail in Figure 3.18. Panel A shows the slices imaged by the confocal microscope. Panel B illustrates the averaged sum of the slices leading to the full projection of the half sphere.
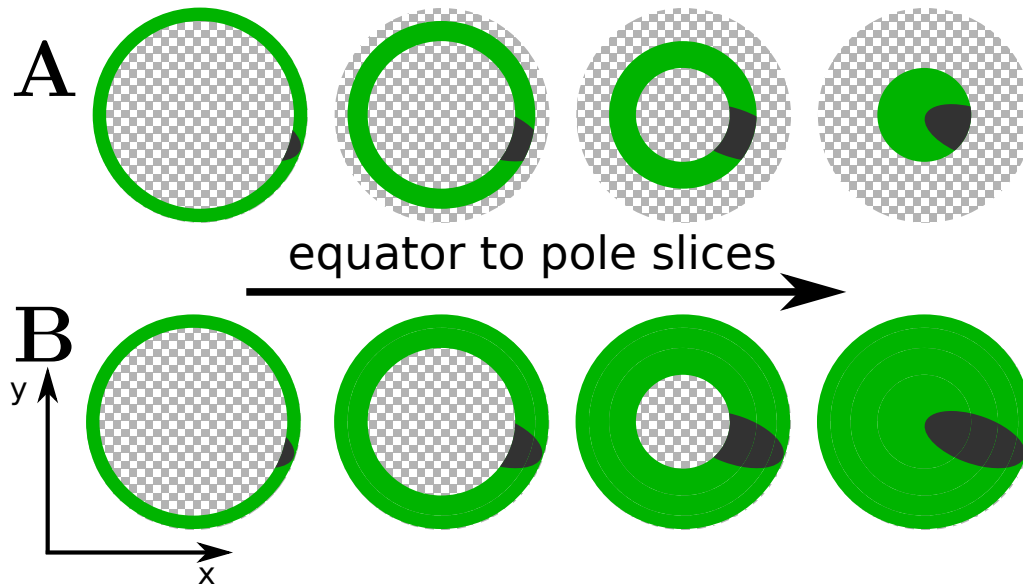
Figure 3.18: Imaging planes used in the orthographic azimuthal projection. **A** single slices are imaged at different z positions. **B** The averaged sum of the slices constructs the projection.

The orthographic azimuthal projection leads to a strong shape and area distortion near the map borders (red circle in Figure 3.17B/C).[116] The distortion of the area can be corrected using the coordinate transformations of the projection. The coordinates of each point on the surface of the half sphere in the spherical representation shown in Figure 3.17B can be described by the spherical coordinates φ and λ with respect to the center of the coordinate system at $\varphi_0 = 90°$ and $\lambda_0 = 0°$. φ corresponds to the latitude and λ to the longitude. The half sphere can be calculated from known positions x,y in the projection (Figure 3.17C) by Equations 3.21 to 3.23.[116]

$$\rho = \sqrt{(x^2 + y^2)}, c = \arcsin\left(\frac{\rho}{R}\right) \tag{3.21}$$

$$\varphi = \arcsin\left(\cos c \sin \varphi_0 + \frac{y \sin c \cos \varphi_0}{\rho}\right) \tag{3.22}$$

$$\lambda = \lambda_0 + \arctan\left(\frac{x \sin c}{\rho \cos \varphi_0 \cos c - y \sin \varphi_0 \sin c}\right) \tag{3.23}$$

The relevant property for the distortion of the area is the latitudinal coordinate φ. For the simple case of $y = 0$ and a spherical radius $R = 1$ Equation 3.22 simplifies to

$$\varphi = \arcsin\left(\cos\left(\arcsin\left(\frac{x}{R}\right)\right)\right) = \arcsin\left(\sqrt{1 - \left(\frac{x}{R}\right)^2}\right). \tag{3.24}$$

A weighting factor $w(\varphi)$ is defined to correct for the area distortion. Its value is used to weight the thresholded images.

$$w(\varphi) = \frac{1}{\varphi/max(\varphi)} \tag{3.25}$$

The process of weighting has to be used because the finite area near the border of the projection ($\varphi=0$) corresponds to a larger area on the surface of the half sphere. To determine the size of objects on the projections this distortion has to be corrected by multiplying the area by the relative weight. This enables to quantify the l_o percentage on phase-separated GUVs.

The evaluation was done using matlab. Figure 3.19 shows the procedure and matlab functions used. Matlab commands are printed *italic*.

Experimental procedure

GUVs filled with sucrose solution ($O \approx 330\,\mathrm{mOsmol\,kg^{-1}}$) were prepared as described in Section 3.2.1. 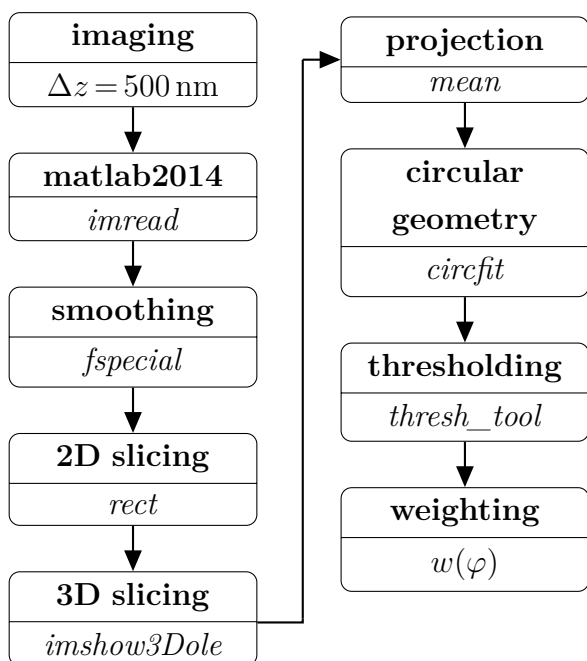The GUVs labeled with Bodipy-PC, TexasRed DHPE or Atto488 DHPE were added to hypoosmotic PBS and the osmotic pressure induces an inflation to a spherical shape. This ensures the spherical shape of the GUV and a low contact area to the petri dish. GUVs were imaged using z-stacks with the CLSM or SDCLM. The distance between two planes in axial direction was chosen to $\Delta z = 500\,\mathrm{nm}$. STxB or STxB-Cy3 (final concentration $60\,\mathrm{nM}$) was added to the solution and the samples were re-imaged after protein binding. Image data was read into matlab2014 using the *imread* function. All slices of the images were processed by *imfilter* using a 2D 3x3 averaging filter created by *fspecial* before re-slicing the image using *rect*. The half spheres of the

Figure 3.19: Evaluation of phase percentages in GUVs. Different **steps** and the *matlab functions* used.

GUV were chosen manually using *imshow3Dole* which was modified from *imshow3D* to allow for the extraction of z coordinates of the top, middle and bottom position of the GUVs.[117] The orthographic azimuthal projection was performed between the top and equatorial slice and the equatorial and bottom slice using *mean* to give two projections which were treated individually. *circfit* was used to find the area of the projections,[118] which were manually thresholded using *thresh_tool*.[119] The l_o percentage was determined by pixel analysis. The weighting function $w(\varphi)$ was employed to correct for the area distortion of the projection. To avoid errors at small φ values which are weighted strongly only the data with $\varphi > 15°$ was used, meaning that 93 % of the GUV membrane were evaluated. Values are given as mean ± standard deviation of whole GUVs. All experiments were conducted at room temperature.

To determine the l_o area percentage after spreading of the GUVs, silicon wafers with a 100 nm thick oxide layer were hydrophilized as described in Section 3.3.4.2. The wafers were mounted in custom made PTFE chambers filled with PBS. The chambers were heated to 55 °C, GUVs were added and allowed to spread for 1 h at 55 °C. After cooling to room temperature the samples were rinsed with PBS and imaged using an epifluorescence microscope. Samples were incubated with STxB as described in Section 3.2.2. The total area of the membrane patch was determined manually using a graphics tablet. The area of the l_d phase were determined by manually thresholding the images.

3.4.2 Locating l_o domains in pore-spanning lipid bilayers

Pore-spanning lipid bilayers offer the possibility to study of phase-separated membranes which are effected by the underlying mesh which offers solid supported and freestanding membrane areas. The preparation methods presented in Section 3.2.3 relies on the use of gold functionalization of the pore rim. No fluorescence signal can be detected due to quenching in these areas, even though the analysed membrane is continuous it is therefore convenient to analyse each pore individually. A data analysis method based on ImageJ and a custom written matlab graphical user interface (GUI) in matlab2012b was developed. The procedure is schematically depicted in Figure 3.20 and 3.21. Matlab commands are printed *italic.*
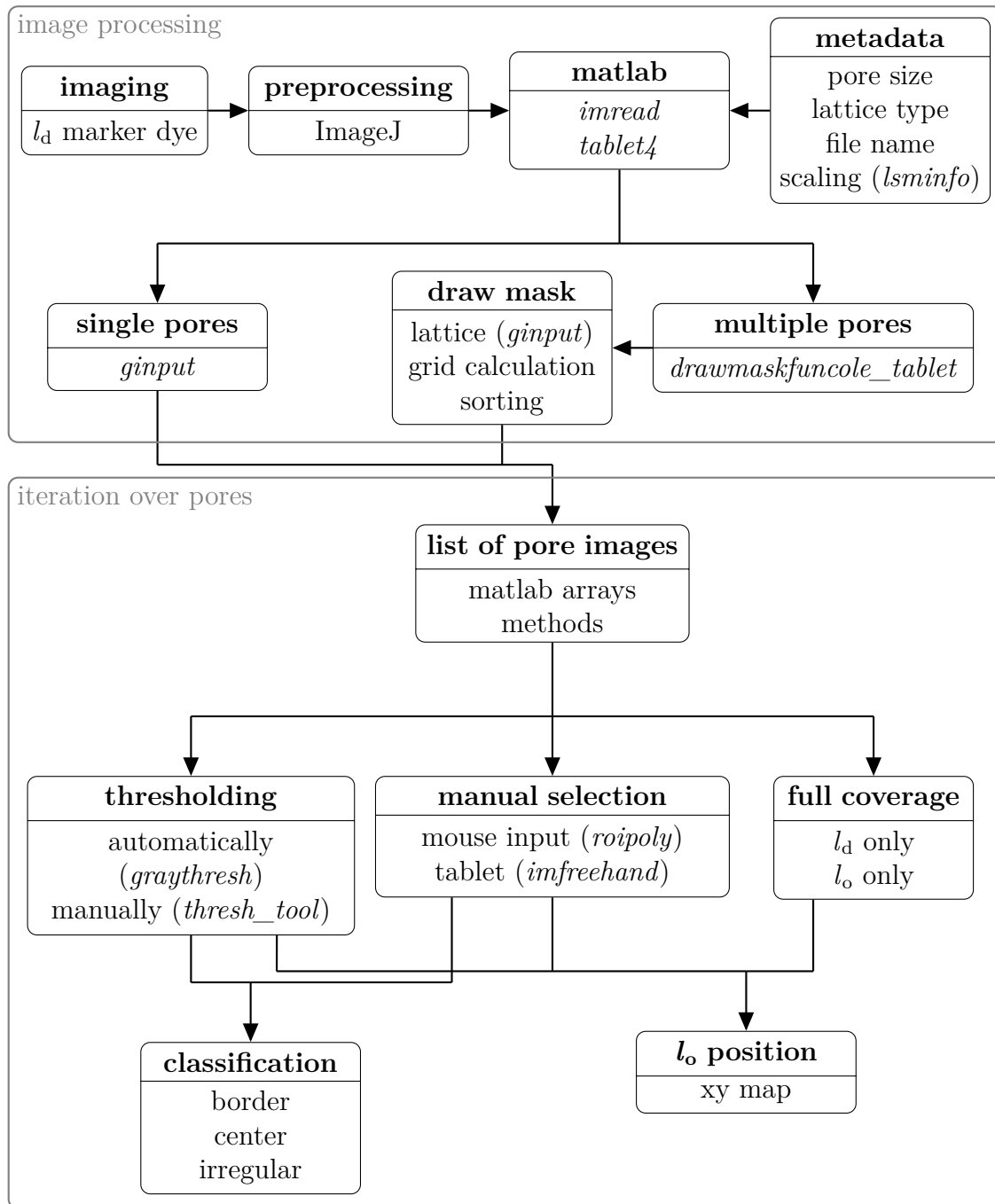
Figure 3.20: Evaluation of l_o domain localization in PSLBs Different **steps** and the *matlab functions* used.

Images acquired by fluorescence microscopy were inspected using ImageJ and an image of the l_d marker dye fluorescence was exported as the green channel of a RGB .png file. The file was loaded into the matlab GUI using *imread*. Meta data of the files was either read from the raw data using *lsminfo* or was manually entered in

the GUI.[120] The actual image processing in matlab involved the extraction of the fluorescence signal of the pore-spanning region disregarding the rim parts.
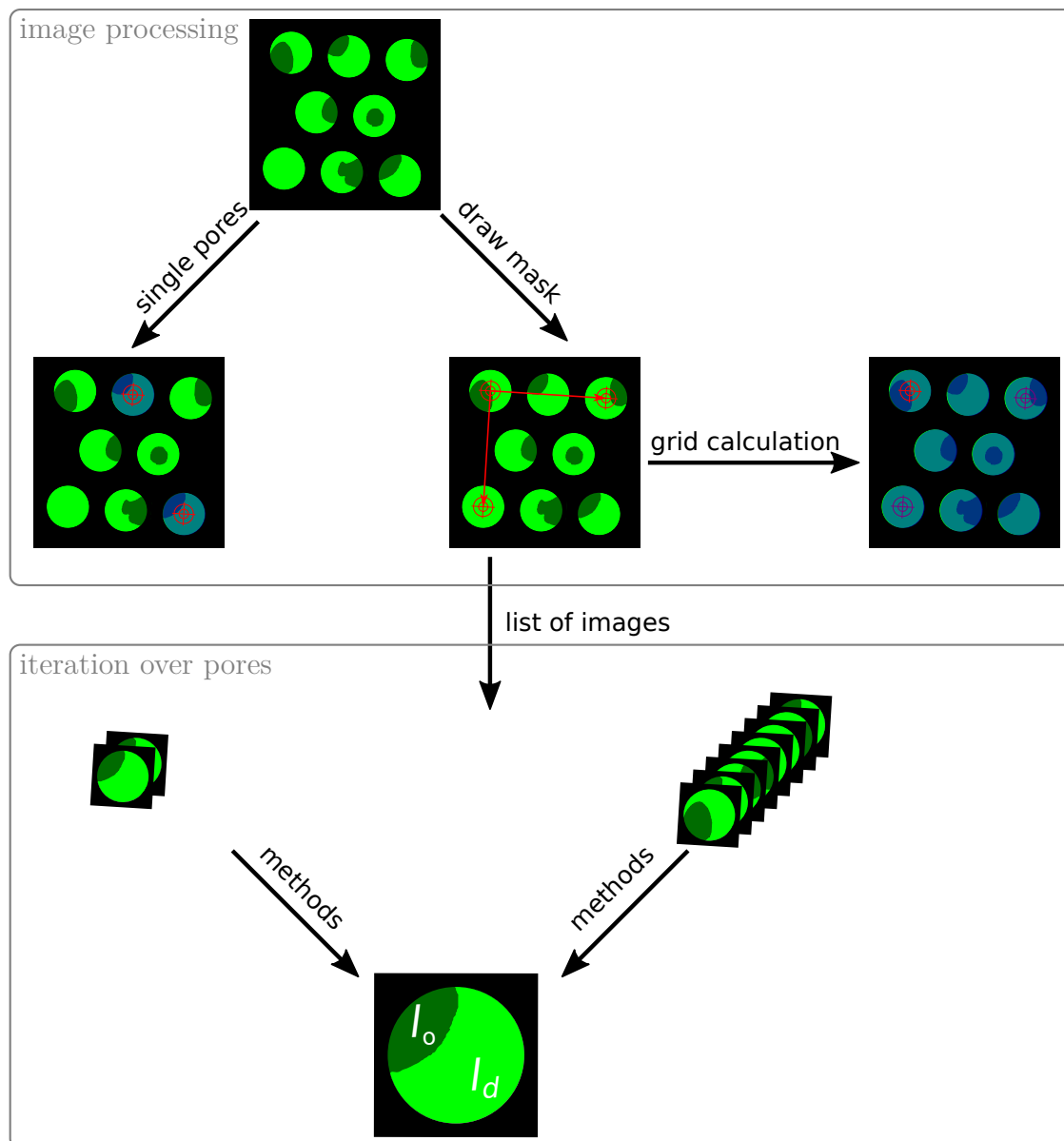
Figure 3.21: Graphical representation of the analysis of lipid domains in pore-spanning membranes. Each pore is extracted and treated individually. The coordinates of the pore centers are either entered manually or calculated after manually determining the lattice constants of the porous grid.

Thresholding of the images proved to be of little help because the dye excluding l_o phase could not be separated from the porous support if it was in close contact to the rim. Instead, a circular mask was created *meshgrid*, the known pore size and the

image scaling of the microscope. The mask was superimposed on the fluorescence image. To achieve this, two methods were used: i) manual localization of the pore center of interest using *ginput* or ii) the semiautomatic calculation of all pore coordinates. The calculation of pore coordinates was implemented in the matlab function *drawmaskfuncole_tablet*. The coordinates of three manually chosen pores determined by *ginput* were used to calculate the lattice constants (x and y spacing of individual pores) of the square or hexagonal lattice fully included in the image. These lattice constants allow to superimpose the pore lattice over the raw data. If necessary, single pores were disregarded or the process was repeated. With this method dozens up to 200 pores could easily be extracted. The image processing resulted in one dataset for each pore which was then treated individually.

To determine the characteristics of the phase separation in the pores the l_o phase in the pores was identified by different methods implemented in the GUI. If no full coverage of a pore either with l_d or l_o phase is present, four different methods can be employed to localize the l_o area. Automatic thresholding using *im2bw* and *graythresh* or the manual definition of a brightness threshold by thresh_tool[119] if the contrast between the phase was sufficiently high. If thresholding proved to be inaccurate the shape of the l_o domains were manually traced using mouse input and *roipoly* or a graphics tablet using *imfreehand*. Domains were further classified by their position (see Figure 5.10 in the results section). The map of the l_o area in the pores was used for further analysis of l_o percentage and radial distribution.

The values given for l_o area percentage only include the freestanding membrane areas and present all covered pores, including those only displaying a single l_o or l_d phase covering the whole pore. Analysis of the pores with a coexisting l_o and l_d phase in the freestanding membrane area gave the same result. The error of the l_o area percentage in the freestanding membrane area σ_m was calculated as the pooled standard variance between the different lipid patches.

$$\sigma_m = \sqrt{\frac{\sum_i g_i \sigma_i^2}{\sum_i g_i - 1}} \tag{3.26}$$

with g_i as the number of covered pores in the patch and $\sigma_i = \bar{x} - x_i$ being the deviation of the l_o percentage of the patch from the mean.

3.4.3 Tracking of lipid domain movement in pore-spanning lipid bilayers

In this thesis pore-spanning lipid bilayers (PSLBs) were used to influence the structure and dynamics of lipid domains. To study the dynamics, PSLBs were prepared as described in Section 3.2.3. The resulting membranes were doped with a dye selectively labeling the disordered phase (Scheme 3.4) and then imaged over time using either the CLSM or the SDCLM (Section 3.3.1). The parameters of the recording were adjusted to the observed domain sizes and dynamics, and are summarized in Table 3.6.

Table 3.6: Parameter used for time series of domains visualized in PSLBs.

Pore diameter / µm	Δt / ms	frames	Pixel size nm^2
0.6/1.0	30	3000	60-200
3.5	30-100	1000	50-130
4.5/5.5	100	3000	222

Image preprocessing

The time series of the domain movement were then preprocessed as described in Figure 3.22. Preprocessing was carried out using custom written matlab scripts based on built-in matlab functions.
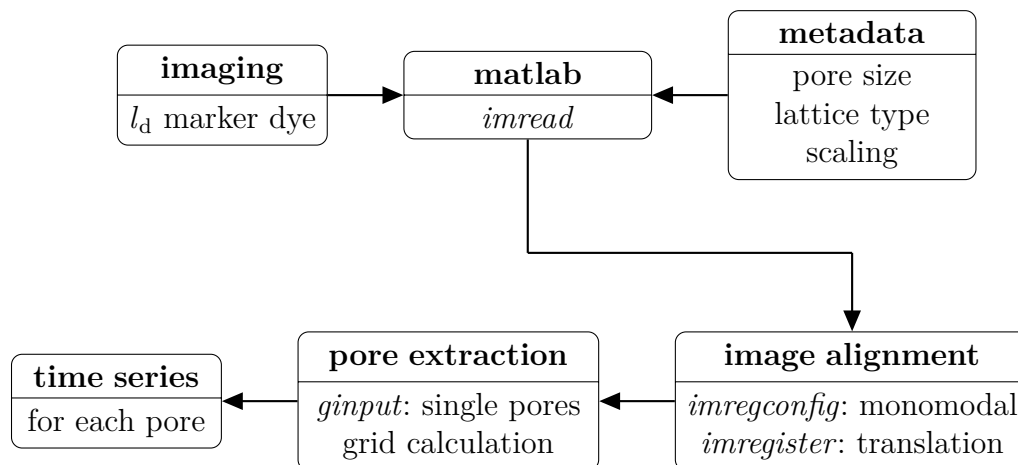

Figure 3.22: Preprocessing of time series of PSLBs. Different **steps** and the *matlab functions* used.

Images were loaded into matlab using *imread*. Metadata of the files (pore size in µm, lattice type, scale factor) was entered manually for each file. The rather long

recording time of the time series of up to $5\,\text{min}$ lead to a x,y shift during the imaging caused by thermal drift. To be able to compare the localization of the domains between the single frames, the shift was corrected using *imregconfig* and *imregister*. A monomodal intensity distribution and translational motion were used as parameters. Each frame was aligned to the first of the time series. In the next step the position of the pore center of each pore was extracted in a similar fashion as described in Section 3.4.2. This resulted in a time series for each of the pores under investigation.

Domain tracking

To track the movement of a domain, its center of mass had to be extracted from each frame of the time series. To process the total of 654000 frames of isolated pores, an automatic matlab based analysis was developed based on a tracking procedure provided by Prof. Dr. Jörg Enderlein (III. Institute of Physics, Georg-August-Universität Göttingen). The procedure is shown exemplary for one frame in Figure 3.23. Starting from the raw data of the fluorescence intensity of the l_d marker the domain has to be extracted. The major problem was to separate the dark, dye excluding l_o domain from the dark pore rim. The raw data was thresholded with an iteratively decreasing threshold. This resulted in images in which several dark areas could be identified. The color coding used in Figure 3.23 assigns a color to each object. Objects in contact with the border of the image were labeled as the rim (yellow, white, green, brown). Decreasing the threshold results in a growth of the identified regions, leading to a merger of formerly isolated objects. The decrease in threshold was continued until the domain (red) fuses with the rim. The threshold prior to this fusion was used to find the domain.
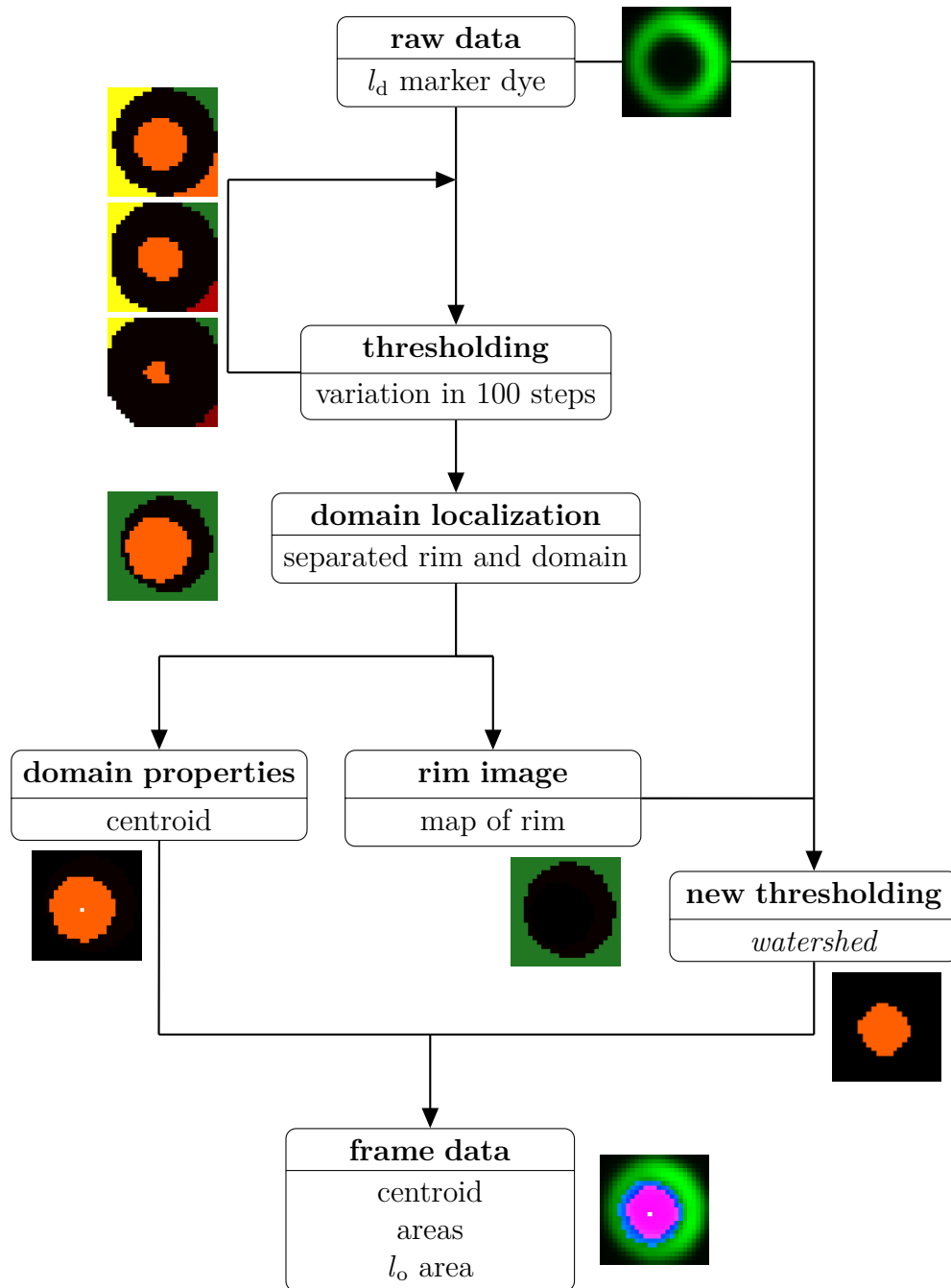
Figure 3.23: Tracking of domains in PSLBs. The process is shown for one frame and was carried out for all 654000 recorded. Different **steps** and the *matlab functions* used.

Subsequently the center of mass of the domain ('centroid') was calculated. This analysis method was only capable of providing data for the centroid. The area assigned to the l_o domain was found to be biased by its position in the pore because the merger of the domain with the rim occurred at lower thresholds if the domain

was localized close to the rim.

A second step of analysis was done to extract a map of the domain and the correct domain area. The map of the rim (green) extracted from the first analysis was used to mask the rim areas in the raw data. New thresholding disregarding this area in conjunction with a water shed algorithm proved to be a suitable tool to extract the map of l_o area. The final data for each frame (centroid, l_o area and map) was saved and the next frame was analysed.

The final resulting data set is shown in the bottom of Figure 3.23. The l_o domain is labeled in blue and magenta. The blue area corresponds to the result of the first thresholding and was not used for further analysis. The magenta area is the l_o domain as identified by the water shed algorithm. The center of mass (white dot) of the domain was found to be identical for both methods.

Data analysis

To be able to fit the data to the theory derived in Section 5.3.4.1 further processing of the data was performed. The x and y coordinates of the center of mass of each domain were used to construct the trajectory of the domain (Figure 5.29A). In the first step mis-detections were disregarded based on three criteria: i) the frame was ignored if no domain could be detected, ii) the frame was ignored if the center of mass of the domain was found to be on the pore rim, iii) the frame was ignored if the step was larger 4σ (standard deviation) of step size distribution (*vide infra*). This filtering resulted in the removal of all frames which would otherwise have impaired the analysis.

The displacement of the center of mass was calculated in x (d_x) and y direction (d_y) at growing time intervals starting from Δt=1 frame to Δt=(length of the time series −1) frame. The distribution of d_x and d_y were summed for each time difference giving 2999 step size histograms (d) as shown in Figure 5.29B for a time series recorded for 3000 frames. Assuming a Gaussian distribution, the mean square displacement (MSD) was calculated as the square of the standard deviation of the distribution.

$$MSD(t) = \sigma^2 = <d^2> - <d>^2 \tag{3.27}$$

To fit Equation 5.8, first the theoretical curve was calculated using the builtin *besselj* and *zerobess* routines to calculate the Bessel functions and its zeros.[121] A

simplex fit was used to fit the experimental data to the theoretical curve.

Further data analysis was performed to quantify the dynamics of the domains. The circularity of each domain in each frame was calculated according to Equation 3.28 with G: perimeter of the domain, A: area of the domain. Values are given as mean $\pm$ standard deviation.

$$C = \frac{G^2}{4\pi \cdot A} \tag{3.28}$$

The size and radius of the domains was calculated based on the thresholded fluorescence images using water shedding. The values are given as mean $\pm$ standard deviation. Values based on this method are denoted as r_{FL}. If not stated otherwise the radii of domains given, always refer to the thresholding method. The values are used to compare to the radius obtained from fitting the diffusion equations (r_{fit}). The maximum distance of the domain's center of mass $d_{\max}$ from the pore center d_0 was calculated from the trajectories by

$$d_{\max} = \max\left(\sqrt{(d_{x,t} - d_{x,0})^2 + (d_{y,t} - d_{y,0})^2}\right). \tag{3.29}$$

4 Phase behavior of Gb$_3$ containing solid supported membranes

In this thesis solid supported phase-separated membranes were used to study the influence of the receptor lipid Gb$_3$ on the phase behavior of the artificial lipid membranes. Gb$_3$ is a naturally occurring glycosphingolipid (Scheme 3.7, page 23) that differs in the fatty acid bound to the ceramide back bone. Surface plasmon resonance spectroscopy was used to quantify the interaction of the Gb$_3$s with the B-subunit of Shiga toxin (STxB). Atomic force microscopy in conjunction with fluorescence microscopy allowed to investigate how the incorporation of different Gb$_3$ species in membranes of the well established 'raft-like' lipid mixture DOPC/SM/Chol 40:40:20 changes the lateral membrane organization. After binding of STxB, the membranes were reexamined by microscopy to quantify the lipid rearrangement induced by Shiga toxin binding.

This chapter is divided into two parts. In Section 4.1 the influence of a saturated (Gb$_3$-C24:0), an unsaturated (Gb$_3$-C24:1), a α-hydroxylated (Gb$_3$-C24:0 2-OH) and an unsaturated and α-hydroxylated Gb$_3$ (Gb$_3$-C24:1 2(R/S)-OH) was investigated systematically to elucidate, how small changes in the chemical structure of the receptor lipid can influence the membrane phase behavior and binding of STxB.

The results and conclusions presented in Section 4.2 extend this model using the two diastereoisomers of the biologically most relevant unsaturated and α-hydroxylated Gb$_3$. A new synthetic route to α-hydroxylated nervonic acid (C24:1 Δ^{15} 2-OH) published by Pawliczek *et al.* in mid 2014, enabled the synthesis of the diastereomerically pure compounds Gb$_3$-C24:1 2(S)-OH and Gb$_3$-C24:1 2(R)-OH. Atomic force in conjunction with fluorescence microscopy were employed and allowed to compare the membrane organization to the diastereomeric mixture used in Section 4.1. Additionally, the binding capacities of the molecules were probed and confocal fluorescence microscopy was used to study how Shiga toxin binding to Gb$_3$ alters the topography of freestanding lipid membranes.

4.1 Influence of acyl chain structure of Gb$_3$ on the phase behavior of solid supported membranes

- Parts of this Section are published as O. M. Schütte, A. Ries, A. Orth, L. J. Patalag, W. Römer, C. Steinem, D. B. Werz, Influence of Gb$_3$ glycosphingolipids differing in their fatty acid chain on the phase behaviour of solid supported membranes: chemical syntheses and impact of Shiga toxin binding, *Chem. Sci.* **2014**, *5*(8), 3104-3114.

- Fluorescence and atomic force microscopy data of solid supported membranes for Gb$_3$-C24:0 2-OH and Gb$_3$-C24:1 were partially measured by Alexander Orth and are included in his PhD thesis.[52] A detailed summary of these contributions is given in Section 4.1.6.1.

- SPR spectroscopy data was partially measured by Anton Römer during his bachelor thesis supervised from June to September 2013.[122]

4.1.1 Abstract

The B-subunit of Shiga toxin (STxB) is involved in cell attachment and the trafficking of Shiga holotoxin in cells. It specifically binds to the glycosphingolipids Gb$_3$ harboring different fatty acids, which influences the binding behavior of Shiga toxin and the latter's intracellular routing. The newly developed synthetic route to Gb$_3$ derivatives bearing saturated, unsaturated and α-hydroxylated C$_{24}$-fatty acids allows to study how these molecules affect the phase behavior of phase-separated membranes and the binding of STxB. Solid supported membranes composed of the 'raft-like' mixture DOPC, sphingomyelin and cholesterol were doped with 5 mol% of the Gb$_3$ derivatives and investigated by atomic force and fluorescence microscopy. α-hydroxylated fatty acids attached to Gb$_3$ alter the ratio of the disordered and ordered phase and unsaturated Gb$_3$ induces a further segregation into a third phase. Upon binding of STxB to membranes containing Gb$_3$ with hydroxylated fatty acids, lipids are redistributed between the phases. Binding to Gb$_3$ with saturated fatty acids results in protein clusters, while unsaturated Gb$_3$ derivatives induce a more homogeneous, areal coverage of the membrane. The results show how the fatty acid of Gb$_3$ influences both, membrane organization and the binding of STxB.
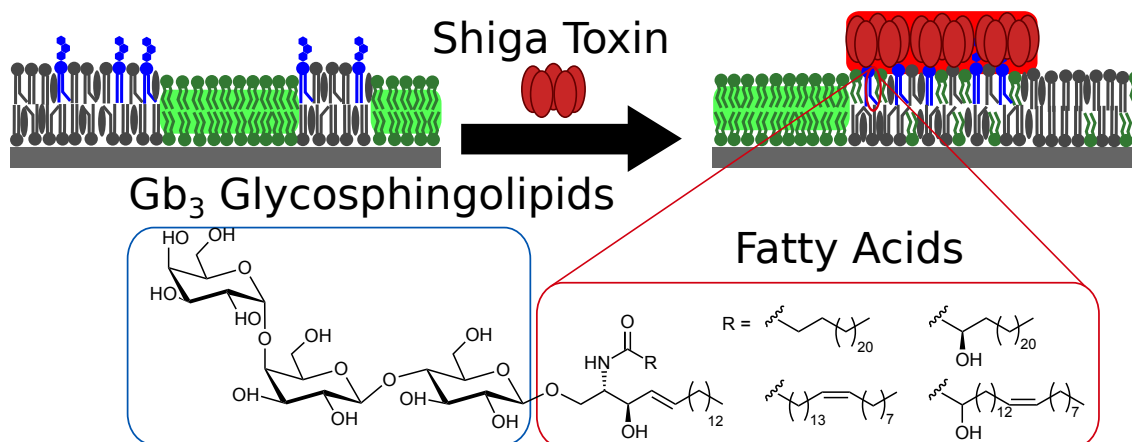
Figure 4.1: Scheme showing the binding of Shiga toxin to different Gb₃ derivatives.[86]

4.1.2 Introduction

Glycosphingolipids are expressed on the extracellular side of the plasma membrane and act as differentiating surface markers.[1] Different viruses and proteins use these receptors to attach to the cell. Lectins recognize glycoconjugates at cell surfaces and are involved in a variety of cellular processes.[123] The ganglioside G_{M1} is recognized by the simian virus 40 and the bacterial protein Cholera toxin (CTx) from *Vibrio cholerea* and facilitates the formation of plasma membrane invaginations, which provide the first step in clathrin independent endocytosis.[72,124]

One of the toxins produced by *Shigella dysenteriae* is the AB₅ protein Shiga toxin (Figure 1.5). Structurally and functionally closely related isoforms, usually called verotoxins or shiga-like toxins, are one of the main pathogenic factors of enterohemorrhagic strains of *Escherichia coli* (EHEC), which are frequently involved in minor epidemics.[56] The protein binds to the plasma membrane by its homo pentameric B-subunit (STxB, Figure 1.7), which specifically recognizes the α-Gal-β-Gal-β-Glu sugar headgroup of the neutral globoside Gb₃.[125,126] Each pentameric B-subunit can bind up to 15 Gb₃ molecules inducing a clustering and headgroup compaction, which induces negative curvature in the membrane as a first step to efficiently cross the cell membrane.[39,60,71,72] In the cell the protein uses the retrograde transport route[127] to the early endosomes. It is then transfered to the endoplasmic reticulum using the golgi network. Upon release to the cytosol the A-subunit can inhibit the function of the rRNA leading to cell death.[59,62,128] Using energy-depleted cells and artificial membrane systems based on giant unilamellar vesicles, Römer *et al.* confirmed that the formation of invaginations is driven by

the STxB-Gb$_3$ interaction.[71] The cytotoxicity of Shiga toxin is influenced by the cell type, Gb$_3$ density and the lipid's association with lipid rafts.[129,130] Several studies in controlled artificial systems led to a closer picture of the steps involved in the process of Shiga toxin internalization. It can be divided into three steps. In the first step the protein binds to the receptor with high affinity,[73,74,107,131] leading to an increased membrane order[132] and headgroup compaction.[55,71,132] Individual proteins then aggregate to larger clusters to minimize line tension.[41,70,71,133] The asymmetric area reduction in one leaflet induces curvature. Sufficiently flexible membranes bend to form invaginations.[39,51,72] The scission is actin driven but can also be induced by artificially changing physical parameters of the membrane.[39]

Cluster formation and the formation of invaginations show a strong coupling to the membrane composition used.[134] In biological systems the fatty acid attached to Gb$_3$ is variable and large differences between cell types are observed.[39] Toxin sensitive HeLa cells show a higher percentage of fatty acid hydroxylation compared to toxin insensitive red blood cells (Table 3.3). The group of Lingwood used microtiter plate staining and thin layer chromatography to determine the binding capacity and affinity of different Gb$_3$ species towards verotoxins. They found that Gb$_3$ with long fatty acid chains (C$_{20}$-C$_{24}$) have a higher affinity than those with shorter chains (C$_{12}$,C$_{14}$) and that unsaturation and α-hydroxylation further enhance binding.[73,74] The finding that mixtures of Gb$_3$ species behave differently than the sole components shows that the interaction with the STxB is complex.[135] Even though their experiments were partially conducted in presence of auxiliary lipids no true planar membrane systems mimicking the cell surface was used.

To study the effect of the fatty acid attached to Gb$_3$ on the lateral organization of membranes and their interactions with STxB a model system based on solid supported membranes can be used.[42,136,137] A chemical approach to Gb$_3$ allowed the synthesis of four Gb$_3$ species based on the biologically most relevant lignoceric (tetracosanoic, C24) fatty acid (Figure 4.1).[39] Glycosphingolipids are believed to be associated with lipid rafts in the plasma membrane. This putative separation into nanoscale clusters of higher molecular order was mimicked using membranes, which phase separate at room temperature into a liquid-ordered (l_o) and liquid-disordered phase l_d.[29] In 2009 Windschiegl *et al.* proved the applicability of the systems using natural Gb$_3$ extracts from porcine erythrocytes.[70]
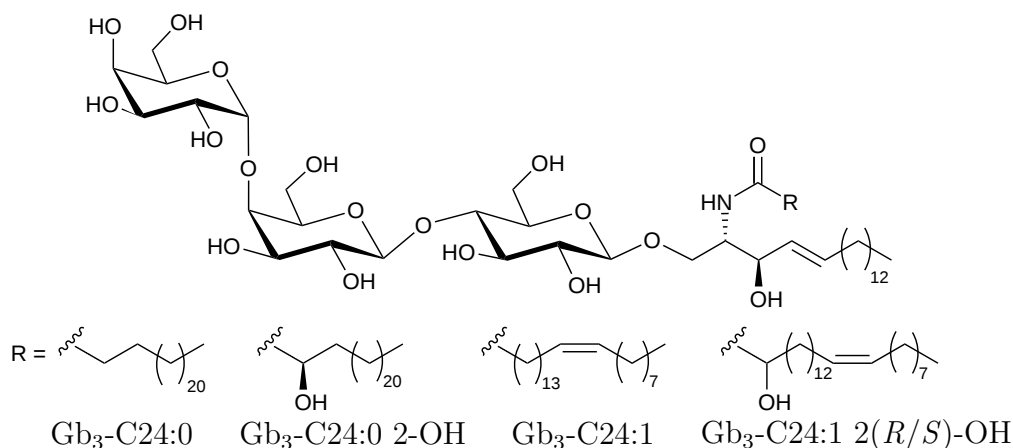
Scheme 4.1: Structure of the Gb₃ derivatives used in this section. The derivatives are all based on the C24:0 fatty acid which is further functionalized by α-hydroxylation and an (Z) unsaturation at position 15 (Δ^{15}).

The derivatives allow to systematically investigate how the fatty acid influences the lateral organization of the membrane and STxB. Gb₃-C24:0 is based on the saturated C24:0 fatty acid. A saturation hydrocarbon chain and the sphingosine backbone should lead to a localization of the molecule in the ordered phase exhibiting strong interactions with cholesterol.[138] Gb₃-C24:1 retains the long fatty acid chain but bears an (Z) unsaturation at position Δ^{15} increasing the molecules steric demand. Gb₃-C24:0 2-OH has an α-hydroxylation which was reported to influence interlipid interactions[139–142] and the headgroup conformation of glycolipids.[142–144] The fourth derivative Gb₃-C24:1 2(R/S)-OH combines unsaturation and α-hydroxylation. Section 4.2 discusses the influence of the configuration of the 2-hydroxy group in more detail. The four derivatives constitute more than 50 % of the total Gb₃ found in HeLa cells, HEp-2 cells and erythrocytes.[39, 145, 146]

Fluorescence microscopy was used to determine the lateral organization of the protein and the membrane. Atomic force microscopy allowed to detect nanometer-sized domains,[29, 137] protein aggregates and estimate STxB's density on the surface.[70] The affinity of STxB to the different Gb₃ derivatives was quantified using surface plasmon resonance spectroscopy.[104, 107]

4.1.3 Results

Two different membrane systems were used to investigate the Gb_3 derivatives. The affinity of STxB towards Gb_3 containing membranes was determined using surface plasmon resonance spectroscopy (SPR, Section 3.3.4.1) in hybrid membranes composed of $DOPC/Gb_3$ 95:5. A raft-like lipid mixture including cholesterol and sphingomyelin was used to study how the Gb_3 derivatives alter the membrane organization and how these changes effect binding of STxB.

4.1.3.1 Quantification of the STxB-Gb_3 interaction by SPR

Previous work has shown that Gb_3 derivatives with different fatty acids have different binding affinities towards STxB. Lingwood and coworkers used microtiter plate experiments with and without auxiliary lipids to determine the affinity and binding capacity of different Gb_3 species.[73,74] They found that even in this simple membrane systems the fatty acid attached to Gb_3 strongly alters its binding behavior.

In this work, binding isotherms were monitored to determine the dissociation constant K_D by means of the SPR technique. A $DOPC/Gb_3$ 95:5 hybrid membrane system was used for SPR measurements to test the functionality of the newly synthesized Gb_3 derivatives. Possible differences in the complex interactions of the Gb_3 derivatives with cholesterol and sphingomyelin are abolished, allowing to elucidate if the fatty acid already has an influence on the binding in a simple phospholipid matrix.

The experimental procedure was adapted from Nakajima *et. al.* and is described in detail in Section 3.3.4.1. To test the system and validate the specificity of the STxB-Gb_3 interaction a blank experiment (Figure 4.2) with a Gb_3 free membrane composed of $100\,mol\%$ DOPC was conducted. Addition of vesicles in PBS (**a**, $DOPC/Gb_3$-C24:1 $2(R/S)$-OH 95:5, final concentration $0.03\,mg\,mL^{-1}$) to an octanethiol functionalized gold sensor chip leads to an increase in reflectivity indicating the formation of a hybrid membrane. Rinsing with PBS (**b**) results in a slow drop in reflectivity caused by the detachment of vesicles and membrane multistacks. Possible hydrophobic defects were blocked by bovine serum albumin (BSA, **c** to **d**, $1\,mg\,mL^{-1}$). The detachment of membrane multistacks is accelerated by the repeated addition of NaOH solution (**e**, $50\,mM$). STxB with a final concentration of $60\,nM$ was added (**f**, **g**). As visible from the zoom in of Figure 4.2A no increase in reflectivity was found, showing that STxB is not binding to Gb_3 free membranes (*vide infra*).
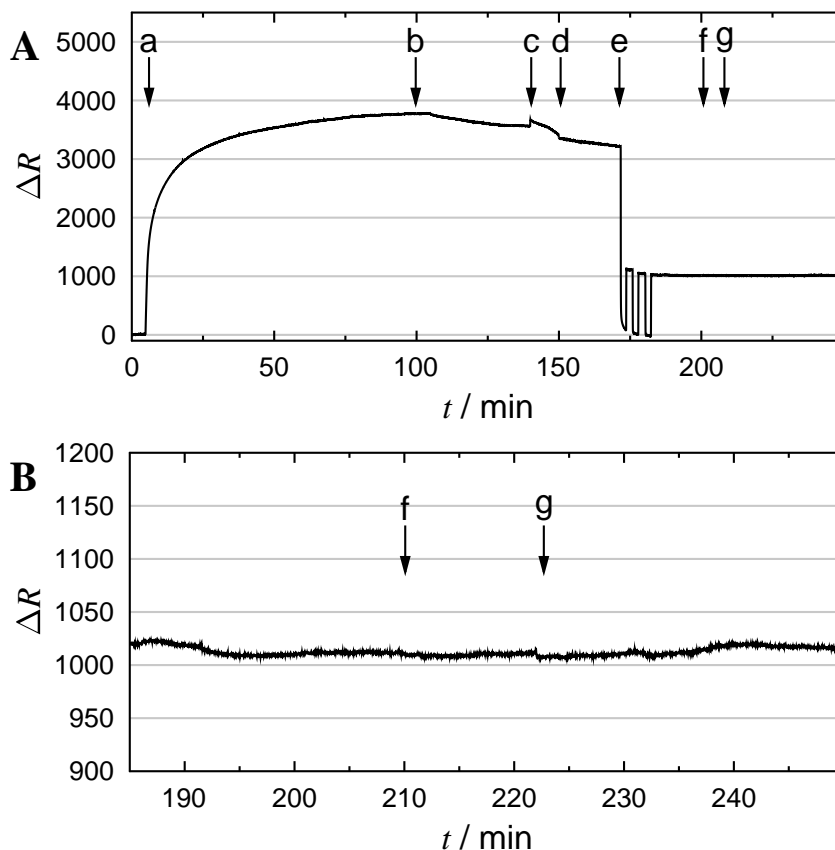
Figure 4.2: SPR experiment proving the specificity of the STxB-Gb$_3$ interaction. (a): Addition of small vesicles (DOPC 100 mol%, final concentration 0.03 mg mL^{-1}) at a flowrate of 50 µL min^{-1}. (b): rinsing. (c): flowrate was lowered to 25 µL min^{-1} to add BSA solution (1 mg mL^{-1}) to block defects in the membrane. (d): rinsing. (e): Addition of NaOH solution (3×50 mM) for 2 min each to remove vesicles and lipid multistacks. (f), (g): Two Additions of STxB ($c = 60$ nM) followed by rinsing with PBS. **B** Zoom in of **A** showing that STxB does not bind to the Gb$_3$ free membrane.

To validate the applicability of the experimental setup, first the commercially available Gb$_3$ extract from porcine erythrocytes (Gb$_3$-Porc) was used. It was found that upon vesicle spreading and protein addition the overall increase in reflectivity strongly varied among the experiments. All values were therefore normalized to the increase in reflectivity near saturation.

The course of experiments was identical for all Gb$_3$ derivatives used and no major differences were found. A characteristic experiment for membranes composed of DOPC/Gb$_3$-C24:1 2(R/S)-OH 95:5 is shown in Figure 4.3. The experimental procedure is identical to the one presented above.
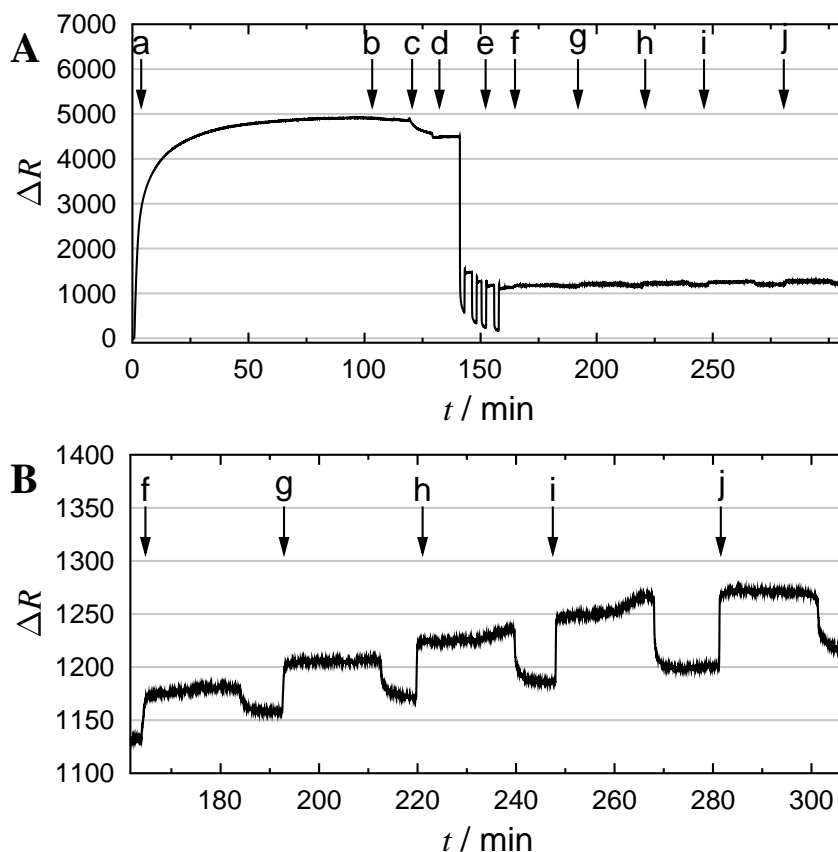
Figure 4.3: Course of an characteristic SPR experiment (a): Addition of small vesicles (DOPC/Gb$_3$-C24:1 2(R/S)-OH 95: final concentration $0.03\,\mathrm{mg\,mL^{-1}}$) at a flowrate of $50\,\mathrm{\mu L\,min^{-1}}$. (b): rinsing. (c): flowrate was lowered to $25\,\mathrm{\mu L\,min^{-1}}$ to add BSA solution ($1\,\mathrm{mg\,mL^{-1}}$) to block defects in the membrane. (d): rinsing. (e): Addition of NaOH solution ($3 \times 50\,\mathrm{mM}$) for 2 min each to remove vesicles and lipid multistacks. (f)-(j): Additions of STxB ($c = 5$, 10, 20, 40, 60 nM) followed by rinsing with PBS. **B** Zoom in of **A** showing the increase in reflectivity upon STxB binding.

In case of Gb$_3$ containing membranes the reflectivity rapidly increases to a steady level upon injection of STxB (4.3B). Rinsing leads to a partial dissociation of the protein ($\approx 30\,\%$). Addition of a larger protein concentration leads to a higher increase in reflectivity. Evaluation of the experiment is described in Section 3.3.4.1. Adsorption isotherms for all Gb$_3$ derivatives are shown in Figure 4.4 together with a fit according to the Langmuir model (Equation 3.15).
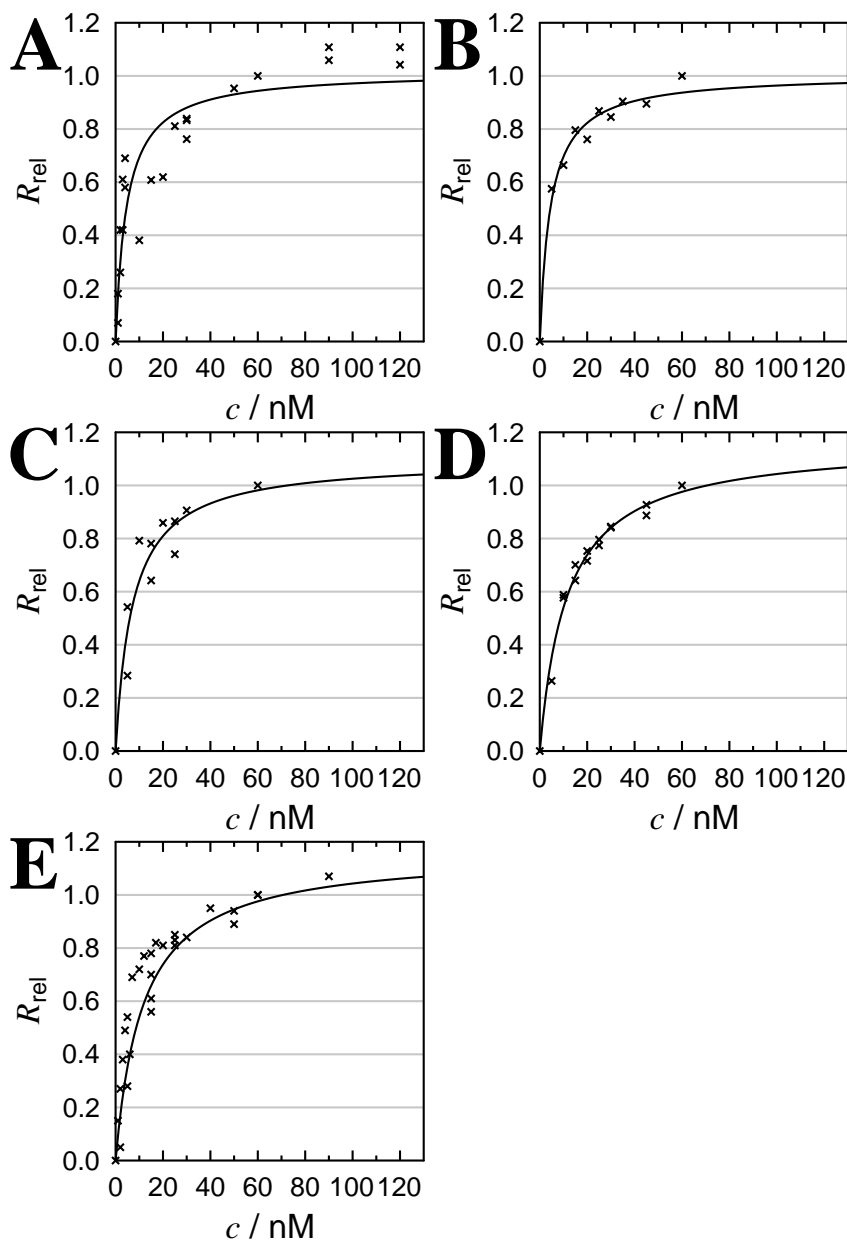
Figure 4.4: SPR adsorption isotherms obtained for membranes composed of DOPC/Gb$_3$ 95:5 with Gb$_3$-Porc (**A**), Gb$_3$-C24:0 (**B**), Gb$_3$-C24:0 2-OH (**C**), Gb$_3$-C24:1 (**D**), Gb$_3$-C24:1 2(R/S)-OH (**E**).

The relative change in reflectivity R_{rel} is proportional to the surface coverage Θ. Isotherms reveal that all derivatives are close to saturation at $c = 60\,\text{nM}$. For some derivatives the curves seem not to be in full saturation indicated by $\Theta_{\text{max,rel}}$ larger than 1. Table 4.1 summarizes the results obtained by SPR in membranes composed of DOPC/Gb$_3$ 95:5. The dissociation constants K_{D} determined are all

Table 4.1: Summary of the SPR measurements. Values were obtained using Equation 3.15.

Gb$_3$-	K_D / nM	θ_rel	$\theta_{60\,\text{nM}}$ / %
Porc	5±1	1.0±0.056	94
C24:0	4±1	1.0±0.03	94
C24:0 2-OH	7±2	1.1±0.101	98
C24:1	12±1	1.1±0.04	98
C24:1 2(R/S)-OH	7±1	1.1±0.048	97

in the low nanomolar regime for all derivatives.[73,74] No clear trend is apparent from the data whether an α-hydroxylation or unsaturation changes the affinity. The calculated receptor coverages at the concentration used for the fluorescence and atomic force microscopy experiments ($c = 60\,\text{nM}$) is $>90\,\%$, showing that the receptor was saturated in the experiments presented in Section 4.1.3.3.

4.1.3.2 Phase behavior of Gb$_3$ containing membranes prior to STxB binding

Solid supported membranes (SSMs) on mica were used to examine the influence of the different Gb$_3$ derivatives on the phase behavior of phase-separated lipid membranes.

Membranes composed of the well established 'raft-like' mixture DOPC, sphingomyelin (SM) and cholesterol (Chol) in a molar ratio of 40:40:20 were used as the matrix.[42,136,147] Spreading was achieved at elevated temperature as described in Section 3.2.2.[30] Cooling the membrane to room temperature leads to the membrane segregating into an liquid-ordered (l_o) and a liquid-disordered (l_d) phase. The l_d phase is identified by the preferential partition of a bulky lipid coupled dye (Texas Red DHPE, Oregon Green DHPE, Bodipy-PC or Atto488 DHPE, see Section 3.1.2) into the phase as seen in Figure 4.5A.[35] Due to polarity and sterical demand these dyes get expelled from the dark l_o phase.[35,36] The integrity of the membrane can be confirmed using the small organic dye perylene, which is distributed more homogeneously between the phases.[35] As shown in Figure 4.5B the blue fluorescence is also located in the dark areas of panel A indicating that a defect free membrane is present in these areas.
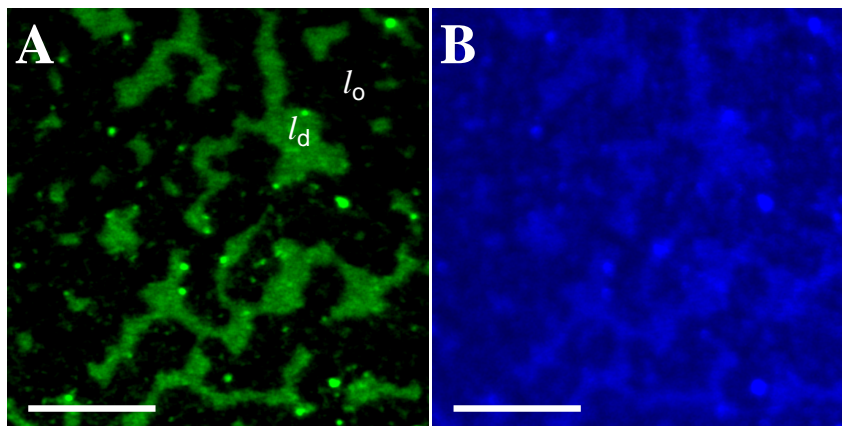
Figure 4.5: Domain organization of membranes composed of DOPC/SM/Chol (40:40:20) doped with perylene (0.5 mol%) and Bodipy-PC (0.1 mol%). **A** Fluorescence micrograph of Bodipy-PC. Membranes segregate into liquid-ordered (l_o, dark) and liquid-disordered domains (l_d, green). **B** Perylene fluorescence is more homogeneous showing that the dark areas in **A** are membrane covered. Scale bars: 10 µm.

Previous studies used the partitioning of perylene between the lipid phases as an indicator of membrane order.[35, 70, 148] In this thesis perylene was found to be mostly located in the l_o phase before protein binding. After protein binding the results strongly varied between experiments and were hampered by low contrast and absolute fluorescence intensity. Perylene images were therefore only used to confirm membrane integrity.

Fluorescence micrographs of fluorescent dyes preferentially locating to the l_d phase allow to quantify the area occupied by the phases (see Section 3.2.2). By pixel analysis of solid supported membranes composed of DOPC/SM/Chol 40:40:20 the dark l_o phase was found to occupy $66 \pm 6\%$ (n = 35) of the total membrane area.[70] The higher order and preferential partitioning of cholesterol into the l_o phase leads to a thickening of the domains elevating $\approx$0.5-1.0 nm above the l_d areas.[97, 140] The percentage of l_d area was found to be independent of the l_d marker dye used (see Table 4.7).

To elucidate the impact of the Gb$_3$ derivatives (Figure 4.1) on the lateral organization of solid supported phase-separated membranes on mica, 5 mol% of the sphingomyelin was replaced by Gb$_3$, retaining the separation into a l_o and a l_d phase.[70] The influence of the fatty acid was systematically studied by starting with the saturated C24:0 fatty acid and subsequent experiments introducing the α-hydroxylation and the unsaturation at position Δ^{15}.

Phase behavior of Gb₃-C24:0 containing membranes before STxB binding

Figure 4.6 shows characteristic images of membranes composed of DOPC/SM/Chol/Gb₃-C24:0 40:35:20:5 on mica support. In panel A and B two different brightnesses of the l_d marker dye TexasRed DHPE are visible. The brighter areas are assigned to the liquid-disordered phase. The majority of the membrane area excludes the bulky fluorophor and can therefore be identified as the liquid-ordered phase. Pixel analysis of 84 fluorescence micrographs of two different l_d marker dyes show that the l_o phase accounts for $74 \pm 7\%$ of the total membrane area in good agreement with previous studies.[70] Influence of the solid support leads to irregular domain structure.
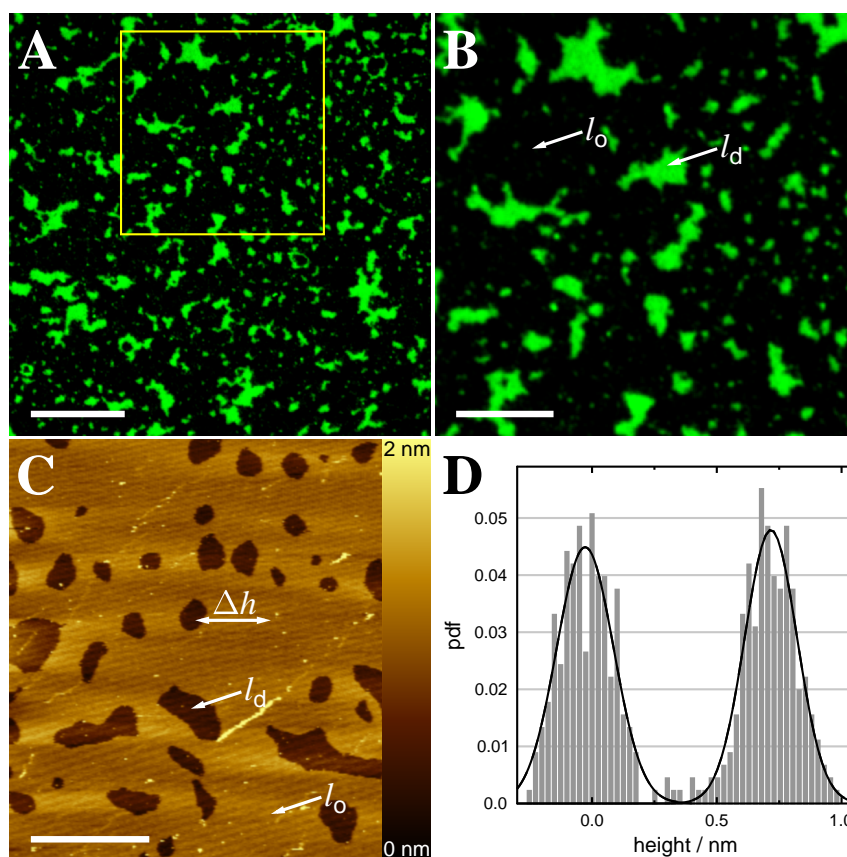

Figure 4.6: Solid supported membranes (DOPC/SM/Chol/Gb₃-C24:0, 40:35:20:5) doped with perylene ($0.5\,\text{mol}\%$) and TexasRed DHPE ($0.1\,\text{mol}\%$) on mica. **A** Fluorescence micrograph of TexasRed DHPE (false colored in green). Fluorophore partition identifies the liquid-ordered (l_o, dark) and liquid-disordered phase (l_d, green). Scale bar: $20\,\mu\text{m}$. **B** Magnified view of the region marked in **A**. Scale bar: $10\,\mu\text{m}$. **C** Topographic AFM image showing a higher l_o phase (lighter color coding) and a lower l_d phase (dark color coding). Scale bar: $5\,\mu\text{m}$. **D** Histogram analysis of a region in **C** showing a height difference of $\Delta h(l_o/l_d) = 0.7 \pm 0.2\,\text{nm}$. Image reproduced from Schütte, Ries *et al.* 2014.[86]

The phase separation of the membrane was confirmed using contact mode atomic force microscopy (AFM, see Section 3.3.2). AFM allows to map the topography of the membranes. For Gb_3-C24:0 containing membranes two different structures were found (Figure 4.6C), differing in their height by Δh. The height difference was found to be 0.6 ± 0.2 nm (n $= 21$) which is in good agreement with published values for the height difference of the higher l_o phase to the surrounding l_d phase.[97] Comparing to the control experiment without Gb_3 (Figure 4.5) no major differences apart from a small increase in l_o percentage were found.

Phase behavior of Gb₃-C24:0 2-OH containing membranes before STxB binding

The α-OH tetracosanoic acid derivative (Gb_3-C24:0 2-OH) is obtained by introducing an (R) α-hydroxylation (2-OH) in the fatty acid (Figure 4.1). Ceramide species bearing a fatty acid hydroxylation play a major role in human metabolism and their deficiency is associated with severe illnesses.[149, 150] Phase-separated membranes (DOPC/SM/Chol/Gb_3-C24:0 2-OH 40:35:20:5) doped with perylene (0.5 mol%) and TexasRed DHPE or Bodipy-PC (0.1 mol%) on mica (Figure 4.7) show a similar phase behavior as membranes doped with Gb_3-C24:0. Again, bright areas of high fluorescence intensity identify the l_d phase enriched in the phase selective dye. On the zoomed fluorescence image (Figure 4.7B) only the single darker l_o phase can be identified by the lower fluorescence intensity. The irregular structure of the domains is retained. Pixel analysis of 56 thresholded fluorescence micrographs of two different l_d marker dyes show that the dark l_o phase accounts for 56 ± 5 % of the total membrane area indicating that Gb_3-C24:0 2-OH induces a lipid rearrangement between the phases. Compared to the Gb_3-C24:0 and Gb_3-free systems the area percentage of l_o is ≈ 20 % lower. Since Gb_3 only accounts for roughly 7 % of the membrane area this change is unexpectedly large.[37, 66] Mapping the topography by atomic force microscopy reveals a single height difference of $\Delta h(l_o/l_d) = 0.8 \pm 0.1$ nm (n $= 87$) which can be assigned to the height difference between the two lipid phases phases observed in the fluorescence micrographs. The height difference only slightly differs from the value found for Gb_3-C24:0 containing membranes (*vide supra*). Height difference were reported to change for different compositions of the phases.[42] The presumed different lipid composition indicated by the lowered l_o area percentage for Gb_3-C24:0 2-OH

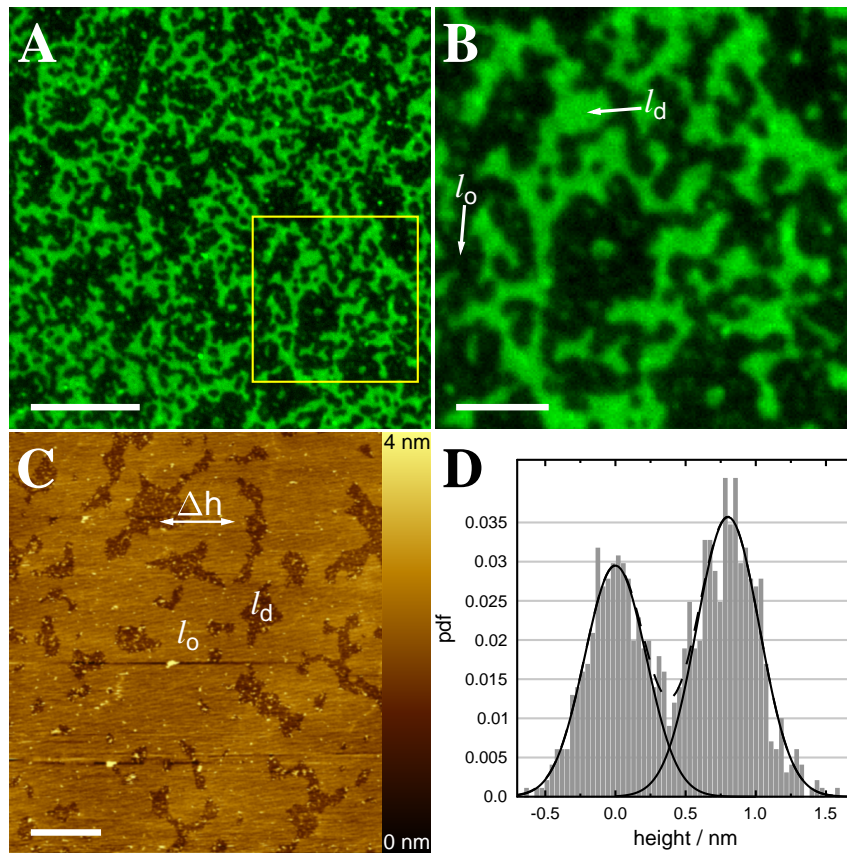containing membranes, could not unambiguously be confirmed using AFM.

Figure 4.7: Solid supported membranes (DOPC/SM/Chol/Gb$_3$-C24:0 2-OH, 40:35:20:5) doped with perylene (0.5 mol%) and TexasRed DHPE (0.1 mol%) on mica. **A** Fluorescence micrograph of TexasRed DHPE (false colored in green). Fluorophore partition identifies the liquid-ordered (l_o, dark) and liquid-disordered phase (l_d , green). Scale bar: 15 µm. **B** Magnified view of the region marked in **A**. Scale bar: 5 µm. **C** Topographic AFM image showing a higher l_o phase (lighter color coding) and a lower l_d phase (dark color coding). Scale bar: 5 µm. **D** Histogram analysis of a region in **C** showing a height difference of $\Delta h(l_o/l_d) = 0.8 \pm 0.4$ nm. Image reproduced from Schütte, Ries *et al.* 2014.[86] Data taken from Orth 2012.[52]

Phase behavior of Gb₃-C24:1 containing membranes before STxB binding

To rationalize the influence of an unsaturated fatty acid, the Gb₃ derivative bearing C24:1 Δ^{15} at its amide group (Gb₃-C24:1) was investigated (Scheme 4.1). Even though it constitutes only a minor fraction of all Gb₃ species in HeLa cells (Table 3.3), it is important to study its influence to develop a systematic insight into the influence of the fatty acid attached to Gb₃ on the lateral organization of phase-separated membranes. Gb₃ is believed to be located in the l_o phase due to its sphingolipid backbone.[1] Usually the high molecular order of the l_o phase and the specific interactions with cholesterol require lipids with saturated fatty acids. The (Z) configuration of the Δ^{15} double bond forms a kink in the membrane and increases the area demand of the molecule.[1]

Phase-separated membranes (DOPC/SM/Chol/Gb₃-C24:0 2-OH 40:35:20:5) doped with perylene (0.5 mol%) and TexasRed DHPE or Bodipy-PC (0.1 mol%) on mica were investigated by fluorescence microscopy. Figure 4.8A shows a characteristic fluorescence micrograph of the l_d selective dye TexasRed DHPE. Clearly three different brightness levels can be identified independent of the l_d marker used (Table 4.7). The homogeneous perylene fluorescence (4.8AB) shows that the area shown in panel A is fully membrane covered. The classical separation of the lipid mixture into two phases is disturbed by Gb₃-C24:1. The lowest brightness is assigned to the l_o phase, the brightest area is assigned to the l_d phase. As no information on the chemical nature of the third phase is available, it is termed 'liquid-intermediate' or l_i phase. In topographic images obtained by contact mode atomic force microscopy the lowest height found was assigned to the l_d phase in accordance with the previous assignment. In most images the l_i and l_o phases were found not to differ in height. The characteristic AFM image in Figure 4.8C shows only one elevated height. The height difference was found to be $\Delta h = 1.2 \pm 0.2$ nm (n = 68), which is higher than expected for the l_o/l_d phase separation.
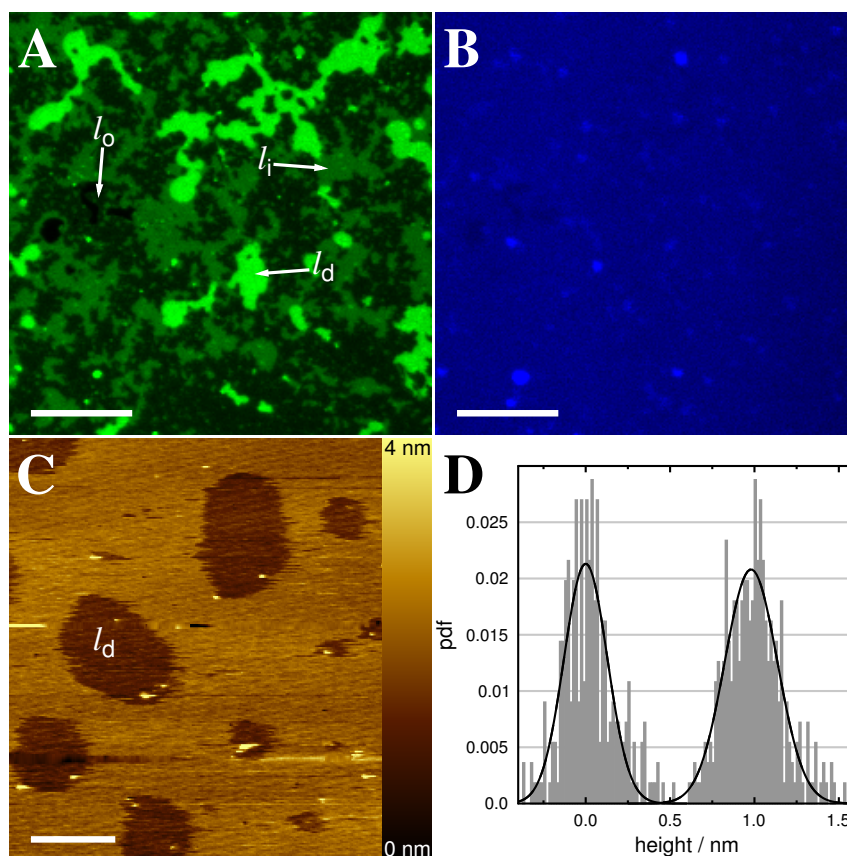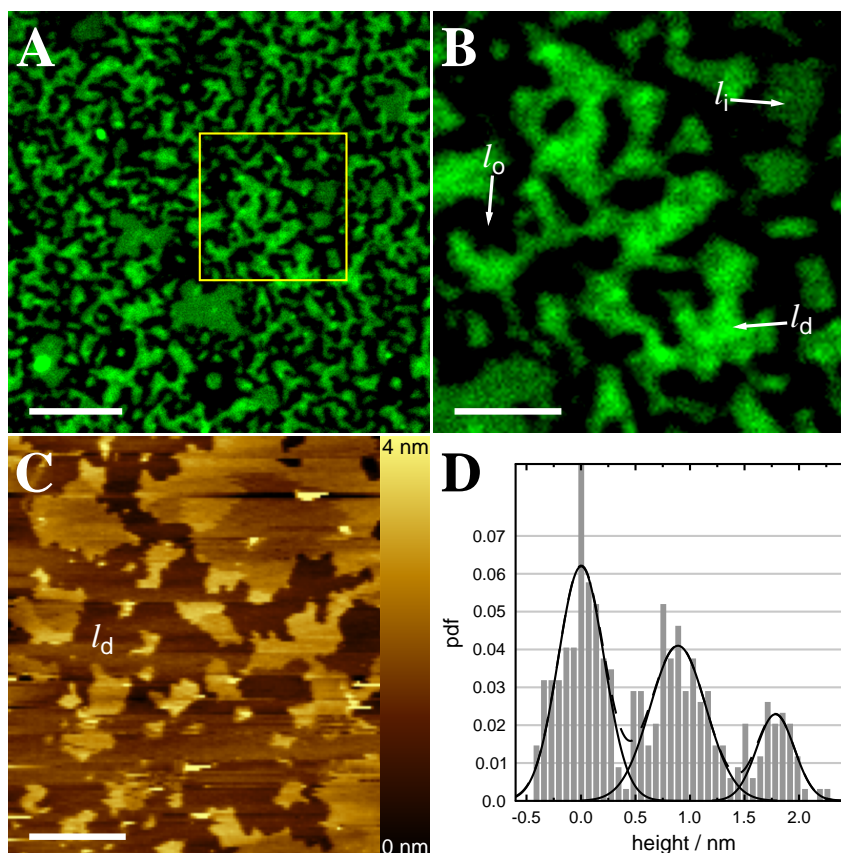
Figure 4.8: Solid supported membranes (DOPC/SM/Chol/Gb$_3$-C24:1, 40:35:20:5) doped with perylene (0.5 mol%) and TexasRed DHPE (0.1 mol%) on mica. **A** Fluorescence micrograph of TexasRed DHPE (false colored in green). Fluorophore partition identifies three brightness levels corresponding to three lipid phases. Scale bar: 15 µm. **B** Fluorescence micrograph of perylene (false colored in blue). The homogeneous blue fluorescence indicates no phase preference of perylene and shows that the three brightness levels in **A** correspond to three lipid phases. Scale bar: 15 µm. **C** AFM image showing the only two phases. The lowest phase is assigned to the l_d phase but the l_o and l_i phase cannot be separated by their height. Scale bar: 3 µm. **D** Histogram analysis of a region in **C** showing a single height differences of $\Delta h = 0.9 \pm 0.3$ nm.

In some samples and images the segregation into three phases could be validated in both fluorescence and atomic force microscopy. Figure 4.9 shows characteristic data. The dark l_o phase covers 40 ± 6 % (n = 73) of the membrane area while the l_i phase accounts for 36 ± 8 %. The sum of both values is close to the l_o percentage observed for Gb$_3$-C24:0 containing membranes, suggesting a further segregation of the l_o phase into two phases (Table 4.2). In Figure 4.9C three different height levels are apparent. The lowest height is assigned to the l_d phase; the two elevated heights ($\Delta h_1 = 1.2 \pm 0.2$ nm (n = 4) and $\Delta h_2 = 1.6 \pm 0.2$ nm, n = 4) cannot be unambiguously

assigned to the l_o and l_i phase as they have a similar morphology and area percentage.

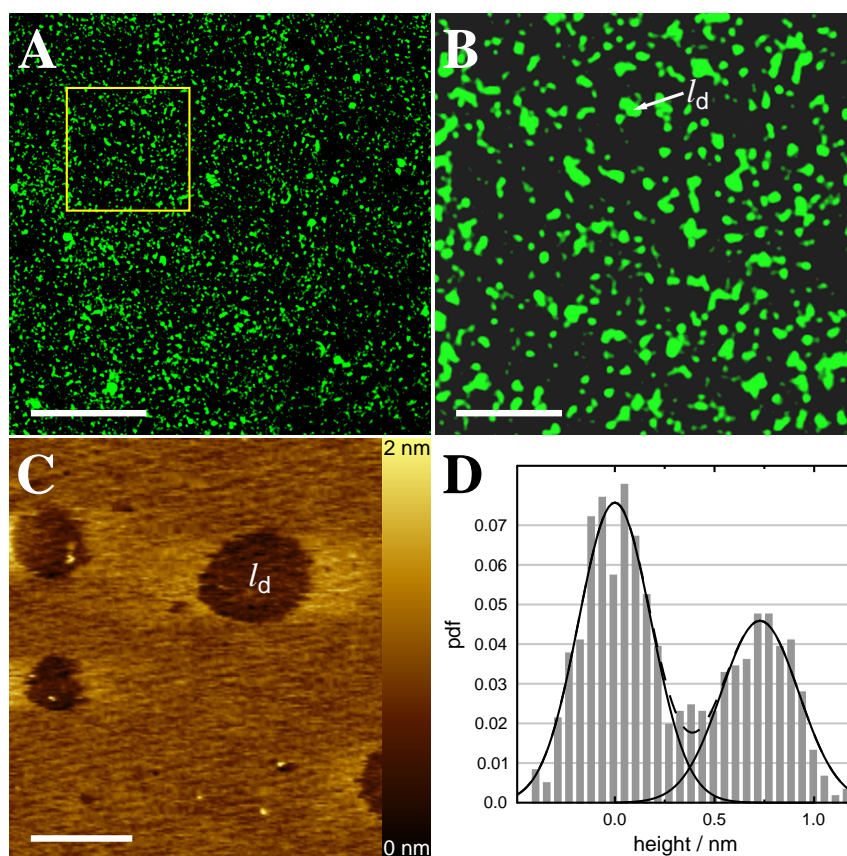**Figure 4.9:** Solid supported membranes (DOPC/SM/Chol/Gb₃-C24:1, 40:35:20:5) doped with perylene (0.5 mol%) and TexasRed DHPE (0.1 mol%) on mica. **A** Fluorescence micrograph of TexasRed DHPE (false colored in green). Fluorophore partition identifies three brightness levels corresponding to three lipid phases. Scale bar: 10 µm. **B** Magnified view of the region marked in **A**. Apart from the bright l_d and the dark l_o phase a third phase phase of intermediate brightness (l_i) is found. Scale bar: 4 µm. **C** AFM image showing the three phases. The lowest phase is assigned to the l_d phase. The other two heights cannot be unambiguously assigned to the l_i and l_o phase from the fluorescence images. Scale bar: 2 µm. **D** Histogram analysis of a region in **C** showing two height differences of $\Delta h_1 = 0.9 \pm 0.4$ nm and $\Delta h_2 = 1.8 \pm 0.4$ nm. Image reproduced from Schütte, Ries *et al.* 2014.[86] Data for panels A and B reproduced from Orth 2012.[51]

Phase behavior of Gb₃-C24:1 2(R/S)-OH containing membranes before STxB binding

The Gb₃ derivative bearing α-hydroxylated nervonic acid (Gb₃-C24:1 2(R/S)-OH) combines the hydroxylation and unsaturation. Its effect on the membrane organization was studied in solid supported membranes composed of

DOPC/SM/Chol/Gb$_3$-C24:1 2(R/S)-OH 40:35:20:5 doped with perylene (0.5 mol%) and TexasRed DHPE or OregonGreen DHPE (0.1 mol%) on mica.

Figure 4.10 shows characteristic fluorescence images and an atomic force microscopic topography map. The overall phase behavior strongly resembles the one of membranes doped with Gb$_3$-C24:0 indicating that the effect of the α-hydroxylation and the (Z) double bond interfere. Membranes only segregate into two different lipid phases identified as the l_d phase and the l_o phase which accounts for $70 \pm 7\%$ (n = 51) of the membrane. The fluorescence micrographs reveal no striking difference compared to the experiments using the fully saturated Gb$_3$.

Figure 4.10: Solid supported membranes (DOPC/SM/Chol/Gb$_3$-C24:1 2(R/S)-OH, 40:35:20:5) doped with perylene (0.5 mol%) and TexasRed DHPE (0.1 mol%) on mica. **A** Fluorescence micrograph of TexasRed DHPE (false colored in green). Fluorophore partition identifies the liquid-ordered (l_o, dark) and liquid-disordered phase (l_d, green). Scale bar: 30 µm. **B** Magnified view of the region marked in **A**. Scale bar: 8 µm. **C** Topographic AFM image showing a higher l_o phase (lighter color coding) and a lower l_d phase (dark color coding). Scale bar: 3 µm. **D** Histogram analysis of a region in **C** showing a height difference of $\Delta h(l_o/l_d) = 0.7 \pm 0.4$ nm. Image reproduced from Schütte, Ries *et al.* 2014.[86]

Using atomic force microscopy the difference in height between the lipid phases is determined to $\Delta h(l_\mathrm{o}/l_\mathrm{d}) = 0.5 \pm 0.2\,\mathrm{nm}$ (n = 31).

Summary of the phase behavior of Gb₃ containing membranes before STxB binding

The values obtained by fluorescence and atomic force microscopy of membranes containing Gb₃-C24:0, Gb₃-C24:0 2-OH, Gb₃-C24:1 or Gb₃-C24:1 2(R/S)-OH are summarized in Table 4.2.

These findings show that the fatty acid attached to Gb₃ influences the phase behavior of the lipid mixture even though it only constitutes 5 mol% of the total lipids. This implies that Gb₃ strongly interacts with other lipids resulting in a membrane reorganization.

Table 4.2: Summary of the results obtained for DOPC/SM/Chol/Gb₃ (40:35:20:5) membranes doped with different Gb₃ derivatives on solid mica support. Ratios of the lipid phase were determined by pixel analysis of fluorescence micrographs. Height differences Δh were obtained by fitting Gaussian distributions to manually binned height histograms. For Gb₃-C24:0, Gb₃-C24:0 2-OH, and Gb₃-C24:1 2(R/S)-OH Δh_2 is the height difference between l_o and l_d phase ($\Delta h(l_\mathrm{o}/l_\mathrm{d})$). Number of analyzed fluorescence micrographs and height histograms is given in brackets.

Gb₃-	$l_\mathrm{o}/\%$	$l_\mathrm{i}/\%$	$\Delta h_2/\mathrm{nm}$	$\Delta h_1/\mathrm{nm}$
C24:0	$74 \pm 7\,(84)$	—	$0.6 \pm 0.2\,(21)$	—
C24:0 2-OH	$56 \pm 5\,(56)^{\ddagger}$	—	$0.8 \pm 0.1\,(87)^{\ddagger}$	—
C24:1	$40 \pm 6\,(73)^{\ddagger}$	$36 \pm 8^{\ddagger}$	$1.6 \pm 0.2\,(5)$	$1.2 \pm 0.2\,(4)$
C24:1 2(R/S)-OH	$70 \pm 7\,(51)$	—	$0.5 \pm 0.2\,(31)$	—

For Gb₃-C24:1 two height differences could rarely be resolved. In most cases an averaged height difference of $\Delta h_{1/2} = 1.2 \pm 0.2\,\mathrm{nm}$ (n = 68) was found.[‡]
[‡] Data partially reproduced from Orth 2012.[51]

4.1.3.3 Phase behavior of Gb₃ containing membranes and lateral protein organization after STxB binding

Binding of the Shiga toxin subunit B to its specific receptor glycolipid Gb₃ is known to alter the lipid membrane organization.[71,134] The protein can bind up to 15 receptor molecules suggesting a mutual influence of the membrane organization on the bound protein and *vice versa*.[71,134]

Solid supported membranes composed of DOPC/SM/Chol/Gb₃ in a molar ratio of 40:35:20:5 on mica were studied by means of fluorescence and atomic force microscopy. The combination of three different fluorescence labels allowed to

determine the membrane integrity, organization and protein localization. $0.5\,mol\%$ perylene was used as non selective marker dye to stain the membrane. TexasRed DHPE, OregonGreen DHPE and Bodipy-PC selectively localize in l_d domains. Shiga toxin covalently labeled with Cy3 (STxB-Cy3, see Scheme 3.6) allows to localize the Shiga toxin and thereby the Gb_3 receptor in fluorescence micrographs. Gb_3 was previously reported to be localized in the l_o phase after STxB binding.[70] Atomic force microscopy allows to study both the lateral organization of the membrane and of the bound protein with high spacial resolution.

To prove that possible alterations of the membrane organization are caused by the specific STxB-Gb_3 interaction, receptor free membranes were tested. Figure 4.11 shows a membrane composed of DOPC/SM/Chol (40:40:20) after incubation with $60\,nM$ STxB-Cy3 for $1\,h$. The phase separation is unaltered by the protein and the l_o phase accounts for $67 \pm 5\,\%$ ($\Delta = 1\,\%$, $n = 25$). Fluorescence of red-labeled STxB-Cy3 is not visible on the membrane indicating no unspecific interaction of the toxin with the receptor free membrane. Only some residual fluorescence is visible in Figure 4.11C due to incomplete separation of the green (Bodipy-PC) and red emission channel (Cy3).
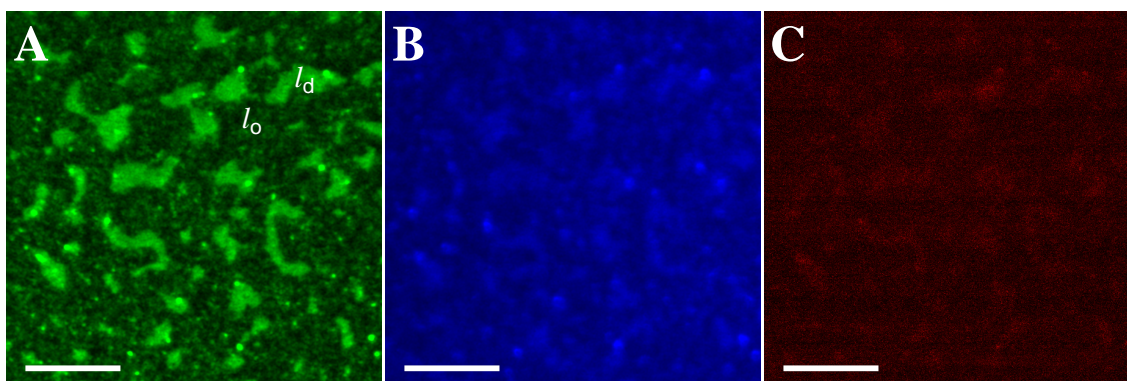
Figure 4.11: Domain organization of membranes composed of DOPC/SM/Chol (40:40:20) doped with perylene ($0.5\,mol\%$) and Bodipy-PC ($0.1\,mol\%$) after incubation with $60\,nM$ STxB-Cy3 for $1\,h$. **A** Fluorescence micrograph of Bodipy-PC. Membranes segregate into liquid-ordered (l_o, dark) and liquid-disordered domains (l_d, green). **B** Perylene fluorescence is more homogeneous showing that the dark areas in **A** are membrane covered. **C** No binding of red-labeled STxB-Cy3 to the Gb_3 free membrane is observed showing the specificity of the STxB-Gb_3 interaction. Neglectable residual intensity due to incomplete separation of the green and red emission channel is visible. Scale bars: $10\,\mu m$.

This experiment clearly demonstrates that any effects shown below can be attributed to STxB mediated reorganization of the membrane.

Phase behavior of Gb₃-C24:0 containing membranes after STxB binding
Figure 4.12 shows characteristic examples of mica supported membranes composed of DOPC/SM/CholGb₃-C24:0 40:35:20:5 doped with perylene (0.5 mol%) and OregonGreen DHPE (0.1 mol%) after incubation with 60 nM STxB-Cy3 for 1 h. Organization of the l_d marker dye and therefore the membrane organization seems unaltered by STxB (Panel A). The phase separation into two lipid phases is unchanged compared to the protein free case and the darker l_o phase covers 76±11 % (n = 52) of the membrane suggesting that no lipid redistribution between the phases took place. Binding of STxB can undoubtedly be verified. In Figure 4.12B the red fluorescence of Cy3 attached to STxB shows that the protein has bound to the l_o phase. The l_d areas are protein free as indicated by the lack of yellow color which would indicate colocalization of the red and green dye in the overlay. The fluorescence of STxB is not homogeneous but has a patchy structure characterized by a basal level of red intensity and small, brighter red areas. This indicates that the protein is unevenly distributed on the l_o phase and enriched in certain areas. Using the topography map obtained by AFM (Figure 4.12C) it is possible to assign the areas of brighter red fluorescence to small cluster-like aggregates of STxB. The lowest height in AFM is assigned to the l_d phase with the l_o phase elevating 0.7±0.2 nm (n = 17) above the l_d areas. The increase compared to the protein free samples is low (Δ = 0.1 nm). Judging from the residual red fluorescence in these areas the l_o phase is still covered with a low protein density and is hereafter denoted as $l_\mathrm{o+STxB}$. A third height in AFM corresponds to higher density protein structures and elevates $\Delta h(l_\mathrm{o+STxB\_clusters}/l_\mathrm{d}) = 1.5±0.5$ nm (n = 19). As the lateral resolution of the AFM images is usually set to 60 nm it is not possible to resolve single proteins. Higher resolutions lead to deformation of the protein layer. A height averaged over the protein bound in this area is obtained (see methods section's Figure 3.6).

Due to the small size of the STxB clusters it was not possible to extract their area percentage from STxB-Cy3 fluorescence micrographs. Instead AFM images were used to manually identify the clusters using a graphic tablet. The percentage of the total membrane area covered by the clusters is 15 %.
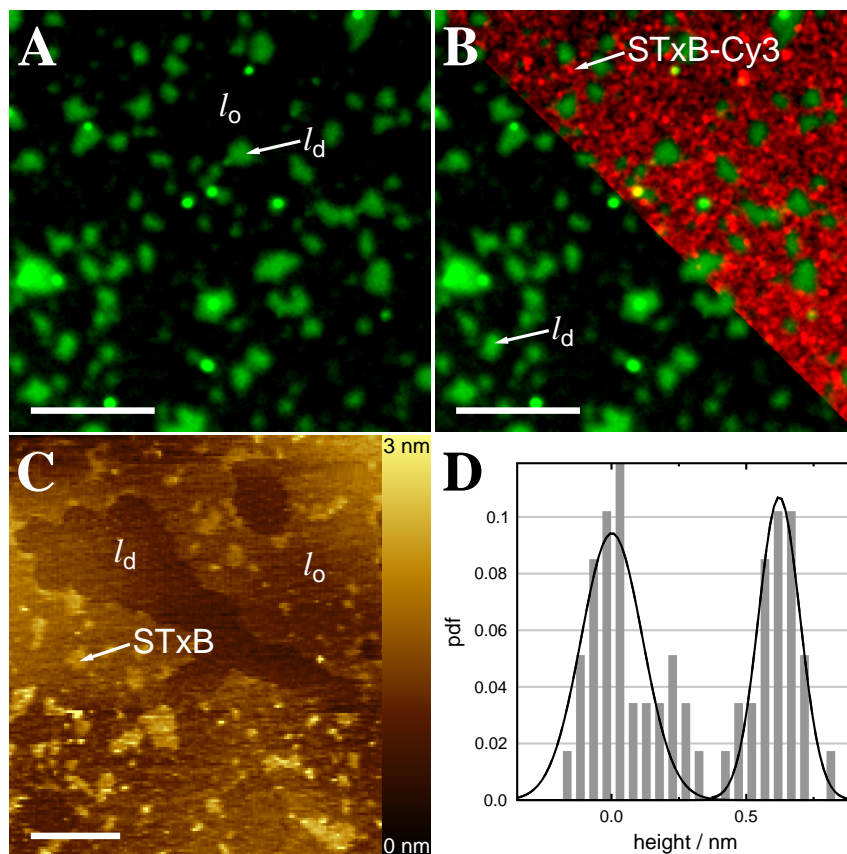
Figure 4.12: Solid supported membranes (DOPC/SM/Chol/Gb$_3$-C24:0, 40:35:20:5) doped with perylene (0.5 mol%) and OregonGreen DHPE (0.1 mol%) after incubation with 60 nM STxB-Cy3 for 1 h. **A** Fluorophore partition identifies the liquid-ordered (l_o, dark) and liquid-disordered phase (l_d, green). Scale bar: 15 μm. **B** Fluorescence micrograph of OregonGreen DHPE and overlay (top right) of STxB-Cy3 fluorescence with Oregon Green. The red STxB-Cy3 fluorescence is only located on the areas assigned to the l_o phase. The intensity is not homogeneous indicating differences in fluorophor density and therefore protein densities. Scale bar: 15 μm. **C** Topographic AFM image showing the l_d phase (dark color coding) and the elevated l_o phase (lighter color coding) which is decorated with STxB clusters. Scale bar: 2 μm. **D** Histogram analysis of a region in **C** showing a height difference of $\Delta h(l_{o+STxB\_clusters}/l_{o+STxB}) = 0.6 \pm 0.2$ nm between the l_o areas and the protein clusters. Image modified from Schütte, Ries *et al.* 2014.[86]

These results show that STxB binding to Gb$_3$-C24:0 does not lead to lipid rearrangement between the phases but to a demixing of the l_o phase into areas with higher Gb$_3$ and STxB concentration and areas depleted in both.

Phase behavior of Gb₃-C24:0 2-OH containing membranes after STxB binding

Phase-separated membranes containing Gb₃-C24:0 2-OH showed a similar lateral organization as Gb₃-C24:0 membranes before protein binding but a reduced area percentage of l_o phase. This lowered percentage is not found after incubation of solid supported membranes on mica (DOPC/SM/Chol/Gb₃-C24:0 2-OH 40:35:20:5 with 0.5 mol% perylene and 0.1 mol% TexasRed DHPE or Bodipy-PC) with 60 nM STxB.
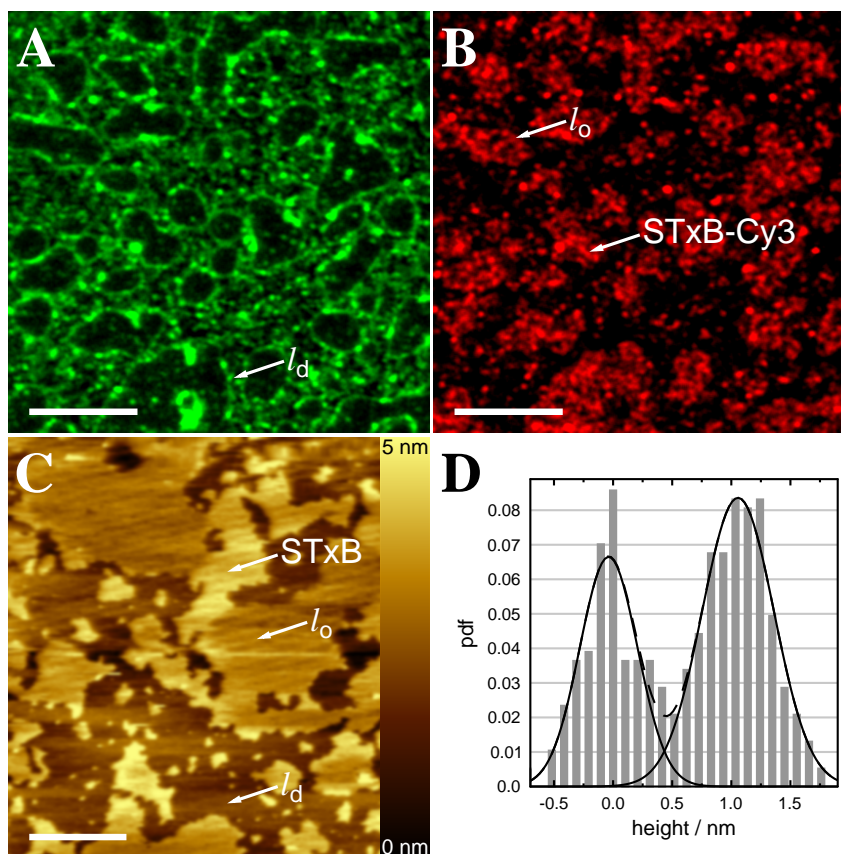

Figure 4.13: Solid supported membranes (DOPC/SM/Chol/Gb₃-C24:0 2-OH, 40:35:20:5) doped with perylene (0.5 mol%) and Bodipy-PC (0.1 mol%) after incubation with 60 nM STxB-Cy3 for 1 h. **A** Fluorophore partition of Bodipy-PC identifies the liquid-ordered (l_o, dark) and liquid-disordered phase (l_d, green). Scale bar: 7 µm. **B** Fluorescence micrograph of STxB-Cy3. The red fluorescence of STxB-Cy3 is inverse to the l_d marker Bodipy-PC. Scale bar: 7 µm. **C** Topographic AFM image showing the low l_d phase (dark color coding), a higher l_o phase (lighter color coding) and protein clusters on the l_o domains. Scale bar: 3 µm. **D** Histogram analysis of a region in **C** showing a height difference of $\Delta h(l_{o+STxB\_clusters}/l_{o+STxB}) = 1.1 \pm 0.5$ nm. Image reproduced from Schütte, Ries *et al.* 2014.[86] Data taken from Orth 2012.[52]

The area of the l_o phase increases by 21% to $77\pm5\%$ (n $=62$) and the overall phase behavior strongly resembles that of membranes containing the saturated Gb_3 derivative. Again, the fluorescence of STxB-Cy3 is inhomogeneously distributed on the l_o phase showing that Gb_3 is located in the l_o phase but demixes from the surrounding lipids (Figure 4.13A/B). The clusters of Gb_3 and STxB are identified by their elevated height of $\Delta h(l_{o+STxB\_clusters}/l_d) = 2.1\pm0.5\,\text{nm}$ (n $=12$) (Figure 4.13C/D). The areas corresponding to the protein covered l_o phase (l_{o+STxB}) show a slight elevation compared to the protein free case indicating some STxB density in these areas (Table 4.3). These results show that the impact of the toxin binding to the membrane is global and not limited to a lipid rearrangement in the l_o phase. The strong increase in l_o percentage of more than 20% indicates that other lipids are also redistributed between the phases.

Phase behavior of Gb_3-C24:1 containing membranes after STxB binding
Phase-separated solid supported membranes (DOPC/SM/Chol/Gb_3 40:35:20:5) on mica containing the unsaturated Gb_3 derivative Gb_3-C24:1 showed an altered phase behavior. The percentage of l_d phase was similar to both cases involving saturated Gb_3 species but a further segregation of the l_o into two phases (l_o and l_i) was observed.
After incubation with $60\,\text{nM}$ STxB-Cy3 for $1\,\text{h}$ fluorescence micrographs of the l_d marker showed that the segregation into three phases is unchanged (Figure 4.14A). Different brightness levels of the l_d marker dye allows to readily identify the phases. The dark l_o phase accounts for $43\pm7\%$ (n $=64$) and the l_i phase covers $31\pm8\%$ of the membrane. Compared to the protein free case, the values are unaltered (Table 4.2) indicating no strong lipid rearrangement between the phases. An overlay of the fluorescence of STxB-Cy3 and the l_d marker (Figure 4.14B) show that STxB is only bound to the l_o phase. l_d and l_i domains are free of protein.
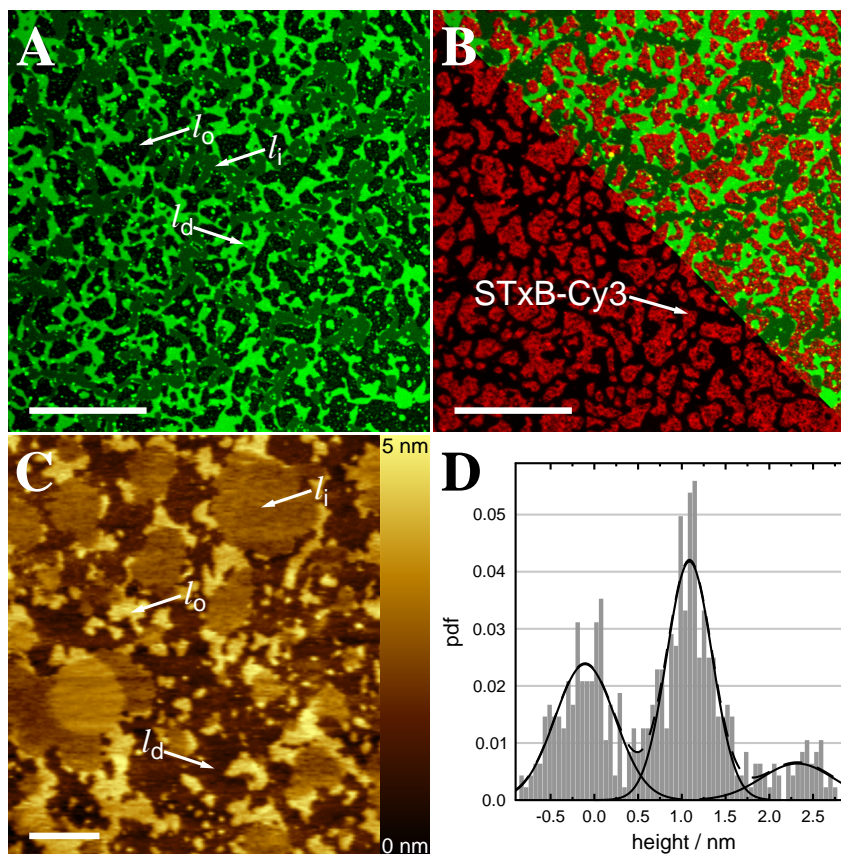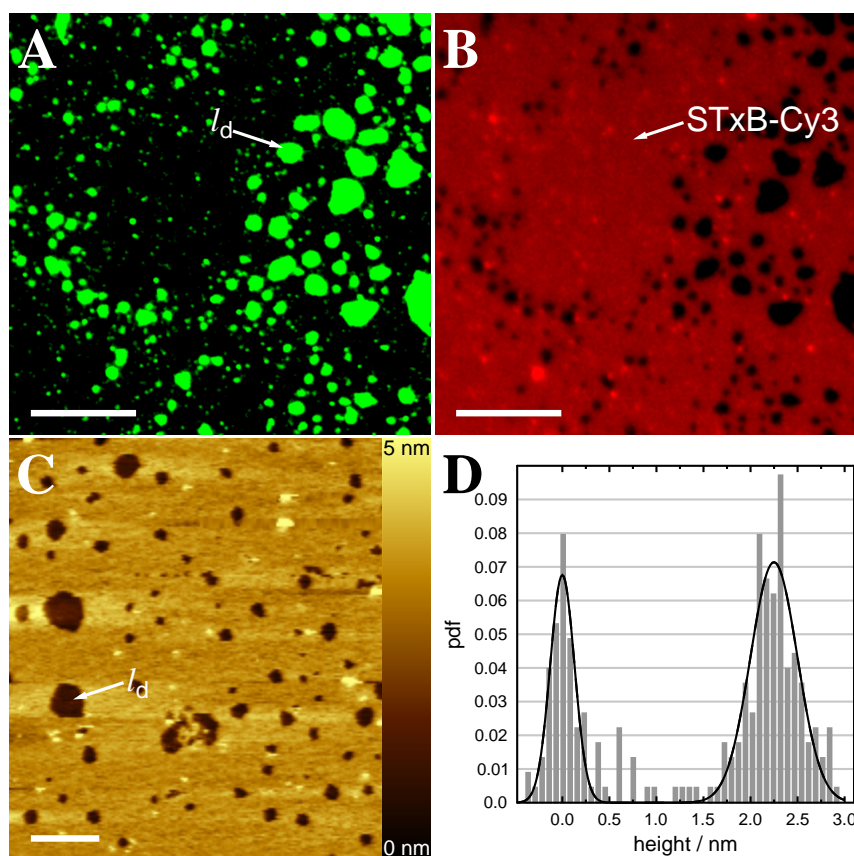
Figure 4.14: Solid supported membranes (DOPC/SM/Chol/Gb$_3$-C24:1, 40:35:20:5) doped with perylene (0.5 mol%) and Bodipy-PC (0.1 mol%) after incubation with 60 nM STxB-Cy3. **A** Fluorophore partition identifies the liquid-ordered (l_o, dark), the l_i (intermediate brightness) and liquid-disordered phase (l_d, green). Scale bar: 15 μm. **B** Fluorescence micrograph of STxB-Cy3 and overlay with **A** (top right). STxB-Cy3 fluorescence is exclusively found on the l_o phase. Scale bar: 15 μm. **C** Topographic AFM image showing three different height levels. Their height in conjunction with the fluorescence overlay images allows to assign them to the three lipid phases. Scale bar: 2 μm. **D** Histogram analysis of a region in **C** showing two height differences of $\Delta h(l_i/l_d) = 1.2 \pm 0.8$ nm and $\Delta h(l_{o+STxB}/l_d) = 2.4 \pm 0.8$ nm. Image reproduced from Schütte, Ries *et al.* 2014.[86] Data for panels A and B reproduced from Orth 2012.[51]

AFM confirms this and the lowest height level is assigned to the l_d phase. The highest elevation of $\Delta h(l_{o+STxB}/l_d) = 2.6 \pm 0.6$ nm (n = 26) is close to the sum of $\Delta h(l_o/l_d)$ and the height of the protein of ≈ 2 nm.[60,70] Such a large height difference can only be caused by the bound protein and the assignment to the protein covered l_o phase is obvious. The intermediate height found in AFM is elevated 1.3 ± 0.7 nm (n = 12) above the l_d phase and is assigned to the l_i phase as it has a similar height as in the protein free case.

Phase behavior of Gb$_3$-C24:1 2(R/S)-OH containing membranes after STxB binding

In the absence of bound protein Gb$_3$-C24:1 2(R/S)-OH combining the unsaturation and hydroxylation induced a membrane phase behavior nearly identical to the one observed for membranes containing Gb$_3$-C24:0.

After incubation of mica supported phase-separated membranes (DOPC/SM/Chol/Gb$_3$-C24:1 2(R/S)-OH 40:35:20:5), doped with perylene and a dye preferentially partitioning into the l_d phase with STxB-Cy3, the membranes were investigated by atomic force and fluorescence microscopy.

Figure 4.15: Solid supported membranes (DOPC/SM/Chol/Gb$_3$-C24:1 2(R/S)-OH, 40:35:20:5) doped with perylene (0.5 mol%) and OregonGreen DHPE (0.1 mol%) after incubation with 60 nM STxB-Cy3. **A** Fluorophore partition identifies the liquid-ordered (l_o, dark) and liquid-disordered phase (l_d, green). Scale bar: 15 µm. **B** Fluorescence micrograph of STxB-Cy3 showing homogeneous fluorescence of STxB-Cy3 (red) on top of the l_o phase. Scale bar: 15 µm. **C** Topographic AFM image showing the single elevated height of the STxB covered l_o phase above the l_d phase. Scale bar: 2 µm. **D** Histogram analysis of a region in **C** showing a height difference of $\Delta h(l_o + \text{STxB}/l_d) = 2.3 \pm 0.5$ nm. Image reproduced from Schütte, Ries *et al.* 2014.[86]

Figure 4.15 shows membranes exemplifying the phase behavior. The l_d marker dyes show that the separation into l_o and l_d domains is not changed. However, the percentage of l_o increases to $87\pm7\,\%$ (n$\,=\,$42). The protein covered l_o phase nearly fully covers the whole membrane (Figure 4.15B). Cy3 fluorescence is homogeneous apart from some adhered vesicles showing a uniform protein coverage. Using AFM only a single elevated height of $2.7\pm0.5\,$nm (n$\,=\,$44) above the l_d phase is found and assigned to a high density protein layer on top of the l_o phase.

Summary of the phase behavior of Gb$_3$ containing membranes after STxB binding

The values obtained by fluorescence and atomic force microscopy of membranes containing Gb$_3$-C24:0, Gb$_3$-C24:0 2-OH, Gb$_3$-C24:1 or Gb$_3$-C24:1 2(R/S)-OH after incubation with $60\,$nM STxB for $1\,$h are summarized in Table 4.3.

The findings show that the fatty acid attached to Gb$_3$ not only influences the phase behavior of the lipid mixture but also strongly influences the lateral organization of STxB on the membrane. The different type of lipid rearrangements show that STxB is able to reorganize the membrane suggesting that this is a crucial function of the protein in its biological context.

Table 4.3: Ratios of the different membrane phases (l_o: liquid-ordered, l_i: liquid-intermediate) in DOPC/SM/Chol/Gb$_3$ (40:35:20:5) bilayers doped with different Gb$_3$s on mica and height differences observed in AFM images after STxB binding. The ratios were determined by pixel analysis using fluorescence images. Height differences were extracted by fitting Gaussians to the height histograms (number of analyzed fluorescence images and height histograms is given in brackets).

Gb$_3$-	l_o/%	l_i/%	$\Delta h(l_\text{i}$ /l_d)/nm	$\Delta h(l_\text{o+STxB\_clusters}$ /$l_\text{o+STxB}$)/nm	$\Delta h(l_\text{o+STxB\_clusters}$ /l_d)/nm	$\Delta h(l_\text{o+STxB}$ /l_d)/nm	$\Delta h(l_\text{o+STxB}$ /l_i)/nm
C24:0	76$\pm$11(52)	—	—	0.8$\pm$0.1(6)	1.5$\pm$0.5(19)	0.7$\pm$0.2(17)	—
C24:0 2-OH	77$\pm$5(62)[‡]	—	—	0.7$\pm$0.2(24)[‡]	2.1$\pm$0.5(12)	1.0$\pm$0.2(69)[‡]	—
C24:1	43$\pm$7(64)[‡]	31$\pm$8[‡]	1.3$\pm$0.7(12)[‡]	—	—	2.6$\pm$0.6(26)[‡]	1.9$\pm$0.6(15)[‡]
C24:1 2-OH	87$\pm$7(42)	—	—	—	—	2.7$\pm$0.5(44)	—

[‡] Data partially reproduced from Orth 2012.[51]

4.1.4 Discussion

Shiga toxin's invasion into cells is facilitated by the formation of plasma membrane invaginations.[39,71] These invaginations are formed after induction of curvature by an asymmetric reduction in membrane area.[72] This reduction is accomplished by lipid compaction upon formation of STxB-Gb_3 aggregates.[151] This implies that the local lipid organization is important.[70] The fatty acid attached to Gb_3 modulates interlipid contacts and is known to influence binding capacity and affinity.[73,74,139,152] In the following three major points will be addressed:

- How does the affinity towards STxB change as a function of the fatty acid?

- In which way does Gb_3 alter the lateral organization of phase-separated membranes?

- How do these alterations influence the binding of STxB?

Additionally the l_o areas observed on solid supported membranes are compared to an example from literature and to the values determined in Chapter 5 using giant unilamellar vesicles and pore-spanning lipid bilayers.

4.1.4.1 Quantification of the STxB-Cy3 interaction

The affinities determined by SPR presented in Table 4.1 show that all Gb_3 derivatives regardless of their fatty acid bind Shiga Toxin with nanomolar affinity. This result was expected as previous studies on simplified membrane systems already reported similar affinities. The group of Lingwood found that Gb_3 with short chains (C_{12}, C_{14}) binds less STxB compared to species with long acyl chain (C_{15}-C_{24}) and unsaturation increases the binding capacity.[73] In a follow up work another increase in binding capacity was found, using α-hydroxylated species.[74] In these studies no detailed interpretation on the molecular level is given but the authors speculate that the local spatial organization of the receptor is more important than changes in the receptor itself.[73] Interestingly they concluded that the receptor density has an effect on STxB binding,[73] indicating that a minimum number of the 15 bindings sites of STxB has to be occupied for stable binding. Both works used radiolabeled STxB in a microtiter plate assay. Even though axillary lipids were used, no planar membrane containing the receptor was formed.

In principle one can imagine two different ways how the fatty acid bound to the ceramide backbone of Gb₃ can influence the binding of STxB. On the one hand the spatial organization of the receptor is important, one the other hand the fatty acid can change the availability of the sugar headgroup for binding.

For glycolipids with α-hydroxylated fatty acids a tilting of the headgroup was reported making it unavailable for binding.[142] The group of Karlsson reported that the tilting effect is required for binding of *Heliobacter pylori* to lactosylceramide.[144] Judging from the crystal structure of STxB with its receptor no clear statement can be made wheter tilting hampers binding, as the Gb₃ molecule bound to binding site I of STxB is highly tilted (see Section 1.3).[60, 153]

For the experiments Gb₃ was embedded in a DOPC membrane. It allows for free lipid diffusion which might lead to the formation of Gb₃ aggregates. In principle these aggregates can form due to sugar-sugar interactions prior to protein binding.[154] Investigating the interaction of Cholera Toxin subunit B with its receptor G_M1, Shi *et al.* found that clustering inhibits further protein binding by making the receptor unavailable. Figure 4.16 visualizes this process.
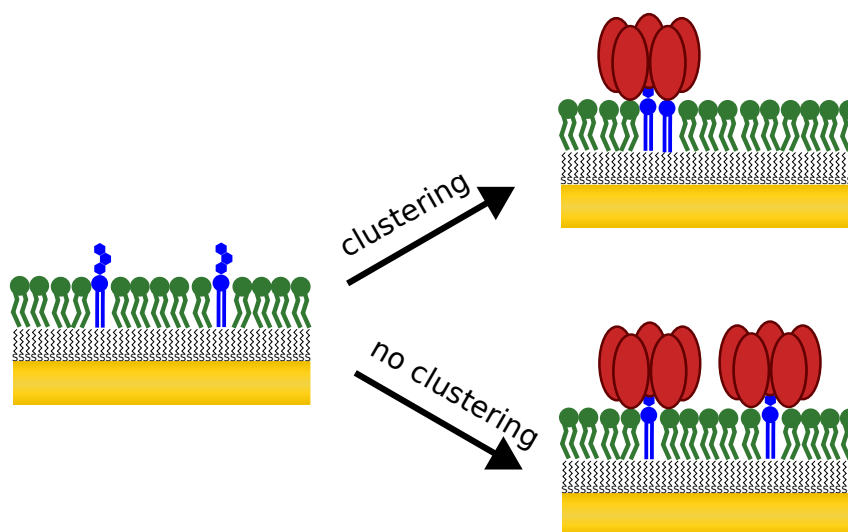
Figure 4.16: Schematic drawing showing STxB binding in the SPR experiment.

STxB can bind to multiple Gb₃ molecules, clustering them. This leads to less Gb₃ available for additional binding.

Clustering should influence the binding capacity as less receptor is available for binding protein.[155] The extraction of binding capacities was not possible using the SPR setup used in this thesis. However, clustering can also influence the affinity

of Gb_3 containing membranes. A binding event is detected when the protein is stably bound to the membrane. This is the case when multiple Gb_3-STxB bonds are formed.[64,156]

The affinities determined in this work are similar and in the low nanomolar regime.[73,74] From the SPR data alone no statement on the possible formation of glycolipid clusters and the lateral organization can be made. However, the values determined show that the concentration of STxB used for fluorescence and atomic force microscopy experiments is high enough to saturate the membranes. The solid supported membranes composed of the 'raft-like' mixture contain both cholesterol and sphingomyelin. They form domains which might drastically alter the binding of STxB.[75,157–159]

4.1.4.2 Lateral membrane and STxB organization

A schematic model summarizing the findings for the lateral organization of membranes composed of DOPC/SM/Chol 40:35:20 and $5\,mol\%$ of the newly developed Gb_3 derivatives was derived. Briefly, four main factors are included in the model:

- Membranes show a different lateral organization prior to protein binding
  - The distribution of lipid components (e. g. DOPC) is altered by α-hydroxylated Gb_3s
  - Unsaturated Gb_3 leads to a further segregation of the membrane

- STxB binding clusters Gb_3 lipids
  - For saturated Gb_3 the l_o phase is demixed, leading to interphase lipid rearrangement
  - Unsaturated Gb_3 induces an evenly distributed bound STxB

The Gb_3 derivatives used were found to strongly influence the phase behavior of the solid supported membranes. Independent of the fatty acid attached, the membranes showed a phase separation into macroscopic domains. Nanoscopic domains which might be stabilized by hybrid-lipids like Gb_3-C24:1 were not found[160,161] They might not be resolved in fluorescence microscopy, but also no indications were found using high resolution AFM. A liquid-ordered domain is usually composed of sphingomyelin with mainly saturated fatty acid chains and cholesterol. It is therefore reasonable to take the results involving the saturated Gb_3-C24:0 as the

basis for the interpretation of the data.[138] Each STxB pentamer can bind up to 15 molecules of its receptor lipid.[39,60] In case of full saturation of the binding pockets roughly 40% of the area under the protein is occupied by Gb₃ resulting in a close packing.[60,66] The packing results in an asymmetric area reduction in one leaflet, leading to the induction of negative curvature and bending of the membrane. This direct relation between protein binding and lipid compaction indicates that the local organization of Gb₃ and its contacts with surrounding lipids are of crucial importance.

Shiga Toxin-membrane interaction can be subdivided into three steps: i) membrane binding (see Section 4.1.4.1), ii) formation of STxB-Gb₃ aggregates and iii) membrane bending. Phase-separated solid supported membranes on mica allow to monitor STxB binding and the formation of STxB aggregates. Fluorescence microscopy helps to quantify the protein's impact on the global membrane organization whereas atomic force microscopy enables one to detect small protein aggregates and the density of the bound protein on the surface. They however do not allow for membrane bending as their topography is fixed due to the close contact with the solid support. The mechanical properties of the membranes which are important for bending[72] are less relevant in this system.

Membranes containing Gb₃-C24:0

Prior to protein binding the l_o phase accounts for roughly 70% of the membrane area; only a slight increase compared to the Gb₃ free case. Due to the saturated fatty acid and the ceramide backbone, Gb₃-C24:0 is expected to be located in the l_o phase.[1] Figure 4.17 shows a schematic drawing of the membrane organization prior to protein binding, roughly taking the phase compositions into account. Exchanging $5\,\text{mol}\%$ sphingomyelin by Gb₃ with a large headgroup, should increase the area per molecule of the l_o phase, explaining the increase in l_o phase. The determined values for the l_o phase area fraction compare well with literature of solid supported membranes composed of DOPC/SM/CholGb₃-Porc,[70] but it has to be noted that the solid support clearly influences the phase separation. In thermodynamic equilibrium all domains are expected to be round-shaped to minimize the line tension[41] and condense to larger domains.[72]
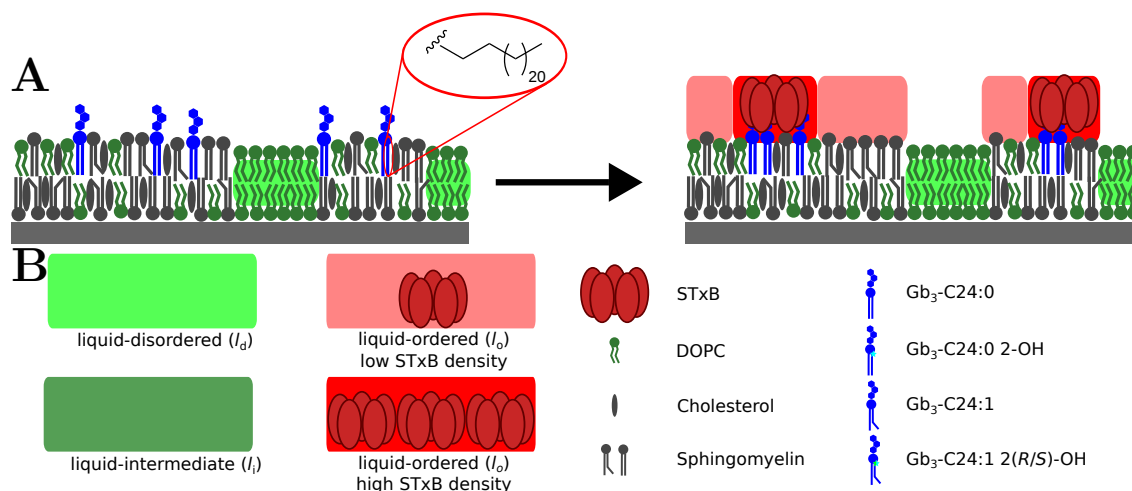
Figure 4.17: A Model describing the protein and membrane organization of Gb_3-C24:0 containing membranes as deduced from fluorescence and atomic force microscopy on mica. **B** Color coding and symbols used throughout the discussion.

The irregular structure of the domains shown in Section 4.1.3 clearly shows that the support either kinetically traps the domains due to low diffusion[136] or induces the domains shape by specific interactions.[42,162] As membranes containing α-hydroxylated Gb_3 shows a strong lipid rearrangement upon STxB binding requiring diffusion, favors to the latter.

Upon binding to the Gb_3-C24:0 containing membranes, STxB does not change the percentage of l_o phase, indicating that the l_d phase is unaffected and that the compositions of the phases remain the same (Table 4.6, Figure 4.17). Fluorescence of Cy3 labeled STxB shows that Gb_3 is fully located in the l_o phase as expected from the saturated hydrophobic moiety of the molecule.[138] It is however important to remark that the partition of Gb_3 into the DOPC rich l_d phase might hamper STxB binding and the detection of the protein by AFM.[163,164] SPR experiments showed that Gb_3 embedded in DOPC still binds to STxB (Section 4.1.4.1). However, experiments elucidating the interaction of Cholera toxin (CTx) with its glycosphingolipid receptor G_{M1} show that the detection of protein clusters on fluid membranes is difficult. At low G_{M1} content (1 mol%) CTx clusters are only found in gel or l_o domains, indicating that the receptor is either solely located in the ordered phase or that the residual percentage of the receptor in the fluid phase does not facilitate binding.[165,166] At higher G_{M1} content (>4 mol%) clusters can also be detected in the fluid portion of the membrane.[163,164] This indicates that the multivalent binding of the receptor is of crucial importance and that at high

dilution of the receptor no stable binding can be established.[72, 155]

The importance of multiple receptor-STxB bonds is also reflected in the mode of binding of Gb$_3$-C24:0. The l_o phase is not homogeneously covered with protein but regions of higher protein density are formed. Formation of clusters indicates that Gb$_3$-C24:0 favors the tight packing and condensation in the membrane to an extent that is large enough to overcome the entropically favored dispersion of the receptor in the l_o phase. This clearly shows that the interaction of Gb$_3$ with the surrounding lipids during the protein cluster formation is a major contribution. For the glycosphingolipid G$_{M1}$ the interactions with surrounding lipids have been studied in more detail by fluorescence techniques and secondary ion mass spectrometry. Sachl *et al.* found that the receptor forms clusters enriched in cholesterol and phospholipids[154] and the group of Boxer *et al.* showed a preferential colocalization of G$_{M1}$ and cholesterol.[167]

Membranes containing Gb$_3$-C24:1

The discussion above assumes that Gb$_3$ adopts a phase behavior similar to the one of sphingomyelin. This might be different for Gb$_3$-C24:1, which combines the large sugar headgroup with a sterically demanding (Z) unsaturation and might induce a phase behavior resembling the one of DOPC. Using the same reasoning as presented for DOPC/SM/Chol 40:40:20 the values for membrane composition of DOPC/SM/Chol 45:35:20 were calculated. The effect on the phase compositions and area percentages are modest (Table 4.8) and cannot explain the strong alterations observed.

Considering the phase behavior of membranes doped with Gb$_3$-C24:0 2-OH and Gb$_3$-C24:1, two main features are apparent: i) the lower percentage of l_o area for the hydroxylated compound and ii) the segregation into a third phase observed for Gb$_3$-C24:1. For the latter case the percentage of l_d phase is about 30 %, close to the values of l_o area percentage found of the other derivatives. It is therefore reasonable to treat the l_i phase as a subphase of the l_o phase.

In principle it would be possible to imagine the l_i phase as a decoupled phase meaning that the interleaflet coupling between the monolayers is disturbed.[168, 169] One monolayer would be the l_d state while the other is in the l_o state excluding the fluorophor. The results obtained after protein binding indicate that the upper layer of the l_i phase is Gb$_3$ free and unaffected by STxB binding. It seems unrealistic to assume a leaflet decoupling as it is only observed for one of the four derivatives

studied and was not reported for similar lipid mixtures.[51,70] The possibility of a decreased interleaflet coupling explaining the intermediate brightness cannot be fully excluded (Figure 4.18 right panel).[168]
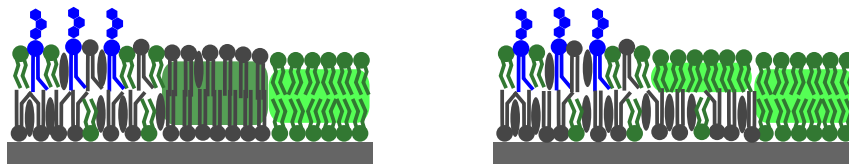

Figure 4.18: Possible organizations of Gb$_3$-C24:1 containing membranes. Left: Membranes segregate due to lipid-lipid interactions. Right: The monolayers are decoupled in the l_i phase. Symbols as in 4.17B.

The phase separation is driven by the specific lipid-lipid interactions between sphingomyelin, cholesterol and Gb$_3$-C24:1. At this composition in the ternary phase diagram the phase separation is not driven by a demixing of cholesterol and the unsaturated DOPC but by the attraction and alignment of the sphingomyelin's fatty acid chains.[37] Assuming that the interactions of sphingomyelin are the main energetic factors might explain the emerging of the l_i phase. The bovine brain SM used in this thesis contains 20 mol% SM-C24:1 (Table 3.1).[80] Experiments using ceramide monolayers revealed that at relevant surface pressures unsaturated molecules can form tight aggregates.[141] Assuming a demixing of the unsaturated sphingomyelin induced by the unsaturated Gb$_3$ explains the observed l_i phase. As the area percentages of l_o and l_i are similar, no assignment of the Gb$_3$ containing phase is possible. Figure 4.18 shows a schematic view of both possible membrane architectures for the membranes containing Gb$_3$-C24:1.
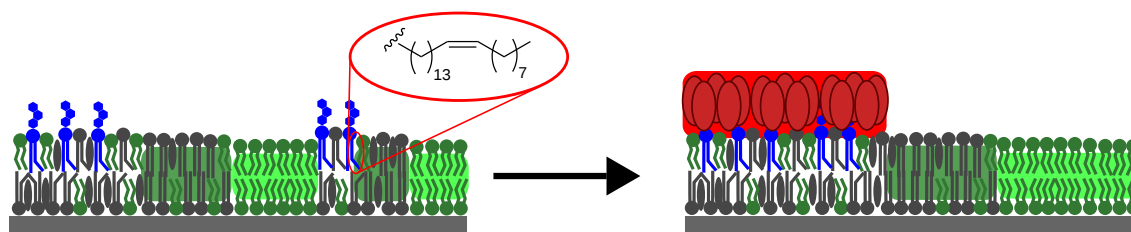
Figure 4.19: Model describing the protein and membrane organization of Gb$_3$-C24:1 containing membranes as deduced from fluorescence and atomic force microscopy on mica. Symbols as in 4.17B.

The localization of Gb_3 is hypothesized on the basis of the localization after protein binding. A further segregation of the l_o phase seems unusual but the heterogeneous structure of the l_o phase has been reported previously. Sodt *et al.* used all atom molecular dynamics simulations of membranes composed of DOPC/DPPC/Chol 40:40:20. Within the l_o phase they observed regions of local hexagonal order of saturated hydrocarbon chains and regions enriched in cholesterol and some unsaturated lipid.[170] Sodeoka and coworkers used Raman microscopy to study the localization of alkyne tagged sphingomyelin in lipid monolayers composed of SM, cholesterol and DOPC.[171] The small alkyne tag allowed them to determine the sphingomyelin density in l_o domains. It was found to vary inside the domains with regions with high SM density and regions which are depleted. These results suggest that indeed subtle lipid-lipid interactions can transfer to macroscopic differences in the organization of lipid domains.

Membranes containing Gb_3-C24:1 show a distinct behavior. Upon STxB binding this phase behavior is not altered as the area percentages of the phases remain the same. STxB is only binding to the l_o phase showing that the l_i and the l_d phase are free of Gb_3. The newly formed STxB-Gb_3-C24:1 aggregate is incompatible with both the saturated sphingomyelin and the unsaturated DOPC. This seems reasonable as the lipid compaction should exclude DOPC and tight packing of unsaturated lipids is only possible in absence of saturated compounds.[141] The protein structure formed on the membrane shows a high density, evenly distributed and homogeneous pattern suggesting that the unsaturated fatty acid is responsible for it. This would imply that the steric demand, packing ability and interactions with surrounding lipids influence the number of receptor lipids bound per STxB pentamer (*vide infra*).

Membranes containing Gb₃-C24:0 2-OH

To understand the low l_o percentage for membranes composed of DOPC/SM/Chol/Gb_3-C24:0 2-OH 40:35:20:5 one has to consider the phase diagram (Figure 4.24) and the phase compositions (Table 4.6). The localization of Gb_3 does not explain the low area percentage of only 56 % as it only accounts for 7 % of the total membrane area. α-hydroxylation of the fatty acid has been reported to condense lipids,[140] strengthen interlipid contacts,[139,149,152,172] change the carbohydrate conformation[142,143] and influence lipid packing.[141] Assuming the l_o phase composition of DOPC/SM/Chol 9:51:40 (Table 4.6), a further condensation of the mainly saturated SM seems unlikely. It is more likely that Gb_3-C24:0 2-OH

condenses the lipid and further lowers the content of DOPC in the l_o domains generating the drop in l_o area (Figure 4.20).
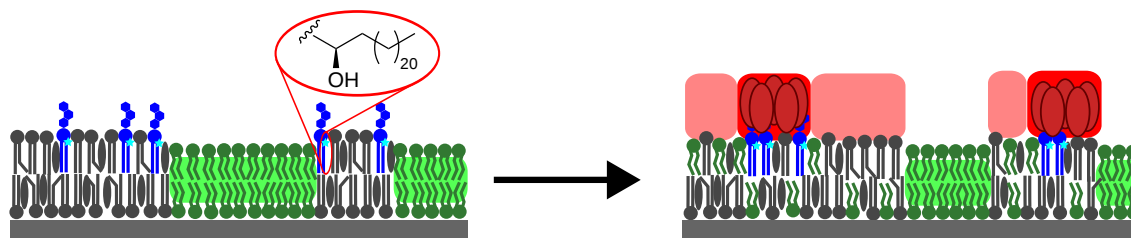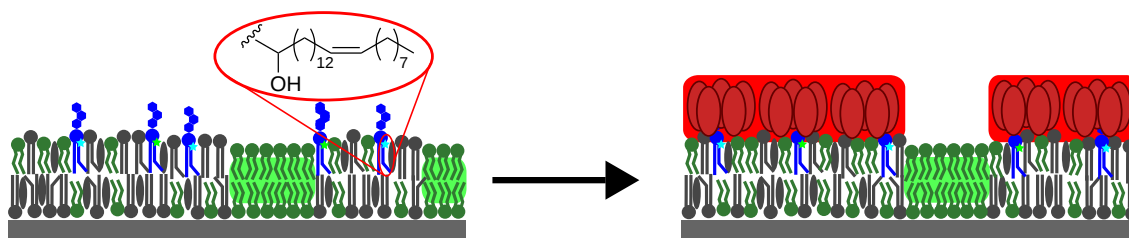

Figure 4.20: Model describing the protein and membrane organization of Gb$_3$-C24:0 2-OH containing membranes as deduced from fluorescence and atomic force microscopy on mica. Symbols as in 4.17B.

For Gb$_3$-C24:0 2-OH containing membranes a similar behavior upon binding of STxB as for Gb$_3$-C24:0 is expected. The saturated fatty acid chain in conjunction with α-hydroxylation should form strong interlipid contacts which can facilitate the enrichment of Gb$_3$ underneath STxB. Atomic force microscopy indeed reveals protein clusters on the l_o phase. The clusters again elevate ≈ 1 nm above the l_o phase, indicating a similar protein density as for Gb$_3$-C24:0. Interestingly the impact of the clustering of Gb$_3$-C24:0 2-OH has a more global impact on the overall phase behavior (Figure 4.20). Figure 4.21 shows the process in more details.
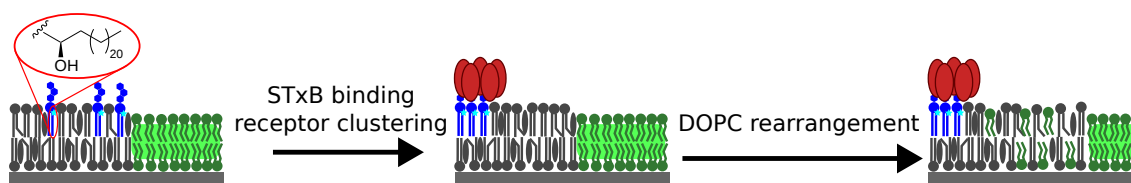
Figure 4.21: Gb$_3$-C24:0 2-OH membranes show a decreased l_o percentage. STxB binding practically Gb$_3$-C24:0 2-OH from the majority of the l_o phase allowing for inclusion of DOPC. Symbols as in 4.17B.

Prior to protein binding Gb$_3$-C24:0 2-OH is dispersed in the l_o phase. The effect of α-hydroxylation has been reported contradictory in literature to fluidize membranes[139] or decrease fluidity.[149] One can imagine the molecule to form tight interactions with the surrounding lipids[141,152] leading to a compaction of the l_o phase which further excludes the residual DOPC content in the l_o phase (Table 4.6). Using the area per molecule (Table 4.8) the total of SM, cholesterol and Gb$_3$ account for 50 % of the membrane area (Table 4.8), a value close to the observed

l_o percentage of 56 %. Protein binding and receptor clustering underneath the protein mitigates this effect as the receptor is excluded from the majority of the l_o phase area. This leads to a redistribution of DOPC into the l_o phase restoring the proposed composition of the l_o phase. The resulting area expansion of l_o phase was observed by fluorescence microscopy.

Membranes containing Gb₃-C24:1 2(R/S)-OH

In case of Gb₃-C24:1 2(R/S)-OH the condensing effect of an 2-hydroxy group and the sterically demanding unsaturated fatty acid have opposing impact. On the one hand, α-hydroxylation might condense the lipids and exclude additional DOPC. On the other hand the unsaturated fatty acid favorably interacts with the unsaturated DOPC. This results in a similar value of the l_o area percentage compared to Gb₃-C24:0 containing membranes (Figure 4.22).

Figure 4.22: Model describing the protein and membrane organization of Gb₃-C24:1 2(R/S)-OH containing membranes as deduced from fluorescence and atomic force microscopy on mica. Symbols as in 4.17B.

Upon binding of STxB membranes containing Gb₃-C24:1 2(R/S)-OH also show an increase in l_o area percentage. AFM reveals no lipid or protein cluster formation for this derivative, indicating that the reasoning developed for Gb₃-C24:0 2-OH is not valid. Both unsaturation and α-hydroxylation of Gb₃ have been shown to increase the affinity and binding capacity to STxB.[73,74] The above mentioned cluster formation for saturated Gb₃ derivatives should decrease binding capacity as shown by the group of Cremer for the interaction of CTxB with G_{M1}.[155] No clusters are observed in the presence of Gb₃-C24:1 2(R/S)-OH but a homogeneous coverage of the whole l_o phase. The large height difference of 2.7 nm corresponds to the sum of $\Delta h(l_o/l_d)$ and the crystallographic height of STxB,[60] implying that STxB forms a mono molecular layer on the membrane which might be related to the previously reported 2D crystals (Figure 4.22).[133] This densely packed structure strongly influences the underlying membrane. The l_d marker dyes are located in

only 13 % of the membrane area which are designated as the l_d phase. Summing up the areas of sphingomyelin, cholesterol and Gb_3 cannot explain this large area percentage of the l_o phase. A large amount of DOPC has to be included in the l_o phase which is still sufficiently tightly packed to exclude the l_d marker. In 2014 Scheve *et al.* reported that the steric pressure between membrane-bound proteins can disrupt the phase separation in giant unilamellar vesicles.[173] They used increasing receptor concentrations and his-tagged proteins of varying size to increase the area demand of the bound protein in the aqueous interface of the membrane. Figure 4.23 illustrates their findings transfered to the STxB-Gb_3 interaction.
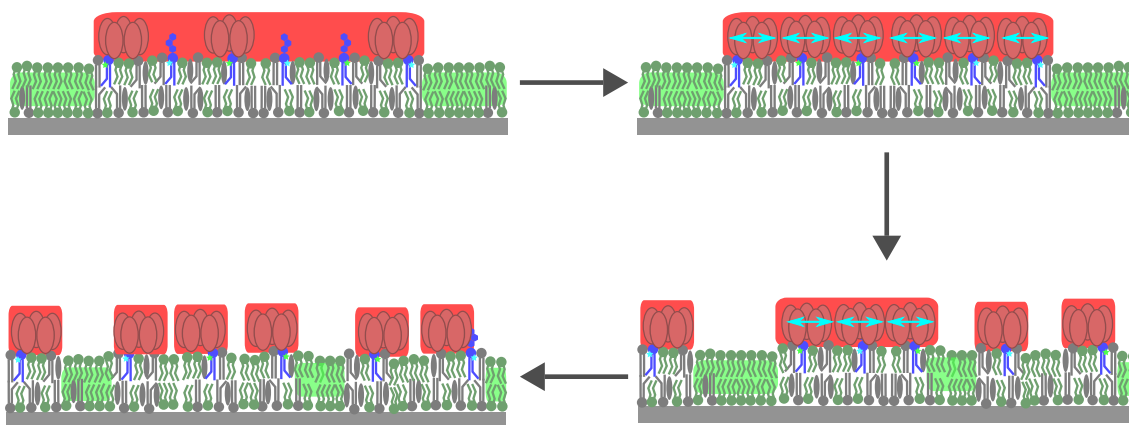
Figure 4.23: Model adapted from Scheve *et al.* describing how the steric pressure of protein binding disrupts the phase separation.[173] Symbols as in 4.17B.

High capacity binding of Shiga Toxin fully covers the l_o phase. The steric pressure reported by Scheve *et al.* can occur when a relatively low number of Gb_3 molecules is bound per STxB, freeing the additional Gb_3 to bind more protein. Because Gb_3 is located in the l_o phase, this induces steric pressure by the protein further dispersing the Gb_3. This is concurrent with the lower packability of Gb_3-C24:1 $2(R/S)$-OH caused by the unsaturation. Both effects lead to the increase of l_o area. To build this large area a large amount of DOPC most be included into the more ordered phase. This would imply that the l_d marker also might be colocalized with STxB. Lack of colocalization of fluorescence of Bodipy-PC and STxB-Cy3 is apparent from Figure 4.15 indicating that even the rather small, fatty acid based Bodipy label is still excluded from the aggregate. The condensing effect of STxB is still strong enough to exclude the dye. Using fluorescence microscopy, it was possible to separate the contributions of both diastereoisomers of Gb_3-C24:1 $2(R/S)$-OH The

results are presented separately in Section 4.2.

Number of Gb₃ molecules bound to STxB

The results and considerations presented above show that the fatty acid of Gb₃ regulates the lateral structure of STxB. Under certain assumptions the number of bound Gb₃ molecules for each STxB pentamer can directly be calculated from the l_o areas determined.

i)   The area occupied by one pentagonally shaped STxB can be estimated to $2500\,\text{Å}^2$ using the crystallographic dimensions.[60] STxB is non-compressible

ii)   Pentagon shaped objects can only be packed up to a surface density of $\Gamma = 0.921$ with the actual density most probably being lower.[133,174] The process of random sequential adsorption of circular objects on a surface predicts $\Gamma \approx 0.547$.[175]

iii) Areas per molecule are as listed in Table 4.8.

iv)   The affinities in the DOPC/SM/Chol/Gb₃ 40:35:20:5 membrane system are comparable to the ones shown in Table 4.1 in the low nanomolar regime. This implies that the number of binding sites is not the limiting factor.

v)   No significant pool of receptor lipid is unavailable due to distribution in the l_d phase or specific interactions with cholesterol.[75,143]

The minimum area occupied by STxB can be estimated. Gb₃ accounts for $\approx 7\,\%$ of the total membrane area. Assuming that 15 Gb₃ molecules are bound one can calculate the minimum area of the protein by using the ratio of the STxB area and the receptor membrane area percentage. Calculation yields $16\,\%$; a value close to the $15\,\%$ coverage observed for STxB-Gb₃-C24:0 clusters.

Using a similar reasoning, the measured percentage of l_o phase can be converted to the number of Gb₃s bound per STxB pentamer (Table 4.5). The calculations result in a reasonable number of Gb₃s bound per pentamer (Table 4.5).

Table 4.5: Theoretical number of Gb$_3$ molecules bound to STxB.

l_o area fraction / %	Gb$_3$ species	Γ	Gb$_3$/STxB
100		0.921	2.6
		0.547	4.3
76	Gb$_3$-C24:0	0.921	3.4
		0.547	5.6
77	Gb$_3$-C24:0 2-OH	0.921	3.3
		0.547	5.6
43	Gb$_3$-C24:1	0.921	6.0
		0.547	10.0
87	Gb$_3$-C24:1 2(R/S)-OH	0.921	2.9
		0.547	5.0

These calculations suggest that the number of Gb$_3$ molecules bound to STxB is influenced by the fatty acid attached to Gb$_3$. This implies that the lipid composition after scission of the invaginations might also differ and influence the fate of the protein during the intracellular transport.[134, 176]

4.1.5 Conclusion

From the results and considerations it is obvious that the fatty acid attached to Gb$_3$ plays a major role in the process of Shiga toxin internalization. The affinities of the headgroup mediated interaction with the protein are similar. The influence of the lateral organization seems to be the most important factor.[134] Shiga toxin binding to saturated Gb$_3$s results in the formation of high density protein-lipid clusters which have been reported to inhibit membrane bending[71] due to their rigid structure.[151, 177] Unsaturated Gb$_3$ seems to be more important as it induces a more even distribution on the l_o phase. Headgroup compaction induced by STxB leads to negative curvature which is stabilized by the area demanding unsaturated fatty acid.[178, 179] The incorporation of DOPC into the rigid l_o phase induced by α-hydroxylated species further softens the membrane, facilitating the formation of invaginations.[179]

4.1.6 Supplements

4.1.6.1 Comparison of the l_o area percentage on SSMs compared to freestanding membranes

The results presented in Section 4.1.3 show that the l_o area percentage in most of the solid supported membranes investigated is in the range of 60 to 80 % of the total area. Determining the l_o area fraction in the freestanding membranes of giant unilamellar vesicles (GUVs, see Sections 3.4.1 and 5.3.1) reveals that GUVs contain roughly 35 % l_o phase. There is a clear dissent between the model systems because a near doubling of the l_o percentage is found in SSMs.

Bezlyepkina et al.[37] used 3D reconstructions of GUVs to determine the tie lines of the ternary phase diagram of mixture of DOPC/eggSM/Chol. The phase diagram is shown in Figure 4.24. The tie lines allow to determine the composition of the l_o and l_d phase for a given lipid mixture.
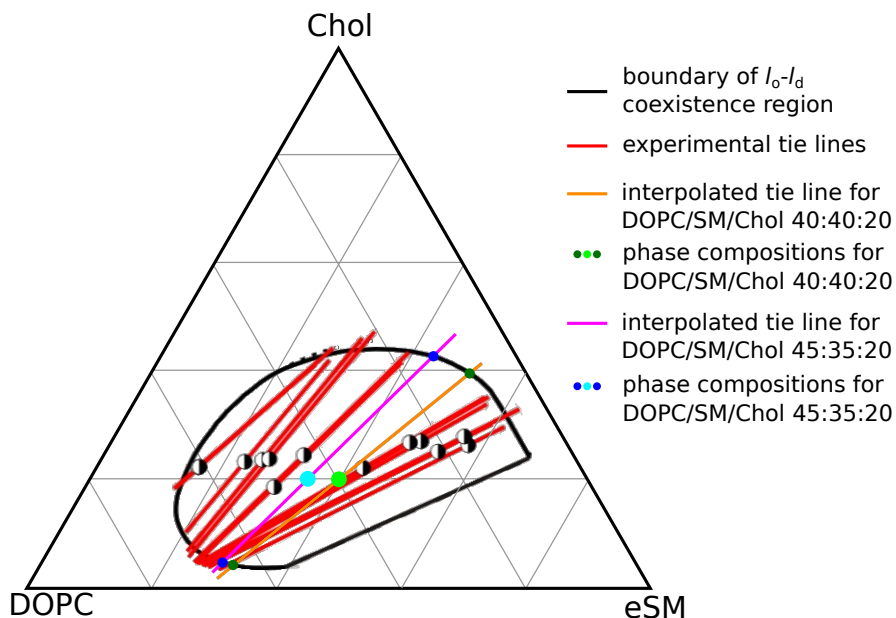
Figure 4.24: Phase diagram for DOPC/eggSM/Chol recreated from Bezlyepkina et al.[37] The black inset corresponds to the region of phase coexistence. Tie lines (red) were determined experimentally.

The red tie lines in 4.24 were determined experimentally for the compositions marked by the black and white dots. No tie line is given for DOPC/SM/Chol 40:40:20 (green dot). Slopes of the tie lines with respect to the DOPC percentage show a linear monotonic increase. A theoretical tine line was determined by using a linear

interpolation of compositions close to DOPC/SM/Chol 40:40:20 and is plotted as the orange line. This allows to determine the phase composition of the l_d and l_o phase (dark green dots). Using the area per molecule (Table 4.8) it is possible to calculate the theoretical area of the phases (Table 4.6).

Table 4.6: Phase composition of phase-separated membranes and their area percentage. The nominal composition is given in bold.

Component	DOPC	SM	Chol	Membrane Area
Lipid mixture	**40 %**	**40 %**	**20 %**	100.0 %
l_o composition	8.9 %	51.3 %	39.8 %	37.5 %
l_d composition	65.1 %	30.9 %	4.1 %	62.5 %
Lipid mixture	**45 %**	**35 %**	**20 %**	100.0 %
l_o composition	13.1 %	43.9 %	42.9 %	33.1 %
l_d composition	66.4 %	29 %	4.5 %	66.9 %

The values show that the l_o phase is nearly exclusively composed of sphingomyelin and cholesterol. Only a minor fraction of DOPC is incorporated. The l_o phase accounts for less than 40 % of the total membrane area. As both the value in this thesis and by Bezlyepkina *et al.* are obtained by fluorescence microscopy, a bias by possible nanoscopic domains with sizes below the resolution of the microscope seems unlikely.[31,32] The solid mica support seems to induce a higher degree of molecular order possibly due a preferential tight packing to maximize headgroup-support interactions.[162] This effect of the solid support is less pronounced on silicon dioxide and porous support.[51,52]

Another explanation is the small size of the domains. The work of Ando *et al.* using Raman microscopy determined the localization of sphingomyelin in lipid domains. They found that the outer parts of the domains are slightly depleted in sphingomyelin. Following this reasoning, depletion of the saturated SM would allow more DOPC to integrate into the outer region of the l_o domain, increasing its area. This effect would be less pronounced for the large round domains found in GUVs where the ratio of domain area to its circumference is much higher.

Influence of the l_d maker dye

Membranes containing the Gb$_3$ derivatives were imaged using different dyes preferentially partitioning into the l_d phase. Table 4.7 summarizes the percentages obtaining by pixel analysis. As expected the percentages determined are identical within the experimental errors. The fluorescence of STxB-Cy3 was not used to

determine the percentages because of the cluster formation observed for Gb$_3$-C24:0 and Gb$_3$-C24:0 2-OH.

Table 4.7: Comparison of the area percentages observed itemized by the l_d marker dye. Percentages were determined using pixel analysis of manually thresholded fluorescence micrographs.

| Gb$_3$- | | −STxB | | | +STxB | | |
| | | l_o | | | l_o | | |
		l_o	l_i	n	l_o	l_i	n
C24:0	Texas Red	70±9		22	78±11		23
	Oregon Green	75±6		62	75±11		29
C24:0 2-OH	Texas Red	56±5[‡]		46	78±5[‡]		52
	Bodipy-PC	56±3[‡]		10	74±3[‡]		10
C24:1	Texas Red	40±6[‡]	37±8[‡]	58	42±8[‡]	32±8[‡]	55
	Bodipy-PC	42±7[‡]	33±8[‡]	15	44±5[‡]	27±6[‡]	9
C24:1 2(R/S)-OH	Texas Red	73±6		29	89±6		24
	Oregon Green	66±7		22	83±8		18

[‡] Data partially reproduced from Orth 2012.[51]

Area per lipid

Table 4.8 lists the area per molecules as reported in literature corrected for the condensing effect of cholesterol.[37,66] The relative area per lipid species is calculated for a membrane composition of DOPC/SM/Chol/Gb$_3$ 40:35:20:5.

Table 4.8: Area per molecule as calculated in Bezlyepkina *et al.*.[37] Values for DOPC and SM had to be adjusted linearly to the cholesterol content due to its condensing effect.[66] The relative area per lipid species is calculated for a membrane composition of DOPC/SM/Chol/Gb$_3$ 40:35:20:5.

Lipid	DOPC	SM	Chol	Gb$_3$
Area / Å^2	67	49	27	80
Area Percentage / %	50	33	10	7

Established state of research

Parts of the data presented in this section were recorded by Alexander Orth and is included in his PhD thesis.[52] Table 4.9 and 4.10 provide a detailed overview. Labeling and designation of the data has been adapted to fit the style used in this section.

Table 4.9: Ratios of the different membrane phases (l_o: liquid-ordered, l_i: liquid-intermediate) in DOPC/SM/Chol/Gb$_3$ (40:35:20:5) bilayers doped with different Gb$_3$s on mica and height differences observed in AFM images after STxB binding as obtained by Orth 2012.[51] The ratios were determined by pixel analysis using fluorescence images. Height differences were extracted by fitting Gaussians to the height histograms (number of analysed fluorescence images and height histograms is given in brackets). For Gb$_3$-C24:0 2-OH Δh corresponds to the height difference between the l_o and the l_d phase. For Gb$_3$-C24:1 Δh corresponds to the averaged height difference of l_d to l_i and l_o.

Gb$_3$-	l_o / %	l_o / %	Δh / nm
C24:0 2-OH	55±5 (36)	—	0.8±0.5 (80)
C24:1	41±6 (43)	36±8	1.2±0.7 (65)

Table 4.10: Ratios of the different membrane phases (l_o: liquid-ordered, l_i: liquid-intermediate) in DOPC/SM/Chol/Gb$_3$ (40:35:20:5) bilayers doped with different Gb$_3$s on mica and height differences observed in AFM images after STxB binding as obtained by Orth 2012.[51] The ratios were determined by pixel analysis using fluorescence images. Height differences were extracted by fitting Gaussians to the height histograms (number of analysed fluorescence images and height histograms is given in brackets).

Gb$_3$-	l_o/%	l_i/%	$\Delta h(l_\mathrm{i}$ /l_d)/nm	$\Delta h(l_\mathrm{o+STxB\_clusters}$ /$l_\mathrm{o+STxB}$)/nm	$\Delta h(l_\mathrm{o+STxB}$ /l_d)/nm	$\Delta h(l_\mathrm{o+STxB}$ /l_i)/nm
C24:0 2-OH	77±5(42)	—	—	—	1.0±0.6(67)	—
C24:1	44±8(40)	30±8	1.3±0.9(10)	0.7±0.6(21)	2.5±1.8(21)	1.9±1.8(11)

The data presented here was extended in this thesis.

- Additional fluorescence micrographs recorded by A. Orth were evaluated for Gb$_3$-C24:0 2-OH containing membranes.

- Additional AFM images recorded by A. Orth were evaluated for Gb$_3$-C24:0 2-OH containing membranes. A new height difference $\Delta h(l_\mathrm{o+STxB\_clusters}/l_\mathrm{d})$ was found.

- Additional fluorescence micrographs were recorded and evaluated for Gb$_3$-C24:1 membranes.

- Additional AFM images were recorded and evaluated for Gb$_3$-C24:1 membranes. Two new height differences expected from the fluorescence micrographs were found.

- Calculation of the values and their errors was adapted to the methodology used in this thesis (see Section 3.3.1 and 3.3.2).

4.2 Gb$_3$ bearing α-hydroxylated nervonic acid: Influence of 2-OH configuration on the binding of Shiga toxin

- Parts of this Section are published as O. M. Schütte, L. J. Patalag, L. M. C. Weber, A. Ries, W. Römer, D. B. Werz, C. Steinem, 2-Hydroxy Fatty Acid Enantiomers of Gb$_3$ Impact Shiga Toxin Binding and Membrane Organization, *Biophys. J.* **2015**, *108*(12), 2775-2778[87]

- Fluorescence and atomic force microscopy data of solid supported membranes was partially measured by Lucas Weber during his bachelor thesis supervised from June to September 2014.[180]

4.2.1 Abstract

Shiga toxin subunit B (STxB) binding to its glycosphingolipid receptor Gb$_3$ leads to the formation of protein-lipid aggregates and subsequent bending of the plasma membrane as a first step of the toxin's endocytosis. As shown in Section 4.1, differences in the fatty acids structure of Gb$_3$ influence the binding of the protein. A new synthetic route allowed to synthesize the biologically most relevant Gb$_3$-C24:1 2-OH species with both configurations of the α-hydroxy group of the fatty acid. Binding of STxB to both derivatives induced the formation of membrane tubules in giant unilamellar vesicles. The effect was more pronounced for the (S)-α-hydroxy configuration. Surface plasmon resonance and reflectometric interference spectroscopy revealed nearly identical binding affinities below 10 nM for both derivatives but an increased binding capacity for Gb$_3$-C24:1 2(S)-OH. Experiments on solid supported membranes using a phase-separated lipid mixture showed differences in the lateral organization of the protein on the membrane. Whereas Gb$_3$-C24:1 2(R)-OH induces high density protein-lipid clusters, its (S) counterpart leads to more evenly distributed protein on the membrane in accordance with the observed increase in binding capacity. Gb$_3$-C24:1 2(S)-OH induces less rigid protein-lipid structures readily forming invaginations.
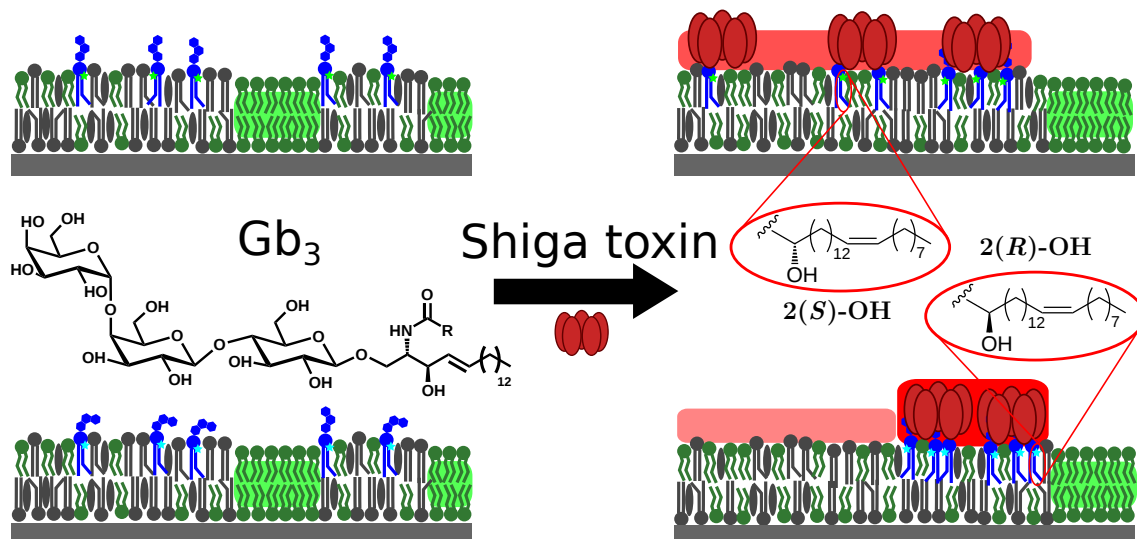
Figure 4.25: Shiga toxin binding to Gb$_3$-C24:1 2(R)-OH and Gb$_3$-C24:1 2(S)-OH alters membrane organization and induces invaginations in GUVs.

4.2.2 Introduction

Shigella dysenteriae produces the AB$_5$ exotoxin Shiga Toxin (STx, Figure 1.5). Enterohemorrhagic strains of *Escherichia coli* (EHEC) use functionally and structurally closely related proteins, denoted as verotoxins or shiga-like toxins.[56] STx binds to the membrane by the homopentameric B-subunit (STxB) which specifically recognizes the globotriaosylceramide (Gb$_3$, see Figure 4.2 and Section 3.1.3) on the cell surface. One STxB pentamer can bind up to 15 Gb$_3$ molecules[60] leading to a clustering of the receptor lipid. The lipid compaction induces of negative curvature in the membrane[71] resulting in the formation of plasma membrane invaginations as an efficient way to enter the cells. After actin driven scission in cells, the toxin is transfered to the endoplasmic reticulum, where it inhibits protein biosynthesis.

In cells Gb$_3$ differs in its fatty acid bound to the amide group. The length, saturation and hydroxylation influence the affinity to bind STxB and their biological function.[71,74,135,181] The fatty acid also might also influence the phase preference of the lipid.

Glycosphingolipids bearing hydroxylated fatty acids are abundant in nature. The main component of natural Gb$_3$ extracts from HeLa cancer cells bears the α-hydroxylated (2-OH) and unsaturated nervonic acid (C24:1 Δ^{15}).[39] In human, hydroxylated ceramides are synthesized by the same enzymes as non-hydroxy

ceramides starting from the already hydroxylated fatty acid.[150] The degree of hydroxylation of the ceramides varies between different cell lines between 1 % up to 50 % in certain epithelial cells and deficiencies are associated with neuronal dysfunction in the brain.[149, 150] Ceramides are subsequently converted to more complex membrane lipids like sphingomyelin (SM) and galactocerebrosides.[150]

The 2-hydroxy fatty acids used for the biosynthesis are produced by the NAD(P)H dependent fatty acid 2-hydroxylase (FA2H).[149] This enzyme stereospecifically produces the (R) enantiomer of the fatty acid. In bacteria and some animals the (S) hydroxylation is also present.[149] In 2012 Guo *et al.* used siRNA to knockdown FA2H in adipocytes. Cells were vital but fluorescence recovery after photobleaching (FRAP) experiments showed that the diffusion of raft associated lipids was accelerated. The authors reasoned that the (R) hydroxylated species forms intermolecular hydrogen bonds, which slow down the diffusion. Feeding exogenous (R) hydroxylated palmitic acid reversed the effect of the knockdown. Its (S) counterpart did not show this effect even though it got incorporated into the ceramide synthesis pathway, indicating that its interactions with other membrane lipids are different.[149]

Biophysical work done on the influence of the configuration of the 2-hydroxy group of fatty acids indicate both a subtle effect on the membrane organization and strong local conformational changes. Löfgren compared the compressibility of monolayers of pure sphingosines using a Langmuir film balance.[141] He found that a (S) hydroxylation inhibits lipid condensation, but the molecules are still densely packed at high surfaces pressures. The (R) diastereomer tends to form a close-packed condensed phase at all surface pressures and has a larger compressibility. An explanation for this behavior is given by Pascher[142] and Löfgren.[141] Figure 4.26A/B shows a model for the arrangement of the (S) and (R) derivatives based on crystal structures of tetracosanoylphytosphingosine and DL-2-hydroxytetradecanoic acid.[141] In the (S) configuration the 2-hydroxy group can act as a donor to the carbonyl group of the amide forming an intramolecular hydrogen bond. This is not possible in the (R) configuration, freeing the OH to form other hydrogen bonds. Cerebrosides form an extensive network of intra- and intermolecular hydrogen bonds involving the 2-OH group.[142] All atom molecular dynamics simulations of galactocerebrosides performed by Yahi *et al.* show that the (R) hydroxylation can form hydrogen bonds with the galactose headgroup inducing a tilting of the sugar towards the membrane

(Figure 4.26C).[143] In non-hydroxylated derivatives, the OH group of cholesterol can fulfill a similar role.[75,143] Nuclear magnetic resonance studies performed by the group of Grant did not find any influence of the fatty acid on the carbohydrate headgroup.[152,182]
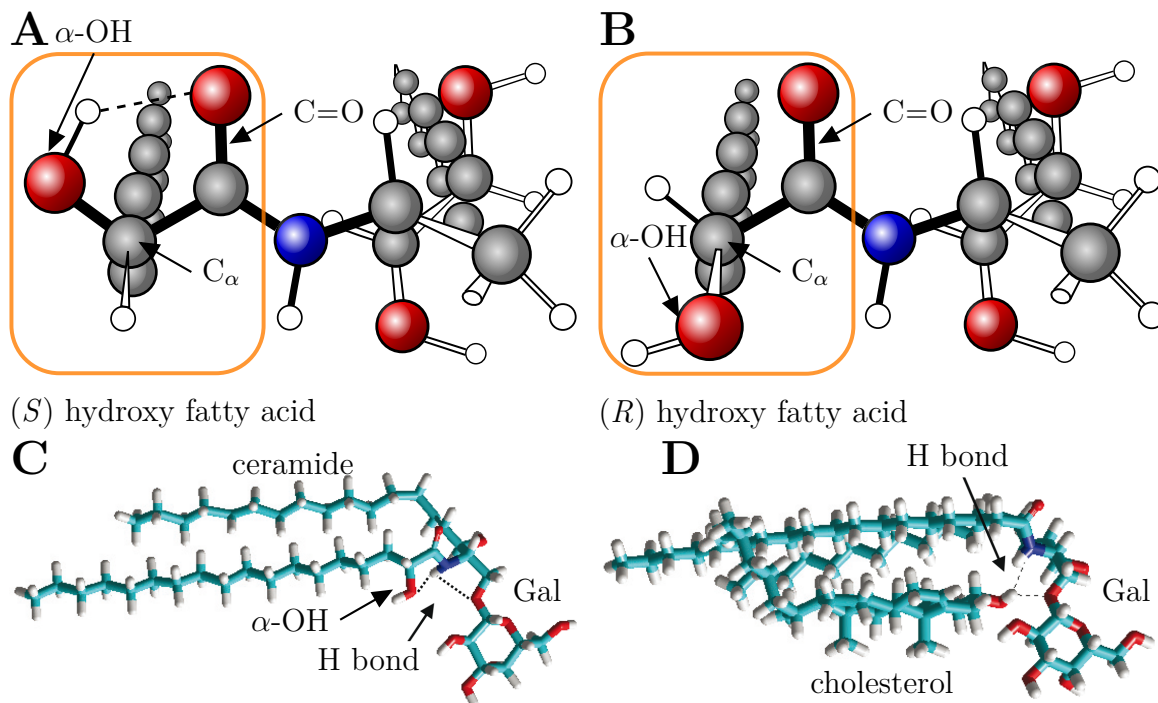
Figure 4.26: Hydrogen bond networks formed by α-hydroxylated fatty acids. **A** (S) hydroxylated fatty acids form intramolecular hydrogen bonds whereas its (R) counterpart (**B**) does not. Images recreated after Löfgren.[141] **C** α-hydroxylation can lead to a tilting of the sugar headgroup in case of galactocerebrosides. **D** The tilting is also facilitated by cholesterol in the membrane. Panel **C** and **D** modified from *Yahi et al.*.[143]

The same group also investigated how the configuration of the 2-OH group of a fatty acid attached to galactosylsphingosin influences the fatty acid tails of the surrounding lipids. The hydroxy group was found to influence packing with the host phospholipids. (R) configuration leads to a higher molecular order while strengthening the interlipid interactions near the membrane surface in agreement with interpretations of Guo *et al.*[183] The (S) derivative does not show this behavior. In 2014 Pawlizek *et al.* published the synthesis of α-hydroxylated nervonic acid.[88] This allowed to assemble both the native Gb₃-C24:1 2(R)-OH and the unnatural derivative Gb₃-C24:1 2(S)-OH (Figure 4.2). Synthetic procedures were adapted from Schütte *et al.*, where the impact of the diastereomeric mixture of both derivatives was investigated (see Section 4.1).[86]
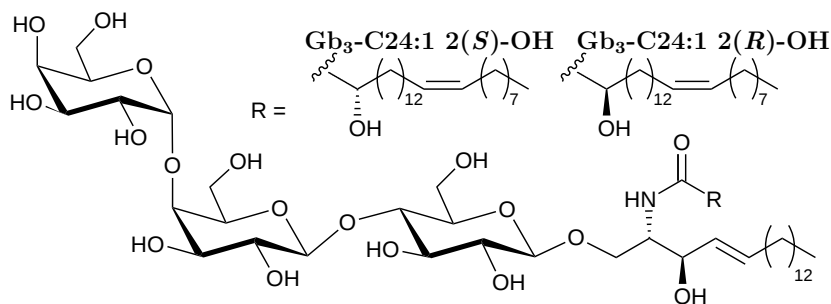
Scheme 4.2: Chemical structure of Gb_3 bearing both the (S) and (R) configuration of the 2-hydroxy group (Gb_3-C24:1 $2(S)$-OH and Gb_3-C24:1 $2(R)$-OH).

4.2.3 Results

Upon binding of STxB to Gb_3 expressing cells, the protein is able to cross the cell membrane in a clathrin independent way.[39,71] A superior way to investigate the mechanism in absence of cellular proteins are model systems in which the composition of the lipid membrane can be controlled. Giant unilamellar vesicles (GUVs) allow to monitor the protein lipid interactions by fluorescence microscopy in three dimensions.

4.2.3.1 Formation of invaginations in GUVs

GUVs composed of DOPC, cholesterol and either Gb_3-C24:1 $2(R)$-OH or Gb_3-C24:1 $2(S)$-OH in a ratio of 75:20:5 were prepared by electroformation (see Section 3.2.1) in sucrose solution. The lipid coupled fluorescent dye Atto488 DHPE (Figure 3.4D) was added to the lipid mixture (0.5 mol%) and allows to visualize the GUVs and the distribution of the fluid l_d phase. After addition of the vesicles to a STxB or STxB-Cy3 solution in PBS (final concentration $c = 60$ nM), the vesicles were incubated for 10 min to allow them to settle to the bottom. The morphology of the vesicles was unaffected by STxB (Figure 4.27A) under hyperosmotic conditions.
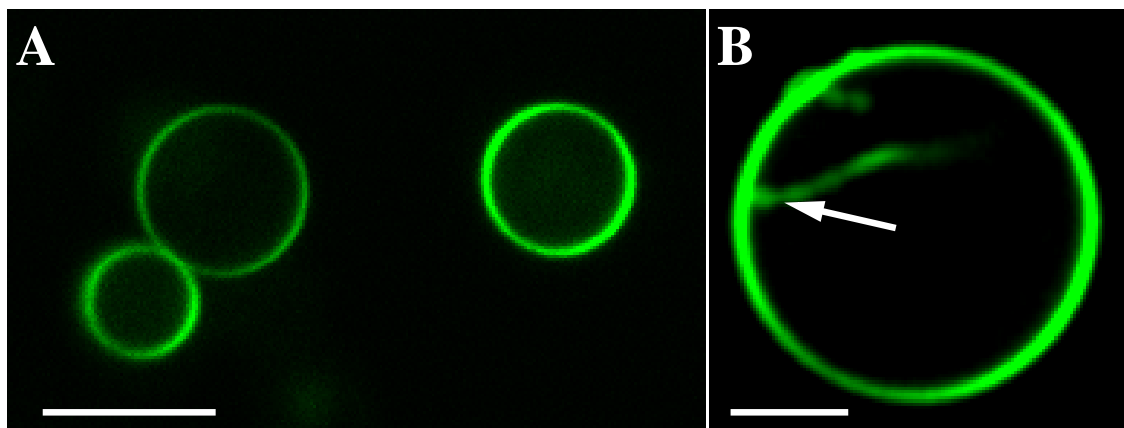
Figure 4.27: A Confocal slice of three GUVs composed of DOPC/Chol/Gb$_3$-C24:1 2(R)-OH 75:20:5 doped with 0.5 mol% of Atto488 DHPE after incubation with 60 nM STxB under hyperosmotic conditions. The GUVs appear round and no alterations of the topography due to STxB binding are visible. Scale bar: 8 μm **B** GUV composed of DOPC/Chol 80:20 doped with 0.5 mol% after incubation with 60 nM STxB. Invaginations in absence of Gb$_3$ or STxB are tube-like and not coiled. Scale bar: 5 μm

Ewers, Römer *et al.* predicted that membrane tension due to osmotic pressure inhibits the formation of invaginations (see Equation 4.6).[72] High osmolarity glucose solution was added to reverse the osmotic gradient. This resulted in a deflating of the GUV and lowers the tension.[71] This results in excess membrane area as the surface area of the GUV is constant while the outflow of water lowers its volume, allowing the formation of invaginations. Deflating resulted in the formation of inward facing membrane tubules. Figure 4.28 shows the influence of STxB binding to GUVs containing Gb$_3$-C24:1 2(S)-OH (left column) or Gb$_3$-C24:1 2(R)-OH (middle column). Binding to the membrane can be observed by the fluorescence of Cy3-labeled STxB (Figure 4.28B/E) and results in the formation of one to several inward facing tubular membrane structures (Figure 4.28B/E). The morphology of the invaginations is spiral or super-coiled and rapid movement of the tubules can be observed (Figure 4.29). The diameter of the tubes cannot be resolved due to the movement and the limited resolution of the microscope but was reported to be in the range of 50 nm.[71,72] Statistical analysis revealed that $34 \pm 11\%$ of the Gb$_3$-C24:1 2(R)-OH containing GUVs have invaginations (n = 393), whereas more GUVs containing Gb$_3$-C24:1 2(S)-OH show invaginations ($75 \pm 13\%$, n = 456). Overlays of the Atto488 DHPE and STxB-Cy3 fluorescence (Figure 4.28C/F) demonstrate that the red protein fluorescence is significantly enhanced in the tubules compared to the surface of the GUV.[134]
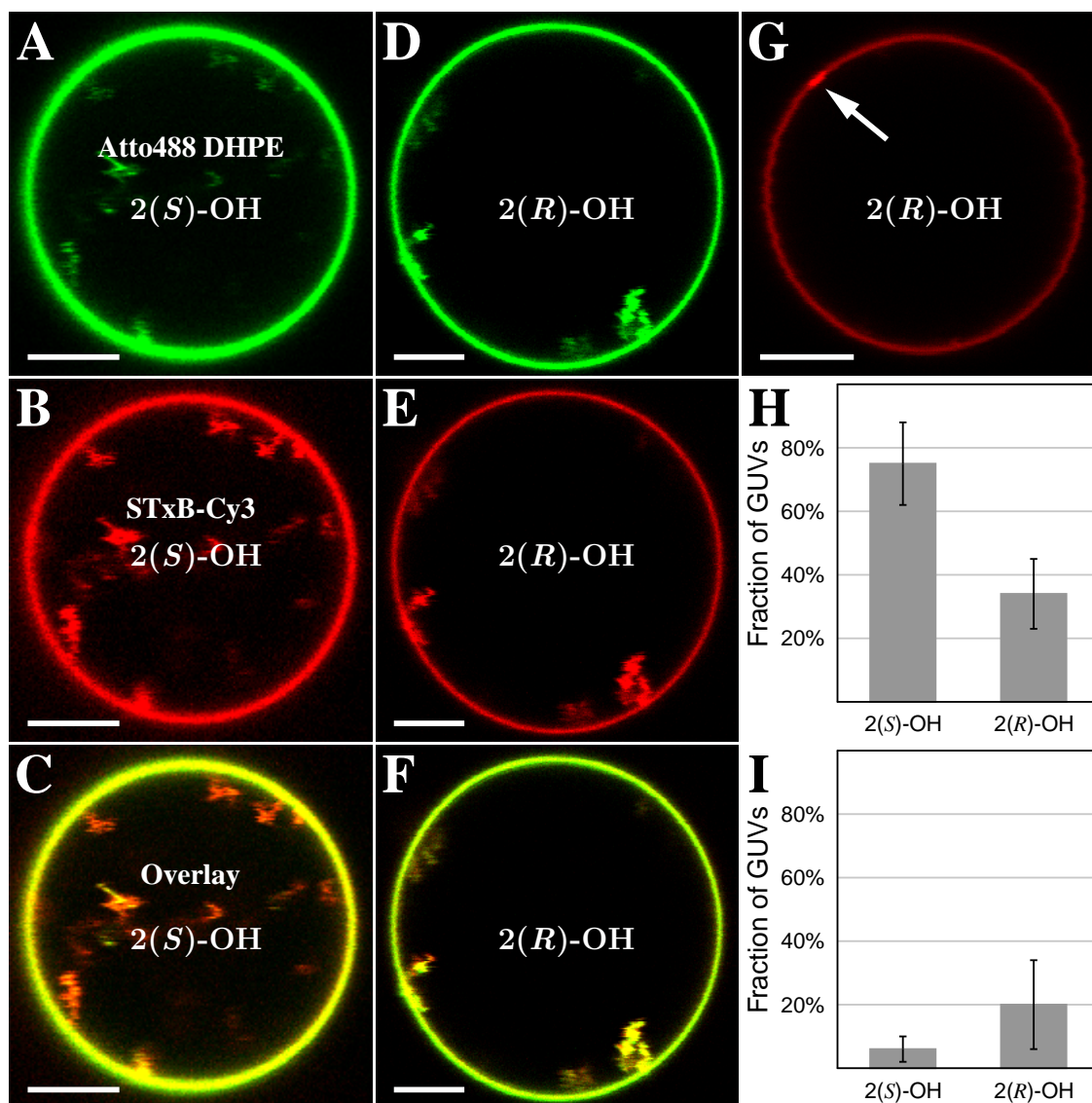
Figure 4.28: Confocal slices of GUVs composed of DOPC/Chol/Gb$_3$-C24:1 2(S)-OH (panels **A**, **B**, **C**) and Gb$_3$-C24:1 2(R)-OH (**E**, **E**, **F**, **G**) 75:20:5 labeled with Atto488 DHPE after incubation with 60 nM of STxB-Cy3. **A-F** GUVs have spiral invaginations, identified by fluorescence of the lipid marker (false colored in green) and STxB-Cy3 (false colored in red). The overlays (**C**, **F**) show an enrichment of STxB in the tubes. **G** In some GUVs only the formation of protein-lipid aggregates (arrow) is observed. Scale bars: 5 µm. **H** A higher percentage of GUVs doped with Gb$_3$-C24:1 2(S)-OH show invaginations as seen in **A-F**. **I** A higher percentage of GUVs doped with Gb$_3$-C24:1 2(R)-OH show protein-lipid aggregates as seen in **G**. Scale bars: 5 µm.

In absence of STxB or Gb$_3$ in the membrane, tubes are also formed, but less frequently and $\approx$15 % of the GUVs show tubules (Table 4.11). Tubes appear linear and not coiled (Figure 4.27B). Additionally to the formation of membrane invagina-

tions, inhomogeneities in the STxB-Cy3 fluorescence on the flat GUV membrane are observed (Figure 4.28G). They can be attributed to the line tension driven formation of STxB aggregates (Equation 4.3). Of note, in some cases the Atto488 DHPE fluorescence is also increased in these areas suggesting that the clusters might be shallow invaginations with a depth below the resolution of the microscope. Aggregate formation is more frequent for Gb$_3$-C24:1 2(R)-OH containing GUVs ($20 \pm 14\,\%$, n $= 393$) compared to Gb$_3$-C24:1 2(S)-OH GUVs ($6 \pm 4\,\%$, n $= 456$, Figure 4.28I, Table 4.11).
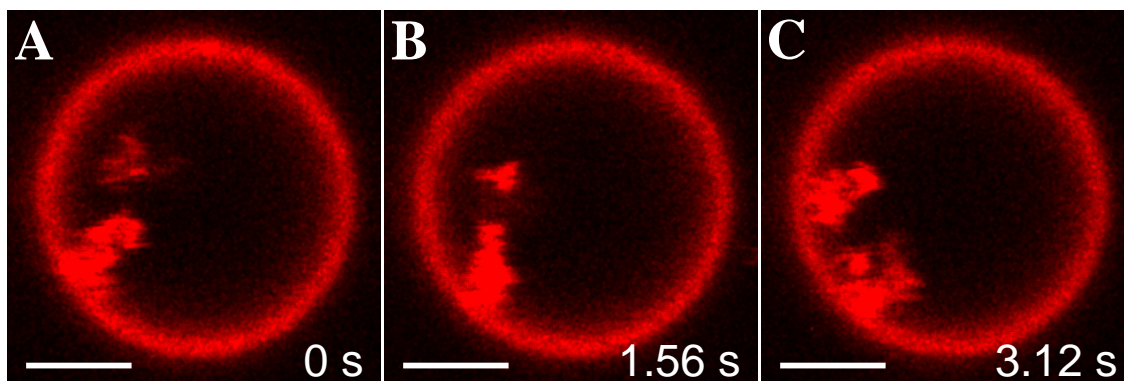
Figure 4.29: Time series of a GUV composed of DOPC/Chol/Gb$_3$-C24:1 2(R)-OH 75:20:5 incubated with $60\,$nM of STxB-Cy3. The STxB-Cy3 fluorescence shows the movement of the tubular invaginations. Scale bars: $3\,\mu$m.

Further increasing the outside osmolarity by adding additional high osmolarity glucose solution enhances the formation of tubular invaginations because the lowered volume increases the excess membrane area. However, under the chosen osmotic conditions GUVs become too flaccid and disintegrate resulting in a mean GUV diameter of the remaining GUVs of about $3\,\mu$m. The remaining GUV show invaginations in $91 \pm 3\,\%$ (n $= 83$) and $76 \pm 13\,\%$ (n $= 148$) for Gb$_3$-C24:1 2(S)-OH and Gb$_3$-C24:1 2(R)-OH respectively. Table 4.11 summarizes the results obtained for the formation of invaginations on membranes doped with Gb$_3$-C24:1 2(S)-OH and Gb$_3$-C24:1 2(R)-OH.

Table 4.11: STxB binding to GUVs composed of DOPC/Chol/Gb$_3$-C24:1 2(R/S)-OH 75:20:5 results in the formation of invaginations and protein lipid clusters.

Gb$_3$-C24:1	GUVs with invaginations	GUVs with aggregates	n	GUVs with invaginations (higher ΔO)	n
2(S)OH +STxB	75±13 %	6±4 %	456	92±3 %	83
2(R)OH +STxB	34±11 %	20±14 %	393	76±13 %	148
2(S)OH –STxB	14±1 %	-	125	29±25 %	119
2(R)OH –STxB	16±7 %	-	116	19±10 %	67
No Gb$_3$ +STxB	21±1 %	-	163	40±15 %	78

4.2.3.2 Quantification of the STxB Gb$_3$ interaction

To investigate the reason for the different capability of Gb$_3$-C24:1 2(S)-OH and Gb$_3$-C24:1 2(R)-OH to form membrane invaginations, the interaction of STxB with both Gb$_3$ derivatives was quantified using surface plasmon resonance (SPR) spectroscopy and reflectometric interference spectroscopy (RIfS).

Surface plasmon resonance spectroscopy

SPR allows to determine the change in reflectivity ΔR, which is proportional to the newly deployed material on top of the sensor surface (Section 3.3.4.1) enabling the determination of the affinity of a solute to the surface. The dissociation constant K_D was determined for two membranes systems; (i) 5 mol% Gb$_3$ in a 95 mol% DOPC matrix and (ii) a system composed of DOPC/Chol/Gb$_3$ 75:20:5. The time course of ΔR of a typical experiment is shown in Figure 4.30A. Experimental procedures were adapted from Nakajima *et al.*.[107]

Upon addition of vesicles in PBS (**a**, DOPC/Gb$_3$-C24:1 2(R)-OH 95:5, final concentration 0.03 mg mL^{-1}) to an octanethiol functionalized gold sensor chip the reflectivity increases indicating the formation of a hybrid bilayer. Rinsing with PBS (**b**) results in a slow and steady drop in reflectivity caused by the detachment of vesicles and membrane multistacks. The process is accelerated by the repeated addition of NaOH solution (**c**, 50 mM). Possible hydrophobic defects are blocked by bovine serum albumin (BSA, **d**, 1 mg mL^{-1}). In most experiments the increase in reflectivity upon BSA addition was fully reversible indicating that no hydrophobic defects were present. STxB in increasing concentrations between 1 and 120 nM was added (**e** to **h**) and the change in reflectivity compared to baseline level after BSA addition was determined. Overall absolute changes in reflectivity for membrane formation and protein binding were found to vary strongly among the

experiments probably due to differences in the roughness of the gold layer.[184] All reflectivity changes were normalized by dividing the value by the reflectivity change at saturation ($c = 120$ nM). Figure 4.30B/C show the adsorption isotherms for DOPC/Gb$_3$-C24:1 2(S)-OH 95:5 and DOPC/Gb$_3$-C24:1 2(R)-OH 95:5 together with a fit according to the Langmuir model (Equation 3.14). Fitting the data yields $K_D = 9 \pm 2$ nM for Gb$_3$-C24:1 2(S)-OH and $K_D = 8 \pm 2$ nM for Gb$_3$-C24:1 2(R)-OH containing membranes. These values are in excellent agreement with the affinity determined for the diastereomeric mixture Gb$_3$-C24:1 2(R/S)-OH (Table 4.1).
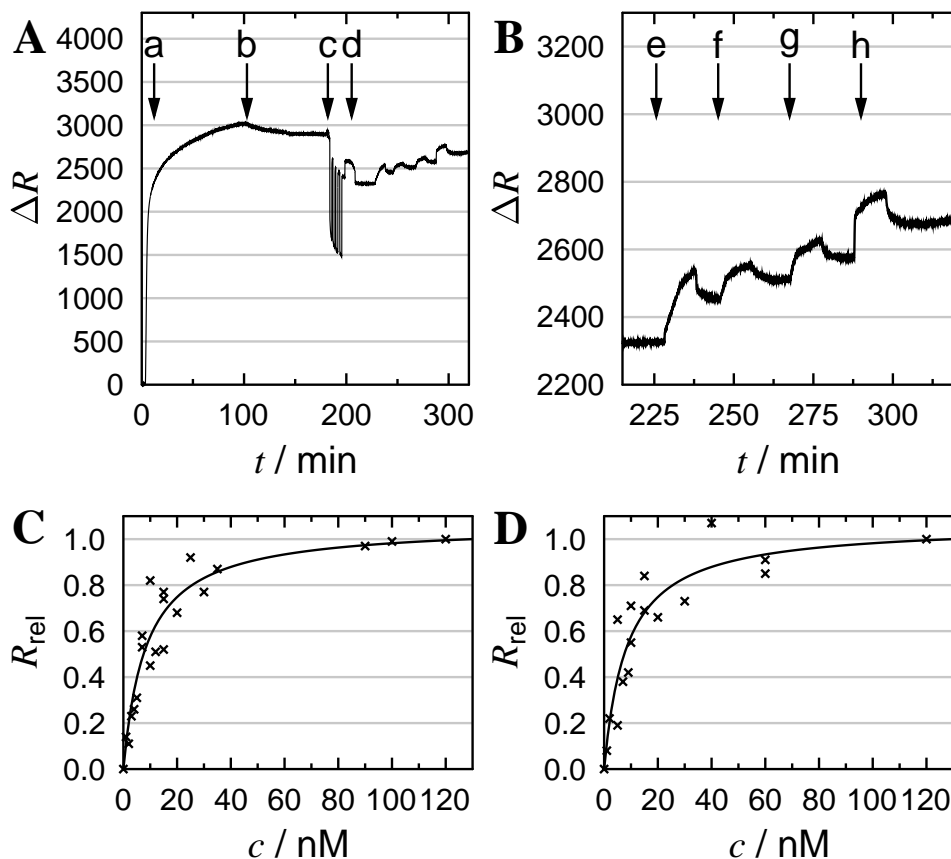
Figure 4.30: SPR analysis of the binding of STxB to hybrid membranes containing 5 mol% of Gb$_3$-C24:1 2(R)-OH and 95 mol% DOPC. **A** Characteristic course of an experiment with a zoom in shown in **B**. (a): Addition of small vesicles (DOPC/Gb$_3$-C24:1 2(S)-OH 95:5, final concentration 0.03 mg mL^{-1}) at a flowrate of 50 µL min^{-1}. (b): rinsing. (c): flowrate was lowered to 25 µL min^{-1} to add NaOH solution (4×50 mM) for 2 min each to remove vesicles and lipid multistacks. (d): Addition of BSA solution (1 mg mL^{-1}) to block defects in the membrane followed by rinsing with PBS. (e)-(h): Additions of STxB ($c = 10$, 15, 20, 120 nM) followed by rinsing with PBS. **C** Adsorption isotherm of STxB to membranes containing Gb$_3$-C24:1 2(S)-OH. Crosses denote data points and the line the fit according to the Langmuir model. **D** Langmuir adsorption isotherm of STxB to membranes containing Gb$_3$-C24:1 2(R)-OH. Crosses denote data points and the line the fit according to the Langmuir model. Image modified from Schütte *et al.* 2015.[87]

Cholesterol was added to the lipid mixture to resemble the free standing membrane of the GUVs more closely. A typical time course of an experiment in a DOPC/Chol/Gb$_3$-C24:1 2(R)-OH 75:20:5 membrane is shown in Figure 4.31A. It closely resembles the cholesterol free case. No apparent differences in membrane formation, multilayer detachment and protein binding were found.
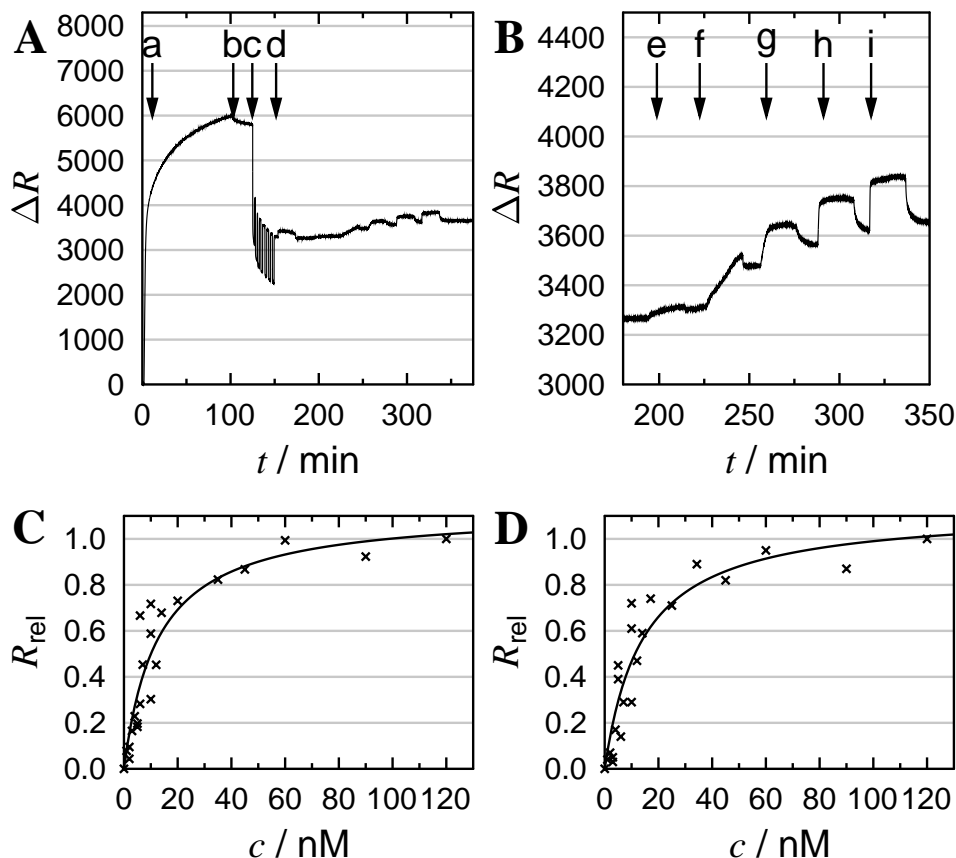
Figure 4.31: SPR analysis of the binding of STxB to hybrid membranes containing 5 mol% of Gb$_3$-C24:1 2(R)-OH, 20 mol% cholesterol and 75 mol% DOPC. **A** Characteristic course of an experiment with a zoom in shown in **B**. (a): Addition of small vesicles (DOPC/Chol/Gb$_3$-C24:1 2(S)-OH 75:5, final concentration 0.03 mg mL^{-1}). (b): rinsing. (c): Addition of NaOH solution (7 × 50 mM) for 2 min each to remove vesicles and lipid multistacks. (d): Addition of BSA solution (1 mg mL^{-1}) to block defects in the membrane followed by rinsing with PBS. f: rinsing. (e)-(i): Additions of STxB ($c = 1$, 7, 14, 45, 120 nM) followed by rinsing with PBS. **C** Adsorption isotherm of STxB to membranes containing Gb$_3$-C24:1 2(S)-OH. Crosses denote data points and the line the fit according to the Langmuir model. **D** Adsorption isotherm of STxB to membranes containing Gb$_3$-C24:1 2(R)-OH. Crosses denote data points and the line the fit according to the Langmuir model. Image partially modified from Schütte *et al.* 2015.[87]

The adsorption isotherms fitted according to the Langmuir model (Figure 4.31B/C) for membranes composed of DOPC/Chol/Gb$_3$-C24:1 2(S)-OH 75:20:5

$(K_D = 13 \pm 3\,\text{nM})$ and DOPC/Chol/Gb₃-C24:1 $2(R)$-OH 75:20:5 $(K_D = 14 \pm 3\,\text{nM})$ give twofold reduced affinity constants (Table 4.31). SPR spectroscopy provided identical affinities of STxB to Gb₃-C24:1 $2(R)$-OH and Gb₃-C24:1 $2(S)$-OH. The differences in the formation of invaginations are not caused by the protein's affinity to the membrane. However, due to the variation in absolute changes of the reflectivity between the experiments no information on the binding capacities of the Gb₃s could be extracted.

Reflectometric interference spectroscopy

Reflectometric interference spectroscopy (RIfS) was used to determine the absolute optical thickness (OT) of the membrane and the adsorbed protein layer (Section 3.3.4.2).[111] In contrast to the SPR experiments membranes prepared for RIfS setup are bilayers formed on hydrophilic silicon dioxide wafers. Using the affinity constants obtained by SPR, the concentration of STxB used for each experiment was adjusted to give 90 % receptor occupancy. Under these conditions, it is possible to compare the binding capacities of the Gb₃ derivatives derived from the absolute changes in height (Figure 4.32). These changes are presumably also a direct measure for the valency of the STxB-Gb₃ interaction.
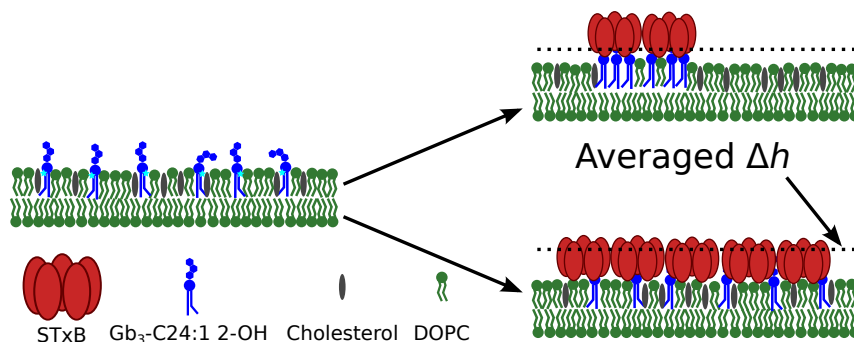
Figure 4.32: Schematic drawing demonstrating that the height difference measured in RIfS (Δh) is proportional to the surface coverage and presumably also indicates the valency of the STxB-Gb₃ interaction.

Typical experiments using DOPC/Gb₃ 95:5 and DOPC/Chol/Gb₃ 75:20:5 membranes are shown in Figure 4.33A/B. Addition of vesicles in PBS results in a rapid increase in optical thickness indicating the formation of a lipid bilayer. Using cholesterol containing membranes, in all experiments a slight overshoot was found, which quickly leveled off to give a constant optical thickness. Rinsing with PBS (**b**), addition of BSA solution (**c**, $1\,\text{mg}\,\text{mL}^{-1}$) and rinsing (**d**) did not change the

optical thickness indicating that after spreading a defect free membrane is formed. Experiments were performed three times per lipid mixture.
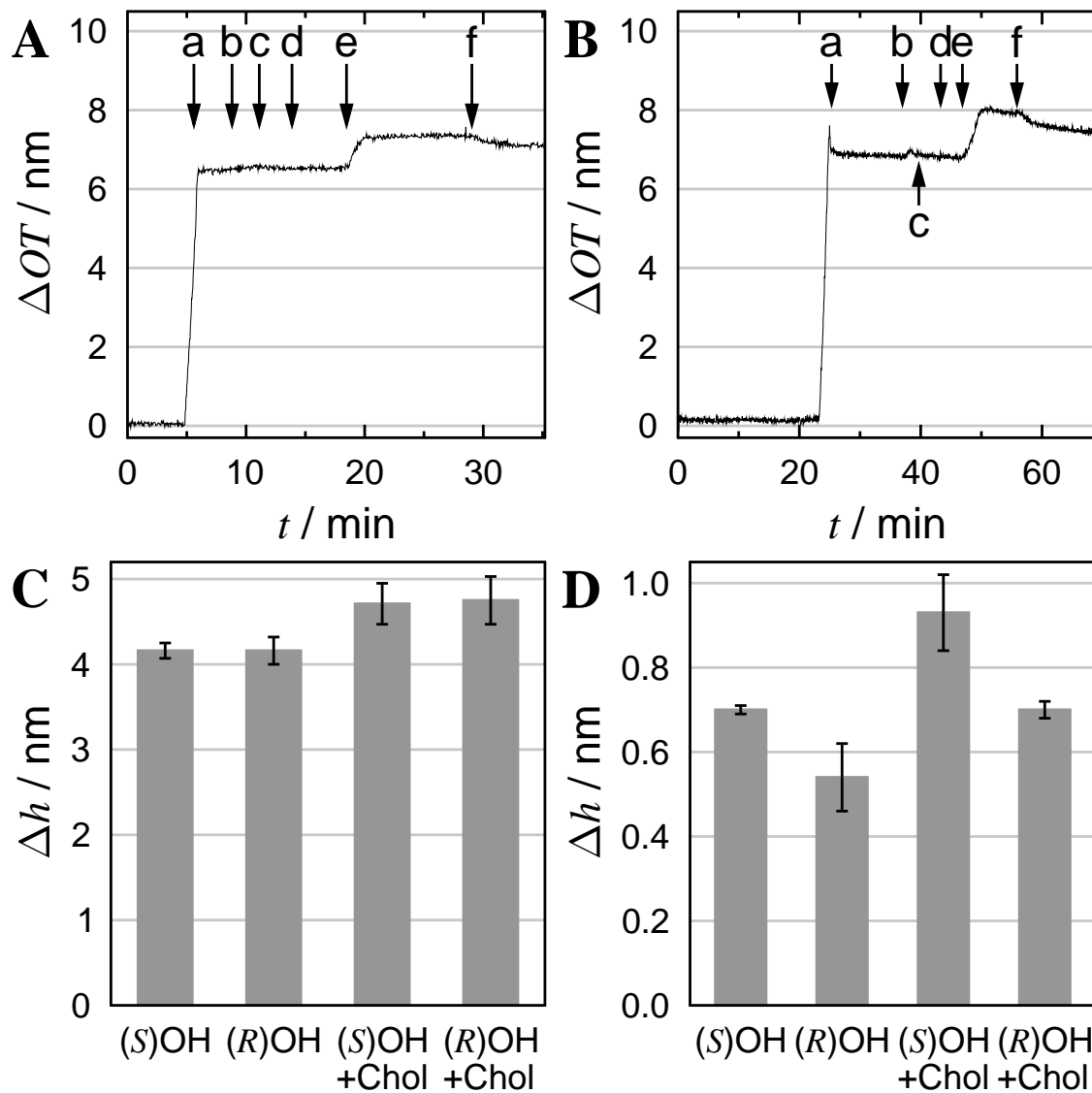
Figure 4.33: A, **B** Examples of typical experiments for DOPC/Gb$_3$ 95:5 membranes (**A**) and DOPC/Chol/Gb$_3$ 75:20:5 membranes (**B**). (a): Addition of small vesicles in PBS (final concentration $0.1\,\mathrm{mg\,mL^{-1}}$, DOPC/Gb$_3$-C24:1 2(*S*)-OH 95:5 (**A**) or DOPC/Chol/Gb$_3$-C24:1 2(*S*)-OH 75:20:5 (**B**)) followed by rinsing with PBS (b). (c): Addition of BSA solution (final concentration $1\,\mathrm{mg\,mL^{-1}}$) to block defects in the membrane followed by rinsing with PBS (d). (e): Addition of STxB (final concentration $72\,\mathrm{nM}$ (**A**) or $117\,\mathrm{nM}$ (**B**)) followed by rinsing with PBS (f). **C** Bilayer thicknesses of the different systems. **D** Thicknesses of the STxB layers after binding to the membrane. Image partially modified from Schütte *et al.* 2015.[87]

The membrane thickness was calculated using a refractive index of 1.49^{112} and is $\Delta h = 4.16 \pm 0.16\,\mathrm{nm}$ for $DOPC/Gb_3$ 95:5 membranes in good agreement with literature (Figure 4.33C).[185] Cholesterol increases the thickness of the membranes by $0.5\,\mathrm{nm}$.[186]

An increase in optical thickness for the binding of STxB was converted to the change in height using a refractive index of 1.47 for a 35 kDa protein (Figure 4.33D).[113] The changes are summarized in Table 4.12 and lie between $\Delta h = 0.54 \pm 0.08\,\mathrm{nm}$ for $DOPC/Gb_3$-C24:1 $2(R)$-OH 95:5 and $\Delta h = 0.93 \pm 0.09\,\mathrm{nm}$ for $DOPC/Chol/Gb_3$-C24:1 $2(S)$-OH 75:20:5.

An increase in the binding capacities for Gb_3-C24:1 $2(S)$-OH membranes was about 30 % compared to Gb_3-C24:1 $2(R)$-OH both in presence and absence of cholesterol. According to the crystal structure of STxB the protein has a height of $2.0\,\mathrm{nm}$.[60] Using this value, the measured heights upon binding can be converted to surface coverages of 27 to 47 % (Table 4.12).

After rinsing with PBS, $\approx$70 % of the protein remained irreversibly bound to the membrane. Cholesterol increases the binding capacity of the membranes suggesting an influence on the conformation of the headgroup of Gb_3 or an alteration of the lateral organization of the receptor in the membrane.[107]

Table 4.12: Dissociation constants K_D from SPR experiments. Thicknesses of the membrane and protein layer as determined by RIfS. Membranes composed of $DOPC/Gb_3$ 95:5 or $DOPC/Chol/Gb_3$ 75:20:5.

Gb_3-C24:1	K_D/nM	Δh(Mem)/nm	Δh(STxB)/nm	irreversible fraction	coverage
$2(S)$OH	9 ± 2	4.16 ± 0.09	0.70 ± 0.01	74 %	35 %
$2(R)$OH	8 ± 2	4.16 ± 0.16	0.54 ± 0.08	63 %	27 %
$2(S)$OH+Chol	13 ± 3	4.71 ± 0.24	0.93 ± 0.09	69 %	47 %
$2(R)$OH+Chol	14 ± 3	4.75 ± 0.28	0.70 ± 0.02	63 %	35 %

The results show a clear difference in binding of STxB and the propensity of the Gb_3 derivatives to facilitate the formation of membrane invaginations. This effect can either be an intrinsic property of the Gb_3 molecule, or be caused by the lateral organization of the receptor in the membrane.

4.2.3.3 Membrane organization prior to protein binding

The lateral membrane organization of the diastereomeric mixture Gb_3-C24:1 $2(R/S)$-OH was studied and the results are shown in Section 4.1. The Gb_3 derivative induces a unique phase behavior and the amount of l_o phase

drastically increased upon STxB binding. The newly developed stereoselective synthesis of the single diastereoisomers allows to rationalize the influence of the configuration of the 2-hydroxy group of the fatty acid.

To understand both the differences in binding capacity and the different ability of Gb_3-C24:1 2(R)-OH and Gb_3-C24:1 2(S)-OH to facilitate the formation of invaginations in GUVs, the organization of the membrane can be studied. In the fluid lipid mixtures used in the experiments presented above no single Gb_3 molecules can be resolved in fluorescence and atomic force microscopy (AFM). Therefore the membrane organization was studied in the well established 'raft-like' lipid mixture DOPC/sphingomyelin (SM)/cholesterol 40:40:20 on mica support which offers sufficient contrast between the lipid phases.[86] Replacing 5 mol% of sphingomyelin by Gb_3 retains the lateral organization of the solid supported membranes (SSMs).[70,86] The techniques enable to study how the configuration of the 2-hydroxy group of Gb_3 changes the lateral organization of the lipid phases.

Membranes were prepared above the phase separation temperature (see Section 3.2.2) and cooled to room temperature. The lateral organization is visualized by the selective partition of the bulky fluorophors Bodipy-PC and TexasRed DHPE (see Figure3.4A/B) into the liquid-disordered (l_d) phase which is enriched in the fluid phospholipid DOPC (see Figure 4.24). The more ordered liquid-ordered (l_o) phase enriched in sphingomyelin, cholesterol and presumably Gb_3, excludes Bodipy-PC.

Gb_3-C24:1 2(R)-OH containing membranes prior to STxB binding

Figure 4.34A shows a phase-separated membrane composed of DOPC/SM/Chol/Gb_3-C24:1 2(R)-OH 40:35:20:5 doped with 0.1 mol% TexasRed DHPE and 0.5 mol% perylene (see Figure 4.5). As expected the membrane segregates into a l_d and the dark l_o phase. No further substructures of the phases are visible from the zoom (Figure 4.34B). By pixel analysis the total area percentage of the l_o phase was determined to 61 ± 14 % (n = 168). AFM was used to resolve structures below the resolution limit of the optical microscope and to determine the topography of the samples.
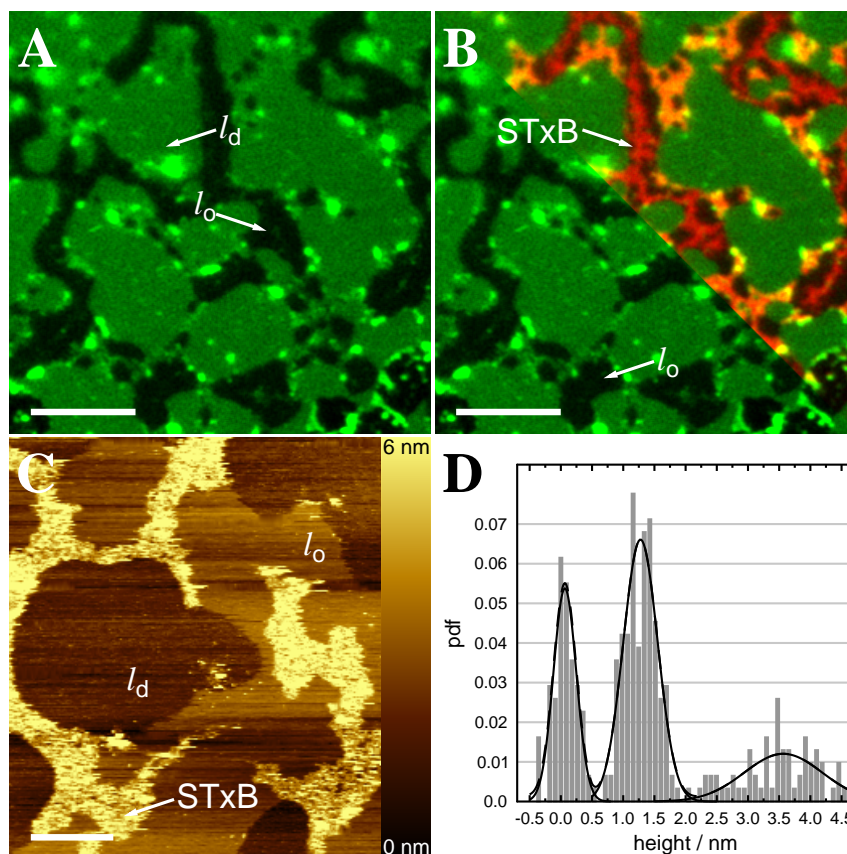
Figure 4.34: Solid supported membranes (DOPC/SM/Chol/Gb$_3$-C24:1 2(R)-OH, 40:35:20:5) doped with perylene (0.5 mol%) and Bodipy-PC (0.1 mol%) on mica. **A** Fluorescence micrograph of Bodipy-PC (false colored in green). Fluorophore partition identifies the liquid-ordered (l_o, dark) and liquid-disordered phase (l_d, green). Scale bar: 20 µm. **B** Magnified view of the region marked in **A**. Scale bar: 5 µm. **C** Topographic AFM image showing a higher l_o phase (lighter color coding) and a lower l_d phase (dark color coding). Scale bar: 5 µm. **D** Histogram analysis of a region in **C** showing a height difference of $\Delta h(l_o/l_d) = 1.1 \pm 0.3$ nm. Image reproduced from Schütte *et al.* 2015.[87]

Including cholesterol in the membrane leads to a thickening of the membrane. This effect that was observed in the RIfS measurements, allowing to identify the l_o domains by their increased height compared to the surrounding l_d phase. Figure 4.34C depicts the topography of a Gb$_3$-C24:1 2(R)-OH containing membrane. The l_o phase (lighter color coding) is elevated above the l_d phase by 0.7 ± 0.2 nm (n = 51).

Gb$_3$-C24:1 2(S)-OH containing membranes prior to STxB binding

Membranes composed of DOPC/SM/Chol/Gb$_3$-C24:1 2(S)-OH 40:35:20:5 doped with 0.1 mol% Bodipy-PC or TexasRed DHPE and 0.5 mol% perylene (see Figure

4.35) show similar features as their (R) counterpart. The l_o phase accounts for $62\pm14\,\%$ (n$\,=\,$87) of the total membrane area. l_o domains are elevated by $\Delta h(l_o/l_d) = 1.3 \pm 0.5\,\text{nm}$ (n$\,=\,$44). The height difference is larger than expected but compares well to the value found for Gb$_3$-C24:1 (see Section 4.1.3).[70,86]
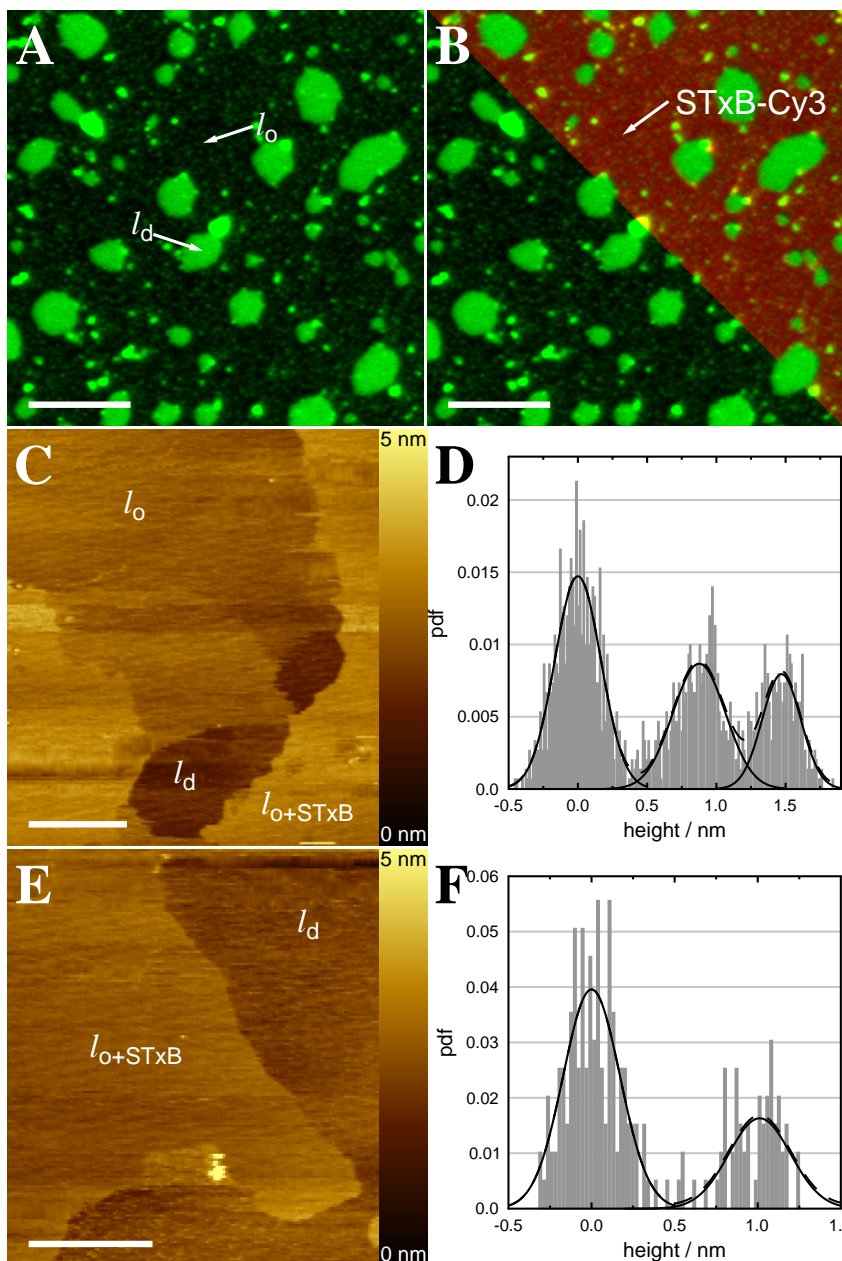

Figure 4.35: Solid supported membranes (DOPC/SM/Chol/Gb$_3$-C24:1 2(S)-OH, 40:35:20:5) doped with perylene (0.5 mol%) and Bodipy-PC (0.1 mol%) on mica. **A** Fluorescence micrograph of Bodipy-PC (false colored in green). Fluorophore partition identifies the liquid-ordered (l_o, dark) and liquid-disordered phase (l_d, green). Scale bar: 10 µm. **B** Magnified view of the region marked in **A**. Scale bar: 5 µm. **C** Topographic AFM image showing a higher l_o phase (lighter color coding) and a lower l_d phase (dark color coding). Scale bar: 5 µm. **D** Histogram analysis of a region in **C** showing a height difference of $\Delta h(l_o/l_d) = 1.2 \pm 0.7\,\text{nm}$. Image reproduced from Schütte *et al.* 2015.[87]

From the data obtained by AFM and fluorescence microscopy before incubation with STxB no clear explanation explaining the deviation in the capability to form invaginations of both Gb$_3$ species is apparent. Table 4.13 summarizes the results obtained prior to protein binding.

Table 4.13: Percentage of the l_o phase determined by pixel analysis of fluorescence images and height difference to the l_d phase as determined from AFM images for membranes containing Gb$_3$-C24:1 2(R)-OH or Gb$_3$-C24:1 2(S)-OH. Number of analyzed images and height histograms is given in brackets. Membranes are composed of DOPC/SM/Chol/Gb$_3$ 40:35:20:5 on mica.

Gb$_3$-C24:1	l_o–STxB / %	$\Delta h(l_o/l_d)$–STxB / nm
2(S)OH	62±14 (87)	1.3±0.5 (44)
2(R)OH	61±14 (168)	0.7±0.2 (51)

4.2.3.4 Lateral membrane and STxB organization after STxB binding

Membranes composed of DOPC/SM/Chol/Gb$_3$ 40:35:20:5 doped with with 0.1 mol% Bodipy-PC or TexasRed DHPE and 0.5 mol% perylene were incubated with 60 nM STxB or STxB-Cy3 to study the lateral organization of STxB on the membrane and its impact on the lipid phase behavior.

Gb$_3$-C24:1 2(R)-OH containing membranes after STxB binding

Figure 4.36A shows a membrane containing 5 mol% Gb$_3$-C24:1 2(R)-OH after incubation with 60 nM STxB-Cy3. Separation into a bright l_d and a darker l_o phase is retained. The percentage of the liquid-ordered phase increases by 6 % to 67±13 % (n = 83) consistent with other Gb$_3$ derivatives bearing an α-hydroxylated fatty acid.[86] No further obvious change in the lipid organization upon STxB binding is apparent from the TexasRed DHPE and Bodipy-PC micrographs. Figure 4.36B shows an overlay of the Bodipy-PC and STxB-Cy3 fluorescence. The protein binds to the l_o phase. No Cy3 fluorescence is found on the l_d phase indicating full partition of Gb$_3$-C24:1 2(R)-OH into the l_o phase.

The protein's Cy3 fluorescence is inhomogeneous with bright stripes surrounded by darker areas. This indicates that the protein forms clusters of higher density. AFM (Figure 4.36C) resolves the clusters which elevate $\Delta h(l_{o+STxB\_clusters}/l_{o+STxB}) = 2.0\pm0.6$ nm (n = 15) above the l_o phase. The remaining l_o area is only partially coated by protein (Table 4.14), indicated by a small increase in height between the l_o and l_d phases by 0.6 nm compared to the protein free case. Some of the clusters are located at the boundary to the l_d phase ($\Delta h(l_{o+STxB\_clusters}/l_d) = 2.7\pm1.0$ nm (n = 28)).

Figure 4.36: Solid supported membranes (DOPC/SM/Chol/Gb$_3$-C24:1 2(R)-OH, 40:35:20:5) doped with perylene (0.5 mol%) and Bodipy-PC (0.1 mol%) after incubation with 60 nM STxB-Cy3. **A** Fluorophore partition identifies the liquid-ordered (l_o, dark) and liquid-disordered phase (l_d, green). Scale bar: 7 µm. **B** Fluorescence micrograph of STxB-Cy3 and overlay with **A** (top right). The two lipid phases are retained according to the green Bodipy-PC fluorescence. STxB-Cy3 fluorescence (red) shows that the protein is only bound to the l_o phase. STxB form stripe-like clusters in the membrane. Scale bar: 7 µm. **C** Topographic AFM image showing the l_d phase (dark color coding) and two elevated heights, which are assigned to the l_o phase and hight density STxB clusters. Scale bar: 3 µm. **D** Histogram analysis of a region in **C** showing a height difference of $\Delta h(l_{o+STxB}/l_d) = 1.2 \pm 0.2$ nm and $\Delta h(l_{o+STxB\_clusters}/l_{o+STxB}) = 2.3 \pm 0.8$ nm. Image modified from Schütte *et al.* 2015.[87]

Gb$_3$-C24:1 2(S)-OH containing membranes after STxB binding

Figure 4.37A shows a membrane containing 5 mol% Gb$_3$-C24:1 2(S)-OH after incubation with 60 nM STxB-Cy3. The area percentage of the dark l_o phase increases to 74±11 % (n = 67). With 12 %, the increase is larger than for Gb$_3$-C24:1 2(R)-OH ($\Delta = 6$ %) indicating a stronger lipid rearrangement between the phases. Figure 4.37B shows that the red fluorescence of STxB-Cy3 is located on the l_o phase.

Figure 4.37: Solid supported membranes (DOPC/SM/Chol/Gb$_3$-C24:1 2(S)-OH, 40:35:20:5) doped with perylene (0.5 mol%) and Bodipy-PC (0.1 mol%) after incubation with 60 nM STxB-Cy3. **A** Fluorophore partition identifies the liquid-ordered (l_o, dark) and liquid-disordered phase (l_d, green). Scale bar: 15 µm. **B** Fluorescence micrograph of STxB-Cy3 and overlay with **A** (top right). STxB-Cy3 fluorescence (red) is homogeneous and inverse to the fluorescence of the l_d marker Bodipy-PC. Scale bar: 15 µm. **C** Topographic AFM image showing the dark l_d phase and regions of two different heights assigned to the l_o phase with different protein density. Scale bar: 3 µm. **D** Histogram analysis of a region in **C** with height differences of $\Delta h(l_{o+\text{STxB\_dense}}/l_d) = 1.5 \pm 0.3$ nm and $\Delta h(l_{o\_\text{loose}}/l_d) = 0.9 \pm 0.4$ nm. **E** Topographic AFM image showing the dark l_d phase and protein covered l_o phase. Scale bar: 3 µm. **F** Histogram analysis of a region in **E** with a height difference of $\Delta h(l_{o+\text{STxB\_dense}}/l_d) = 1.0 \pm 0.3$ nm. Image modified from Schütte *et al.* 2015.[87]

The intensity is homogeneously distributed indicating an even distribution of the protein and its Gb_3 receptor. In most AFM images the homogeneous distribution of STxB is confirmed. Only a low increase in height to $\Delta h(l_{o+STxB\_dense}/l_d) = 1.4 \pm 0.5\,nm$ (n = 64) is measured (Figure 4.37C/D). In some topography maps substructures of STxB can be resolved (Figure 4.37E/F, Table 4.14). The low height difference of $\Delta h(l_{o+STxB\_loose}/l_d) = 0.8 \pm 0.1\,nm$ (n = 10) might be caused by a depletion of Gb_3 and STxB in these areas.

Table 4.14 summarizes the results obtained for phase-separated membranes containing Gb_3-C24:1 2(*R*)-OH or Gb_3-C24:1 2(*S*)-OH after incubation with STxB.

Table 4.14: Membranes composed of DOPC/SM/Chol/Gb_3 40:35:20:5 on mica after incubation with STxB containing Gb_3-C24:1 2(*R*)-OH or Gb_3-C24:1 2(*S*)-OH. Percentage of the l_o phase determined by pixel analysis of fluorescence images. Height difference between the different lipid phases and protein structures as determined from AFM images. For Gb_3-C24:1 2(*R*)-OH l_{o+STxB_dense} corresponds to $l_{o+STxB\_clusters}$. Number of analyzed images and height histograms is given in brackets.

Gb_3-C24:1	l_o+STxB/%	$\Delta h(l_{o+STxB\_dense}$ $/l_{o+STxB\_loose})$ / nm	$\Delta h(l_{o+STxB\_dense}$ $/l_d)$ / nm	$\Delta h(l_{o+STxB\_loose}$ $/l_d)$ / nm
2(*S*)OH	74±11 (67)	0.8±0.1 (10)	1.4±0.5(64)	0.8±0.1 (10)
2(*R*)OH	67±13 (83)	2.0±0.6 (15)	2.7±1.0 (28)	1.3±0.6 (19)

4.2.4 Discussion

The experiments described in Section 4.2.3 allow to rationalize the influence of the configuration of the 2-hydroxy group of the fatty acid bound to Gb_3. Results published in literature using ceramides with an (*R*) or (*S*) configuration, have shown differences in the hydrogen bonding network[187] mediating interlipid contacts. Experiments using NMR[152, 182, 183] and the Langmuir film balance[141] found small differences with respect to the membrane organization caused by the hydroxylation in fluid membranes under low surface pressure. These observations support the results obtained by SPR spectroscopy and fluorescence and atomic force microscopy. Only small differences are observed between membranes containing Gb_3-C24:1 2(*S*)-OH or Gb_3-C24:1 2(*R*)-OH . Shiga toxin binding multiple molecules of its receptor Gb_3 induces a lipid compaction.[70, 151] Under these conditions the hydroxylation's configuration becomes a major determinant of the organization of both the membrane and bound protein.

4.2.4.1 Lateral organization of the membrane

Figure 4.38 illustrates a schematic model derived from the data obtained by fluorescence and atomic force microscopy on solid supported membranes. In absence of STxB the overall phase behavior of the membranes is nearly identical for Gb_3-C24:1 2(S)-OH and Gb_3-C24:1 2(R)-OH containing membranes. The percentage of l_o phase is $\approx 60\,\%$. This is $10\,\%$ lower than for the saturated Gb_3-C24:0 presented in Section 4.1.3, indicating an altered partitioning of the lipids between the phases or a lipid condensation in the l_o phase caused by the α-hydroxylation.[70,86,140] Localization of Gb_3 before protein binding is unknown but it is believed to be located in the l_o phase.[70] In case of Gb_3-C24:1 2(S)-OH containing membranes the l_o phase is elevated $1.3\,\text{nm}$ above the l_d phase suggesting that the headgroup of Gb_3 ($h \approx 1.5$-$2.0\,\text{nm}$)[60] contributes to the elevated height further supporting the idea that Gb_3 is located in the l_o phase prior to STxB binding.[188] In the l_o phase the hydroxylation could lead to a lipid condensation,[140] which increases thermostability of the domains, while interactions with cholesterol are impaired.[139] Using monolayers of neat hydroxylated ceramides, Löfgren found differences in the packing ability with regard to the stereochemistry suggesting that interlipid contacts are altered by the hydroxylation.[141] A condensation of the l_o phase seems possible but not likely because the unsaturation of the fatty acid of the derivatives should impair tight packing with saturated sphingomyelin.

Molecular dynamics simulations by Yahi *et al.* show that a (R) hydroxylation forms intramolecular hydrogen bonds to the sugar headgroup of galactocerebrosides leading to a tilting of the headgroup towards the membranes.[143] A similar effect is found for cholesterol.[75,143] This tilting might be less pronounced for Gb_3-C24:1 2(S)-OH explaining the larger height difference of the lipid phases.

Sphingomyelin, cholesterol and Gb_3 only account for $50\,\%$ of the membrane area (see Table 4.8). To account for the l_o area of $\approx 60\,\%$ additionally to sphingomyelin, Gb_3 and cholesterol also DOPC has to be incorporated into the l_o phase. A condensing effect of the hydroxy group might hinder this, expelling the phospholipid to the l_d phase and thus explain the lowered l_d percentage while still explaining the elevated height of l_o phase.

The overall lateral organization of the membrane in absence of bound protein is hardly influenced by the configuration of the 2-hydroxy group of the fatty acid bound to Gb_3.
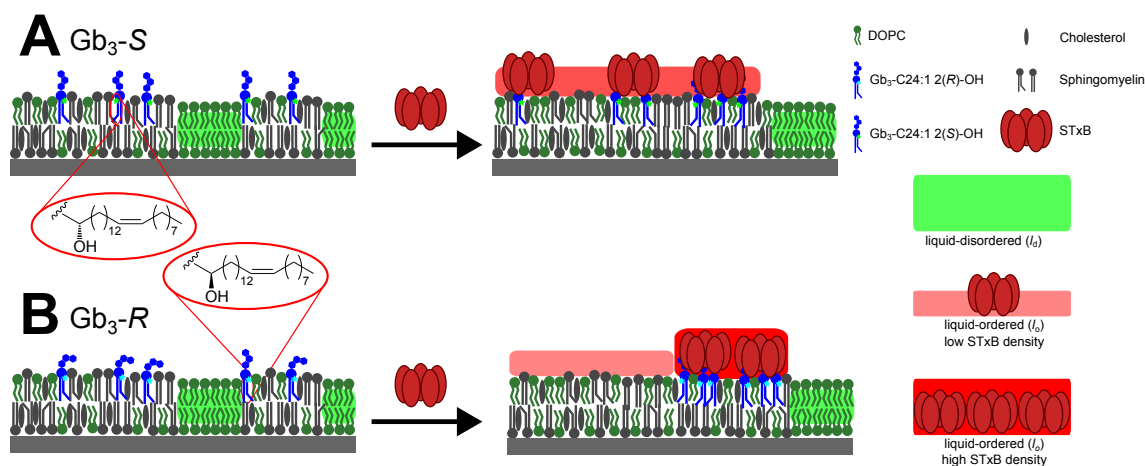
Figure 4.38: Model describing the protein and membrane organization of Gb$_3$-C24:1 2(R)-OH (**A**) and Gb$_3$-C24:1 2(S)-OH (**B**) containing membranes as deduced from fluorescence and atomic force microscopy on mica. Prior to protein binding the lateral organization is similar in both cases. Gb$_3$ is located in the l_o phase after protein binding. Gb$_3$-C24:1 2(R)-OH induces single isolated Gb$_3$ clusters. Gb$_3$-C24:1 2(S)-OH leads to a more homogeneous distribution of the protein on the membrane.

A different picture is found after incubation with STxB. The protein binds to both Gb$_3$ derivatives and the STxB-Cy3 fluorescence shows that the Gb$_3$ is located in the l_o phase. This proofs that despite the unnatural (S) hydroxylation of Gb$_3$-C24:1 2(S)-OH, interlipid interactions are strong enough to retain the phase preference of Gb$_3$ in phase-separated membranes. Following the argumentation of Section 4.1.4, the different protein structures induced are caused by the compressibility of the lipids and their sterical demand.[141] Gb$_3$-C24:1 2(R)-OH is readily condensed underneath the pentameric STxB and can bind with high valency. This leads to a strong lipid compaction inducing line tension, which is the reason for the formation of the high density STxB clusters (Figure 4.36, see Equation 4.3).[72,141] Gb$_3$-C24:1 2(S)-OH packs less densely, leading to a more homogeneous distribution in the membrane upon Shiga toxin binding.

Comparing the area percentages of the l_o phase and heights obtained using AFM to the results summarized in Chapter 4.1, both stereoisomers show an increase in l_o phase upon protein binding which was also found for hydroxylated derivatives Gb$_3$-C24:0 2-OH and the diastereomeric mixture Gb$_3$-C24:1 2(R/S)-OH. The observed increase in l_o percentage upon STxB binding is presumably caused by the additional incorporation of DOPC into the l_o phase. Both Gb$_3$-C24:1 2(R)-

OH and Gb_3-C24:1 2(S)-OH are hybrid lipids bearing a both (Z) unsaturated and an elongated (E) fatty acid. This was previously reported to mediate the contact between the ordered phase and unsaturated DOPC.[189] STxB binding to Gb_3 containing membranes is believed induce membrane ordering.[39,71] This would contradict the relocalization of DOPC into the ordered phase. Solovyeva *et al.* used polarization two-photon fluorescence microscopy to study the texture and long range order of membranes containing Gb_3, exhibiting a gel-liquid phase separation.[132] They found that preformed gel domains show no lipid ordering effect due to STxB binding. The authors reason that the low diffusivity of the lipids in these systems hampers the multivalency of the STxB-Gb_3 interaction. This shows that the local interaction of Gb_3 with the surrounding lipids, which might differ for the diastereomers, the localization before protein binding and the interaction with STxB are of crucial importance for the overall membrane organization.

Compared to the results found for the diastereomeric mixture, Gb_3-C24:1 2(R/S)-OH (see Section 4.1.3), the percentages of the lipid phases found, are slightly decreased indicating a possible error in the concentrations used. However, the AFM results obtained for Gb_3-C24:1 2(R/S)-OH (Table 4.3) are a proper mix of the high and dense Gb_3 clusters found for Gb_3-C24:1 2(R)-OH and the more homogeneous STxB distribution found for Gb_3-C24:1 2(S)-OH.

4.2.4.2 Binding affinity and capacity

The binding affinity and capacity of Gb_3-C24:1 2(R)-OH and Gb_3-C24:1 2(S)-OH containing membranes can be influenced by the lateral distribution of Gb_3 in the membrane after Shiga toxin binding and the accessibility of the headgroup for binding.

Using SPR spectroscopy the affinity of STxB both stereoisomers was found to be identical in DOPC membranes despite possible differences in the headgroup orientation and lateral organization of Gb_3 in the membrane. The same affinity was also determined for the diastereomeric mixture Gb_3-C24:1 2(R/S)-OH (Table 4.1). The found low nanomolar affinities compare well with previously published values using radiolabeling[66,74] or antibody labeling experiments.[75] Pina *et al.* showed that upon STxB binding to Gb_3 the different binding pockets are sequentially occupied by Gb_3 (Figure 4.39B). This suggests that at the relatively high Gb_3 density of $5\,mol\%$, to a certain extent, the initial binding is sufficient to allow additional Gb_3 to adapt its headgroup to the already bound protein.[107] Adding cholesterol decreases the

affinity for both isomers consistent with the idea that cholesterol is able to further burrow the Gb_3 headgroup in the membrane.[75]

The decrease in affinity caused by cholesterol is accompanied by an increase in binding capacity as determined by RIfS. In contrast to the membranes used for SPR measurements, membranes used for RIfS are bilayers offering full lateral mobility.[185] Due to the tilting of the headgroup towards the membrane Gb_3 is not instantly clustered underneath the protein but free to diffuse in the membrane leading to a more homogeneous Gb_3 distribution. This leads to more STxB able to bind, resulting in the observed higher surface coverage. This reasoning also explains the decreased binding capacity of Gb_3-C24:1 $2(R)$-OH as it is more prone to form high valency protein lipid clusters as presented in the AFM data. In literature the influence of cholesterol on the Shiga toxin binding is discussed controversially. Nakajima *et al.* found an increase in binding capacity upon addition of cholesterol using SPR spectroscopy on hybrid bilayers and immobilized vesicles, Lingwood and coworkers reported a drop of binding capacity larger than 50 % and an unchanged affinity using a biosensing system based on carbon electrode surfaces.[75, 107] While Lingwood uses a similar cholesterol:Gb_3 ratio as in this thesis, the overall cholesterol content in the membrane was only 5 %. This indicates that both the organization and dynamics of the receptor in the membrane strongly influence the results obtained by different techniques.

No information on the lateral organization of Gb_3 in pure DOPC or DOPC/Chol membranes is available. It is possible that Gb_3 forms transient nanoaggregates due to specific sugar-sugar interactions.[143] Nanodomains would create areas of receptor ligand concentrations, which binding STxB with high affinity.[156, 158, 159] Cholesterol is known to facilitate the formation of nanodomains but also changes the carbohydrate headgroup orientation complicating its effect on protein binding. In 2012 Sachl et al. used fluorescently labeled G_{M1} glycosphingolipids to determine their lateral organization in nanodomains by fluorescence correlation spectroscopy and fluorescence antibunching.[154] They found that the glycosphingolipids indeed form nanoclusters and dense G_{M1} packing lowers the binding of G_{M1}'s natural binding partner CTxB. Interestingly cholesterol decreases binding at low G_{M1} concentrations but this effect ceases at receptor concentrations higher 4 mol%. Their results clearly show that nanoscale dynamics and subtle lipid-lipid interactions influence the glycosphingolipid-protein binding. Similar studies using STxB/Gb_3 are currently hampered by the lack of fluorescently labeled Gb_3 derivatives.

4.2.4.3 Formation of invaginations in freestanding membranes

Figure 4.39 shows the derived model for protein binding and the formation of invaginations of membranes containing Gb$_3$-C24:1 2(S)-OH and Gb$_3$-C24:1 2(R)-OH. The latter forms clusters with high Gb$_3$ content due to its good compressibility and strong lipid-lipid interactions.
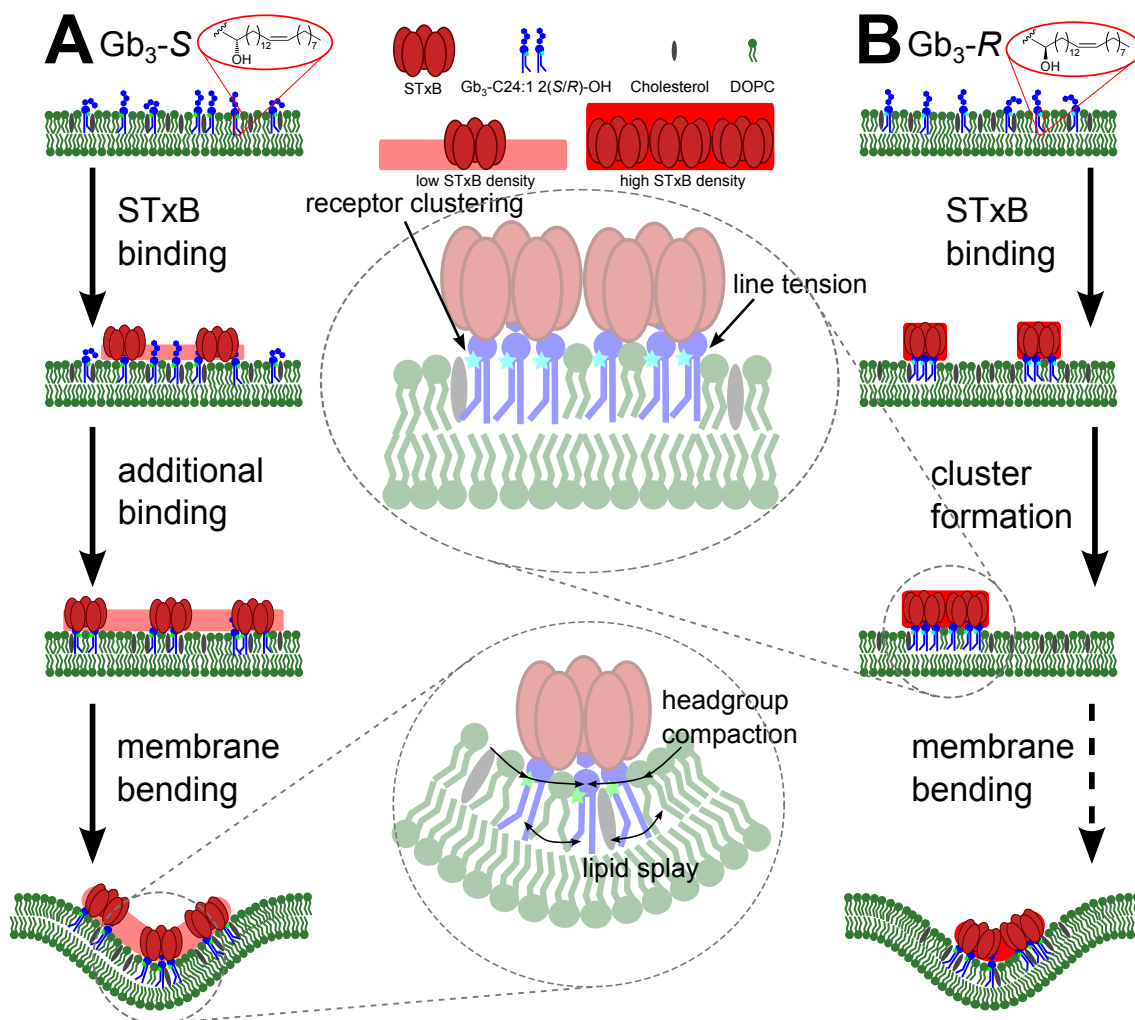
Figure 4.39: Model describing the mode of action of STxB on membranes of GUVs containing Gb$_3$-C24:1 2(S)-OH (**A**) and Gb$_3$-C24:1 2(R)-OH (**B**). **A** STxB binds to Gb$_3$-C24:1 2(S)-OH with high binding capacity. Membrane bending is induced by headgroup compaction and is further stabilized by the lipid splay of unsaturated lipids. **B** Gb$_3$-C24:1 2(R)-OH is more prone to cluster receptor lipids leading to a tight packing which impedes bending. Image reproduced from Schütte *et al.* 2015.[87]

These structures facilitate the formation of invaginations to a less extent than the (S) counterpart. Gb$_3$-C24:1 2(S)-OH allows for a more homogeneous mode of binding with higher binding capacity. Due to the lipids underneath the protein it readily

facilitates the formation of invaginations. Differences between the stereoisomers might be explained using these different structures of the STxB-Gb_3 aggregate. Tubes formed by STxB are enriched in sphingomyelin and Gb_3 but also contain other lipids which might help to facilitate the process of membrane bending.

In 2010 Ewers, Römer *et al.* published a theory on the energies involved in protein cluster formation and invaginations in lipid membranes. Starting from a planar membrane, the overall energy change upon formation of a membrane tube (Δe) can be divided into three contributions. The contribution of deformation (Δe_{deform}) depends on the mechanical properties of the membrane. Changes in membrane composition (Δe_{comp}) effect the entropy of the system and the adhesion energy of the particle (Δe_{adhe}) depends on the 3D structure of the membrane.[72]

$$\Delta e = \Delta e_{\text{adhe}} + \Delta e_{\text{comp}} + \Delta e_{\text{deform}} \tag{4.1}$$

For viral capsides, where the radius of the formed membrane tube is similar to the size of the particle, the adhesion energy dominates the other terms due to the three dimensional arrangement of the membrane around the particle. This is not the case for bacterial proteins like Shiga toxin because the contact area per monomer is the same in the tube and on the flat membrane ($\Delta e_{\text{adhe}} = 0$).[72]

In the first step after binding, the protein starts to aggregate on the flat membrane. This process is controlled by the trade off between line tension (μ) induced by the lipid compaction ($\mu \approx 0.1\,k_{\text{B}}T\ \text{nm}^{-1}$) and the entropic cost of demixing. Aggregation of N circular proteins with radius a reduces the circumference of the aggregate by $\sqrt{N}$ resulting in an energy difference (ΔF_{N}) for flat domains (E_{domain}) compared to the dispersed monomers on the membrane (E_{monomers}).[72]

$$\Delta F_{\text{N}} = E_{\text{domain}} - E_{\text{monomers}} \tag{4.2}$$
$$= 2\pi\mu a\sqrt{N} - N\left(2\pi\mu a + k_{\text{B}}T\log\phi\right) \tag{4.3}$$

At $\Delta F_N = 0$ one can calculate the minimum nucleation size N_{c} which is dependent of the surface coverage ϕ.[72]

$$N_{\text{c}} = \left(\frac{\pi\mu a}{2\pi\mu a + k_{\text{B}}T\log\phi}\right)^2 \tag{4.4}$$

The critical concentration needed for the formation of clusters is $\phi_1^* = e^{-2\pi\mu a/k_{\text{B}}T}$. The value is below $5\,\%$ and also below the surface coverages used in the experiments shown in Section 4.2.3 (see Table 4.12 and 4.14).

Line tension is not sufficient to induce tubes with high curvature.[72] To extend the equations to the formation of tubes one needs to take the mechanical properties of the membrane into account. Bending of the membrane is dependent on the bending modulus $\kappa \approx 20\, k_\mathrm{B}T$ for fluid membranes.[72] Spontaneous curvature is not taken into account in this theory.

Tubule formation requires an additional term for membrane tension of $\gamma\pi a^2$ per monomer (surface tension $\gamma \approx 10^{-6} - 10^{-3}\,\mathrm{J\,m^2}$). Formation of the tube removes surface area from the GUV to the inside, impeding thermal undulation. This results in an energy E_neck including E_domain from Equation 4.3 and the additional mechanical forces present at the neck. The energy needed for forming a tubular domain is:

$$\Delta F_N = E_\mathrm{neck} - E_\mathrm{monomers} \tag{4.5}$$
$$= 2\pi a\sqrt{N}\left(\mu + \sqrt{\kappa\gamma}/2\right) - N\left(2\pi\mu a - \pi a^2\gamma + k_\mathrm{B}T\log\phi\right). \tag{4.6}$$

The critical concentration for tubule formation ($\phi_1^* = e^{\pi(\gamma a^2 - 2\mu a)/k_\mathrm{B}T}$) in this case also depends on the membrane tension γ. Tensions $\gamma > 2\mu/a \approx 10^{-4}\,\mathrm{J\,m^{-2}}$ inhibit the deformation at the neck. This explains the lack of invaginations at hyperosmotic conditions (see Section 4.2.3.1) which increases membrane tension of the GUV membrane. Lowering or reversing the osmotic gradient reduces tension and allows for the formation of invaginations.[72]

From Equation 4.6 it becomes clear that the process is dependent on the local bending rigidity of the STxB-Gb$_3$ aggregate (κ), the curvature H and the spontaneous curvature of the lipids (c_0).

$$E_\mathrm{bending} = \frac{1}{2}\kappa\left(2H - c_0\right)^2 \tag{4.7}$$

Tubules and protein clusters are observed for both stereoisomers. More clusters are observed for Gb$_3$-C24:1 2(R)-OH containing membranes showing that either the line tension is larger or that the process stops before bending the membrane. The single 2-hydroxylation does not explain differences in the bending rigidity. Differences observed are instead a variation of the bending rigidity of the STxB lipid aggregate which is composed of Gb$_3$, STxB and the surrounding membrane lipids. Römer *et al.* found that membranes composed of DOPC and cholesterol doped with saturated Gb$_3$-C22:0 are not forming invaginations. This effect is explained by the findings of Watkins *et al.* using x-ray reflectivity and Pezeshkian *et al.* using molecular dynamics simulations, indicating that saturated Gb$_3$ forms rigid,

non bending aggregates which interdigitate into the opposing leaflet this further rigidifying the bilayer.[148,151,168,177] High density STxB clusters were also observed for Gb$_3$-C24:0 further supporting the hypothesis. Unsaturated Gb$_3$-C22:1 forms less rigid structures and invaginations in GUVs are observed.[71] The lipid splay of the (*Z*) stabilizes the negative curvature induced by headgroup compaction (Figure 4.39).

Both isomers used in this work are unsaturated and show invaginations. According to NMR studies the influence of the hydroxylation on the neighboring membrane lipids is small independent of the configuration.[152,182] A change in rigidity due to the hydroxyl group therefore seems negligible. It is more plausible to assume that the local membrane composition underneath the STxB clusters might play an important role. Unsaturated Gb$_3$-C24:1 and Gb$_3$-C24:1 2(*S*)-OH have a similar mode of binding in the form of a homogeneous coverage of the membrane.[86] The presumably lower valency of STxB in these cases might allow for the incorporation of more cholesterol and DOPC into the protein-lipid-aggregate to stabilize the induced negative curvature.[178] Using FRET experiments Sachl *et al.* could show that in absence of proteins bound to the membrane, a lipid mixture of DOPC, cholesterol and G$_{M1}$ forms glycolipid clusters including a high content of phospholipid and cholesterol.[154]

Mechanical properties of the membrane which govern the formation of invaginations are determined by the individual contributions of the membrane components. The spontaneous curvature c_0 of a lipid mixture is additive.[178] Due to the large headgroup and the sphingosine backbone Gb$_3$ is expected to induce positive curvature which is overcome by the headgroup compaction upon STxB binding. DOPC and cholesterol favor negative curvature.[178] According to Equation 4.7 the integration of both lipids in the STxB-Gb$_3$ aggregate should facilitate to bend the membrane. Cholesterol was reported to increase the bending rigidity κ but the effect is not present in membranes composed of the doubly unsaturated lipid DOPC.[179,186] These membranes have a several times lower rigidity compared to eggSM/Chol membranes suggesting that the incorporation of DOPC and cholesterol in the lipid aggregate lowers the overall energy required for bending.[179] Changing the matrix phospholipid to 1-palmitoyl-2-oleoyl-*sn*-glycero-3-phosphocholine (POPC) might drastically alter the process. POPC is known to favor nanoscopic lipid domains due to reduced line tension[31,32,77,160] possibly altering the STxB organization Induction of membrane

invaginations might also be influenced because the interaction of POPC and cholesterol in the STxB-lipid aggregate might stiffen the membrane inhibiting membrane invaginations.[134,179,186]

Arnaud *et al.* used artificially engineered neolectins to show that both multivalent binding and the position of the binding pockets influence the ability to induce invaginations in lipid membranes.[123,190] Using molecular dynamics simulations of the structurally closely related Cholera toxin bound to its receptor G_{M1}, Basu *et al.* found that dynamic unbinding of the receptor lipid leading to a lower occupancy of the bindings sites might also be favorable for the induction of curvature.[191] Local lipid organization underneath the protein seems to be of greater importance than the sheer number of bound receptor molecules.

These results and considerations show that the capability of Gb_3-C24:1 2(R)-OH and Gb_3-C24:1 2(S)-OH to facilitate the formation of membrane invaginations is influenced by a variety of different factors. Differences in the local lipid-lipid interaction translate to a changes in lateral organization of Gb_3. The organization influences the bindings capacity towards STxB and leads to the formation of different STxB structures on the membrane. These structures differ in protein density and this influences the mechanical properties of the membrane.

4.2.5 Conclusion

The fatty acid of Gb_3 was previously shown to alter the membrane organization and the binding of Shiga toxin. Data presented in this Section extends the view on the mechanism even further. For the first time the influence of the stereochemistry of a α-hydroxylation of a glycolipid on its receptor function and membrane organization was studied. The organization of the membrane is hardly effected by the configuration. While the binding affinity towards Shiga toxin is unaffected, the binding capacity differs. The lateral organization of bound Shiga toxin strongly varies between both diastereomers and the bound fatty acid shifts the balance between high density protein clusters and loose protein structures. Organization of STxB on the membrane has a major contribution to the induction of negative curvature in the membrane.

4.3 Summary of the lateral organization of solid supported membranes

Shiga toxin binding to biological membranes by its receptor Gb_3 alters the membrane organization which is the first step of the toxin's endocytosis.[39, 54, 71] Solid supported membranes of the raft like mixture DOPC/SM/Chol 40:40:20 were doped with $5 \, mol\%$ of the STxB receptor lipid Gb_3. The impact of five Gb_3 derivatives (Scheme 3.7) bearing different fatty acids, on the lateral organization of the membrane was investigated by fluorescence and atomic force microscopy. The models, based on the more detailed discussions in Section 4.1.4 and 4.2.4, for the lateral organization in absence and presence of bound STxB are presented in Figure 4.40.
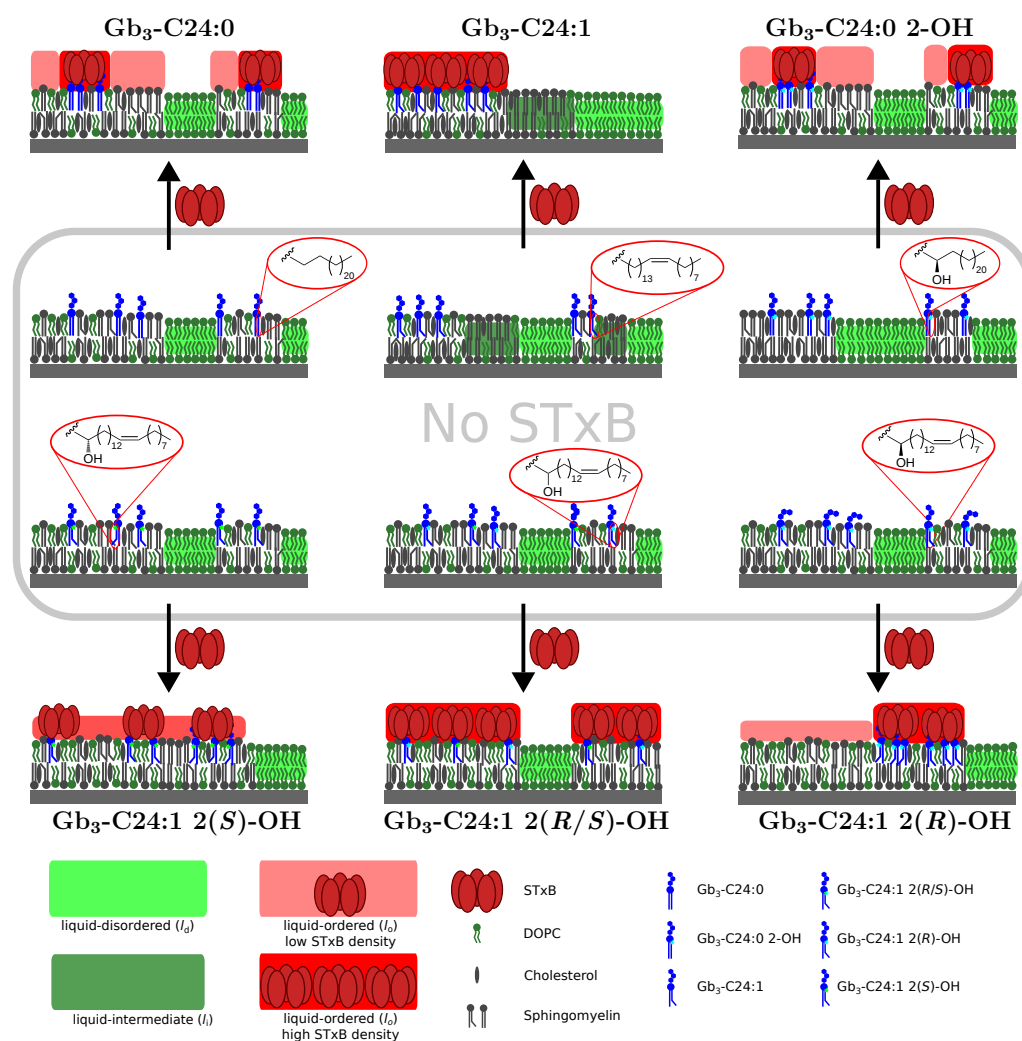
Figure 4.40: Protein and membrane organization of phase-separated membranes containing different Gb_3 derivatives. A detailed description is given in the text. For reasons of simplicity Gb_3 has been omitted in the bottom leaflet.

Membranes doped with the saturated Gb_3-C24:0 show a similar phase behavior as membranes without the glycolipid. Gb_3 derivatives with a α-hydroxylated fatty acid showed slightly reduced l_o area percentages. This and the fact that the drop in l_o area is more pronounced for the saturated, α-hydroxylated Gb_3 compared to unsaturated, α-hydroxylated derivatives, indicates that the hydroxylation can condense the lipids in the l_o phase and exclude any unsaturated phospholipid from the ordered phase. This reordering of the l_o phase is even more distinct for the unsaturated derivative Gb_3-C24:1, which induces a further segregation of the l_o phase into two phases of differing molecular order, as identified by atomic force microscopy and the partition of a phase selective fluorescent dye.

Incubation of membranes with STxB had vastly different effects despite similar nanomolar affinities to the protein. Three major effects were observed. Lipids were redistributed within and between the lipid phases and the lateral structures formed by STxB on the membrane differed.

STxB binding to membranes containing Gb_3-C24:0 does not change the l_o area percentage. This indicates that the glycosphingolipid is localized in the l_o phase and Shiga toxin simply binds to the exposed receptor. However, atomic force microscopy revealed that the multivalent binding of STxB clusters the receptor, forming tightly packed protein-lipid aggregates within the l_o phase. A similar segregation of the receptor was found for the hydroxylated Gb_3-C24:0 2-OH and Gb_3-C24:1 2(R)-OH. Additionally to this interphase lipid redistribution, the amount of l_o area increased for all four hydroxylated Gb_3s studied (Gb_3-C24:0 2-OH, Gb_3-C24:1 2(R/S)-OH, Gb_3-C24:1 2(S)-OH, Gb_3-C24:1 2(S)-OH). Comparing the found l_o areas to published values for the area per molecule leads to the conclusion that upon STxB binding lipids from the l_d phase are relocated to the more ordered phase. In case of the diastereomeric mixture Gb_3-C24:1 2(R/S)-OH large areas of high density STxB were observed by atomic force microscopy. This mode of binding could be dissected into the individual contributions of both stereoisomers. Gb_3-C24:1 2(R)-OH allows for high density STxB binding, while Gb_3-C24:1 2(S)-OH induces a more homogeneous mode of binding. The latter was also found for unsaturated Gb_3-C24:1. In this case STxB binding does not lead to inter- or intraphase lipid rearrangement but a homogeneously covered l_o phase.

These findings show that the fatty acid bound to Gb_3 considerably modulates the organization of the membrane both in absence and presence of bound STxB. The complex lateral structures alter the mode of binding of the protein, indicating that the derivatives serve different biological functions regarding the process of Shiga toxin endocytosis.

5 Structure and dynamics of pore-spanning lipid membranes

5.1 Abstract

Pore-spanning lipid bilayers (PSLBs) are a suitable system to model processes occurring at the plasma membrane *in vitro*. They combine the advantages of solid supported and freestanding membranes and act as a minimal model system for the effect of the actin cytoskeleton on the lateral organization and dynamics of phase-separated membranes. Scanning ion-conductance microscopy was employed to study the topography of the membranes which was found to be nearly flat with small, highly curved areas at the border between the freestanding and solid supported part. Lateral organization of the membrane was probed by fluorescence microscopy. The membranes obtained from spreading of phase-separated giant unilamellar vesicles formed dispersed, small liquid-ordered and liquid-disordered domains of distinct chemical composition. Contact of domains to the solid support leads to a pinning at the pore rim. Domains in the pore center freely diffuse inside a single pore-spanning membrane. A model was developed to describe the motion of the domains. Shiga toxin binding to the PSLBs does not alter the membrane topography but the lateral organization of the membrane is heavily modulated. Protein binding induces the formation of distinct STxB clusters as well as a redistribution of lipids between the phases and the solid supported and freestanding membrane areas.
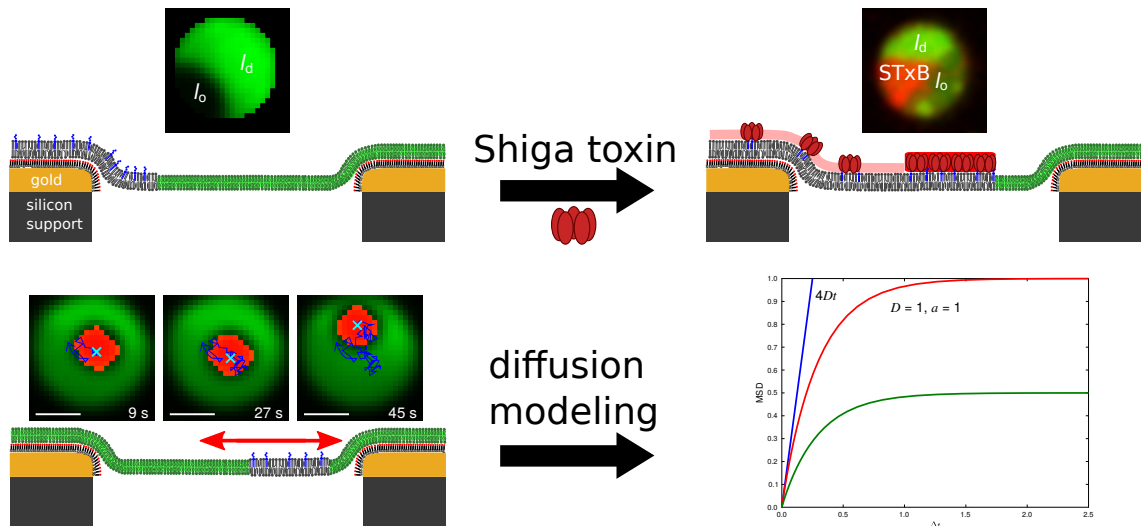
Figure 5.1: Scheme illustrating the free movement of lipid domains and Shiga toxin binding to pore-spanning lipid bilayers.

5.2 Introduction

The model of the plasma membrane developed by Singer and Nicolson in the 1970s[2] has evolved, as new experimental techniques showed a more complex picture of the lateral organization of the membrane.[3,8,10] The sheer number of different lipid species present in the membrane, hints to their functional role in cellular processes like endocytosis and signaling.[3,4] The outer leaflet is enriched in sphingomyelin (SM), cholesterol and glycosphingolipids (GSLs).[1,3] New techniques like high speed single particle tracking[16] and super-resolution optical microscopy[13,14] revealed a lateral heterogeneity of the membrane. Both proteins and lipids form short lived, highly dynamic nanoscopic aggregates which serve as platforms e.g. for signaling.[10] Simons and coworkers introduced the term 'lipid raft' to describe the clustering of cholesterol with (glyco-)sphingolipids (Figure 5.2).[8,11]
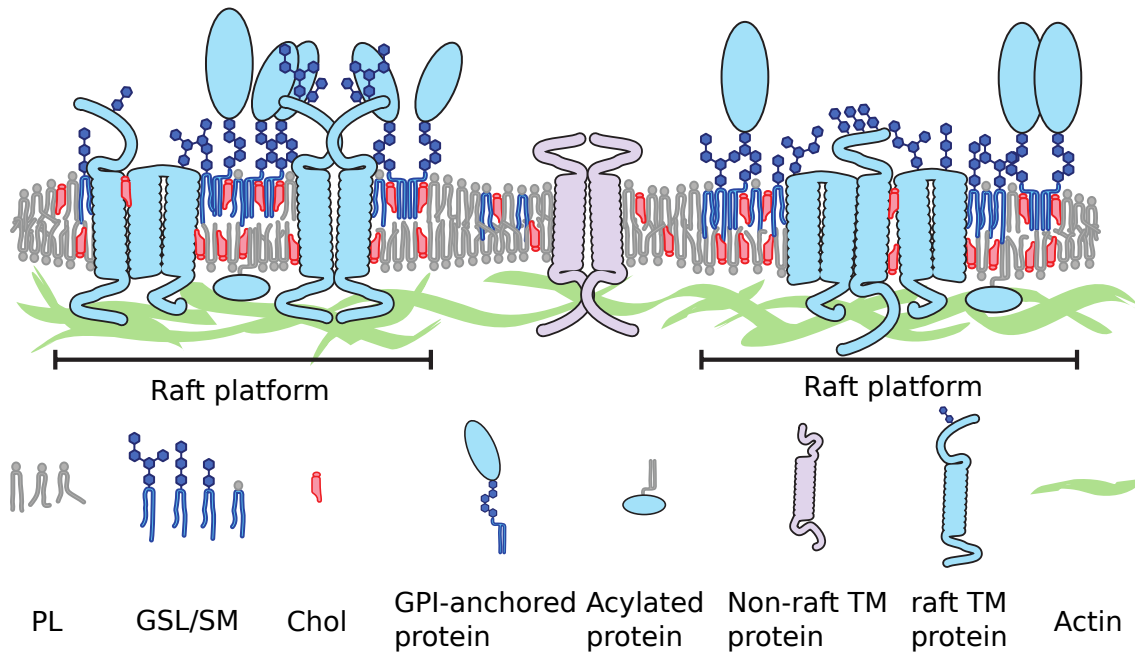
Figure 5.2: Schematic organization of the plasma membrane according to Lingwood *et al.*.[11] Membranes segregate into different compartments composed either of phospholipids (PL) or cholesterol, SM and GSLs. The compartments differ in their affinity to transmembrane (TM) and anchored proteins. The compartmentalization is influenced by the underlying actin mesh. Image modified from Lingwood *et al.*.[11]

The different membrane compartments are selectively enriched in certain proteins forming signaling platforms.[10] They differ in their hydrophobic thickness, membrane order and fluidity.[3,8,36,192,193] Direct observation of rafts has been proven difficult and most approaches rely on monitoring the diffusion of lipid probes in the membrane. Kusumi *et al.* used high speed particle tracking of labeled lipids and proteins to determine their diffusion in the plasma membrane. They found a similar compartmentalization of the membrane into distinct regions.[16,17] Analyzing the trajectories of the particles led to the conclusion that the actin mesh has a major influence in changing the dynamics of the membrane (Figure 5.3). The cytoskeleton forms the mechanical support of the cell. Dynamic polymerization of actin occurs near the plasma membrane, forming filaments (F-actin) close to the inner leaflet of the plasma membrane. F-actin fulfills different roles in processes like cell movement and endocytosis and is linked to the membrane by proteins.[18] Cross-linking of actin bundles forms a mesh below the membrane.[1]
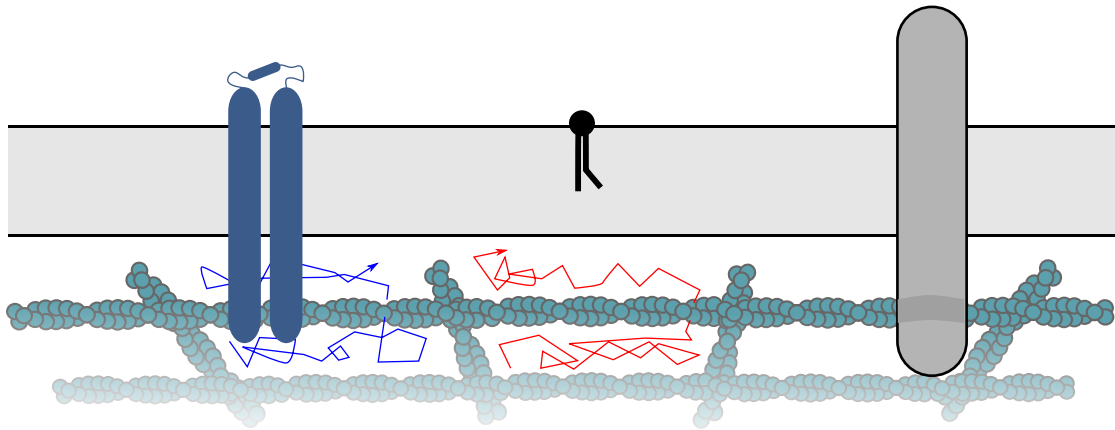
Figure 5.3: A Scheme of the picket-fence model of the plasma membrane according to Kusumi *et al.*.[16] Proteins (blue) and lipids (black) are moving within the compartments defined by the cytoskeleton. They rarely 'hop' from on compartment to another. The protein on the right (gray) is pinned to actin as it acts as a picket.

Using several biochemical approaches, Kusumi proved that the diffusion of lipids and proteins in the membrane is correlated with the size and position of the actin mesh, which serves as a second membrane ordering effect like the putative rafts. Analyzing the diffusion trajectories, they found that i) lipids and proteins are free to diffuse inside a compartment and that the 'hopping' event of a particle diffusing into the next compartment is rarely observed, ii) membrane components like transmembrane proteins are linked to the actin mesh and are fully immobilized. They can act as a picket in the membrane altering the diffusion of other membrane components. The picket-fence model therefore has two mechanisms of controlling the diffusion in the membrane: direct immobilization of particles and the confinement in distinct areas.

Work by Eggeling and coworkers, using spot variation STED fluorescence correlation spectroscopy (FCS) and different lipid anchored fluorescent probes, linked the idea of lipid domains and the actin influence.[14] The authors proved that both effects lead to different types of anomalous diffusion of the lipids in the membrane, which can be readily distinguished by FCS. Notably, they found the anomalous diffusion for the raft component sphingomyelin but the non-raft lipid phosphatidylethanolamine showed unaffected diffusion.

As rafts are difficult to observe in cells, tremendous efforts have been made to understand their properties using artificial membrane systems.[3] Extraction of the plasma membrane lipids using cold detergent and the generation of giant plasma

membrane vesicles (GPMVs) directly link the complex biological membrane to simplified models systems.[21,192] GPMVs allow to transfer the lipid material of the plasma membrane into a giant vesicle and enable studies of the membrane organization in absence of the cellular protein machinery.[192] Several studies found that the membranes form large macroscopic domains below room temperature. In cells these large domains are not found but experiments suggest that small, highly fluctuating domains, that are influenced by the cytoskeleton, are present.[22–26]

Macroscopic phase separation observed in artificial membrane systems composed of a fluid phospholipid, sphingomyelin and cholesterol resembles the structures formed in GPMVs and ramps up the chemical differences between the lipid phases.[29,30] The liquid-disordered (l_d) phase surrounds cholesterol enriched liquid domains of higher order (l_o). The model systems based on this 'raft-like' mixture have been widely employed to study protein binding,[71] physical properties of the membrane[39,179,194] and their dynamics.[195,196] Lipids and domains freely diffuse in the membrane and their motion can be described by approaches like the Saffman-Delbrück model.[197–199] To further augment the artificial membrane systems the lateral organization of the membrane needs to be controlled in an actin mesh like fashion. Spreading of phase-separated giant unilamellar vesicles on porous substrate allows to create micrometer sized, freestanding membrane areas surrounded by solid support.[43,45,51,200] The role of the putative rafts as receptor enriched signaling platforms, can be modeled by introducing the glycosphingolipid Gb_3 in the membrane. It is the naturally occurring receptor for Shiga toxin (STx).[54,71] Binding of the B-subunit of the protein (STxB) to the membrane leads to a clustering of the receptor lipid and a dynamic reorganization of the membrane.[72,134] Pore-spanning lipid bilayers are a superior tool to monitor this first step of the toxin's endocytosis as they offer a controlled lipid composition, small dispersed domains, like in the cell, while retaining the high lipid mobility needed for large scale membrane reorganization.

5.3 Results

Spreading of phase-separated giant unilamellar vesicles on porous support is used to create a model system, mimicking the plasma membrane and the underlying cytoskeleton. Using fluorescence microscopy the organization of the membrane can be studied.

5.3.1 Phase separation of giant unilamellar vesicles

Phase-separated giant unilamellar vesicles were produced by electroformation as described in Section 3.2.1. The vesicles were composed of the phospholipid DOPC, sphingomyelin, cholesterol and the Shiga toxin receptor lipid globotriaosylceramide (Gb_3) in a molar ratio of 40:35:20:5. In this chapter, Gb_3 from porcine erythrocytes (Gb_3-Porc) bearing different fatty acids was used (Section 3.1.3).

Figure 5.4A shows a fluorescence confocal slice of a GUV. The phase separation at room temperature into l_d and l_o domains was visualized by the enrichment of a lipid coupled fluorophor in the disordered phase. The bright green regions correspond to l_d domains. Darker regions on the circumference correspond to the l_o phase excluding the fluorophor.
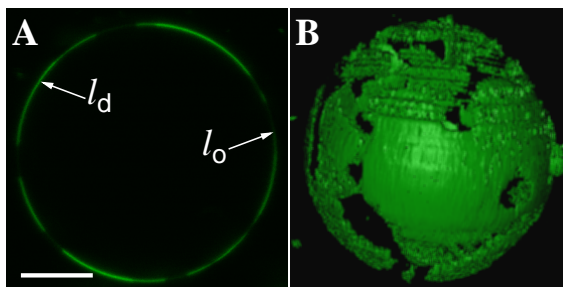
Figure 5.4: Fluorescence micrographs of a phase-separated GUV composed of DOPC/SM/Chol/Gb_3-Porc 40:35:20:5 doped with 0.5 mol% of TexasRed DHPE (false colored in green). **A** Confocal slice imaged at the equatorial position of the GUV. Bright green fluorescence depicts the enrichment of TexasRed in the l_d phase. Dark regions along the circular circumference correspond to l_o domains. Scale bar 10 µm. **B** 3D reconstruction of a z-stack of the GUV shown in **A**.

In panel B a 3D reconstruction of the GUV is shown. The l_d phase forms large domains with diameters of several micrometers on the surface of the GUV.[42, 136] Due to the large size of the GUV (diameter ≈ 40 µm) the surface can be considered as fully flat on the molecular level.

Determination of the l_o percentage in GUVs

To understand the phase behavior of the lipid membrane, area percentages of the l_d and l_o phase were quantified as described in Section 3.4.1. Briefly, z-stacks of inflated GUVs were separated into two half spheres. Each was projected onto a plane using an orthographic azimuthal projection. The resulting projections were thresholded. To correct for the area distortion of the projection the appropriate weighting

function was employed. Figure 5.5 shows the projection of a GUV composed of DOPC/SM/Chol/Gb$_3$-Porc (40:35:20:5) doped with $0.5 \, \text{mol}\%$ TexasRed DHPE.
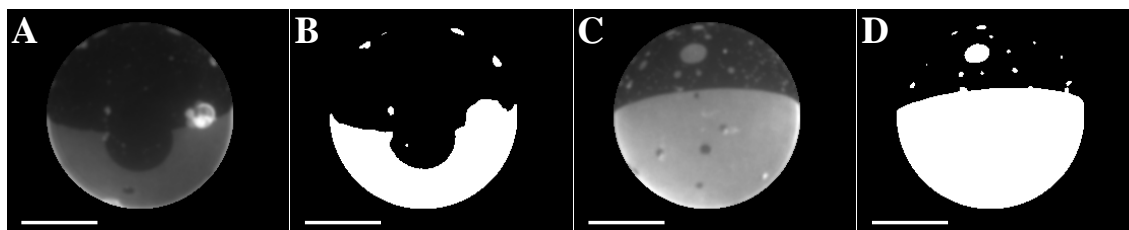
Figure 5.5: Orthographic projections and thresholded images showing the l_d phase of a vesicle composed of DOPC/SM/Chol/Gb$_3$-Porc (40:35:20:5) doped with $0.5 \, \text{mol}\%$ TexasRed DHPE, imaged under hyperosmotic conditions in PBS. **A** Projection of the bottom cap of the GUV. The l_d phase is identified by the stronger fluorescence intensity. **B** Thresholded image of **A**. White areas correspond to the l_d phase. **C** Projection of the upper cap of the GUV. Identification of the l_d phase by the stronger fluorescence intensity is possible. **B** Thresholded image of **C**. Scale bars: $10 \, \mu\text{m}$.

The projections presented in Figure 5.5A/C were manually thresholded. Pixel analysis of the thresholded images compared to the total area of the projection yielded the l_o phase percentage which was corrected for the area distortion of the projection.

Analysis of 112 GUVs with a mean diameter of $15 \pm 9 \, \mu\text{m}$ gave a l_o percentage of $36 \pm 10 \, \%$ in good agreement with values reported in literature.[37,115] As the distribution of the lipid domains in a non adhering GUV is random, the correction for the area distortion did not alter the l_o percentage compared to the uncorrected case. Three different lipid dyes (Bodipy-PC, Atto488 DHPE, TexasRed DHPE) were employed and the percentage was found to be independent of the dye used.

Shiga toxin binding to Gb$_3$ containing GUVs

STxB binding to Gb$_3$ is known to alter the membrane organization.[70,71,86,134] The area of the l_o phase of the GUVs after STxB binding was quantified. GUVs were incubated with STxB or Cy3-labeled STxB (STxB-Cy3) at a final concentration of $60 \, \text{nM}$. Figure 5.6 shows the projections of a GUV after STxB-Cy3 incubation for $1 \, \text{h}$.
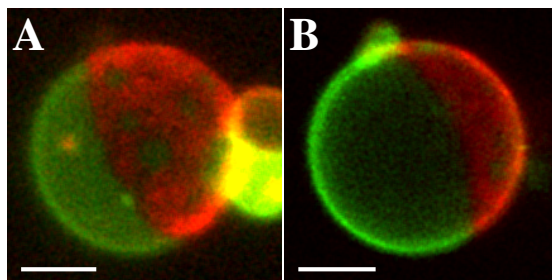
Figure 5.6: Orthographic projections of a GUV composed of DOPC/SM/Chol/Gb$_3$-Porc (40:35:20:5) doped with 0.5 mol% Bodipy-PC imaged under hyperosmotic conditions in PBS after incubation with STxB-Cy3. **A** Projection of the bottom cap of the GUV. The l_d phase is identified by the stronger green Bodipy fluorescence intensity. The l_o phase is stained red by STxB-Cy3 binding to Gb$_3$-Porc. In the right part several adhered vesicles are imaged. **B** Projection of the upper cap of the GUV. Scale bars: 10 μm.

The red fluorescence shows that STxB binds to Gb$_3$-Porc in the giant vesicles. The fluorescence signal of STxB-Cy3 is only located on the l_o domain.[70] l_d domains can again be identified by the fluorescence of the l_d marker dye.

To elucidate if STxB binding changes the lateral organization by lipid redistribution between the phases, the area percentage of the l_o phase was determined by thresholding fluorescence micrographs of the l_d marker dye. Figure 5.7 shows an exemplary GUV after STxB binding.
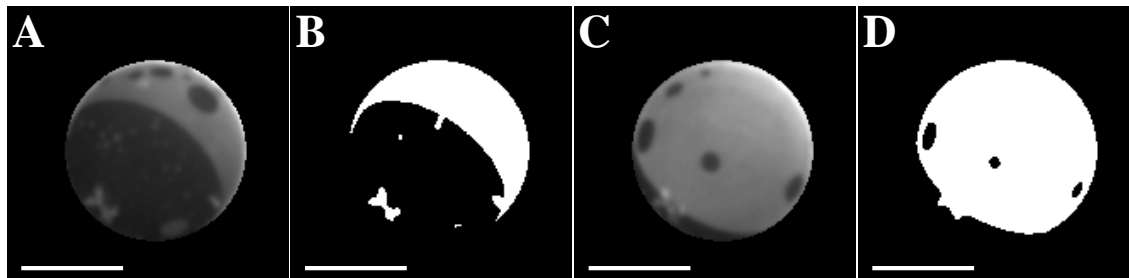
Figure 5.7: Orthographic projections and thresholded images showing the l_d phase of a vesicle composed of DOPC/SM/Chol/Gb$_3$-Porc (40:35:20:5) doped with 0.5 mol% TexasRed DHPE, imaged under hyperosmotic conditions in PBS after incubation with STxB-Cy3. **A** Projection of the bottom cap of the GUV. The l_d phase is identified by the stronger fluorescence intensity. **B** Thresholded image of **A**. The white areas correspond to the l_d phase. **C** Projection of the upper cap of the GUV. The l_d phase is identified by the stronger fluorescence intensity of the l_d marker dye TexasRed DHPE. **B** Thresholded image of **C**. Some small domains were not properly detected during thresholding. Scale bars: 8 μm.

The analysis of 99 GUVs with a mean diameter of $14 \pm 6\,\mu m$ gave a l_o percentage of $34 \pm 12\,\%$. Three different lipid dyes (Bodipy-PC, Atto488 DHPE, TexasRed DHPE) were used and the percentage was found to be independent of the dye.

Determination of l_o area percentage after spreading of GUVs

To test whether a solid support has an influence on the phase separation, GUVs were spread on silicon dioxide wafers above the phase transition temperature as described in Section 3.4.1. Figure 5.8 shows characteristic fluorescence micrographs obtained after spreading.
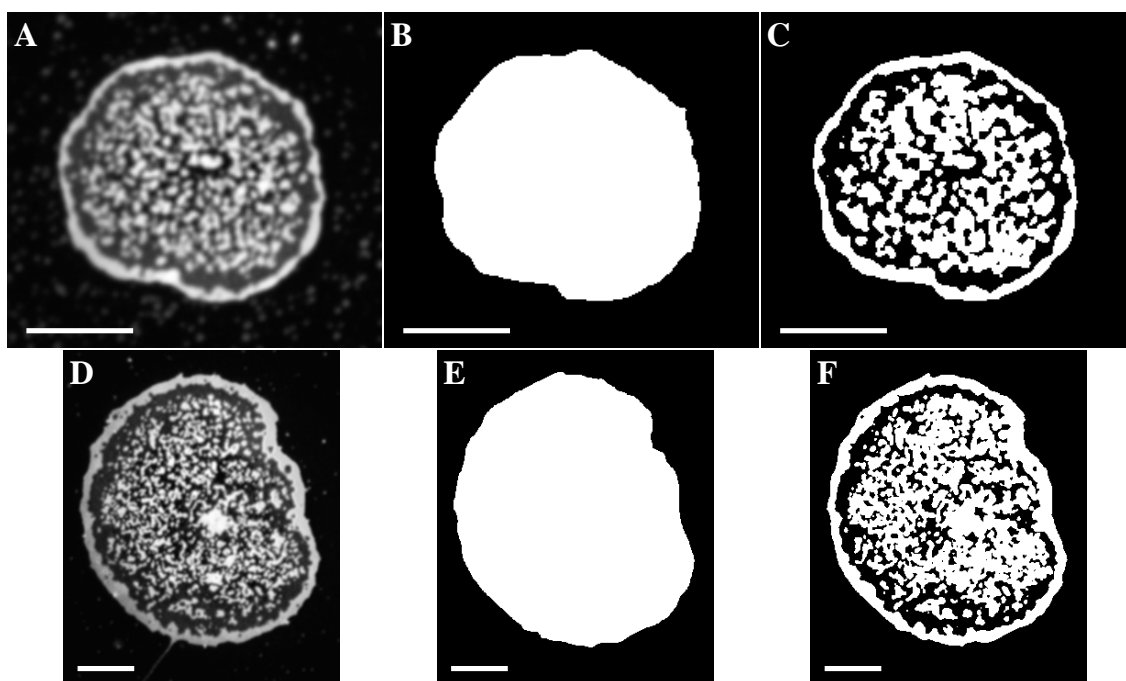
Figure 5.8: Fluorescence micrographs of phase-separated GUVs composed of DOPC/SM/Chol/Gb$_3$-Porc (40:35:20:5) doped with 0.5 mol% TexasRed DHPE spread on silicon dioxide wafers. Top row: Imaged prior to protein binding. Bottom row: Imaged after incubation with STxB. **A/D** Fluorescence micrographs of TexasRed show the two different lipids phases. **B/E** Total areas of the membrane patches. **C/F** Regions identified as the l_d phase. Scale bars: 10 μm.

The substrate is not fully covered with membrane but isolated patches that correspond to the lipid material of single GUVs are found.[45, 201] The total area of the patch was determined and compared to the area of the l_d phase obtained from thresholding the fluorescence micrographs. The total area was used to calculate the diameter of the GUV that was spread on the surface. In absence of bound STxB

the l_o percentage was determined to be $38 \pm 11\,\%$ (n $= 22$). After STxB binding the area percentage was $38 \pm 8\,\%$ (n $= 21$), showing that the areas of the phases are the same as in the GUV.

Table 5.1 summarizes the results obtained for the l_o percentages in GUVs. Correction for the area distortion did not alter the l_o percentage compared to the uncorrected case.

Table 5.1: Summary of the l_o area percentages determined in GUVs and in membranes obtained from GUV spreading. For the latter the radius was calculated from the area of the obtained membrane patch.

		% l_o phase	GUV diameter / μm	n
GUVs	–STxB	36±10	15±9	112
	+STxB	34±12	14±6	99
spread	–STxB	38±11	12±4	22
GUVs	+STxB	38±8	16±6	21

Binding of STxB to the membrane lead to no alteration of the l_o phase percentage. This indicates that no major rearrangement of lipid between the phases took place.

5.3.2 Lipid domains in pore-spanning lipid membranes

To study the influence of a porous support on phase-separated membranes, silicon based substrates with different geometries were used (see Section 3.2.3). Pore size was varied between a diameter of 0.8 to 5.5 μm. Substrates with porosities between 14 and 41 % were employed to shift the ratio between freestanding and supported membrane areas. Two different pore lattices were used. Pores $d = 0.8\text{-}2.0$ μm are arranged in a regular hexagonal lattice whereas larger pores with diameters of 3.5, 4.5 and 5.5 μm have a square array.

Structure of pore-spanning lipid membranes
Pore-spanning lipid bilayers (PSLBs) were produced as described in Section 3.2.3. Briefly, phase-separated giant unilamellar vesicles (GUVs) were heated above the phase-transition temperature of the lipid mixture of $\approx 40\,°C^{30}$ and spread on hydrophilically functionalized gold-covered porous substrates. Membranes were subsequently cooled to room temperature.
Figure 5.9 shows fluorescence micrographs of pore-spanning membranes composed of

DOPC/SM/Chol/Gb$_3$-Porc 40:35:20:5 doped with 0.5 mol% perylene and 0.5 mol% Bodipy-PC.
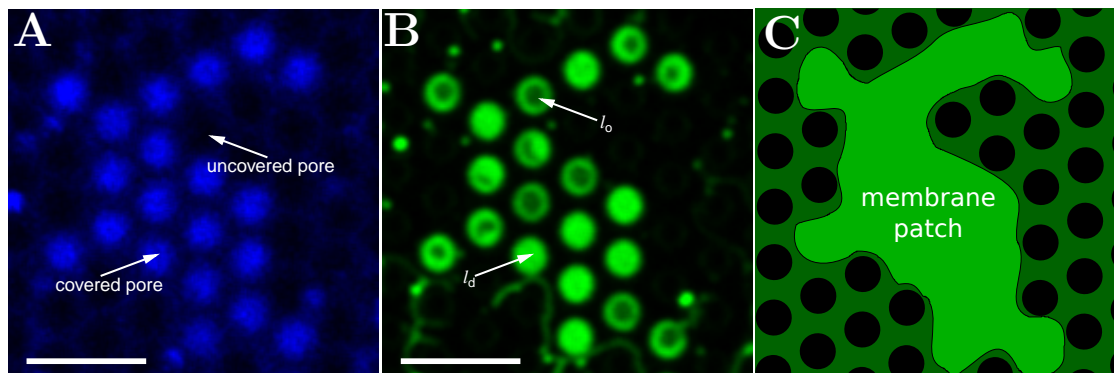
Figure 5.9: Fluorescence micrographs of pore-spanning lipid bilayers composed of DOPC/SM/Chol/Gb$_3$-Porc 40:35:20:5 doped with 0.5 mol% perylene and 0.5 mol% Bodipy-PC. **A** Perylene fluorescence false colored in blue shows bright circular region which correspond to covered pores as fluorescence on the rim is quenched by the underlying gold layer. **B** Bodipy-PC fluorescence is solely visible on the membrane covered regions identified in **A**. The brightness distribution is not homogeneous and two brightness levels are apparent. Darker regions can be assigned to the l_o phase. Brighter region correspond to the l_d phase. Fluorescence on the rims is quenched and no information on the phase behavior can be extracted. Pore diameter: 1.2 μm. Scale bars: 4 μm. **C** Scheme showing a proposed structure of the membrane patch produced by spreading of a single GUV.

Panel A illustrates the fluorescence signal of the non phase specific dye perylene. Blue circular areas of high intensity correspond to membrane spanned pores. The distribution of the signal shows the hexagonal lattice structure of the porous support. No fluorescence signal is observed on the pore rims due to quenching by the underlying gold layer.[45, 202] Opposed to the nearly full area coverage obtained by spreading small vesicles on a solid support, the spreading of GUVs on porous substrates does not lead to a full coverage of the substrate. Only isolated membrane patches are obtained, which correspond to the lipid material of a single GUV rupturing on the surface (Figure 5.9C).[45, 201] The fluorescence signal of Bodipy-PC in the freestanding areas is inhomogeneous. Two brightness levels are found and can be assigned to the bright l_d and the dye excluding, dark l_o phase. Dark l_o areas are easily identified as membranes by the perylene fluorescence at these positions. The residual intensity of the phase selective dye in the l_o phase was found to be sufficient to confirm membrane integrity and perylene use was omitted in most experiments. No information on the lateral organization of the membrane on the

rim regions can be extracted due to the quenching of the fluorescence by the gold functionalization. Using confocal imaging, the area of brightest intensity was always found to be in the plane of the substrate's surface. This indicates that all pore-spanning membranes on all types of substrates are flat (see Section 5.3.5). The pores-spanning membranes are connected by a continuous bilayer on the pore rims as previously determined from FRAP experiments.[52,53]

Characterization of the lateral membrane organization

An analysis strategy, treating each membrane spanned pore individually, was developed to characterize the phase behavior in the freestanding membrane parts (Section 3.4.2). Analysis was conducted considering two aspects of the phase separation. i) The percentage of l_o area in the freestanding membrane area was quantified by pixel analysis (Figure 5.10A). ii) Position and shape of the domains were investigated. Four different types of domains are distinguished.[51,52] The pore can be fully covered with the l_d or l_o phase (Figure 5.10B/C). If both a l_o and a l_d domain are present in the pore the l_o domain might be localized in the pore center (Figure 5.10D) or at the pore rim (Figure 5.10E).
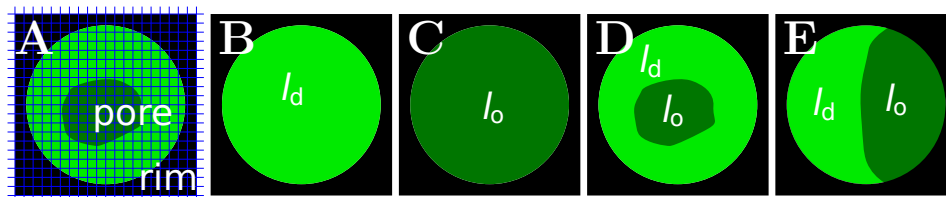
Figure 5.10: Evaluation of lipid domains in pore-spanning membranes. **A** Pixel raster defined by the resolution of the microscope. **B** A l_o domain in the center of the pore surrounded by l_d area. **C** A l_o domain in contact with the pore rim. **D** The pore is fully covered by an l_d domain. **E** Reverse case where the pore is fully covered by an l_o domain.

Six different porous substrates were investigated. The pore size was varied between 0.8 and 3.5 µm. Porosities, meaning the ratio of freestanding membrane to the total area, was varied between 14 and 41 % (Section 3.2.3). In this chapter the terms pore-spanning lipid bilayer (PSLB) and pore-spanning membrane (PSM) are used to describe individually spanned pores and not the full membrane patch.

Phase separation of pore-spanning membranes with diameters of 0.8, 1.2 and 2.0 µm

Figure 5.11 to 5.13 show characteristic fluorescence micrographs of l_o domains

on substrates with different pore diameters of 0.8, 1.2 and 2.0 µm. The scale was chosen identical for all images to allow for a direct comparison of the domain and pore sizes. Analysis of 4363 individual pore-spanning membranes in 82 membrane patches was used to determine the influence of the pore size and porosity of the porous support on the lateral phase separation.

Figure 5.11 depicts a membrane on a support with a pore diameter of 0.8 µm. Bright spots correspond to l_d domains whereas the darker green fluorescence indicates a l_o domain. In most cases (84 %) a single domain (l_d or l_o) covers the whole pore and can be assigned to the type of domain shown in Figure 5.10B/C. Using pixel analysis, the area percentage of l_o phase on the freestanding membrane regions was found to be 30 ± 13 %.
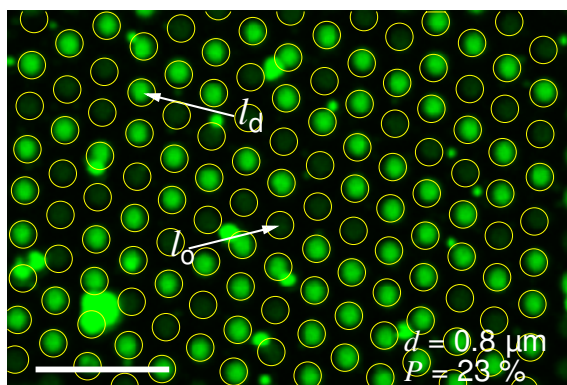
Figure 5.11: Fluorescence micrograph showing the phase separation of a membrane prepared on a porous substrate with pore diameters of 0.8 µm. Yellow circles illustrate the hexagonal porous mesh. Membrane is composed of DOPC/SM/Chol/Gb$_3$-Porc 40:35:20:5 doped with 0.5 % Bodipy-PC. The pores are mostly covered by a single domain. No uncovered pores are present in the image. Scale bar: 5 µm.

In Figure 5.12 a membrane patch on a porous mesh with a pore diameter of 1.2 µm is shown. In the top part dozens of pores are covered and most of them exhibit a separation into l_o and l_d side by side. In the bottom part the pores are not spanned, resulting in the dark area.
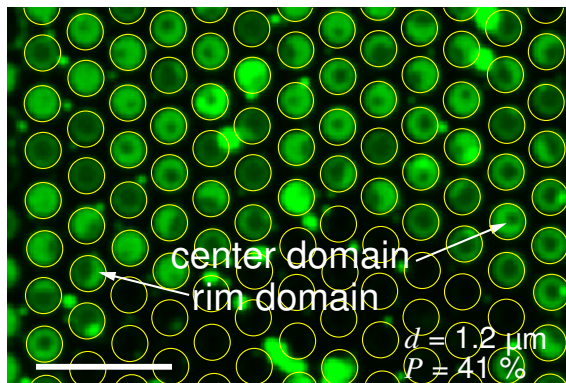
Figure 5.12: Fluorescence micrograph showing the phase separation of a membrane prepared on a porous substrate with pore diameters of $1.2\,\mu m$. Yellow circles illustrate the hexagonal porous mesh. Membrane is composed of DOPC/SM/Chol/Gb$_3$-Porc 40:35:20:5 doped with $0.5\,\%$ Bodipy-PC. On $d = 1.2\,\mu m$ pores more pore-spanning membranes contain both phases in parallel. Uncovered pores are visible at the bottom of the image. Scale bar: $5\,\mu m$.

Various sizes and positions of the l_o domains are found. Some domains are located in the center of the PSM and have no contact to the rim as schematically shown in Figure 5.10B. However, they account only for a minor fraction ($10\,\%$) of the total spanned pores investigated. These domains were found to move within the pore-spanning membrane and their dynamics are described in more detail in Section 5.3.4. $58\,\%$ of the pore-spanning membranes only show either a single l_o or l_d domain that covers the whole pore. Some l_o domains are in contact to the pore border. These domains are static, do not move and are found in $32\,\%$ of the total pore-spanning membranes (Figure 5.10B). The porosity of the substrates with pore diameters of $1.2\,\mu m$ is $41\,\%$ and therefore higher than on substrates with $0.8\,\mu m$ pores ($P = 23\,\%$). This change in the ratio of solid supported and freestanding membrane areas could influence the distribution of lipids between these two distinct compartments. The percentage of l_o area is $20 \pm 11\,\%$ of the total freestanding membrane area and therefore lower compared to the membranes prepared on substrates with a pore diameter of $0.8\,\mu m$ and lower porosity.

Figure 5.13 shows a membrane preapred on a porous mesh with pore diameters of $2.0\,\mu m$ and a porosity of $41\,\%$. Most of the lipid domains are located at the rim of the pore-spanning membrane and adopt a bud like shape.
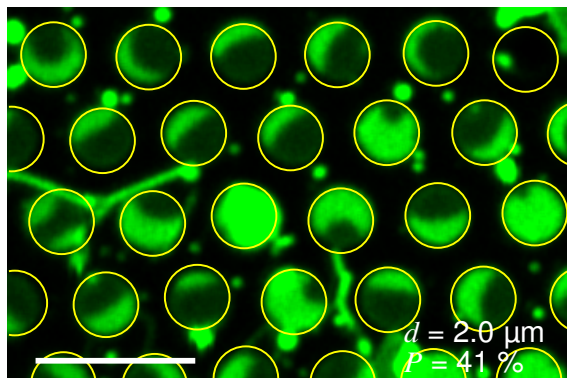
Figure 5.13: Fluorescence micrograph showing the phase separation of a membrane prepared on a porous substrate with pore diameters of 2.0 µm. Yellow circles illustrate the hexagonal porous mesh. Membrane is composed of DOPC/SM/Chol/Gb$_3$-Porc 40:35:20:5 doped with 0.5 % Bodipy-PC. On $d = 2.0$ µm pores usually only a single l_o domain is present in each pore-spanning membrane and most of the pores show both l_o and l_d domains. The bright spots on the rim correspond to adhered vesicles. Scale bar: 5 µm.

The overall phase behavior is similar compared to that of membranes prepared on porous substrates with pore diameters of 0.8 and 1.2 µm. The percentage of l_o phase is 30 ± 13 % of the total freestanding membrane area, indicating that this value is not influenced by the pore size. Most pore-spanning membranes exhibit a separation into l_o and l_d domains. The trend observed for PSMs with a diameter of 0.8 and 1.2 µm, that a larger pore-spanning membrane has a higher probability to contain both phases side by side is continued. In 8 % of the membrane spanned pores the l_o domain is located in the center. 61 % of the PSMs show a l_o domain in contact to the pore border. Single domains covering the whole pore are even less frequent (31 %).

Phase separation of membranes with diameters of 3.5 µm

On the substrates with pore diameters of 0.8, 1.2 and 2.0 µm there is a clear relation between the individual pore-spanning membrane and the lipid domains. Only a single l_o domain was found in each PSM and the domains could be classified according to Figure 5.10. Membranes spanned over pores with pore diameters of 3.5 µm were used to test whether this also holds true in even larger PSLBs. Substrates with three porosities (39, 28 and 14 %) were used to study if the ratio of solid supported to freestanding membrane area has an influence on the phase separation.

Figure 5.14 shows fluorescence micrographs of phase-separated membranes prepared on substrates with pore diameters of 3.5 µm and porosities of 39, 28 and 14 %. Membrane composition is DOPC/SM/Chol/Gb$_3$-Porc 40:35:20:5. The scale was chosen identical for all images to allow a direct comparison of the domain and pore sizes with Figures 5.11 to 5.13.
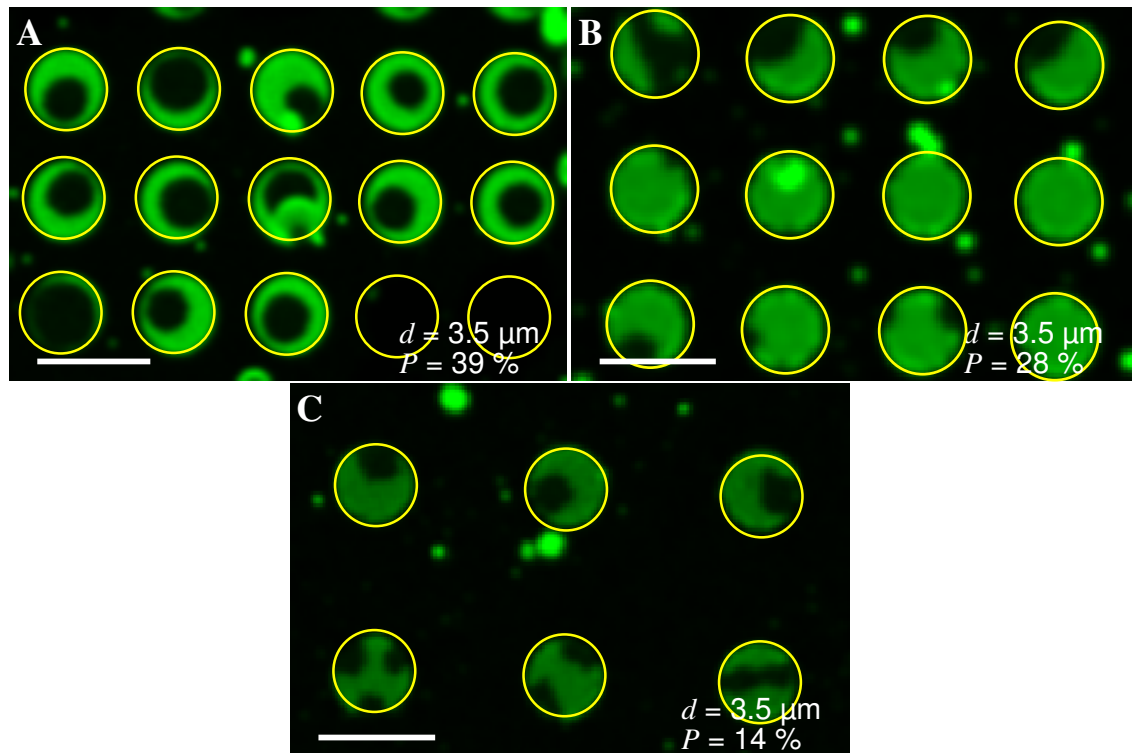
Figure 5.14: Fluorescence micrographs showing the phase separation of membranes prepared on different porous substrates with pore diameters of 3.5 µm. Yellow circles illustrate the square porous mesh. The membranes are composed of DOPC/SM/Chol/Gb$_3$-Porc 40:35:20:5 doped with 0.5 % TexasRed. In contrast to pores with diameters of 0.8, 1.2 and 2.0 µm, frequently multiple l_o domains are found in a single pore. **A** Both domains in contact with the pore rim and freely moving domain are observed. **B/C** The shape of the domain was sometimes found to be irregular and multiple l_o domain occur in a single pore. Scale bars: 5 µm.

Whereas in Figure 5.14A only one domain is found in each pore-spanning membrane, panel B and C show that also multiple domains can occur in a pore. The l_o domains are linked to the pore rim at multiple positions (panel C, bottom left). In most cases the morphology of the domains still adopts circular shapes but also irregular morphologies as in panel C are observed. A total of 90 % of the pore-spanning membranes show l_o and l_d domains side by side. Only in 10 % of the cases a single

domain is fully covering a pore. Domains in the center of a PSM are only observed if a single domain is present. The dynamics of the domains presented in Section 5.3.4, explain this finding, as multiple, moving domains can condense (see Figure 5.26 and Figure 5.27). The structure of the domains was found to be the same independent of the porosity, indicating that the pore size is the deciding factor for the domain morphology.

Three types of substrates with pores with diameters of 3.5 μm were used. In all three cases the pores are arranged in a square lattice but the porosity is different. This allows to investigate if a change in porosity, meaning a change of the ratio of freestanding to solid supported membrane area, alters the percentage of liquid-ordered phase observed in the PSLBs.

On substrates with a porosity of 39 % an area percentage of the l_o phase of 28 ± 13 % was found. Substrates with 3.5 μm pores with lower porosities of 28 and 14 % showed an increased l_o percentage of 49 ± 17 % and 55 ± 10 %. This indicates an influence of the surface porosity on the l_o area percentage which is discussed in Section 5.4.3 Table 5.2 summarizes the results obtained for membranes prepared on all porous substrates used. Four different lipid dyes (Bodipy-PC, OregonGreen, Atto488 DHPE, TexasRed DHPE) were used and the results were found to be independent of the dye.

Table 5.2: Table summarizing the phase separation of pore-spanning membranes composed of DOPC/SM/Chol/Gb$_3$-Porc 40:35:20:5 on different porous supports. On larger pores a higher percentage of pore-spanning membranes containing both a l_o and l_d phase is found.

d / μm	P / %	Area percentage %l_o / %	fraction of pores l_o+l_d pores / %	pores	patches
0.8	23	30±13	16	1531	21
1.2	41	20±11	32	1391	35
2.0	41	30±13	61	1441	26
3.5	39	28±13	88	391	27
3.5	28	49±17	90	219	17
3.5	14	55±10	82	153	8

5.3.3 STxB binding to lipid domain in pore-spanning lipid membranes

The last section showed that using pores with different diameters influences the morphology of domains in phase-separated pore-spanning membranes. Shiga toxin

binding to its receptor lipid Gb_3 is known to alter the lipid organization in artificial membranes,[70,71,86,134] and living cells.[39,71] Binding of STxB to pore-spanning membranes allows to visualize the protein and membrane organization in a dynamic, two dimensional model system. Phase-separated pore-spanning lipid bilayers were prepared by spreading GUVs composed of DOPC/SM/Chol/Gb_3-Porc 40:35:20:5 on hydrophilically functionalized porous substrates. After spreading, the samples were incubated with STxB or Cy3-labeled STxB for one hour at a concentration of 60 nM at room temperature.

Figure 5.15 shows fluorescence micrographs of a membrane composed of DOPC/SM/Chol/Gb_3-Porc 40:35:20:5 doped with 0.5 mol% of Bodipy-PC after incubation with 60 nM STxB-Cy3 for 1 h. From the Bodipy-PC fluorescence in panel A it is apparent that the separation into l_d and l_o domains is retained. However the abundance of l_o domains is increased (*vide infra*).
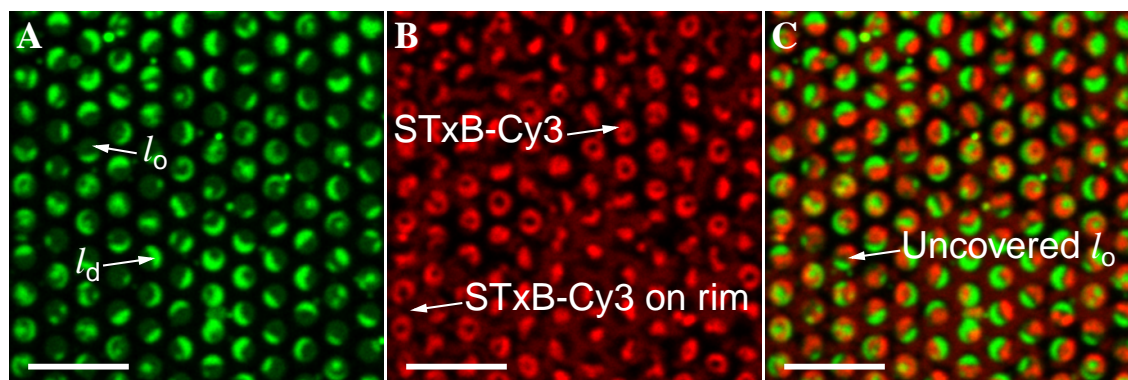
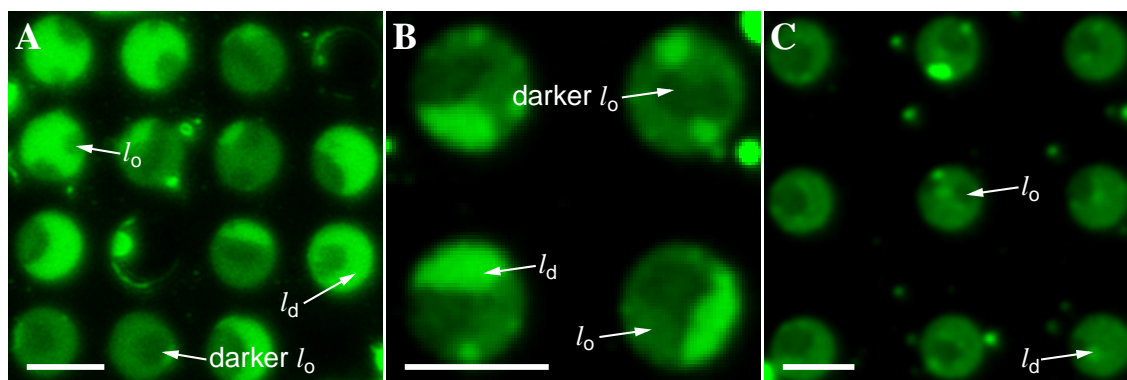**Figure 5.15:** Fluorescence micrographs of pore-spanning lipid bilayers composed of DOPC/SM/Chol/Gb_3-Porc 40:35:20:5 doped with 0.5 mol% Bodipy-PC after incubation with 60 nM STxB-Cy3 for 1 h. **A** Bodipy-PC fluorescence shows two brightness levels in the pore-spanning parts which are assigned to the l_o and l_d phase. Fluorescence on the rims is quenched and no information on the phase behavior can be extracted. **B** Fluorescence of STxB-Cy3, false colored in red, is only located on the membrane areas which were assigned to the l_o phase. On the rims residual fluorescence signal can be detected. **C** Overlay of **A** and **B**. No colocalization of Bodipy-PC and STxB-Cy3 is found. The overlay shows that the l_o phase is not necessarily fully covered with STxB-Cy3. Pore diameter: 1.2 μm. Scale bars: 5 μm.

The use of fluorescently labeled Shiga toxin subunit B (STxB-Cy3) allows to localize the protein bound to the freestanding membrane areas by its red fluorescence. In Figure 5.15B areas of bright red fluorescence are found on the pore-spanning membranes and the overlay in Figure 5.15C proves that STxB is selectively bound

to the areas assigned to the l_o phase. Binding to the l_d domains would be indicated by colocalization of the Bodipy-PC and Cy3 fluorescence which would result in blended yellow color coding.

The biological function of STxB is to induce negative curvature and invaginations in the plasma membrane.[71] Using confocal fluorescence microscopy no alterations of the membrane topography upon STxB binding were observed which can be attributed to the mechanical properties of the membrane (see Section 5.4.1). The data obtained from mapping the topography with high resolution scanning ion-conductance microscopy is shown in Section 5.3.5.

Phase separation of pore-spanning membranes with diameters of 0.8, 1.2 and 2.0 μm after incubation with STxB

Figure 5.16 shows fluorescence micrographs of pore-spanning lipid membranes composed of DOPC/SM/Chol/Gb$_3$-Porc 40:35:20:5 doped with Bodipy-PC after incubation with STxB-Cy3. Pore diameters are 0.8, 1.2 and 2.0 μm. Bodipy-PC fluorescence (panels A, D and G) allowed to determine the percentage of liquid-ordered phase. The area covered by the l_o phase was determined by pixel analysis of 4091 pores in 71 membrane patches to be 60 % of the total freestanding membrane area independent of the pore size and porosity (Table 5.3). This corresponds to doubling of the ordered membrane area compared to the STxB free case.

The lateral structure of the domain was found to be strongly dependent on the size of the pore. Similarly to the STxB free case, pore-spanning membranes with a diameter of 0.8 μm mostly (59 %) contain exclusively a single l_o or l_d as shown by the round green structures in Figure 5.16A.
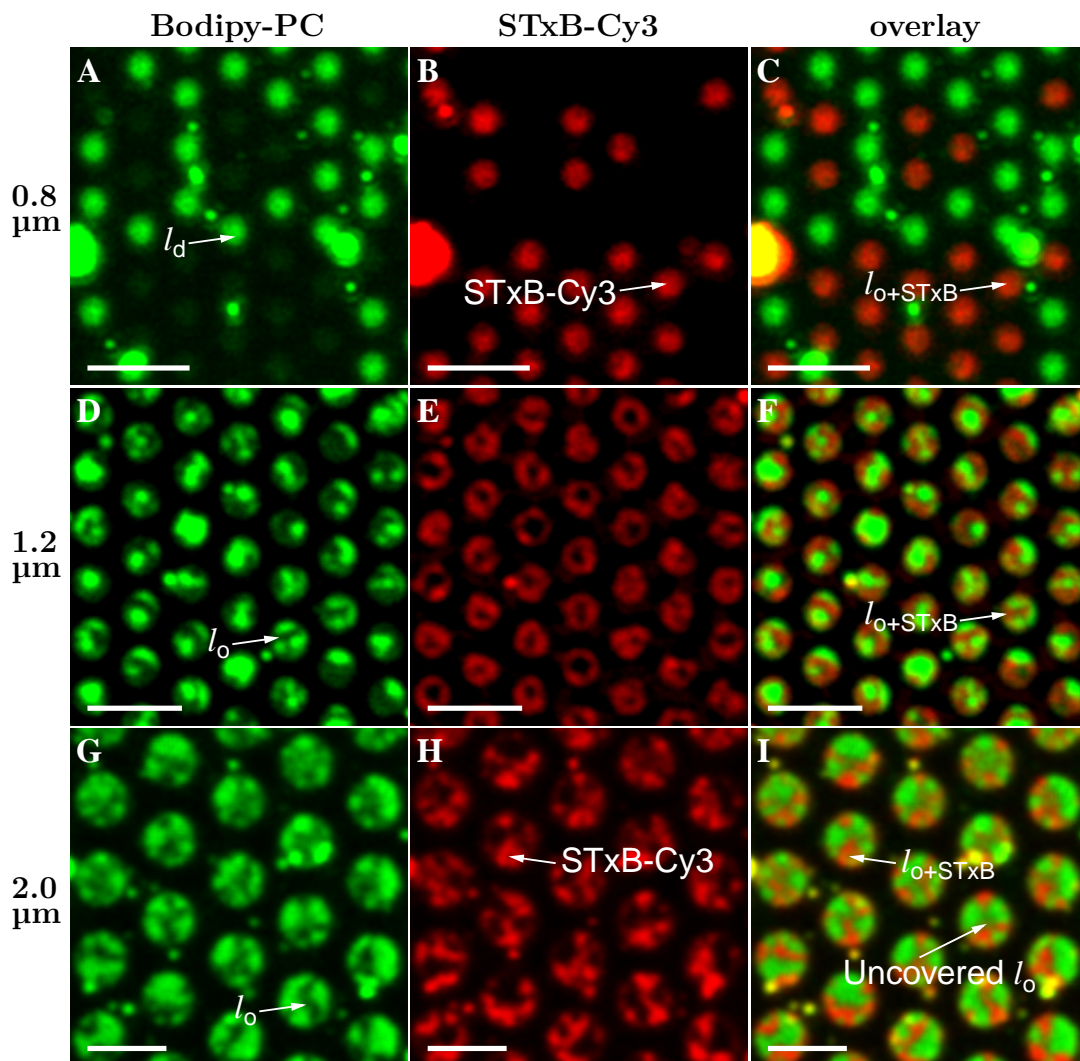
Figure 5.16: Fluorescence micrographs of pore-spanning lipid bilayers with different diameters (0.8, 1.2 and 2.0 μm) composed of DOPC/SM/Chol/Gb$_3$-Porc 40:35:20:5 doped with 0.5 mol% Bodipy-PC after incubation with 60 nM STxB-Cy3 for 1 h. Pore diameter 0.8 μm: **A** Bodipy-PC fluorescence shows the l_d phase while STxB-Cy3 (**B**) selectively labels the l_o phase. The overlay (**C**) shows no colocalization of the fluorophors. Pore diameter 1.2 μm: **D** Bodipy-PC fluorescence on the pore-spanning membrane area is inhomogeneous showing that each pore contains both l_o and l_d phase. Cy3 fluorescence (**E**) and the overlay (**F**) show that STxB is located on the l_o phase. Pore diameter 2.0 μm: The overlay (**I**) constructed from the Bodipy-PC (**G**) and Cy3 fluorescence (**H**) shows that the l_o phase is not fully covered with STxB. Scale bars: 3 μm.

Substrates with larger pore sizes of 1.2 and 2.0 μm show more pore-spanning membranes which both contain l_o and l_d domains (65 and 95 %). Due to the overall increase of l_o phase, nearly all l_o domains are in contact with the pore rim. Compared to the protein free case the structure of the domains is less roundish and

more irregular (Figure 5.16D/G). In most cases only one l_o domain is present in each pore.

The overlays of the Bodipy-PC and STxB fluorescence presented in panels C, F and I, illustrate that the STxB-Cy3 is only located on the l_o areas. However, on pores with a diameter of $2.0\,\mu m$ the fluorescence intensity of STxB-Cy3 on the l_o phase is not fully homogeneous (panel I). Some l_o areas only show low STxB-Cy3 fluorescence. Other regions are bright, indicating that the STxB-Cy3 density in these regions is higher. A detailed fluorescence overlay of the different brightness levels is shown in Figure 5.19D.

Modulation of the protein organization

The different intensities of the STxB-Cy3 fluorescence on the l_o phase indicates that the density of bound STxB varies. To test whether the lateral protein organization can be artificially changed, cholesterol extraction using methyl-β-cyclodextrin (mβCD) was employed (Section 3.2.3). This process was previously found to alter the membrane composition and lower the amount of l_o area.[52,91] Figure 5.17 shows the effect of mβCD on a phase-separated pore-spanning membrane. Prior to the addition of mβCD, the l_o phase accounts for $73\pm25\,\%$ of the freestanding membrane area. The l_o phase is only partially covered by protein ($47\pm13\,\%$ of the area). After addition of $1\,mM$ mβCD, the l_o phase shrinks due to the extraction of cholesterol. After $2\,min$ the l_o phase accounts for $44\pm13\,\%$ of the membrane area and the fluorescence micrograph in Figure 5.17B shows that the l_o phase is nearly completely covered with STxB. Further extraction of cholesterol leads to a lowered l_o phase fraction of $26\pm5\,\%$, concurrent with a shrinking of the area fraction occupied by STxB to $23\pm6\,\%$. This shows that artificially lowering the area percentage of l_o phase either leads to a condensation of the protein to higher density or STxB is detached from the membrane. In accordance with a previous result, STxB bound peripherally to the membrane, inhibits further extraction of cholesterol from the membrane.[51,52]
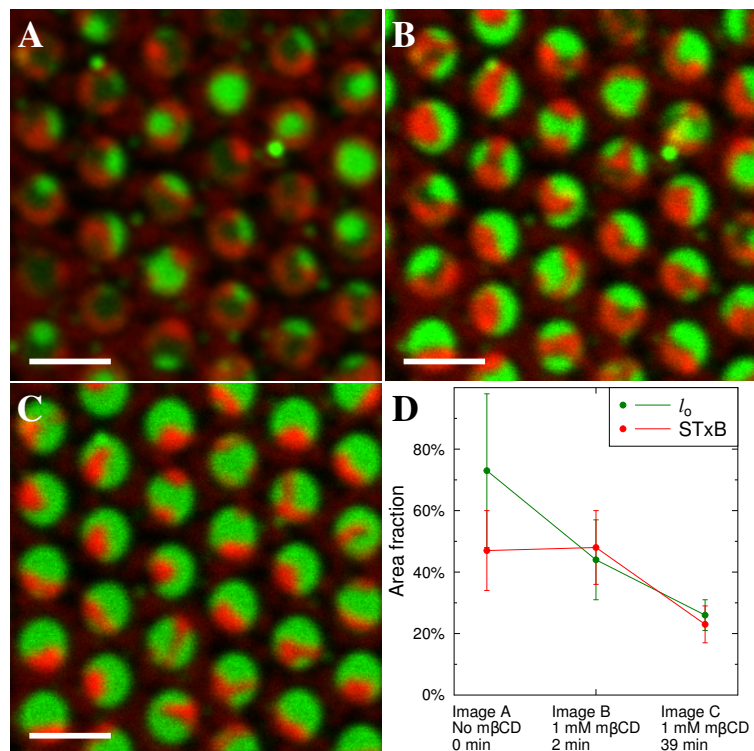
Figure 5.17: Effect of cholesterol extraction by mβCD on pore-spanning lipid bilayers composed of DOPC/SM/Chol/Gb$_3$-Porc 40:35:20:5 doped with 0.5 mol% Bodipy-PC after incubation with 60 nM STxB-Cy3 for 1 h on a substrate with pore diameter of 1.2 μm. Image recording and brightness settings for all images are identical. **A** Overlay of the Bodipy-PC and STxB-Cy3 fluorescence shows that STxB is only located on the l_o phase but does not fully cover it (**D**). **B** Incubation with 1 mM mβCD for 2 min leads to a shrinking of the l_o phase (**D**) while the area covered by STxB is constant. **C** After 39 min the l_o phase area and the area occupied by STxB is further reduced. Scale bars: 2 μm. **D** Time course of the areas occupied by STxB (red) and the l_o phase for the images presented in **A**-**C**.

Phase separation of pore-spanning membranes with diameters of 3.5 μm after incubation with STxB

Figure 5.18 shows fluorescence micrographs of pore-spanning membranes prepared on substrates with a pore diameter of 3.5 μm and porosities of 14, 28 and 39 % after incubation with STxB. The analysis of 1398 pores in 64 membrane patches revealed a similar lateral structure independent of the porosity. 98 % of the pore-spanning membranes contain both l_o and l_d areas. Occasionally a third brightness level of the l_d marker dye is observed inside the l_o phase. Both brightness levels were assigned to the ordered l_o phase.

Figure 5.18: Fluorescence micrographs of pore-spanning lipid bilayers composed of DOPC/SM/Chol/Gb$_3$-Porc 40:35:20:5 doped with 0.5 mol% Atto488 DHPE prepared on porous substrates with pore diameters of 3.5 μm and different porosities (39, 28, 14 %) after incubation with 60 nM STxB-Cy3 for 1 h. **A** (Porosity 39 %): the Atto488 (green) fluorescence shows the membrane segregating into l_o and l_d phase. Darker areas in the l_o phase are found. A similar morphology of the domains is also found on substrates with lower porosity (**B**: 28 %, **C**: 14 %). Scale bars: 4 μm.

The l_o area percentage after STxB binding was quantified for all three porosities. Figure 5.18A shows a substrate with a surface porosity of 39 %. Analysis revealed that the total area occupied by the l_o phase increases from 28 ± 13 to 59 ± 13 % of the total freestanding membrane area upon binding of STxB. This value is in excellent agreement with the values found for membranes prepared on substrates with pore diameters of 1.2 and 2.0 μm and a porosity of 41 %.

Figure 5.18B shows an characteristic micrographs of pore-spanning lipid bilayers on a substrate with a porosity of 28 %. Incubation with STxB led to decrease of freestanding l_o area from 49 ± 17 to 41 ± 8 %. This decrease was even stronger at lower porosities (14 %, Figure 5.18C). The total freestanding membrane area occupied by l_o domains decreases from 55 ± 10 to 32 ± 13 %.

Figure 5.19 shows the overlay of STxB-Cy3 fluorescence with the Atto488 DHPE fluorescence as shown in Figure 5.18. The l_o phase is not fully covered with protein but isolated STxB clusters are frequently observed in the areas of lowest Atto488 fluorescence (Figure 5.19).
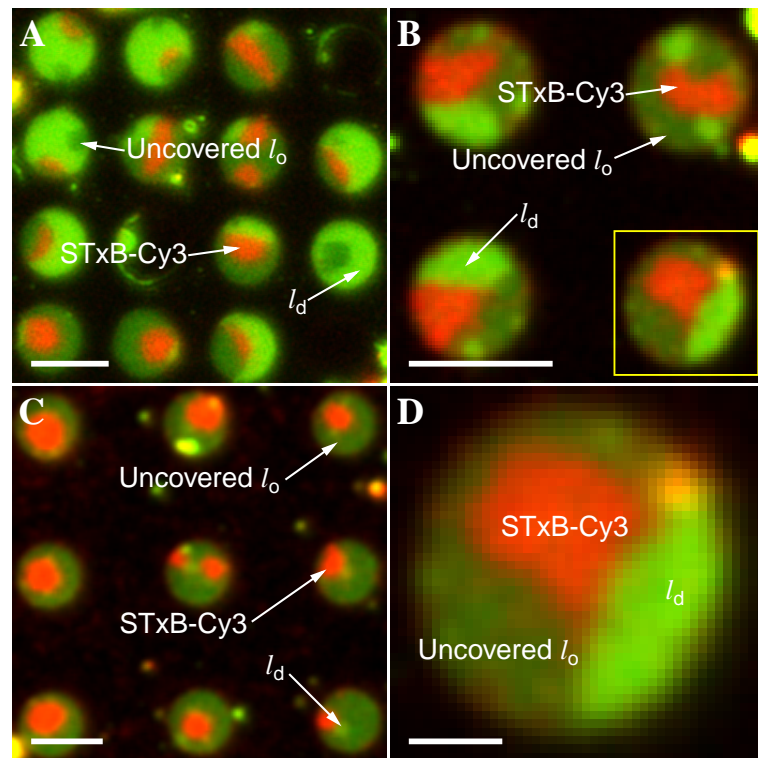
Figure 5.19: Fluorescence micrographs of pore-spanning lipid bilayers composed of DOPC/SM/Chol/Gb$_3$-Porc 40:35:20:5 doped with 0.5 mol% Atto488 DHPE on porous substrates with pore diameters of 3.5 μm and different porosities (39, 28, 14 %) after incubation with 60 nM STxB-Cy3 for 1 h. **A** (Porosity 39 %): overlay of the Atto488 (green) and STxB-Cy3 (red) fluorescence, showing the membrane segregating into l_o and l_d phase. The l_o phase is only partially covered with STxB. A similar mode of binding is also found on substrates with lower porosity (**B**: 28 %, **C**: 14 %). Scale bars: 4 μm. **D** Zoom of the region marked in **B**. Scale bar: 1 μm.

The larger area of the pores allows to resolve the clusters in more detail, as both the domains and the structures formed by STxB are larger in size. Clusters are usually found at the border between the l_o and l_d phase.[70,87] Large parts of the l_o phase show no red STxB-Cy3 fluorescence, indicating that these areas are depleted of the Gb$_3$ receptor lipid. In most cases the clusters were static but occasionally their movement could be observed. Figure shows 5.20 a time series of a STxB cluster moving in the freestanding membrane area.
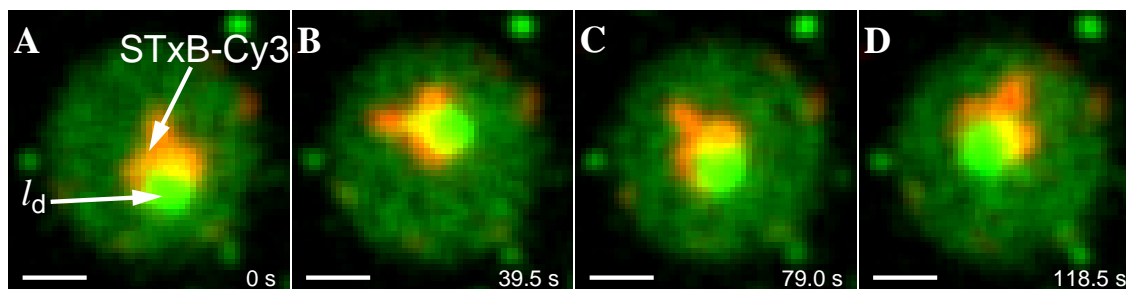
Figure 5.20: Fluorescence micrographs of a pore-spanning lipid bilayer composed of DOPC/SM/Chol/Gb$_3$-Porc 40:35:20:5 doped with 0.5 mol% Bodipy-PC on a pore with a diameter of 3.5 µm after incubation with 60 nM STxB-Cy3 showing the movement of a STxB cluster. **A-D** Fluorescence overlays of the Bodipy-PC (green) and STxB-Cy3 (red) fluorescence. The bright green l_d domain and the red STxB-Cy3 cluster are moving in the l_o domain that covers the pore. Scale bars: 1 µm.

The cluster (red) is located on the border to a l_d domain (green spot). Over time the cluster and the l_d domain move in the l_o domain that forms the pore-spanning membrane, but do not leave the freestanding membrane area. As expected, the diffusion in the l_o domain is slow.[203]

Table 5.3 summarizes the results obtained on the different porous substrates after incubation with STxB. Four different lipid dyes (Bodipy-PC, OregonGreen, Atto488 DHPE, TexasRed DHPE) were used and the results were found to be independent of the dye.

Table 5.3: Table summarizing the phase separation of pore-spanning membranes composed of DOPC/SM/Chol/Gb$_3$-Porc 40:35:20:5 on different porous supports after incubation with STxB. On larger pores a higher percentage of pore-spanning membranes containing both a l_o and l_d phase is found.

d / µm	P / %	Area percentage %l_o / %	fraction of pores l_o+l_d pores / %	pores	patches
0.8	23	60±16	41	1192	20
1.2	41	58±16	65	1914	25
2.0	41	59±12	95	985	26
3.5	39	59±13	99	436	26
3.5	28	41±8	98	550	19
3.5	14	32±13	99	412	19

STxB binding to phase-separated pore-spanning lipid membranes containing Gb$_3$ leads to a massive change in the lateral organization. The area percentage of ordered

phase on the freestanding membrane areas changes upon STxB binding. The effect is not found in GUVs (Table 5.1), indicating an influence of the interplay between freestanding and solid supported membrane areas. The morphology of the domains and lateral structure of bound Shiga toxin depend on the pore size. In PSLBs with diameters smaller than 2.0 µm only one domain is present in each pore. Larger PSLBs mostly show multiple domains per pore and Shiga toxin clusters are observed.

Radial distribution of l_o area in the pore-spanning membrane

The values obtained for the area covered by l_o domains show no simple relation with pore size or substrate porosity. A simple classification in 'rim domains' and 'center domains' is rather qualitatively. To obtain a more quantitative measure, the radial distribution of l_o area in each pore was investigated. Figure 5.21 shows the evaluation procedure.
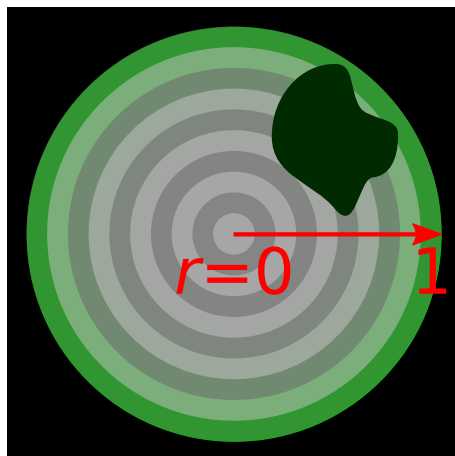
Figure 5.21: Evaluation of radial density of l_o area in pore-spanning membranes. Pore center is defined as $r = 0$, the rim as $r = 1$. The distance from the pore for each pixel allocated to the l_o phase is calculated and binned in annuli (gray).

The distribution is described making use of the radial symmetry of the pores. The pore center is defined as the position $r(\text{center}) = 0$. Distance from the center to the outmost border (rim) of the pore is described using the relative distance $r(\text{rim}) = 1$. This allows to compare different pore sizes. For each pixel allocated to the l_o phase, its relative distance to the pore center was calculated. Data was then binned in annuli (radial shells) as shown in Figure 5.21. Bin count was set to 12, resulting in bin sizes of 33 to 146 nm for pores with a diameter of 0.8 and 3.5 µm respectively. The area included in each annulus grows proportionally to the distance r, meaning

that the center annulus has a smaller area than the outer ones. To correct for this bias, the values were normalized to the growth in radius allowing for quantitative comparison of the different annuli by multiplication with the mean radius of each shell. After normalizing the area under each curve to one, this yields a quantitative distribution of the l_o phase as a function of the distance from the pore center (Section 7.3).

The data obtained for the l_o area percentage on different substrates differed between 20 and 60 %. To allow for comparison of the radial densities, the binned data for each pore size was normalized to an area of one. This gives the true density distribution of l_o area in the pores. Values for different porosities of the pore diameter 3.5 µm were pooled in one curve as the domain structure was found to be similar.

Figure 5.22A shows the data extracted from analyzing the distribution of l_o domains in all 5126 individual pores investigated. The relative radial density of l_o areas is plotted as a function of the distance from the pore center. Figure 5.22B shows the distribution after STxB binding (n = 5489).
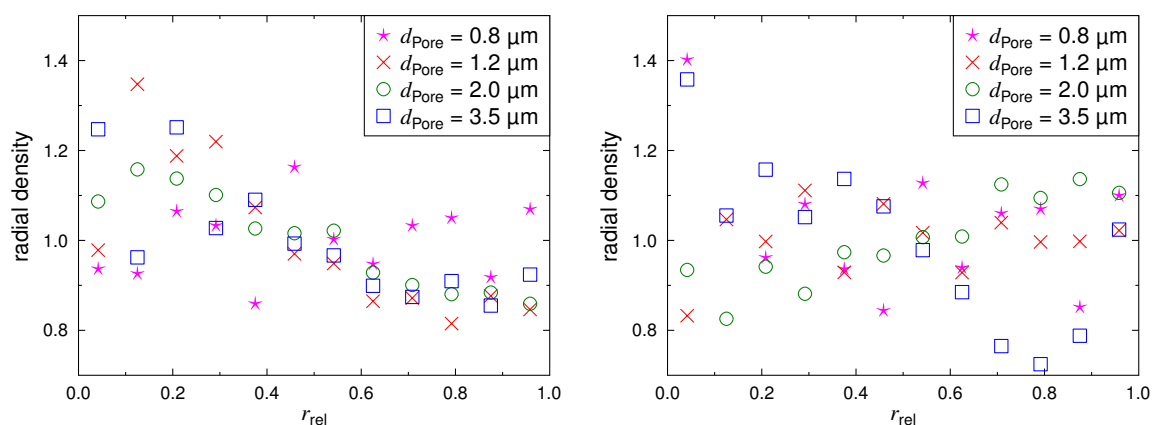
Figure 5.22: Relative radial density of l_o areas in pores of different diameter spanned by membranes composed of DOPC/SM/Chol/Gb$_3$-Porc 40:35:20:5.

In absence of bound protein the radial density in all annuli is similar, but a slight increase is found in the pore center. This indicates that l_o areas are preferentially located in the pore center and not at the pore border. A possible explanation for this behavior is given in Section 5.4.2. After protein binding the preference for the pore center is not found anymore. The density shown in Figure 5.22A can be compared to the density of freely moving domains shown in Figure 5.39B.

5.3.4 Dynamics of pore-spanning lipid membranes

All data and results presented in Sections 5.3.2 and 5.3.3 are based on the static observation of lipid domains in the pore-spanning membranes. Phase-separated membranes spread on a porous support can be envisioned as a minimal model system for the interaction of the plasma membrane and the cytoskeleton. In this context not only the static structure but also influences on the dynamics of the lipid bilayer are important.

Lipid mobility

Fluorescence recovery after photobleaching experiments (FRAP) adapted from Orth *et al.* were used to prove the mobility of lipids across the pore rim (Section 3.3.1).[51,52] An array of several pores was bleached and the recovery of fluorescence over time was recorded.[51,53] The diffusion coefficient of membranes composed of DOPC/SM/Chol/Gb$_3$-Porc 40:35:20:5 on substrates with a porosity of 41 % was found to be $D = 0.2 \pm 0.1 \, \mu m^2 \, s^{-1}$ (n = 13, immobile fraction 40 %). This shows that the membrane forms a continuous bilayer connecting the individual pore-spanning membranes. The diffusion coefficient for the freestanding membranes of GUVs and pore-spanning membranes has been reported to be in the range of 8 to $12 \, \mu m^2 \, s^{-1}$.[47,48,195,204,205] The lower determined value here is caused by diffusion of lipids between the pores on the pore rim. In solid supported membranes the friction to the support slows down diffusion considerably and values between 1 and $4 \, \mu m^2 \, s^{-1}$ and significantly lowered mobile fractions are observed.[185,206,207] The diffusion in the liquid-ordered phase is additionally slowed down by at least a factor of 10.[203]

The analysis was focussed on the dynamics of the domains in the pore-spanning parts of the membrane. Two types of domains are analysed: domains in contact to the pore rim and domains in the center of the pore.

Dynamics of rim adhered domains

Figure 5.23B-G shows a time series of a rim adhered domain imaged over 5 min. A membrane composed of DOPC/SM/Chol/Gb$_3$-Porc 40:35:20:5 is spanned over a pore with a diameter of 5.5 μm. The area obtained from thresholding, corresponding to the l_o domain is outlined in red atop the green fluorescence of the l_d marker Bodipy-PC.
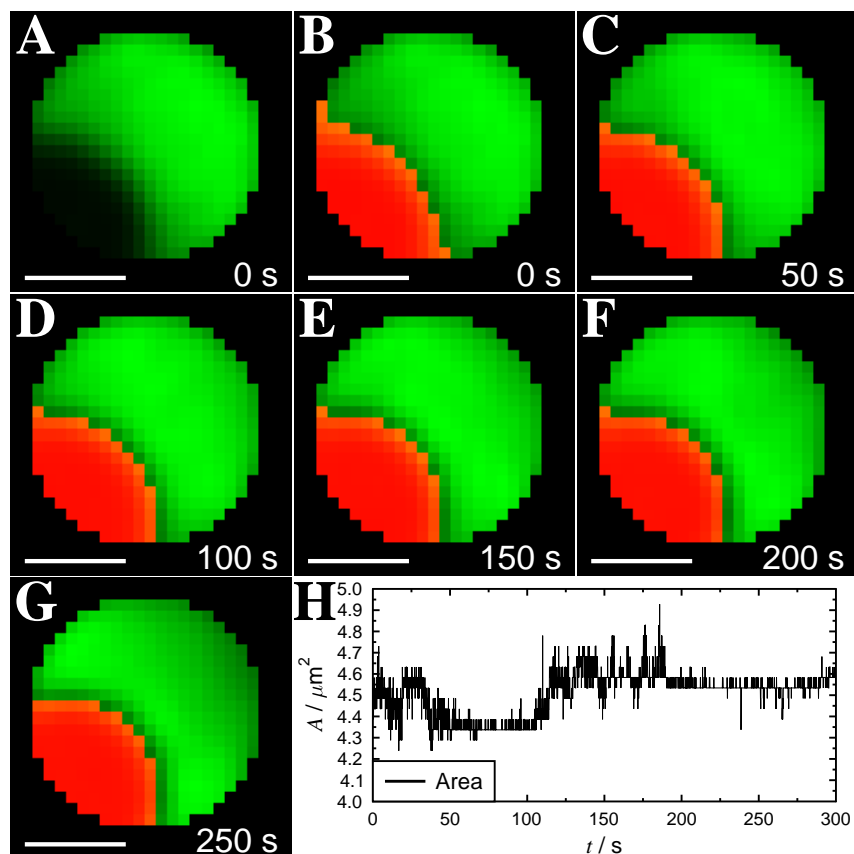
Figure 5.23: Dynamics of a lipid domain in contact with the pore rim. Membrane is composed of DOPC/SM/Chol/Gb$_3$-Porc 40:35:20:5 doped with 0.5 mol% Texas Red DHPE. Pore diameter is 5.5 µm and the pore was imaged for 5 min with $\Delta t = 0.1$ s. **A** A dark l_o domain is embedded in the green labeled l_d phase. The domain is in contact with the dark pore rim. **B** The red area corresponds to the pixels assigned to the l_o phase at $t = 0$ s. **C-G** During the time series the domain is neither moving nor shape or size changes are observed. Scale bars: 2 µm. **H** The size of the domain hardly fluctuates during the time series and is 4.5 ± 0.1 µm^2.

The domain is not moving. The average displacement of its center of mass is ≈ 30 nm per time frame ($\Delta t = 100$ ms). At the given pixel size of 222 nm^2 no net movement is detected. This shows that the domain is pinned to the solid support. However, the domain shape and size (Figure 5.23H) slightly fluctuate and the domain area is 4.5 ± 0.1 µm^2. The shape fluctuation indicates a dynamic association and dissociation of lipids from the l_o domain.

Dynamics of domains in the center of pore-spanning membranes

Some l_o domains were found to be located in the center of pore-spanning lipid

bilayers, with no contact to the pore rim. Figure 5.24B-G shows an characteristic time series of a pore-spanning membrane composed of DOPC/SM/Chol/Gb$_3$-Porc 40:35:20:5. The pore diameter is 5.5 µm. Frames were extracted from a time series with a length of 300 s.
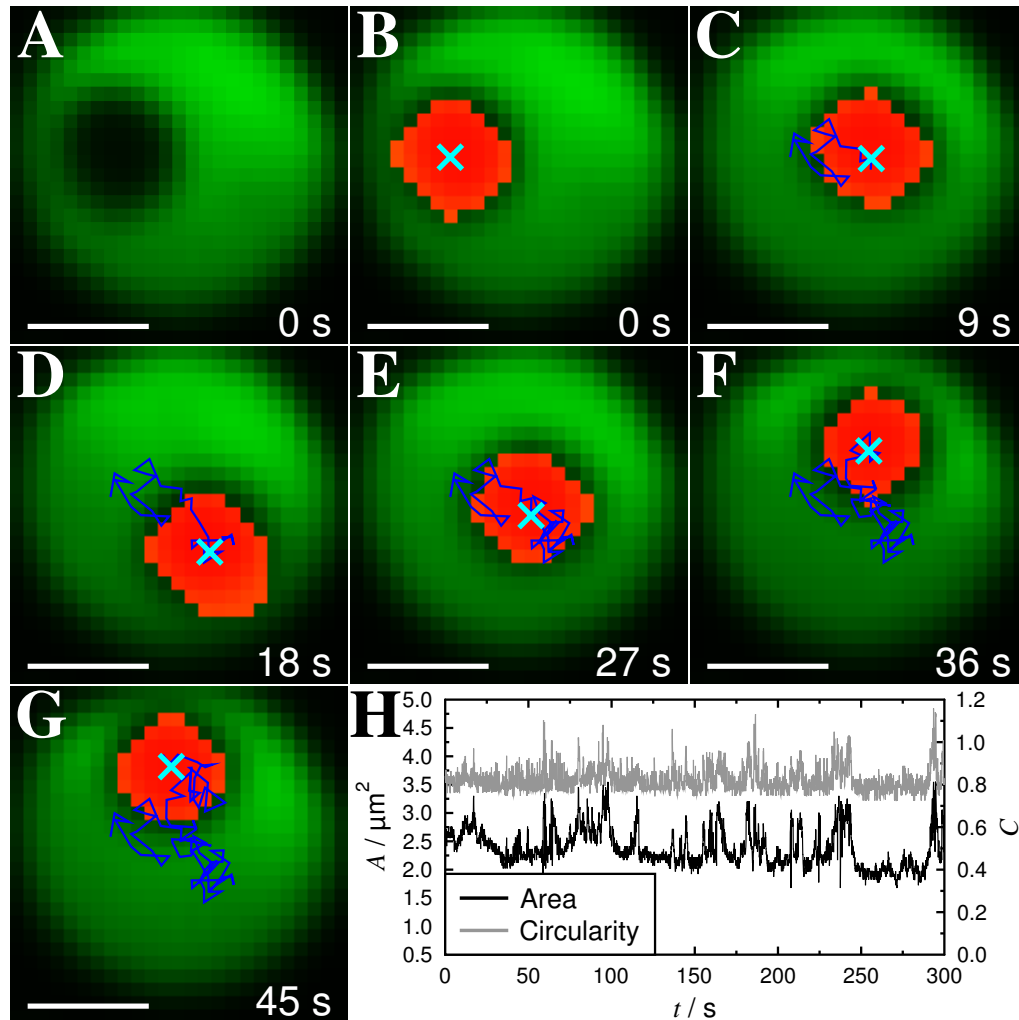
Figure 5.24: Dynamics of a lipid domain in the center of a pore. Membrane is composed of DOPC/SM/Chol/Gb$_3$-Porc 40:35:20:5 doped with 0.5 mol% Texas Red DHPE. Pore diameter is 5.5 µm and the pore was imaged for 5 min with $\Delta t = 0.1$ s. **A** A dark l_o domain is embedded in the green labeled l_d phase. The domain is located in the freestanding membrane and is not in contact with the solid support. **B** The area colored in red corresponds to the pixels assigned to the l_o phase at $t = 0$ s. **C-G** During the time series the domain is moving and its size and shape are fluctuating. A teal cross marks the center of mass of the domain in each frame. The movement of the domain is depicted by the blue trajectory. Only every fifth data point ($\Delta t = 0.5$ s) is shown for clarity. Scale bars: 2 µm. **H** Overall size of the domain only marginally fluctuates during the time series and is 2.5 ± 0.3 µm^2 and the domain adopts a round shape with a circularity of 0.8 ± 0.1.

The l_d phase is visible by its green fluorescence. The area assigned to the dye excluding l_o domain (panel A) is false colored in red (panel B). The domain was tracked as described in Section 3.4.3. It freely moves in the pore and its center of mass (teal cross) is traced in the time series. A blue line drawn depicts the trajectory. Only every 5th data point is drawn for clarity. Despite the movement in the pore-spanning membrane, the domain does not leave the freestanding membrane area during the time series. Analysis of the trajectory is shown in Section 5.3.4.1. Area and circularity can be extracted by thresholding the individual frames of the time series. The area (Figure 5.24H) is $2.5 \pm 0.3\,\mathrm{\mu m^2}$ and fluctuates over time while the circularity is 0.8 ± 0.1, indicating that the domains adopt a round shape to minimize line tension.[42]

Size changes of domains in PSLBs
Most of the domains imaged only move in the freestanding membrane areas, but in some cases different dynamics were observed. Figure 5.25 shows two time series of lipid domains changing their size.
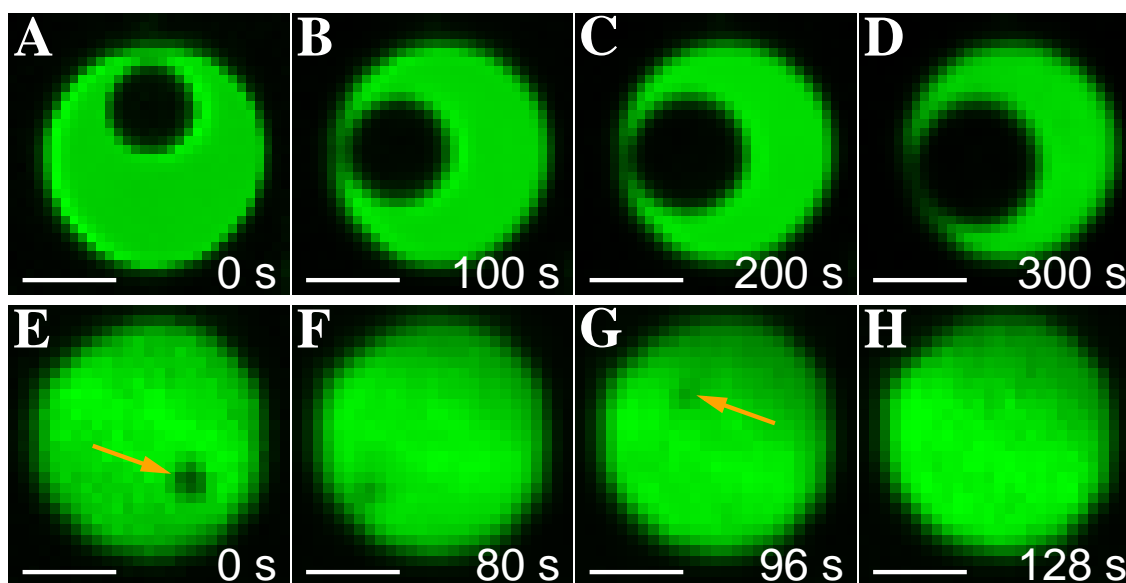
Figure 5.25: Growing and shrinking of lipid domains in PSLBs. Membranes are composed of DOPC/SM/Chol/Gb$_3$-Porc 40:35:20:5 doped with 0.5 mol% Texas Red DHPE. Pore diameters are 5.5 µm and the pores were imaged for 5 min with $\Delta t = 0.1$ s. **A-D** The dark l_o domain is embedded in the green labeled l_d phase and is growing over time and reaches 160 % of its initial size. **E-F** A small l_o domain (orange arrow) is moving in the freestanding membrane area and shrinks. It cannot be resolved anymore in **H**. It does not reappear during the time series ($t = 300$ s). Scale bars: 2 µm.

The domain imaged in panel A-D is growing in size over time to 160% of its starting area. Growing can only take place when further lipids or nanodomains associate with the large l_o domain to minimize line tension. The reverse process is depicted in Figure 5.25E-H. A small domain shrinks to the point at which it cannot be resolved anymore and does not reappear during the time series ($t = 300\,\text{s}$).

Merging of lipid domains

The structure of the lipid domains described in Section 5.3.2 shows that in the majority of the pores-spanning membranes only one lipid domain is present. Figure 5.26 shows a time series of a membrane composed of DOPC/SM/Chol/Gb$_3$-Porc 40:35:20:5 of two l_o domains in a pore with a diameter of $5.5\,\text{µm}$.
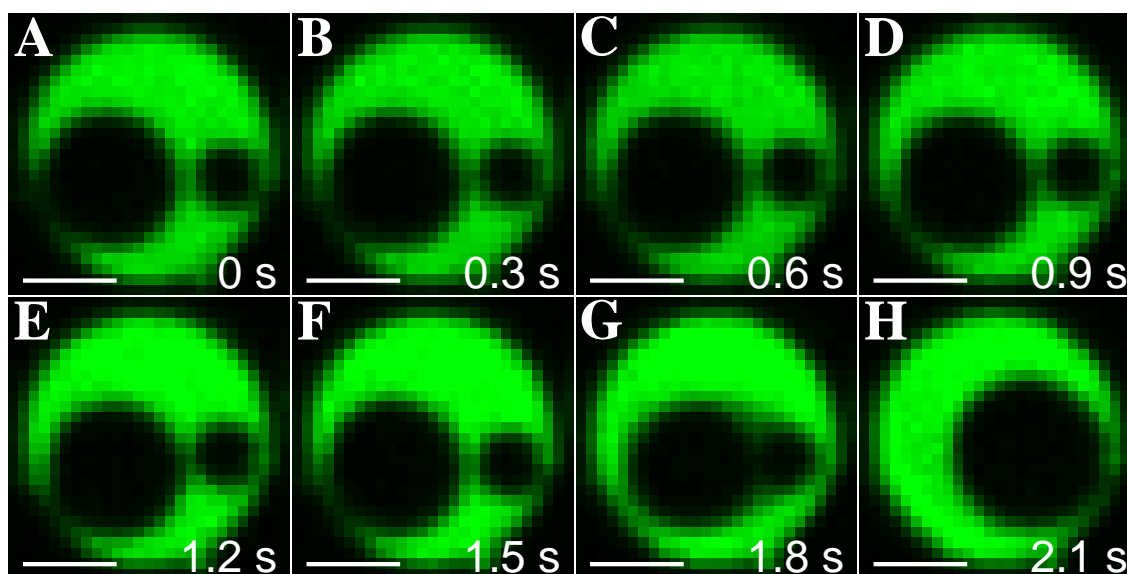
Figure 5.26: Time series of two lipid domains merging in the freestanding membrane area. Membrane is composed of DOPC/SM/Chol/Gb$_3$-Porc 40:35:20:5 doped with $0.5\,\text{mol}\%$ Texas Red DHPE. Pore diameter is $5.5\,\text{µm}$ and the pore was imaged for $5\,\text{min}$ with $\Delta t = 0.1\,\text{s}$. **A-F** Two dark l_o domains are present within the green labeled l_d phase that spans the pore. Both domains move in the pore. **G** Upon contact the domains start merging to minimize line tension. **H** The newly formed domain is stable until the end of the time series ($t = 300\,\text{s}$). Scale bars: $2\,\text{µm}$.

The domains presented in panel A are slightly moving and are not adhered to the pore rim. After $1.8\,\text{s}$ the domains come in contact and start to merge to form a larger domain (panel G). Domains have an area of 6.8 and $1.1\,\text{µm}^2$ with perimeters of 9.4 and $3.9\,\text{µm}$. After merging the area is constant but the perimeter only accounts for $10.3\,\text{µm}$. This reduction lowers the overall energy of line tension

(Equation 5.13, Table 5.5) by $\approx -900\, k_{\mathrm{B}}T$.

In the static pictures shown in Section 5.3.2 on large pores, frequently multiple domains per pore are observed but never more than one freely moving. Figure 5.27 shows a similar process as presented above. Two dark l_{o} domains are in the PSM. The freely moving center domain comes in contact with a small domain located at the pore rim and the domains merge forming a larger, bud like domain at the rim.
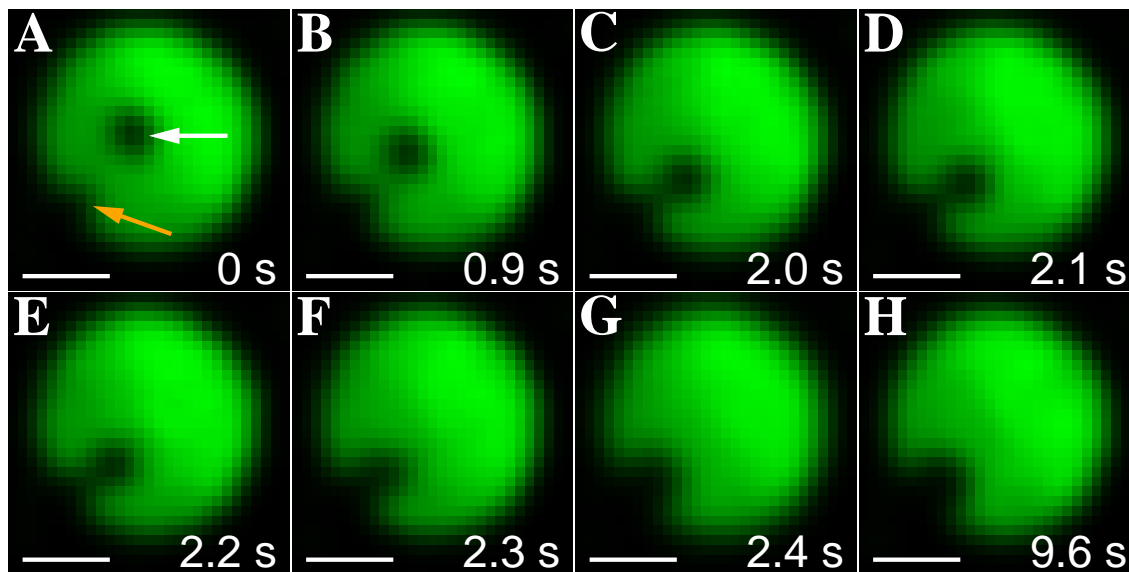
Figure 5.27: Time series of a lipid domain merging to a rim adhered domain. The membrane is composed of DOPC/SM/Chol/Gb$_3$-Porc 40:35:20:5 doped with 0.5 mol% Texas Red DHPE. The pore diameter is 5.5 µm and the pore was imaged for 5 min with $\Delta t = 0.1$ s. **A-B** Two dark l_{o} domains are present within the green labeled l_{d} phase that spans the pore. One of the domains (orange arrow) is immobile and in contact to the rim. A second domain (white arrow) freely moves. **D-G** Upon contact the domains start merging to minimize line tension. **H** The newly formed domain is stable until the end of the time series ($t = 300$ s) and does not move anymore. Scale bars: 2 µm.

In this case no round object is formed but the typical bud shape of domains at the pore rim. After the fusion the resulting domain is immobile during the remaining time series ($t = 300$ s). These results reveal that the porous support is able to influence the dynamics of lipid domains in two major ways i) l_{o} domains getting in contact to the rims are pinned to the substrate in a similar fashion as conjectured for the actin cytoskeleton ii) the movement of the domain is restricted by the geometry of the pore.

5.3.4.1 Quantification of domain movement

To quantify the dynamics of the l_o domains, 205 domains imaged in membranes spanning pores with diameters of 1.2, 2.0, 3.5, 4.5 and 5.5 µm were analysed. Figure 5.28 shows characteristic time courses of all five pore sizes used. (Section 5.3.3).
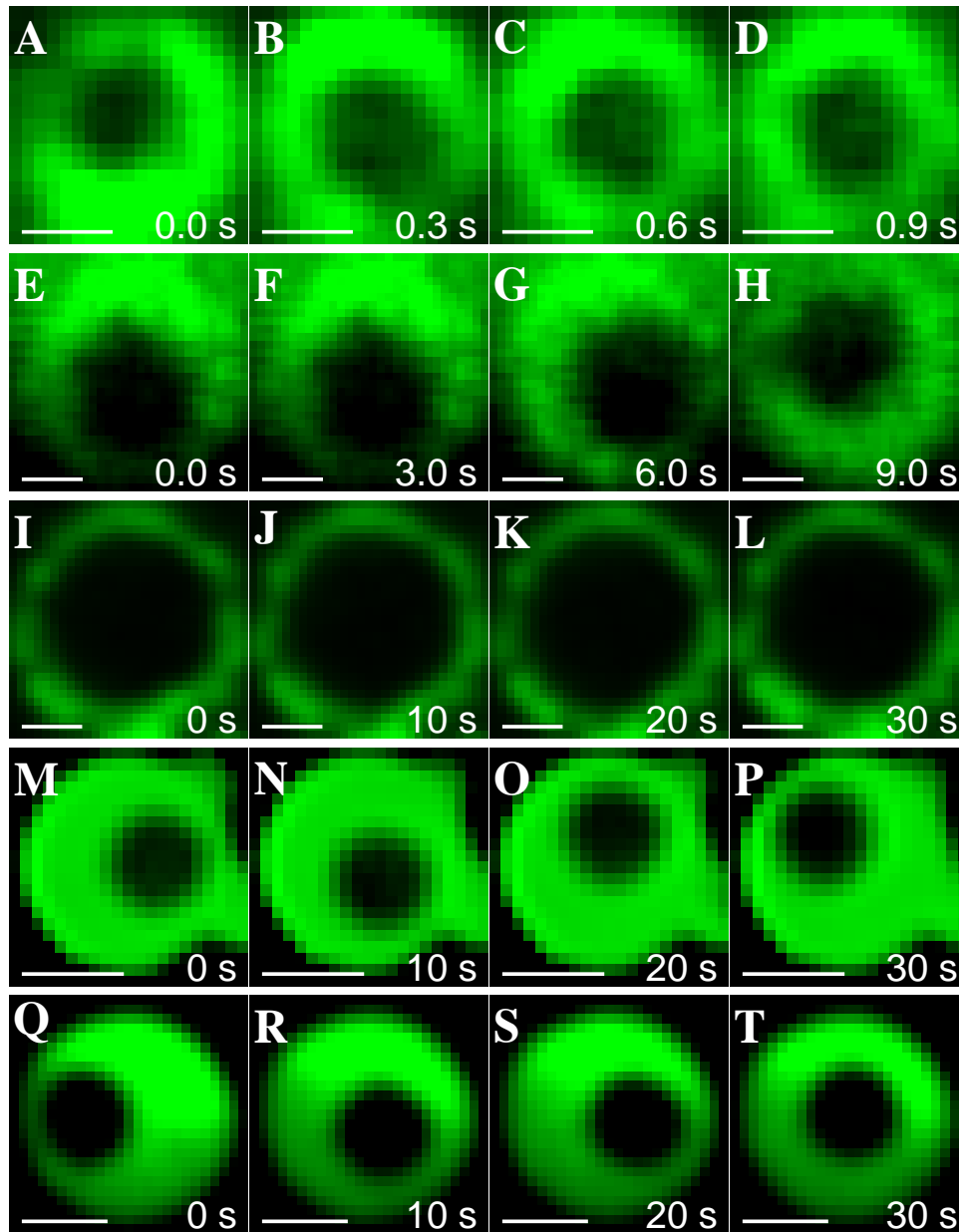
Figure 5.28: Time series' of lipids domain moving in PSMs. Membranes are composed of DOPC/SM/Chol/Gb$_3$-Porc 40:35:20:5 doped with 0.5 mol% Texas Red DHPE. Time stepping is given in the images. **A-D**: Pore diameter 1.2 µm. Scale bars: 0.5 µm. **E-H**: Pore diameter 2.0 µm. Scale bars: 0.5 µm. **I-L**: Pore diameter 3.5 µm. The large size constricts the movement. Scale bars: 1 µm. **M-P**: Pore diameter 4.5 µm. Scale bars: 2 µm. **Q-T**: Pore diameter 5.5 µm. Scale bars: 2 µm.

For pores with a diameter of 1.2 and 2.0 µm the time step between two frames (Δt) was 30 ms, for larger pores 100 ms. Using even smaller pores was hindered by both the limited resolution hampering the automated detection of the domain and the sparsity of domains in the pore center. A total of 581472 frames was investigated. The mean circularity of the domains is 0.9 ± 0.1 showing that they adopt a round shape to minimize line tension.

From each moving domain its trajectory was extracted as described in Section 3.4.3. Figure 5.29A shows an characteristic trajectory of a domain moving in a pore with a radius of 2.75 µm. The blue line indicates the movement of the domain's center of mass. The size of the domain hinders the approach to the pore rim which is depicted as the black circle.
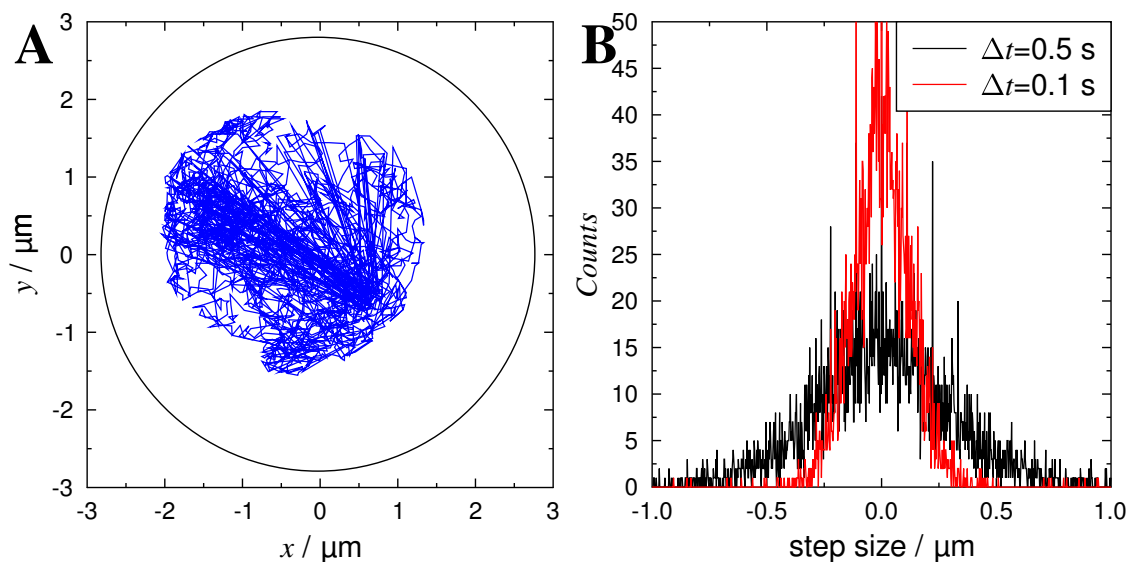
Figure 5.29: A Characteristic trajectory of a domain moving in a pore with a diameter of 5.5 µm. The blue curve shows the trajectory of the center of mass moving in the domain which dimension is depicted by the black circle. **B** Displacement (step size) calculated for two different time intervals used to calculate the mean square displacement. At $\Delta t = 0.1$ s the distribution is narrow. At $\Delta t = 0.5$ s the distribution broadens.

The coordinates of the center of mass of the domain during the time series were used to extract the mean square displacement of the domain. Plotting the step size the domain moved during increasing time intervals (Δt) results in the displacement histograms shown in panel B. The distribution is narrow at short time intervals (red) and rapidly grows wider with increasing time difference (black). The width of

the distribution is a measure for the mean square displacement (see Section 3.4.3). Knowing the mean square displacement, the diffusion coefficient can be calculated. However, the constriction of the movement by the pore border requires to adapt the equations used, because no free two dimensional diffusion takes place.

Model for the diffusion of domains in pore-spanning membranes

To describe the diffusion of lipid domains in pore-spanning lipid membranes, Prof. Dr. Jörg Enderlein (III. Institute of Physics, Georg-August-Universität Göttingen) developed a model to describe the motion of a point-like particle in a circular pore with the radius *a*. Figures 5.30 and 5.31 give schematic representations of the theory. In general the function G describes the movement of a particle (Figure 5.30A) as a function of its spatio-temporal coordinates p and t (Figure 5.30B). Equation 5.1 depends on the diffusion coefficient D:

$$\frac{\delta G\left(p,t\right)}{\delta t} = \nabla\left[D\left(G,p\right)\nabla G\left(p,t\right)\right]. \tag{5.1}$$

To describe the motion of a particle in the circular pores (Figure 5.30A) it is convenient to use the polar coordinates ρ and ϕ with respect to the pore center (ρ_0, ϕ_0). Under the assumption of a constant diffusion coefficient the differential equation to describe the diffusion reads:

$$\frac{\delta G}{\delta t} = D\left(\frac{1}{\rho}\frac{\delta}{\delta\rho}\rho\frac{\delta G}{\delta\rho} + \frac{1}{\rho^2}\frac{\delta^2 G}{\delta\phi^2}\right). \tag{5.2}$$
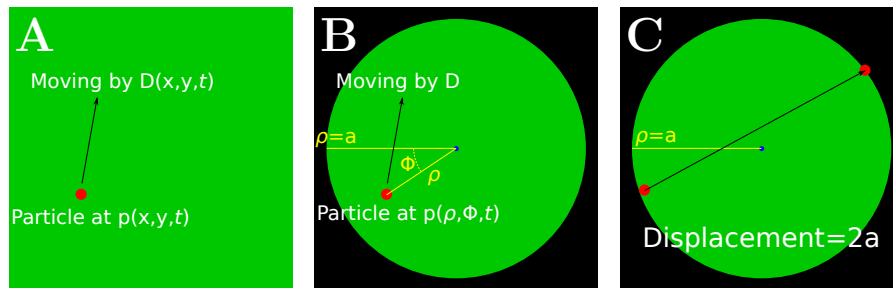
Figure 5.30: Scheme describing the diffusion of a particle (red) in a membrane (green) spanning a pore (black) with radius *a*. **A** Free diffusion can be described by the diffusion coefficient D. **B** In circular pores it is beneficial to use polar coordinates. **C** The particle cannot diffuse out of the pore.

From the data recorded it is apparent that a diffusing domain does not leave the freestanding membrane (Figure 5.24 and 5.29A). This defines the boundary condition that the probability of finding the particle at the position of the pore rim $\rho = a$ is 0. *Eigenfunctions* $\Psi_{n,\alpha}$ to solve Equation 5.2 are based on the Bessel functions of the first kind J_n and the discrete solutions $k_{n,\alpha}$ of the transcendental equation $[dJ_n(x)/dx]_{x=k_{n,\alpha}} = 0$:

$$\left(\frac{\delta G}{\delta \rho}\right)_{\rho=a} = 0 \rightarrow \Psi_{n,\alpha}(\boldsymbol{p}) = J_n\left(k_{n,\alpha}\frac{\rho}{a}\right)\exp(in\phi). \tag{5.3}$$

The boundary conditions at $\rho = a$ is automatically fulfilled and the functions are *eigenfunctions* of the Laplace operator for any kind of subscripts:

$$\Delta\Psi_{n,\alpha}(\boldsymbol{p}) = -\left(\frac{k_{n,\alpha}}{a}\right)^2 \Psi_{n,\alpha}(\boldsymbol{p}). \tag{5.4}$$

The orthogonal functional basis for the given boundary condition is

$$\int\limits_0^a d\rho\rho \int\limits_0^{2\pi} d\phi \overline{\Psi}_{n',\alpha'}(\boldsymbol{p})\,\Psi_{n,\alpha}(\boldsymbol{p}) = \pi a^2\left(1 - \frac{n^2}{k_{n,\alpha}^2}\right)J_n^2(k_{n,\alpha})\,\delta_{n,n'}\delta_{\alpha,\alpha'} \tag{5.5}$$

with $\overline{\Psi}_{n',\alpha'}$ being the complex conjugation. The fundamental solution $G(\boldsymbol{p} - \boldsymbol{p}_0, t)$ (Green's function) which fulfills $\lim\limits_{t\to 0}(\boldsymbol{p} - \boldsymbol{p}_0, t) = \delta(\boldsymbol{p}_0)$ is given by Equation 5.6.

$$G(\rho,\phi,t,|\rho_0) =$$
$$\frac{1}{\pi a^2}\sum_{n=-\infty}^{\infty}\sum_{\alpha=1}^{\infty}\frac{J_n(k_{n,\alpha}\rho_0/a)\,J_n(k_{n,\alpha}\rho/a)}{1 - n^2/k_{n,\alpha}^2 J_n^2(k_{n,\alpha})}\exp\left(in\phi - Dk_{n,\alpha}^2 t/a^2\right) \tag{5.6}$$

To use this equation to describe the movement of particles in the pore-spanning membrane the mean square displacement (MSD) of the particles needs to be calculated. Figure 5.31A/B schematically depicts the determination.
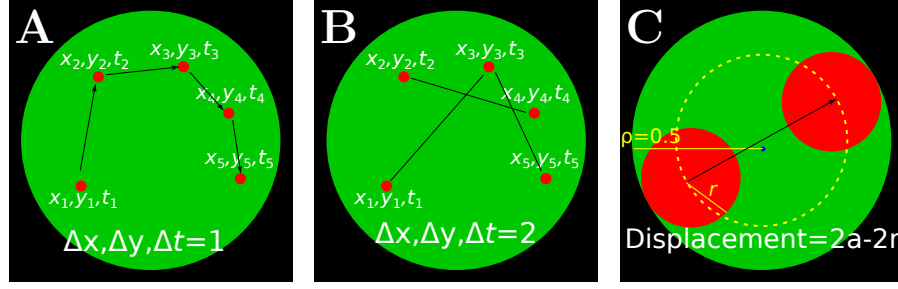
Figure 5.31: Calculation of MSD and diffusion of objects with finite size. **A** Calculation of the displacement for $\Delta t = 1$. **B** Calculation of the displacement for $\Delta t = 2$. **C** Larger objects will effectively diffuse distances shorted by their radius.

The displacement d is calculated in growing time intervals Δt between the coordinates of the centroid extracted during the tracking process (Section 3.4.3). This allows to calculate the mean square displacement (MSD) of a point-like particle diffusing inside the pore by:

$$\text{MSD}(t) = \frac{2}{a^2} \int\limits_0^a d\rho_0 \rho_0 \int\limits_0^a d\rho \rho \int\limits_0^{2\pi} d\phi G\left(\rho, \phi, t, |\rho_0\right) \left(\rho_0^2 + \rho^2 - 2\rho_0\rho\cos\phi\right). \quad (5.7)$$

Explicit integration gives the final equation:

$$
\begin{aligned}
\text{MSD}(t) = 8a^2 \sum_{\alpha=1}^{\infty} \Bigg\{ &\frac{\left[2J_2\left(k_{0,\alpha}\right) - k_{0,\alpha}J_3\left(k_{0,\alpha}\right)\right]J_1\left(k_{0,\alpha}\right)}{k_{0,\alpha}^3 J_0^2\left(k_{0,\alpha}\right)} \exp^{\left(-Dk_{0,\alpha}^2 t/a^2\right)} \\
&- \frac{J_2^2\left(k_{1,\alpha}\right)}{\left(k_{1,\alpha} - 1\right)J_1^2\left(k_{1,\alpha}\right)} \exp^{\left(-Dk_{1,\alpha}^2 t/a^2\right)} \Bigg\}.
\end{aligned}
\quad (5.8)
$$

Using Equation 5.8 one can calculate the MSD numerically. Using $\alpha_{\text{max}} = 500$ yields sufficient numerical precision. The calculation gets further simplified by two factors: i) a change in diffusion coefficient from D to D' only results in a rescaling of the time axis by D/D', ii) a change in pore radius from a to a' rescales the curve by $(a/a')^2$ along both the time and MSD axis. This allows to calculate Equation 5.8 for only one pair of the diffusion coefficient D and pore radius a and use an affine fit function to computationally efficiently 'deform' the theoretical curve to the experimental data.

The theory presented above assumes the diffusion of a point-like particle. In the experimental data the size of the domains is approx. 10-70 % of the total pore-

spanning membrane area, the domain border does not cross the pore border and is repelled. Figure 5.31C shows how this can be accounted for. Effective movement of a domain with radius r stops before the center of mass of the round domain reaches the rim. The maximum displacement of the domain is therefore limited by both the pore size a and its radius r. Fitting Equation 5.8, the pore radius a in corresponds to the effective radius of the pore the centroid of the domain can reach. Knowing the pore size from scanning electron microscopy data (Section 3.2.3) and fitting the equation to the data yields the radius of the domain as:

$$r_{\text{fit}} = a_{\text{pore}} - \sqrt{a_{\text{fit}}}. \tag{5.9}$$

Figure 5.32 shows theoretical curves calculated according to Equation 5.8.
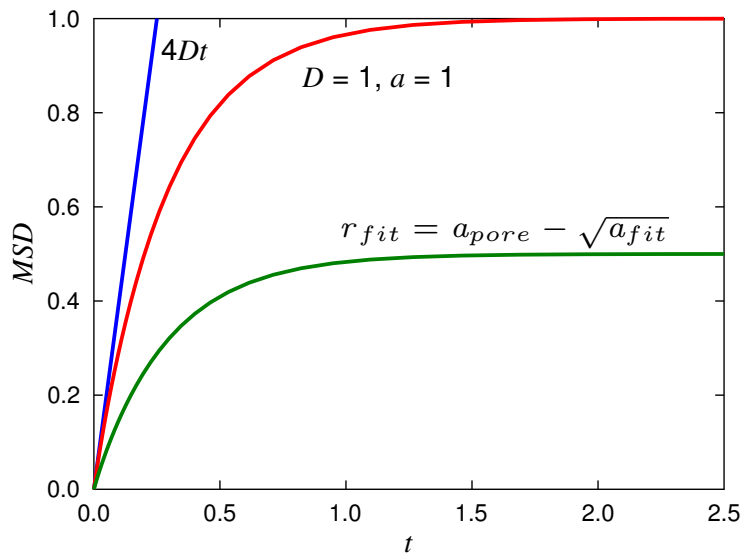
Figure 5.32: Calculated average mean square displacement for the diffusion of a disc with radius a and a diffusion coefficient $D = 1$. Blue curve corresponds to the displacement in the unbound case; the red curve under the assumptions presented in Equations 5.3 to 5.8. The green curve is valid for a larger particle diffusing in the pore.

The blue curve corresponds to the MSD for free diffusion; the red curve takes the finite size of the pore into account. At long time intervals Δt the curve tends towards a limiting value which corresponds to the pore radius $\sqrt{a_{\text{pore}}}$ for the diffusion of a point-like particle. As shown in the green curve the effective limit for a domain is lower due to its size.

Fitting of experimental data

Figure 5.33 shows characteristic MSD curves and fits according to Equation 5.8 for the five domains in pores of different sizes as presented in Figure 5.28.
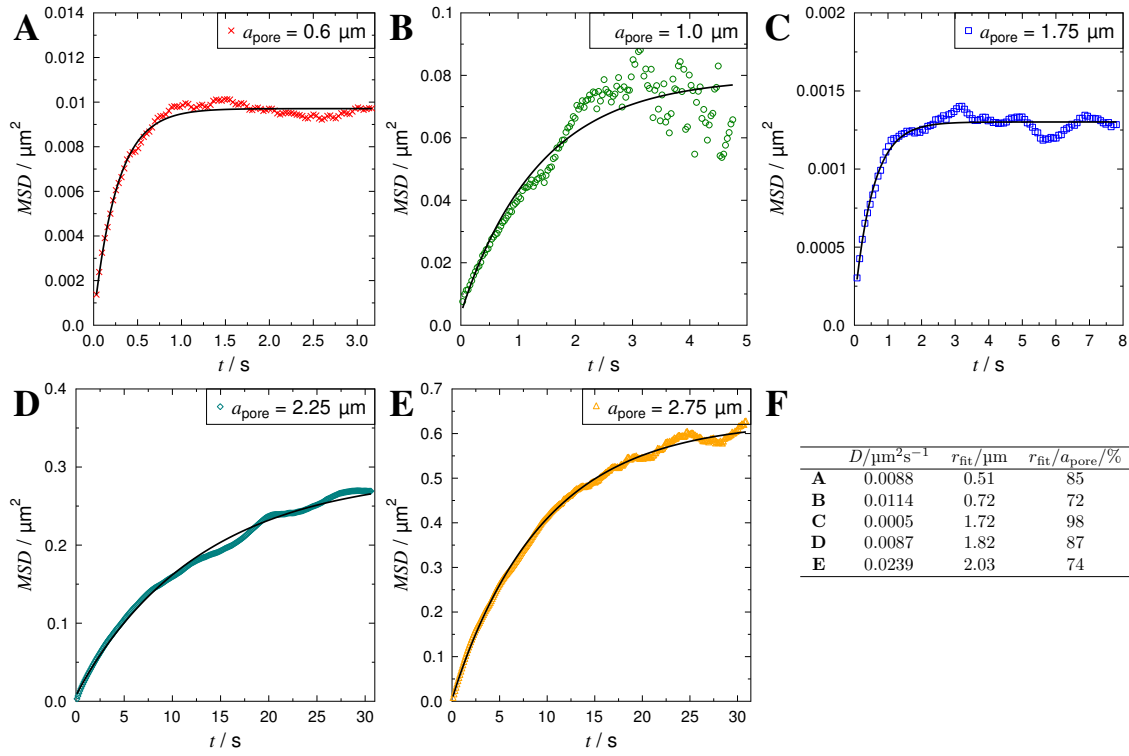
Figure 5.33: Characteristic MSD curves and fits according to Equation 5.8. Time scales and diffusion coefficients are vastly different due to the different pore sizes and domain radii.

Agreement between the experimental data and the fit is excellent. Different pore and domain sizes lead to a large difference in both the MSD and the time scales of the diffusion. For Figure 5.33A the limiting value is reached within the shown time frame. Time scales and resolution chosen for the experiments (Section 3.4.3) were sufficient to monitor the influence of the pore size on the movement of the domain. From the curves the diffusion coefficient and pore radius can directly be extracted as shown in panel F. Analysis was carried out for all 205 pores. The calculated diffusion coefficients lie in the range of $2 \cdot 10^{-4}$ to $2 \cdot 10^{-1} \, \mu m^2 \, s^{-1}$.

Comparison to theoretical diffusion coefficients

To test the validity of the results one can compare them to theoretical values.

In 1980 Hughes, Pailthorpe and White published a general approach to describe

the diffusion of objects in a membrane based on linearized Navier-Stokes equations (HPW model).[198] It described the two dimensional movement of a cylinder in a viscous membrane and takes translational and rotational drag into account. Its widespread use was hampered by computational demanding complex calculations needed to adapt to the physical parameters of the systems.[199] In 2008 Petrov and Schwille presented a numerical approximation of the model and validated it on experimental data provided by the group of Sarah Veatch.[199, 208] The diffusion coefficient of a particle with radius R and height h in a membrane with the surface viscosity $\eta_m = \mu_m \cdot h$ surrounded by two (aqueous) compartments with the viscosity μ_s is described by Equation 5.10 which depends on the reduced radius $\epsilon = \dfrac{R(\mu_1 + \mu_2)}{\eta_m}$.

$$D(\epsilon) = \frac{k_B T}{4\pi\eta_m} \cdot \frac{\ln(2/\epsilon) - \gamma + 4\epsilon/\pi(\epsilon^2/2)\ln(2/\epsilon)}{1 - (\epsilon^3/\pi)\ln(2/\epsilon) + c_1\epsilon^{b_1}/(1 + c_2\epsilon^{b_2})} \tag{5.10}$$

with c_1, c_2, b_1 and b_2 being empirical constants. Values for the physical parameters are given in Table 5.4.

Table 5.4: Parameters and typical values used in the Petrov-Schwille approximation of the HPW model.

property	value	description
μ_m	$1\,\mathrm{Pa\,s}$	viscosity of the membrane[199]
h	$4\,\mathrm{nm}$	membrane thickness[199]
k_B	$13.8\,\mathrm{yJ\,K^{-1}}$	Boltzmann's constant
T	$293\,\mathrm{K}$	temperature
μ_s	$0.001\,\mathrm{Pa\,s}$	viscosity of water[209]
γ	0.5772156649	Euler's constant
b_1	2.74819	empirical constant[199]
b_2	0.51465	empirical constant[199]
c_1	0.73761	empirical constant[199]
c_2	0.52119	empirical constant[199]

Equation 5.10 allows to calculate theoretical diffusion coefficients for the domains in pore-spanning lipid membranes. Figure 5.34 shows the results obtained by fitting the diffusion equation (Equation 5.8) to the experimental data and the theoretical curve according to the Petrov-Schwille approximation.
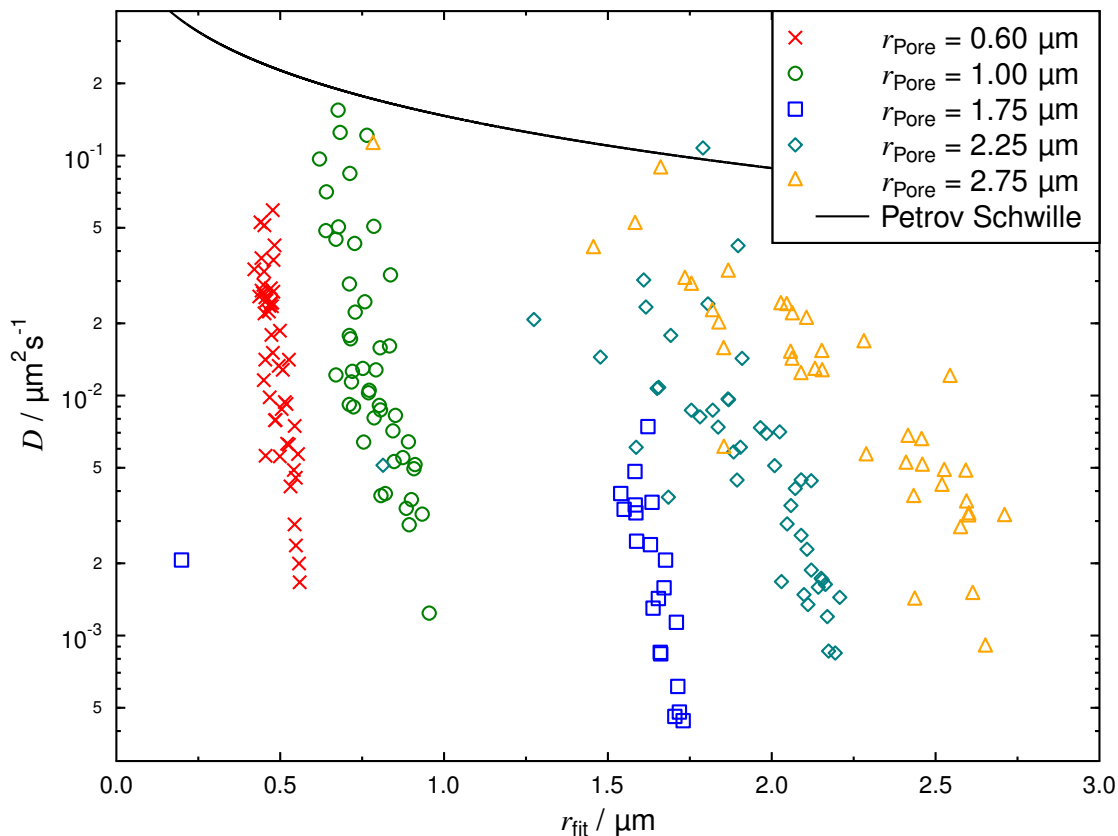
Figure 5.34: Summary of the diffusion coefficients of lipid domains in pore-spanning lipid membranes composed of DOPC/SM/Chol/Gb$_3$-Porc 40:35:20:5. Data extracted from substrates with different pore size are distinguished by their color and symbol. Analysis of 205 domains moving in PSMs of five different sizes was carried out. For each pore size, domains which are small compared to the area of the pore-spanning membrane are in the range of the theoretically predicted curve (black). The diffusion coefficient drastically drops when the domain occupies larger parts of the pore. This trend is visible for all 5 pore sizes.

The different pore sizes used are indicated by different symbols and colors. Obtained diffusion coefficients are generally lower than the theoretically expected values (black curve) and lie in the range of $2 \cdot 10^{-4}$ to $2 \cdot 10^{-1} \, \mu m^2 \, s^{-1}$. Domains in all five pore sizes show a drop in diffusion coefficient when the domain gets larger compared to the pore radius. This means that a small domain can rather freely move in the pore but the movement of large domains is slowed down even stronger than expected. As the effect is seen for all pore sizes, this retardation is not a function of the absolute domain size but its area fraction of the whole pore-spanning membrane.

The theory developed to describe the motion of domains in pore-spanning membranes is based on the assumption of a point-like particle or a disk diffusing in a circular confinement. An additional factor which is not included in the theory further influences the diffusion.

To understand this behavior two analyses were performed: i) the fitted domain radius (r_{fit}) was compared to the domain radius determined from thresholding the individual fluorescence micrographs of the time series (r_{FL}), ii) the lateral distribution of the domains in the pore-spanning membrane was analyzed. Figure 5.35 shows two schemes illustrating the analysis done in Figure 5.36.
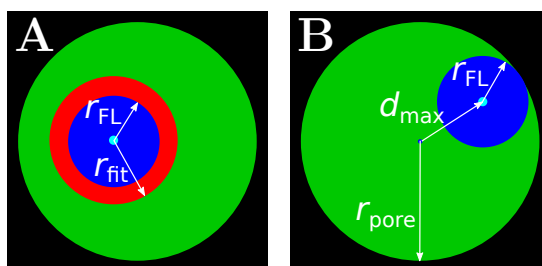
Figure 5.35: Analysis of the domain distribution. **A** The radius obtained from thresholding fluorescence micrographs (blue domain) r_{FL} can be compared to the radius from fitting r_{fit} (red area). **B** One can compare the maximum distance d_{max} of the domain's center of mass (teal) from the pore center to the difference of domain and pore radius.

Comparison of the domain radii

Figure 5.36A shows the comparison of the fitted (r_{fit}) and domain radius obtained from analysing the fluorescence micrographs (r_{FL}) as illustrated in Figure 5.35A. The values determined by the two methods are not identical and Equation 5.8 yields values which are larger by $70 \pm 50\,\%$ indicating that the equation leads to too large domain radii. To validate if the radius determined from the fluorescence micrographs or fitting the diffusion equation is the better measure for the actual domain size, the maximum distance of the center of mass of the domains from the pore center during the time series (d_{max}) was determined from the trajectories by Equation 3.29. This value is a direct indicator of the domain radius because the border of the domain hitting the pore border stops the movement (Figure 5.35B). It can be compared to the theoretical possible movement which is determined by $d' = r_{\text{pore}} - r_{\text{FL}}$.
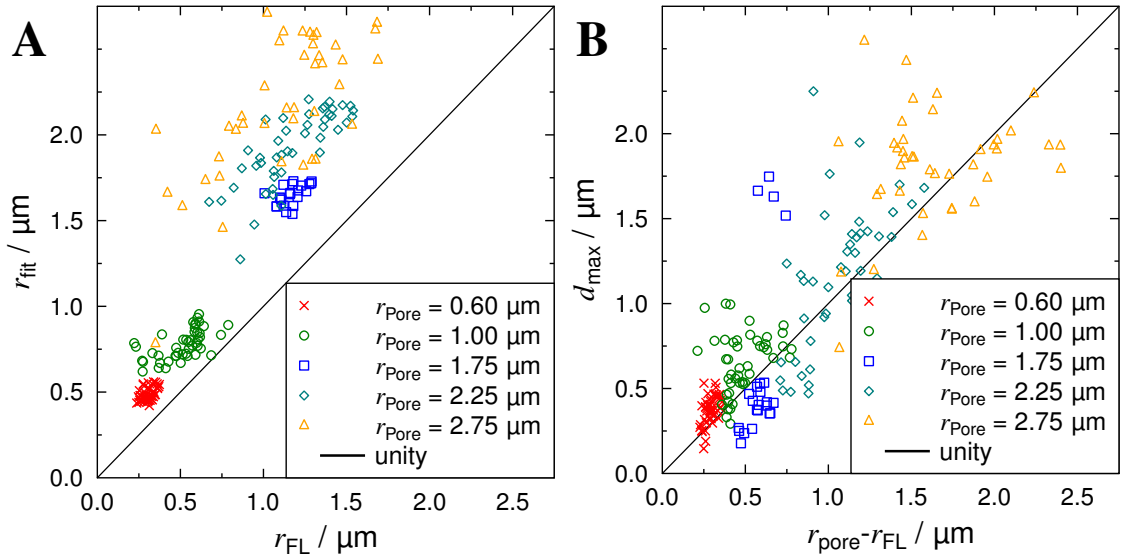
Figure 5.36: Comparison of the fitted domain radius and the radius obtained from fluorescence micrographs.. Data extracted from PSMs with different sizes are distinguished by their color and symbol. Analysis of 205 domains in five different PSM sizes was carried out. **A** Domain radius obtained from fitting the diffusion equation is considerably larger than the radius obtained from the fluorescence micrographs. **B** The maximum distance of the domain from the pore center is in good agreement with the predicted value from the fluorescence images.

Figure 5.36B shows the relation for the different domain and pore sizes. Agreement is good as the values are close to unity. The deviation is only $15 \pm 13\,\%$. This proves that the domain radii are determined too large using Equation 5.8. However, the values obtained from thresholding the fluorescence micrographs of the l_d marker dye are a good measure of the actual size of the domains.

Localization of the domains during the time series

The localization of the domain during the time series was investigated in more detail to find the reason why the domain radii are determined too large while the diffusion coefficients are underestimated. Trajectories as presented in Figure 5.29A can be used to construct the radial density distribution of the center of mass of the domain with respect to the center of the PSM.
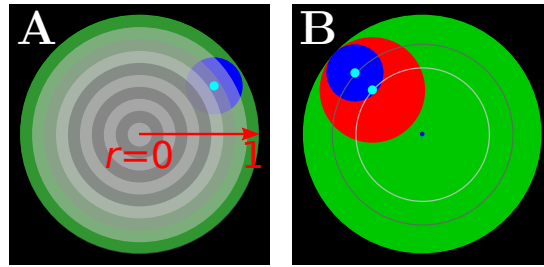
Figure 5.37: Analysis of the domain distribution. **A** The position of the center of mass (teal) of the domain can be localized in annuli. The area of the annuli is growing with distance from the pore center. **B** Comparison of the maximum distance of the domain from the pore center for domain sizes determined by thresholding (blue, dark gray line) and fitting Equation 5.8 (red, light gray line).

The distance of each center of mass to the pore center (teal dot) was calculated. Data was binned in 50 annuli (Figure 5.37A) resulting in the distribution shown in 5.38A but the distribution in panel A is biased. As the bin size is constant, steps towards the rim corresponds to an annulus of growing area. Correcting for this increase in area results in the distribution shown in panel B (Section 7.3). One finds that there is a drop in probability to find the domain towards the pore rim at $r = 1\,\mu m$.

The centroid of the domain is not located at large r ($>0.55\,\mu m$) because the contact of the domain ($r_{FL} = 0.54\,\mu m$) with the rim prevents the domain moving closer.

The dark gray line corresponds to the maximum displacement expected from r_{FL} before the domain's border comes in contact to the rim. The value is in good agreement with the found displacements (Figure 5.37B). The light gray line corresponds the situation using the radius obtained from fitting Equation 5.8 and as expected, the value is too small. However, at intermediate radii ($0.2\,\mu m < r < 0.55\,\mu m$) there is a drop in probability to find the domains even though it is still not in contact with the pore border.
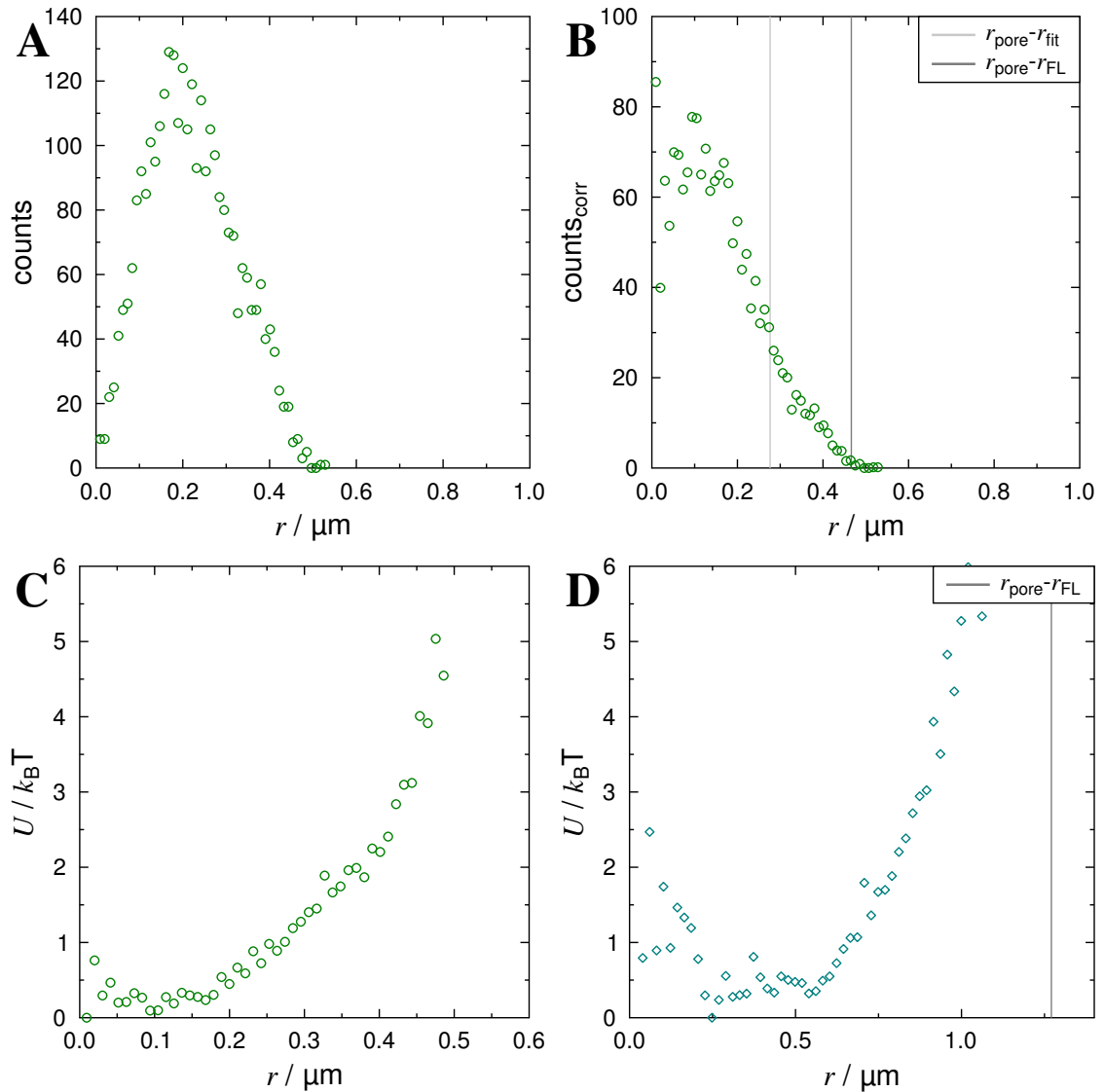
Figure 5.38: Radial distribution of the domains and resulting energy profiles. **A** Distribution of the centroid of a domain in a pore with radius 1.0 µm. **B** Data in **A** corrected for the growing areas included in each binning interval. The light gray line depicts the maximum displacement predicted from the fitted domain radius. The dark gray line depicts the maximum displacement predicted from the thresholding. **C** Relative energy profile determined from the distribution shown in **B**. **D** Energy profile for a domain in a pore with radius 2.25 µm. The profile is shaped differently and has second energy maximum at the center of the PSM.

It is more probable to find the domain in the pore center. The probability can be used to calculate a relative radial energy profile describing the energetics responsible for the localization of the domain in the pore. The curve in panel B is converted to the probability density (g) by normalizing the area under the curve to 1 to give

$g(r)$. Using Boltzmann's distribution (Equation 5.11), the probability is converted to the energy distribution.

$$g(r) \propto e^{\left(\frac{U(r)}{k_{\mathrm{B}}T}\right)} \rightarrow \left(\frac{U(r)}{k_{\mathrm{B}}T}\right) \propto \ln g(r) \qquad (5.11)$$

The lowest value is set to 0 and the energy distribution depicted in Figure 5.38C shows that a domain which is located in the pore center has the lowest energy. Energy afflicted with the diffusion is constant close to the pore center forming an energetic plateau ($\approx 0.2\,\mu\text{m}$ in Figure 5.38C). Moving the domain towards the rim is associated with an energetic penalty. For larger domains the plateau in the pore center is smaller, indicating that the approach of the domain area to the rim is responsible for the energetic penalty. The absolute energies and shapes of the curves were found to be independent of the pore size for most of the domains studied, showing that the ratio of domain and pore sizes determines the energetic profile. A possible reason for this energy barrier is discussed in Section 5.4.4.

This type of energy profile was found for 69 % of the domains studied. For 20 % of the pores a second type of energy distribution was found which is shown in Figure 5.38D. The energetic penalty to move towards the pore border is also present, but a second energy barrier is located in the pore center. Of note, this type of profile was exclusively observed using pores with a diameter of 3.5, 4.5 and 5.5 µm. The remaining pores had profiles with a linear increase towards the rim or could not be easily described.

As most of the domains exhibit a similar energy profile a pooled curve was calculated to illustrate the influence of the pore geometry on the domain's energetics. To compare different pore sizes the radius shown on the x axis was converted to relative coordinates by dividing by the pore radius. To compensate for different domain size the curves were compressed in x direction between the pore center and the maximum distance from the center the domain's center of mass was found (d_{max}). The curves were normalized in y direction to values between 0 and 1 (Figure 5.39A).
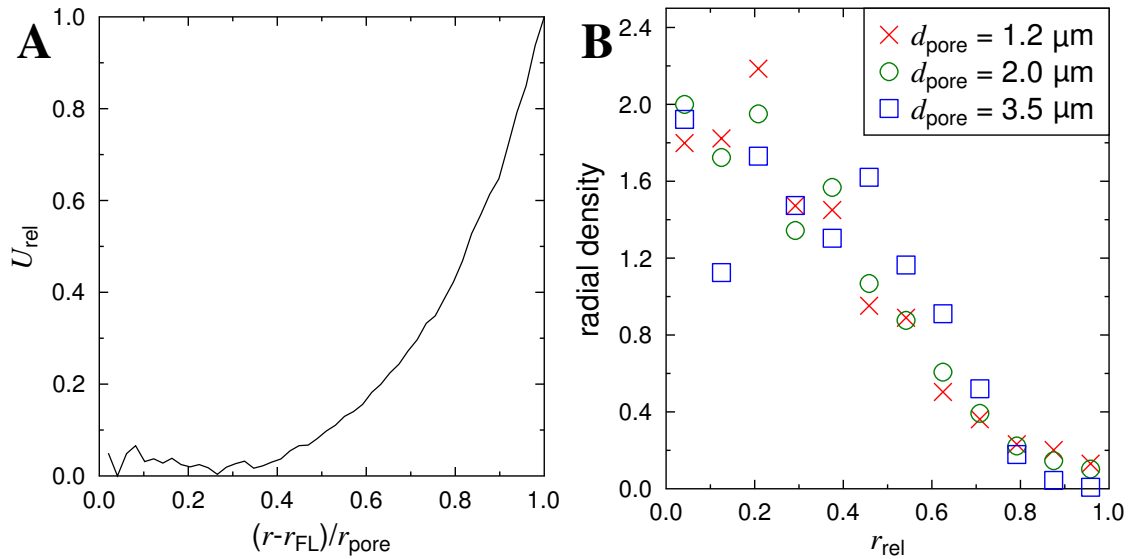
Figure 5.39: Radial distribution of the center of domains and the l_o area in PSMs. **A** Energy profiles extracted from 205 domains moving in PSMs pooled into one curve. The y axis has been normalized to lie between 0 and 1. **B** Radial density distribution of l_o area in PSMs extracted from time series of moving domains.

The resulting curve adopts a shape having an energetic plateau at the pore center and an energy barrier at the rim, substantiating that the proximity of the domain to the rim seems to be the major contribution to the energetic penalty.

The radial density distribution of l_o area in the pore-spanning membranes during the time series was constructed for pores with radii of 0.6, 1.0 and 1.75 μm (Figure 5.39B). The distribution differs from the one in panel A in the way that not the center of mass of the domain is taken into account but each pixel associated with l_o phase is evaluated. The distribution of l_o area further supports the conclusions drawn. It is less probable to find l_o area at the rim compared to the center and the density is close to 0 at the border of the pore. It can be compared to the density distributions shown in Figure 5.22 extracted from snapshots of the membrane organization, where domains are also located at the pore border, leading to a homogeneous distribution of l_o area in the pore.

Results presented in this Section prove that porous substrates are a powerful tool to influence the dynamics of lipid domains in pore-spanning lipid bilayers. Domains in contact with the solid support mimic the pinning of domains by the cytoskeleton. Movement of a domain in the pore center is impaired by the fence like pore geometry

allowing to study the complex dynamics of the domains. A newly developed theory can describe the movement of the pores but an additional influence is superimposed and further changes the diffusion of domainsin the freestanding membrane area.

5.3.5 Topography mapped by SICM

Tracking the movement of lipids domains in PSLBs revealed an additional energetic barrier for the diffusion at the border of the pore. To elucidate a possible relation to the three dimensional structure of the pore-spanning lipid bilayers, scanning ion-conductance microscopy (SICM) was used to map the topography of the PSLBs. Experiments were conducted on membranes prepared on substrates with pore diameters of 1.2 and 5.5 μm in PBS as described in Section 3.3.3. Figure 5.40 shows the topography of pore-spanning membranes composed of DOPC/SM/Chol/Gb$_3$-Porc 40:35:20:5 imaged by SICM on a substrate with pores with a diameter of 1.2 μm. In the center of the image membrane spanned pores were detected. The rim is slightly elevated (lighter color coding) and the hexagonal structure of the porous mesh can be seen. Pores are slightly lower than the rim, indicated by the darker color coding. On pores with a diameter of 1.2 μm the height difference between rim and center of the PSMs was found to be $\Delta h = 50 \pm 28$ nm (n $= 110$). Ratio of depth and pore radius $\Delta h/r$ is only 0.08 ± 0.05 proving that the topography is nearly flat. The line profile along the red line (Figure 5.40B) shows that no sharp drop in height is found at the pore border but a gradual decay in height from the rim to the center of the PSM. In the top right corner of panel A, non membrane covered pores were imaged (black color coding). On the bottom of panel A the flat structure of a rim is visible. Bright spots correspond to adhered vesicles which were imaged.
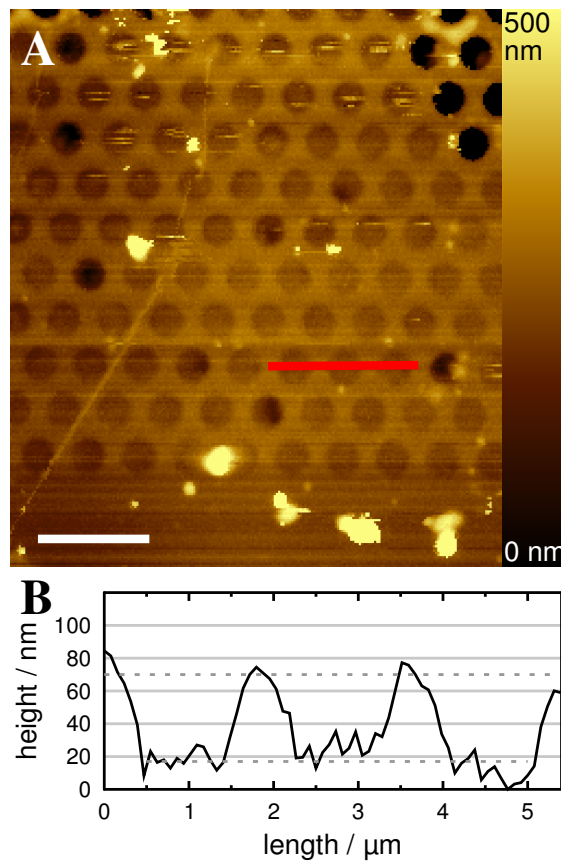
Figure 5.40: Scanning ion-conductance micrograph of a membrane composed of DOPC/SM/Chol/Gb$_3$-Porc 40:35:20:5 in PBS on a porous substrate with pore diameters of 1.2 µm. **A** On the bottom the flat surface of the rim is visible. In the center of the image the pores are covered with membrane as indicated by their slight lower height (darker color coding). In the top right non covered pores are visible (black color coding). Scale bar: 4 µm. **B** Cross section along the red line in **A** showing a height difference between rim and pore of $\approx$50 nm.

Figure 5.41 shows two characteristic topography maps of pore-spanning membranes with diameters for 5.5 µm. On pores with a diameter of 5.5 µm the height difference between rim and the center of the PSM was found to be $\Delta h = 134 \pm 55$ nm (n = 12). The ratio $\Delta h/r$ is 0.05 ± 0.02 indicating a direct relation between pore diameter and the z position of the pore-spanning membrane.
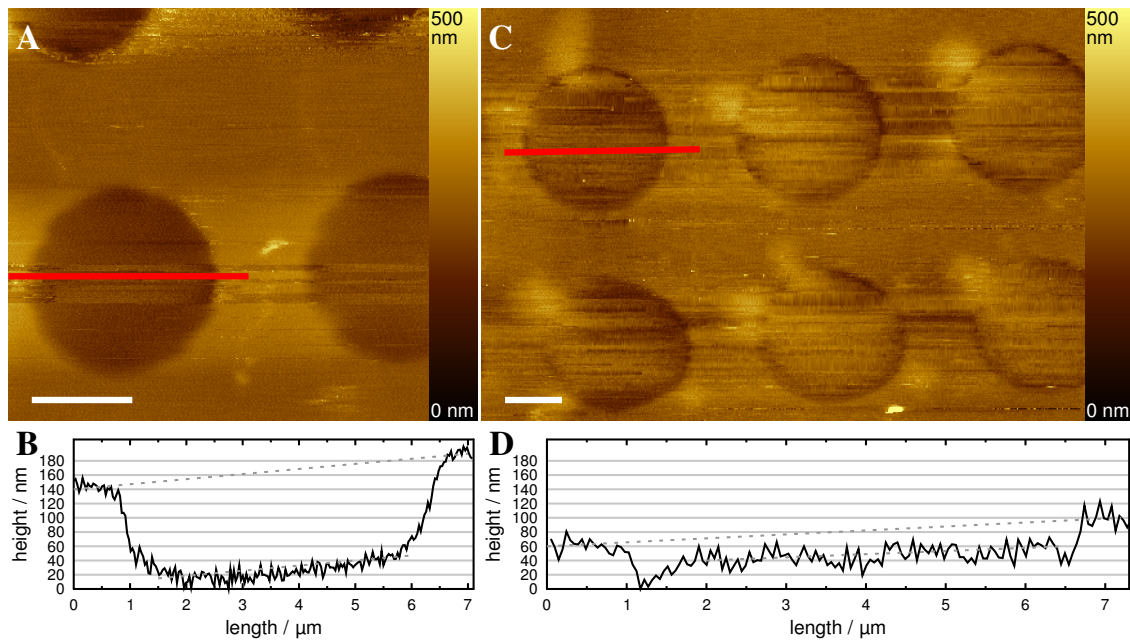
Figure 5.41: Scanning ion-conductance micrographs of a membrane composed of DOPC/SM/Chol/Gb$_3$-Porc 40:35:20:5 in PBS on a porous substrate with pore diameters of 5.5 µm. **A** Image depicting pore-spanning membranes with high resolution. **B** Line profile along the red line in **A** shows that the membrane covering the pore is flat. No sharp drop in height at the pore rims is found but a gradual descend. **C** Image depicting pore-spanning membranes with high resolution. **D** Line profile along the red line in **C** shows a drop in height at the pore rim and a slightly elevated, bulged structure in the center of the membrane spanned pore. Scale bars: 3 µm.

For these PSMs two different types of membrane topographies could be imaged. Panel A and B show a case which closely resembles the situation imaged on pores with a diameter of 1.2 µm. The larger pore radii allow to image the topography with better spatial resolution (174 data points per scan axis and pore diameter). One finds that the membrane is located flat in the center of the spanned pore. At the pore rim a gradual increase in height towards the rim is imaged. No steep increase in height as expected from the SEM images was found (see Section 3.2.3). Some pores exhibit a different topography (Figure 5.41C/D). The height at the rim region is lower than in the center of the PSM. Possible mechanisms explaining this behavior are given in Section 5.4.1.

PSLBs imaged by SICM after binding of STxB

STxB binding to Gb$_3$ in lipid membranes induces negative curvature.[71] SICM enables to monitor the possible alterations induced by STxB with hight axial resolution.

Figure 5.42 shows a membrane composed of DOPC/SM/Chol/Gb$_3$-Porc 40:35:20:5 prepapred on a substrate with pore diameters of 1.2 μm. In panel A the topography is imaged prior to incubation with STxB and a height difference between the center of the PSM and the rim of $\Delta h = 56 \pm 39$ nm (n $= 20$) was found.
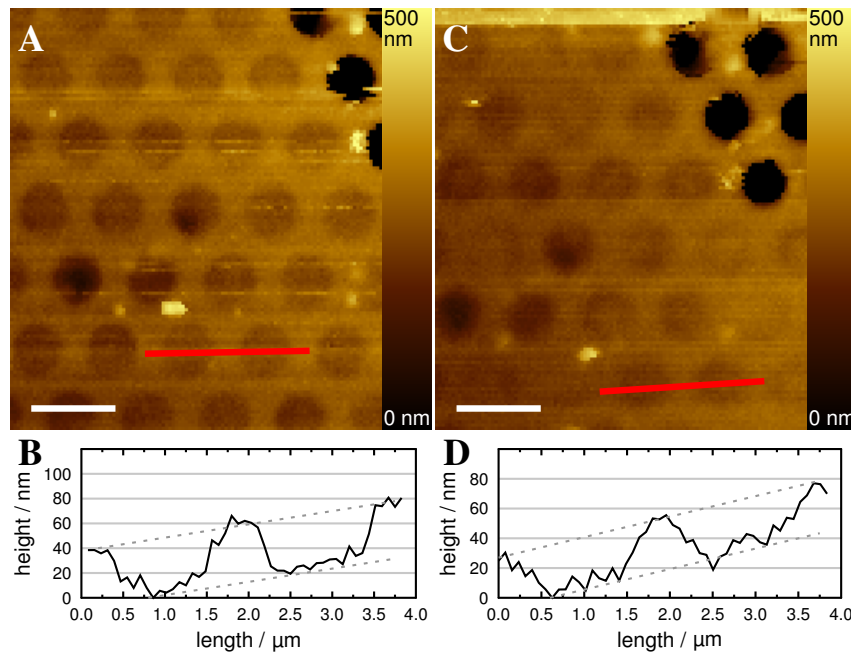
Figure 5.42: Scanning ion-conductance micrographs of membranes composed of DOPC/SM/Chol/Gb$_3$-Porc 40:35:20:5 in PBS. **A** Membrane patch imaged prior to protein incubations. Pore-spanning membranes are localized slightly below the pore rim. Open pores were imaged in the top right corner. **B** Cross section along the red line in **A**. A slight tilt of the substrate is visible but two height levels (pore and rim) can be identified. **C** Membrane patch after incubation with 60 nM STxB for 100 min. Despite a slight x-y drift no changes in topography occurred **D** Cross section along the red line in **C**. Scale bars: 2 μm

Panel C shows the same pore-spanning lipid membrane after incubation with 60 nM STxB for 100 min. The pores mapped in A can readily be identified with respect to the uncovered pores at the top right and the height difference was found to be $\Delta h = 39 \pm 30$ nm (n $= 20$). Binding of STxB does not alter the topography of the membranes. No invaginations induced by STxB are visible from the line scan exemplary shown in panel B and D.

5.4 Discussion

In recent years the picture of the plasma membrane has become more and more complex. Starting from the fluid mosaic model published by Singer and Nicolson in the 1970s,[2] newly developed chemical and physical techniques have revealed complex substructures in the membrane.[8,10,16,17] Today it is widely accepted that the plasma membrane harbors lipid domains of distinct chemical composition which play a decisive role e.g. in signaling processes.[10] The exact nature of the membrane heterogeneity is still under debate.[14,210] Different theories suggest lipid-lipid driven compartmentalization, actin driven membrane segregation and protein-lipid-cluster formation.[16,200,210] Despite new techniques like super-resolution optical microscopy,[13] studying the lateral organization in the plasma membrane of living cells is still a major challenge.

Experiments involving giant plasma membrane vesicles (GPMVs) showed that the liquid-ordered/liquid-disordered phase separation found in artificial membrane systems can resemble to putative rafts in the cell membrane.[3,27] However, the size of the domains formed in GPMVs and artificial membranes is in the range of several dozens to hundreds of square microns. Cells from which the GPMVs were derived do not show any lipid domains on the micron scale indicating that the underlying actin cytoskeleton is of major importance.[3,16]

Several groups have used different approaches to influence the phase separation of artificial membranes using pore-spanning lipid bilayers,[51] mixed polymer-lipid membranes,[211] micro patterned substrates[212,213] and artificially attached cytoskeletal networks.[196,214] The mechanisms to control the phase separation are based on different physical aspects: membrane fluidity can control the aggregation of nanodomains to microscopically large structures,[213] engineered surface chemistry can induce order and disorder in the membrane,[212] micropatterned substrates induces curvature in the membrane,[215–217] and the controlled physical attachment to a support[51] can modulate the phase separation.

In this chapter the impact of a porous mesh as a mimic for the actin cytoskeleton on the organization of artificial membranes was studied. Pore-spanning lipid bilayers (PSLBs) combine the benefits of solid supported membranes and giant unilamellar

vesicles yielding long-term stable membranes with high dynamics. In the discussion the main properties and features of the PSLBs will be taken into consideration and their relevance to mimic biological processes will be examined. Starting with the membrane topography, the structure and dynamics of lipid domains will be discussed.

Figure 5.43 illustrates the model for the structure of phase-separated lipid membranes composed of 1,2-dioleoyl-*sn*-glycero-3-phosphocholine (DOPC), sphingomyelin (SM), cholesterol (Chol) and Gb_3-Porc in a molar ratio of 40:35:20:5 in absence of bound Shiga toxin subunit B (STxB). It includes the major findings derived from the data in Section 5.3. The membrane covers both the solid supported and freestanding areas as a continuous bilayer. l_d phase is identified by the marker dye shown in green. At the border between the solid support and the pore the membrane follows the gold functionalization into the pore, forming a curved membrane region. The dimensions in x,y and z are not drawn to scale. For simplicity, Gb_3 in the bottom leaflet is omitted.

Two major classes of l_o domains were found in pore-spanning membranes with coexisting lipid phases. Figure 5.43A shows a l_o domain (dark) in contact to the pore rim. It is bent due to the curvature at the pore border. Energetics of this arrangement are discussed in more detail in Section 5.4.2. The second class of domains is located only in the freestanding membrane (Figure 5.43B). These domains are highly mobile but do not leave the freestanding membrane area. Analysis of the movement (Section 5.3.4) is discussed in more detail in Section 5.4.4.
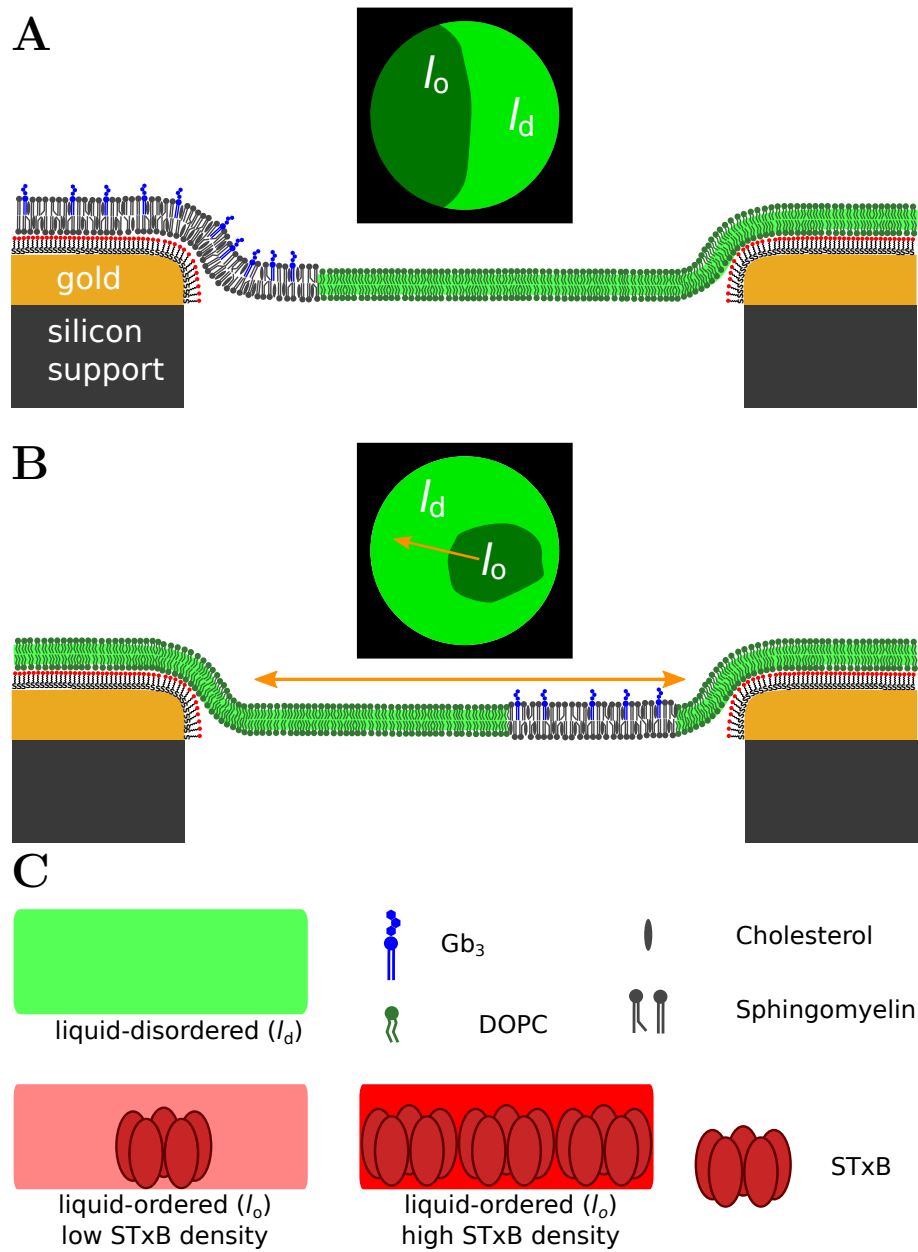
Figure 5.43: Proposed model for the membrane organization prior to STxB binding. The insets illustrate the top view. **A** A liquid-ordered domain is in contact to the pore rim. **B** A l_o domain is located in the freestanding membrane part and is moving. **C** Color coding and symbols used throughout the discussion.

5.4.1 Membrane topography

The topography of phase-separated lipid membranes composed of DOPC/SM/Chol/Gb$_3$-Porc 40:35:20:5 prepared on substrates with pore diameters of 1.2 and 5.5 µm was investigated using scanning ion-conductance microscopy (SICM). In the center of the pores the membrane is slightly lowered compared to the membrane covered rim as previously reported for painted pore-spanning membranes[100] and solvent free pore-spanning membranes (Figure 5.43).[218] Membranes spanning the pores have a height difference compared to the rim of 30-200 nm. PSLBs on pores with a diameter for 5.5 µm are located lower inside the pore, but the ratio of the height in the pore center compared to the diameter of the pore is similar. This relation is most likely caused by the membrane following the gold functionalization into the pore.[43, 44, 100] Only the regions at the pore rim exhibit curvature (*vide infra*).

Phase separation into liquid-ordered and liquid-disordered domains cannot be imaged using the SICM. The height difference of ≈1 nm between the l_o and l_d domains is below the axial resolution of about 10 nm.[86, 100, 101] However, one could imagine visualizing the phase separation by the difference in electrical properties of the phases caused by the larger thickness of the l_o phase, which would result in a lower membrane capacity and higher electrical resistance.[219] Figure 5.44 shows a scheme of the SICM pipette approaching a pore-spanning membrane and the corresponding equivalent circuit to calculate the total resistance (R_{tot}).
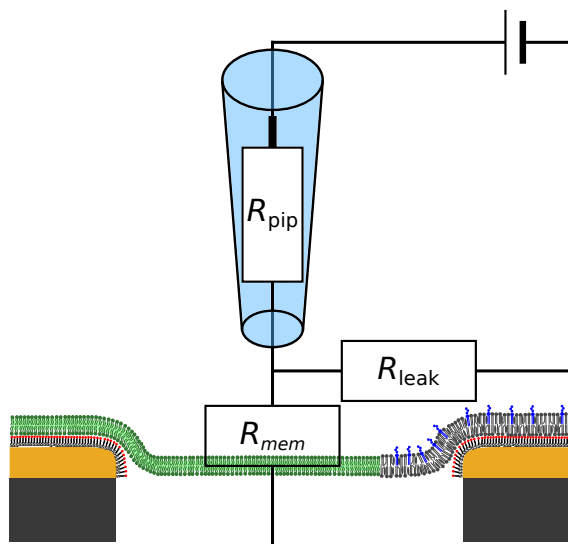
Figure 5.44: Scheme and equivalent circuit of the SICM pipette in close proximity to the partially ion conductive pore-spanning membrane.

Current flowing through the membrane can be modeled as a resistance R_{mem} in parallel to the z dependent leakage resistance R_{leak}.

$$R_{\text{tot}} = R_{\text{pip}} + \frac{R_{\text{leak}} \cdot R_{\text{mem}}}{R_{\text{leak}} + R_{\text{mem}}} \tag{5.12}$$

The pipette resistance (R_{pip}) is constant and does not depend on the z position. The resistance of a pore-spanning membrane is typically $>1\,\text{G}\Omega$.[220] Leakage resistance can be calculated according to Equation 3.9 (page 43). Typical values ($\kappa = 1\,\text{S}\,\text{m}^{-1}$, $r_{\text{i}} = 100\,\text{nm}$, $r_{\text{a}} \approx \frac{r_{\text{i}}}{0.58}$, $z \approx \frac{1}{2}r_{\text{i}}$) give a resistance R_{leak} in the low megaohm regime. The total resistance according to Equation 5.12 hence exclusively depends on the leakage and pipette resistance and no contribution of ions passing through the membrane will be detected. It is therefore impossible to image the phase separation using the SICM. Height differences observed are truly caused by the actual topography of the membranes.

In the high resolution line profile of the topography of a single pore-spanning membrane with a diameter of $5.5\,\mu\text{m}$ shown in Figure 5.41C, no steep drop in height at the pore rim is observed. This previously reported feature is either the real topography or an artifact caused by the imaging technique.[100] In 2013 Thatenhorst *et al.* used micro structured substrates in conjunction with finite element simulations of the ion flow to answer the question, if a defined current signal in SICM always corresponds to the same tip-sample separation.[101] Figure 5.45A illustrates a scheme of a nanopipette approaching a sample surface with a steep slope. The authors found that not the actual axial position d_{v} is measured but in first approximation that the height corresponds to the normal distance d_{n}.[101]
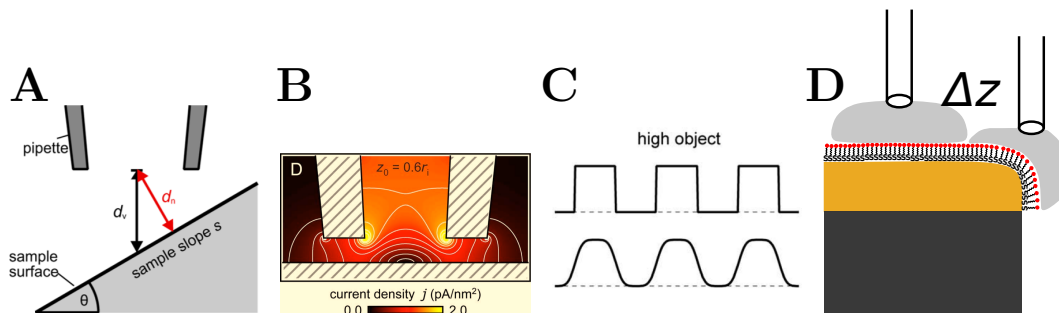
Figure 5.45: Convolution of SICM pipette geometry with the substrate topography. **A** On a steep surface the z position of the pipette depends on the slope of the sample. **B** Current density profile for SICM pipette approaching a flat surface. **C** The z profile of high objects (top row) with steep height changes is convoluted with the pipette geometry. The resulting height profile is shown in the bottom row. **D** Scheme depicting the effect on the steep pore rim. Ion flow into the pipette from the gray region which slowly increases upon lateral approach to the pore. The change in height will be blurred during imaging. Panel **A** reproduced from Thatenhorst *et al.*.[101] Panel **B** and **C** reproduced from Rheinländer *et al.*.[221]

The reason is the current density profile (Figure 5.45B) as published by Rheinländer *et al.*.[221] On a flat surface the current flow has a radial symmetry with respect to the pipette. Imaging high objects with a steep descends will convolute the actual topography of the sample with the pipette geometry by a transfer function resulting in a smoothing of the height changes (bottom row in Figure 5.45C). To extract the true three dimensional structure of pore-spanning lipid membranes from the SICM data, finite element simulations describing the ion flow would be beneficial. Figure 5.45D shows a simplified representation of the phenomenon. A pipette scanning the pore is effectively detecting ions from the shaded volume. At the pore rim the threshold is reached at a lower point because an additional ion current in z direction is present, resulting in a smoothed drop at the pore rim. A more detailed view on the shape and mechanics of pore-spanning membranes is given in Section 5.4.2.

Protruded pore-spanning membranes

Membranes spanning pores with a diameter of 5.5 μm occasionally have a second topographic feature where the membrane at the center of the pore is elevated again (Figure 5.41C/D). Heights can reach values slightly above the level of the rim height.

Simon *et al.* reported the possibility to fill the compartment below the pore-spanning membrane with an air bubble, which could lead to an elevation of the membrane at

the center.[200,218] The air entrapment was found using substrates with hydrophobic surface functionalization and it seems unlikely that this effect occurs using the hydrophilic functionalization used in this work.

A possible additional electrical resistance in the pore center caused by the full surrounding of the pipette by the pore rim is also no the explantion for the protrusion. Böcker *et al.* found this effect for deep immersion in pores with a diameter of 450 nm. The effect was already less pronounced for larger pores (800 nm) and is negligible for the large pores used in this study.[100]

In the height profile shown in Figure 5.41C, a low height is measured directly at the rim. Even though membrane permeability seems improbable to cause this it cannot be ruled out that the high membrane curvature at the rim partially permeabilizes the lipid bilayer causing an apparent lower height.[222]

According to Rheinländer and Clarke *et al.* the interactions between the pipette and the surface are able to deform the latter.[223,224] However in both studies the interaction was repulsive and a possible rising of the membrane due to a fast pipette retraction seem rather unlikely due to the high membrane tension.[44]

Frese and Gleisner reported the production of micrometer high protruded pore-spanning membranes.[46,53] The protrusion was induced by an inflow of water into a sealed compartment below the membrane. Substrates used in this thesis are based on the manufacturing procedure for pores with closed cavities published in Frese *et al.*.[53] Deliberate overetching was used to connect the cavities at the bottom, forming a sieve like structure. It cannot be ruled out that this process is incomplete. However, evaporation of buffer solution during the SICM experiment would lead to the converse effect and push the membrane in the pore. Therefore a mechanism driven by osmotic pressure is also not the explantion for the protrusion observed. Whether the topography is an artifact of the scanning technique or a feature of the large pore diameters is still elusive. The reasoning of a protruded structure will be considered in some more detail in Section 5.4.4.

Influence of STxB binding on the topography

STxB binding to Gb_3 containing membranes induces negative curvature, resulting in the formation of inward facing membrane tubes with a diameter of ≈ 50 nm.[71] At the lateral resolution of the SICM it seems unlikely to directly detect these invaginations, but the induction of negative curvature might change the topography of the PSM. However, incubation of the Gb_3 containing pore-spanning membrane

with STxB did not change topography (Figure 5.42). Several mechanism will inhibit the induction of negative curvature in the pore-spanning membranes used in this thesis. Figure 5.46 shows three possible mechanisms.

After initial binding of STxB to Gb$_3$ located in the l_o domains the protein asymmetrically compresses the upper leaflet leading to the induction of negative curvature. In the chosen lipid system DOPC/SM/Chol/Gb$_3$-Porc 40:35:20:5 macroscopic domains are present. Windschiegl *et al.* showed that binding to macroscopic domains only leads to shallow invaginations with STxB being enriched in the border region.[70] This interplay of domain structure and specific lipid curvature has been previously reported by Baumgart *et al.*.[148] Detecting these "dimples" is difficult as the change in membrane height is only low.
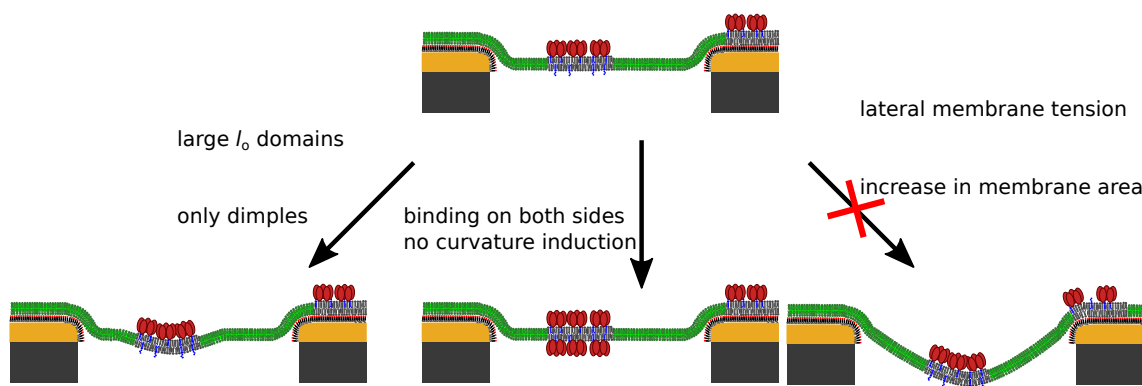
Figure 5.46: Mechanisms inhibiting the formation of invaginations on pore-spanning membranes. Left: Windschiegl *et al.* reported that freestanding phase-separated membranes will only form shallow invaginations.[70] Center: The open pore structure might allows additional STxB to bind to the bottom leaflet of the membrane. Right: For the formation, lipid material has to flow into the freestanding membrane area.

A second mechanism inhibiting membrane bending might be caused by the open pore structure of the substrates used (Section 3.2.3). Spreading of GUVs leads to the formation of isolated membrane patches. In principle, protein can enter an open pore and diffuse to the bottom leaflet of the pore-spanning membrane. This would lead to an equal lipid compaction in both leaflets resulting in no change in membrane topography. Both factors can be overcome by using homogeneous, fluid membranes on closed pore arrays.[46] However, a third influence would still effectively prevent any changes in topography.

The right panel of 5.46 illustrates that curving a pore-spanning membrane requires additional lipid material. Contact of the membrane to the solid support

support induces a tension in the range of $1\,\mathrm{mN\,m^{-1}}$,.[43, 44, 46] Ewers, Römer *et al.* found that membrane tension above $10^{-2}\,\mathrm{mN\,m^{-1}}$ will inhibit the formation of invaginations on reasonable time scales.[72] To overcome the large tensions the surface functionalization would have to be changed to lower the membrane tension.

Using scanning ion-conductance microscopy the presumed topography of pore-spanning lipid bilayers was validated for the first time for phase-separated membranes. SICM enables to map the topography independent of the exact membrane composition. Membranes were found to be flat in the center of the PSLBs, but the data recorded shows curved membrane regions at the pore border which might influence the dynamics and structure of lipid domains in the freestanding membrane area. Shiga toxin binding to the membrane did not alter the membrane topography.

5.4.2 Domain structure

In Section 5.3.1 giant unilamellar vesicles were used to visualize the lipid domains by confocal fluorescence microscopy.[29] In accordance with results published in literature, the domains were found to have diameters of several micrometers and frequently only two lipid domains remain in the GUV.[29, 30, 37, 115] The diffusion of lipids and domains in GUVs is free and unhindered, leading to the condensation of the domains to minimize line tension.[29, 30, 208] This is in clear contrast to the smaller domains found in cells and on solid support.[3, 89] Bhatia *et al.* used confocal microscopy to quantify the amount of l_o phase in GUVs and visualize the domain structure.[115] They found that spreading a phase-separated GUV below its phase transition temperature 'imprints' the domain structure of large domains onto the solid support.

Phase-separated pore-spanning membranes were formed by spreading of GUVs on porous support. To elucidate the influence of the support on the lateral organization of the membrane, GUVs composed of DOPC/SM/Chol/Gb$_3$-Porc 40:35:20:5, were spread above the phase transition temperature. Upon cooling to room temperature while the membrane is in contact to the substrate, the membrane phases separate. The influence of the support on formations of domains and their morphology can be analyzed.

Energetics of rim-domain interactions

The position of l_o domains observed by fluorescence microscopy in PSLBs was determined and two major types of domains were found: domains in the pore center and domains in contact to the rim.

To quantify the position of l_o area in the freestanding part of the membrane, radial density distributions were constructed (Figures 5.22 and 5.39B). Values determined depict the observed distribution of l_o area in the pore as a function of the distance from the pore center. However, one has to be careful in interpreting the data. The l_o area is not homogeneously distributed in the pore-spanning membrane (PSM) but the domains adopt circular shapes to minimize line tension. This shape influences the distribution of l_o area is the pore, for example a domain in contact to the rim adopts a bud like shape, which extends further towards the pore center compared to a domain that flattens out at the pore border to form a crescent shape. The radial density profile of moving domains (Figure 5.39B) shows that domains are rarely localized at the pore rim, indicating an energetic penalty to move the domain to the rim. However, in the static observation of the PSLBs, domains in contact with the rim are frequently observed (Figure 5.22), indicating an additional energetic contribution.

Figure 5.26 and 5.27 show that multiple l_o domains in the freestanding membrane areas coalesce to form larger domains. This indicates that line tension is a major factor contributing to the energetics of the lipid domains in the freestanding membrane areas.[148] Line tension (μ) arises from the difference in hydrophobic thickness of the liquid-ordered and liquid-disordered phase and is highly dependent on the difference in thickness.[41] μ has been experimentally and theoretically determined to be in the order of tenths to thousands of femtonewton.[42,225] For a lipid mixture DOPC/SM/Chol 40:40:20 similar to the one used in this thesis, García-Sáez *et al.* determined a value of $\mu = 1.2 \pm 0.5\,\mathrm{pN}$ at room temperature.[42]

Figure 5.47 shows a possible explanation why domains can be localized at the pore rim, taking into account the line tension of domains and the bending of the membrane at the rim found using SICM experiments.
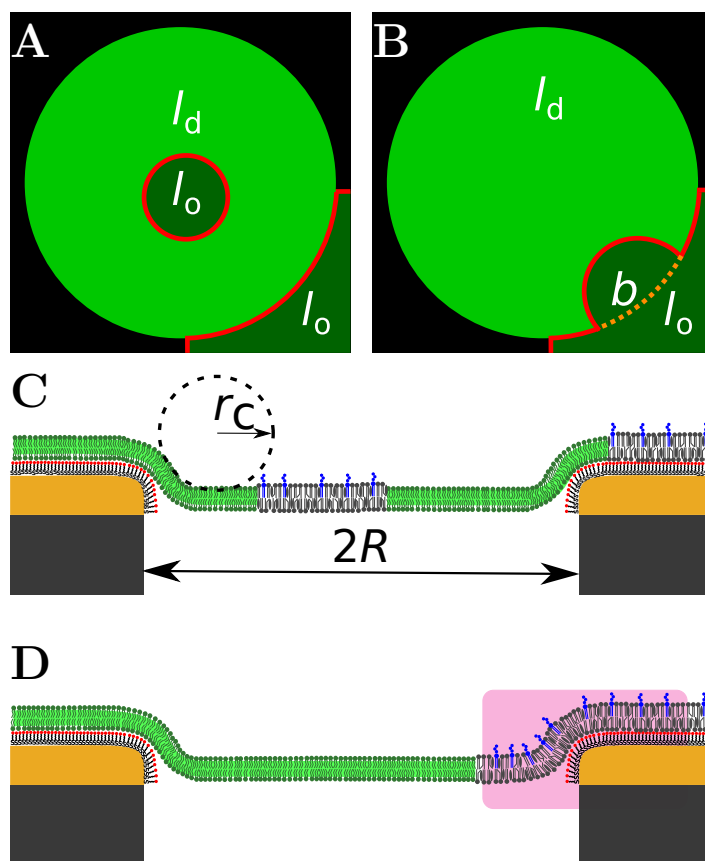
Figure 5.47: Schematic comparison of domains moving or in contact with the pore rim. **A** The l_o domain in the center of the pore is moving. Another l_o domain on the rim is hypothesized. The red line indicates the length relevant for line tension. **B** Same as in **A** but with a domain of similar size condensed to the l_o domain on the rim. The energy of line tension is reduced by the length b. **C** Schematic side view of the domain in **A**. Geometry of the membrane spanning a pore of diameter $2R$. The membrane is assumed to follow the thiol functionalization, resulting in a bending radius of r_c. **D** Scheme showing a bent, condensed l_o phase as in **B** (magenta box).

The energy E_{LT} of line tension can be calculated knowing the length of the phase border x.

$$E_{LT} = \mu \cdot x \tag{5.13}$$

Considering the case presented in Figure 5.47 with a l_o domain condensing to a rim based l_o area, line tension reduction by the length of the newly formed contact line b will be a driving force. The l_o domain on the rim is hypothesized. Assuming the pore radius to be much larger than the domain radius and the formed bud to have a half circular shape, b can be expressed as a multiple of the domain radius r: $b = 2\sqrt{2}r$. The exact value is not important for the reasoning below (see Section

7.2). An opposing force to the condensation of the domains as shown in Figure 5.47B will be bending of the stiffer l_o domain at the pore border. The bending rigidity of the l_d phase is around $10\,k_B T$.[34, 148, 215] Values published in literature for the bending rigidity of l_o domains greatly differ between 12 and 30 $k_B T$.[34, 148, 179, 215, 226, 227]

Based on observations by Böcker *et al.* the membrane will follow the functionalization into the pore and form a flat membrane,[228] resulting in the geometry of the pore-spanning lipid membrane as drawn in Figure 5.47C. It is therefore bent with a bending radius r_c at the border of the pore.[100] The energy needed for bending a membrane around a cylinder is:

$$E_{B, \text{ cylinder}} = \pi \kappa_B \frac{L_c}{r_c}, \tag{5.14}$$

with $E_{B, \text{ cylinder}}$: bending energy, κ_B: bending rigidity of the membrane and L_c: length of the cylinder.[228] The geometry of the pore can be described as a toroid with the length $L = 2\pi(R - r_c)$. Böcker *et al.* assumed that the membrane covers 1/4 of the cylinder surface and the overall energy of bending can then be expressed as:

$$E_B = \frac{1}{4} \pi \kappa_B \frac{2\pi (R - r_c)}{r_c} = \frac{1}{2} \pi^2 \kappa_B \left(\frac{R}{r_c} - 1 \right). \tag{5.15}$$

Taking into account the energy of tension ($E_\sigma = \sigma \cdot A$, A: area of the PSM)[43–45, 228] and assuming $r_c \ll R$ the bending radius can be calculated.[100, 228]

$$r_c = \sqrt{\frac{1}{2} \frac{\pi^2}{\pi^2 - 2\pi}} \cdot \sqrt{\frac{\kappa_B}{\sigma}} \approx 1.173 \cdot \sqrt{\frac{\kappa_B}{\sigma}} \tag{5.16}$$

The bending radius is $r_c \approx 10\,\text{nm}$ for typical values of κ_B and σ (Table 5.5). Parthasarathy *et al.* reported that curvature radii smaller 800 nm influence the localization of stiffer l_o domains.[217]

To get an estimate if line tension is sufficient to anchor a l_o domain to a l_o covered rim one needs to calculate the difference in bending energies of a l_d domain in contact to the rim (Figure 5.47A) compared to the case when the l_o domain is displacing the l_d phase at the pore border (Figure 5.47B). This will result in a change of the bending energy because the bending rigidity for the l_o domain is higher.

$$\Delta E_B = E_{B,l_o} - E_{B,l_d} \tag{5.17}$$

The bending radius of the membrane r_c is small compared to the pore radii R (400-2750 nm). It is valid to use Equation 5.14, assuming a cylindrical geometry with the membrane covering 1/4 of the cylinder, to calculate the bending energies E_B. Table 5.5 summarizes the values for different published bending rigidities. Energy of the line tension was calculated using Equation 5.13. Values for two cases are given: i) an arbitrary length, ii) an example for the energies at $b = 500$ nm.

Table 5.5: Physical properties and energies relevant for localizing a l_o domain at the pore rim. Calculation of the energy of line tension (E_{LT}) and energy difference of bending (ΔE_B) are given for an arbitrary length and $b = 500$ nm.

property	high κ_{B,l_o}	low κ_{B,l_o}	description
σ / mN m^{-1}	1.0[228]		membrane tension
μ / pN	1.2[42]		line tension
κ_{B,l_o} / $k_B T$	29.0[34]	12.5[148,215]	bending rigidity l_o
κ_{B,l_d} / $k_B T$	10.6[34]	10.0[148,215]	bending rigidity l_d
r_{l_o} / nm	12.9	8.4	curvature radius l_o
r_{l_d} / nm	7.8	7.5	curvature radius l_d
E_{LT} / pJ m^{-1}	−1.2		energy of line tension
ΔE_B / pJ m^{-1}	2.9	0.5	energy of bending
$E_{LT}(500\,\text{nm})$ / $k_B T$	−144.9		energy of line tension ($b=500$ nm)
$\Delta E_B(500\,\text{nm})$ / $k_B T$	349.4	61.4	energy of bending ($b=500$ nm)
$|E_{LT}/\Delta E_B|$	0.4	2.4	ratio of energies

Because the values published in literature for the bending rigidity greatly differ,[34,148,215] two values ('high κ_{B,l_o}' and 'low κ_{B,l_o}') are given as an estimate. Line tension reduction is in a similar order of magnitude as the energy difference between bending the l_o domain compared to a l_d domain. The ratio of the energy of line tension to the difference in bending energies ($|E_{LT}/\Delta E_B|$) is close to 1. It might therefore be thermodynamically stable to localize the l_o domain at the rim, if a line tension reduction to l_o areas on the solid support can lower the overall energy. Notably, this only describes the situation after a domain is already in contact to another domain at the pore rim. There still might be a kinetic energy barrier to form the contact. The kinetic effect can be seen in Figure 5.27. After condensing to a rim based l_o area, the domain stays in a bud like shape and does not form a full half circle or even fully flattens out to maximize the gain in line tension energy. Possible differences in adhesion energies of the different domains can be neglected.

The van-der-Waals interactions of l_o and l_d domains with the substrate are similar as the Hamaker constants determined between membrane multilayers for l_o and l_d have been reported to be remarkably similar.[34]

Formation of small lipid domains

The domains observed on pore-spanning membranes are smaller compared to those found in GUVs, indicating that the support disperses the domains (Figures 5.11 to 5.13 and 5.14). Using molecular dynamics stimulations, in 2012 Fischer *et al.* reported that phase-separated membranes form smaller domains when the bilayer is in physical contact to particles.[229]

with interleaflet coupling
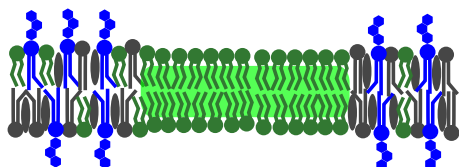
no interleaflet coupling
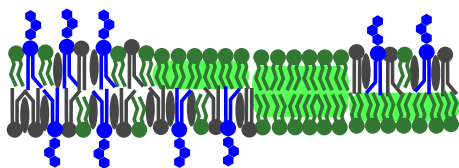
Figure 5.48: A lack of interleaflet coupling would lead to intermediate brightness levels.

They found that contact of the membrane to obstacles like a cytoskeletal filament, a solid support, or a protein can lead to the formation of smaller domains opposed to large assemblies. This effect termed 'quenched disorder' is based on the fact that the movement of lipids at this contact points is slowed down or the lipid is fully pinned to the obstacle, forming a seed for the growth of a small domain. If the interleaflet coupling is strong enough, a phase separation in both leaflets can be induced even if only one leaflet is in contact to the obstacle, e.g. the solid support.[229–231] In the lipid mixture used in the experiments on porous substrates, the interleaflet coupling is strong enough to induce domains in both leaflets simultaneously.[168] In the fluorescence images presented in the results section the l_d marker dye always has only two brightness levels in absence of bound STxB. Figure 5.48 shows that the lack of interleaflet coupling would lead to a third brightness, as half of the membrane would be enriched in l_d marker dye while the other is depleted. Figure 5.49 shows the model by Fischer *et al.* and how it can be adapted to the case of pore-spanning membranes.
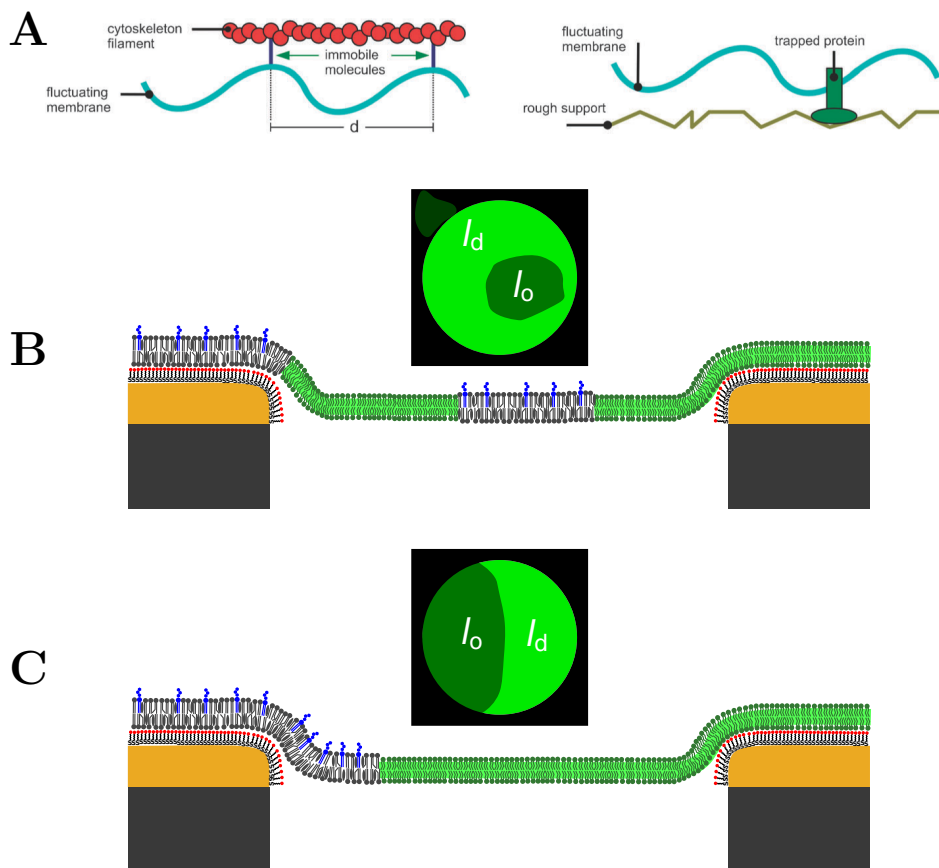
Figure 5.49: Mechanism of the inductions of domain on the porous mesh. **A** A membrane in contact to e.g. a cytoskeleton filament or a solid support leads to the immobilization of membrane components. They act as the starter for the formation of lipid domains in these regions. Panel reproduced from Fischer *et al.*.[229] **B** Domains might be formed on the solid support but no observation by fluorescence microscopy is possible. **C** Rim adhered domains are formed close to the pore border and extend into the freestanding membrane area.

The pinning point leading to the formation of a lipid domain is the solid support. Domains that form close to the pore border are in contact to the support. They are immobilized because a part of the domain is in contact to the solid support where lipid diffusion is slow. In this regard, pore-spanning lipid bilayers fully represent a mixture of solid supported and freestanding membrane areas. The solid supported part leads to the formation and immobilization of small domains, resembling the picket like effect of the actin cytoskeleton (Figure 5.3). High lipid and domain mobility in the freestanding membrane part let the domain adopt the thermodynamically favored round shape in contrast to domains on full solid support which have irregular shapes. This unique feature, combining domain movement and

the creation of small domains can also explain the differences in the structure of the observed domains in PSMs with different diameters.

Controlling phase separation of membranes *in vitro*

Modifying the adhesion points of membranes to a support to modulate the structure of l_o domains was demonstrated both experimentally[196,214] and theoretically.[231] Honigmann *et al.* used solid supported lipid membranes and artificially attached an overlying actin cytoskeleton to the membrane.[214] The mesh prevented macroscopic phase separation and the diffusion of lipids in the membrane was slowed down. Applying super resolving STED microscopy, they studied the small domains induced by the actin mesh. Interestingly, they were able to change the attachment site of the actin by using different lipid coupled receptors binding to actin. A lipid that partitions into the l_d phase led to the colocalization of the actin mesh and the disordered phase. In contrast, a receptor that partitions into the l_o phase led to the reversed case. This convincingly shows that the type of pinning site inducing the quenched disorder can lead to the formation of different types of domains at the pinning site. Their work had the drawback that the domains were investigated on a solid support which already influences the phase behavior.[230] Arumugam *et al.* extended their work to the freestanding membranes of GUVs.[196] Using a prokaryotic tubulin homolog, they created a cytoskeleton with varying mesh size and found the same suppression of large-scale phase separation and an increased temperature range for phase coexistence.[196] By artificially creating different mesh sizes of the cytoskeletal network, they were able to control the size of the domains.

Transferring these results to pore-spanning membranes implies that the size of the freestanding membrane should influence the size of the domain formed. This correlation was found for PSMs with diameters of 0.8, 1.2 and 2.0 μm, where only one domain is present in each pore and the relative area percentage of the l_o phase in the pore is ≈30 %. Using pores with a diameter of 3.5 μm, multiple domains were frequently found in one pore-spanning membrane, indicating that the concept of a single pore controlling the formation of a single l_o domain is not valid.[51] Multiple domains were only found when the domains are in contact to the solid support surrounding the freestanding membrane area (Figure 5.50).

Each of the domains is immobilized by the contact to the support and no coalescence of the domains in the freestanding membrane area will take place on the time scale of the experiment.[232] One could imagine decreasing the substrate-membrane contact by using polymer cushions[207] or increasing the porosity. Both should increase the diffusivity of the domains and the lipids on the rim, decouple the membrane from the substrate and increase the propensity of domains to coalesce into thermodynamically stable large domains. Dabkowska *et al.* produced vertical nanowire surfaces which resemble a highly porous surface, which might

Figure 5.50: Multiple domains in PSM cannot condense when in contact to the rim.

be suited to allow for fast lipid and domain movement.[233] However, they found that spreading vesicles on these substrates does not lead to the formation of freestanding membranes. The high porosity led to a full coverage of the surface with a solid supported membrane, meaning that the membrane is lining the nanowires.[201,234]

Influence of pore size on the formation of domains and their morphology
Formation of lipid domains in pore-spanning lipid bilayers is related to the interplay of solid supported membrane areas and the spanned porous regions. The radial density shown in Figure 5.22A reveals that the l_o area distribution in the freestanding membrane area is similar for all four pore sizes used. The distinct three dimensional structure of the porous mesh will influence the position of domain formation. Figure 5.51 shows how the different pore sizes influence the structure of the domains observed in the pore-spanning membrane. In this scheme the positions of the l_o domains are chosen arbitrary and are identical for all four pore sizes to illustrate how the lateral dynamics of the membrane shape the domain morphology. Diameters of the pores (black) are drawn to scale.
Starting from the homogeneous membrane, l_o domains (dark green) will start to form. Pore-spanning membranes with a diameter of $0.8\,\mu\mathrm{m}$ nearly exclusively contain a single phase consistent with the idea that the 'field of view' contains either l_o or l_d area. The probability to find both a l_o and a l_d domain in one membrane spanned pore increases to $90\,\%$ on larger pores. This is consistent with the idea that the larger area of the pore-spanning membrane increases the observed area and therefore the probability to observe more than one domain.
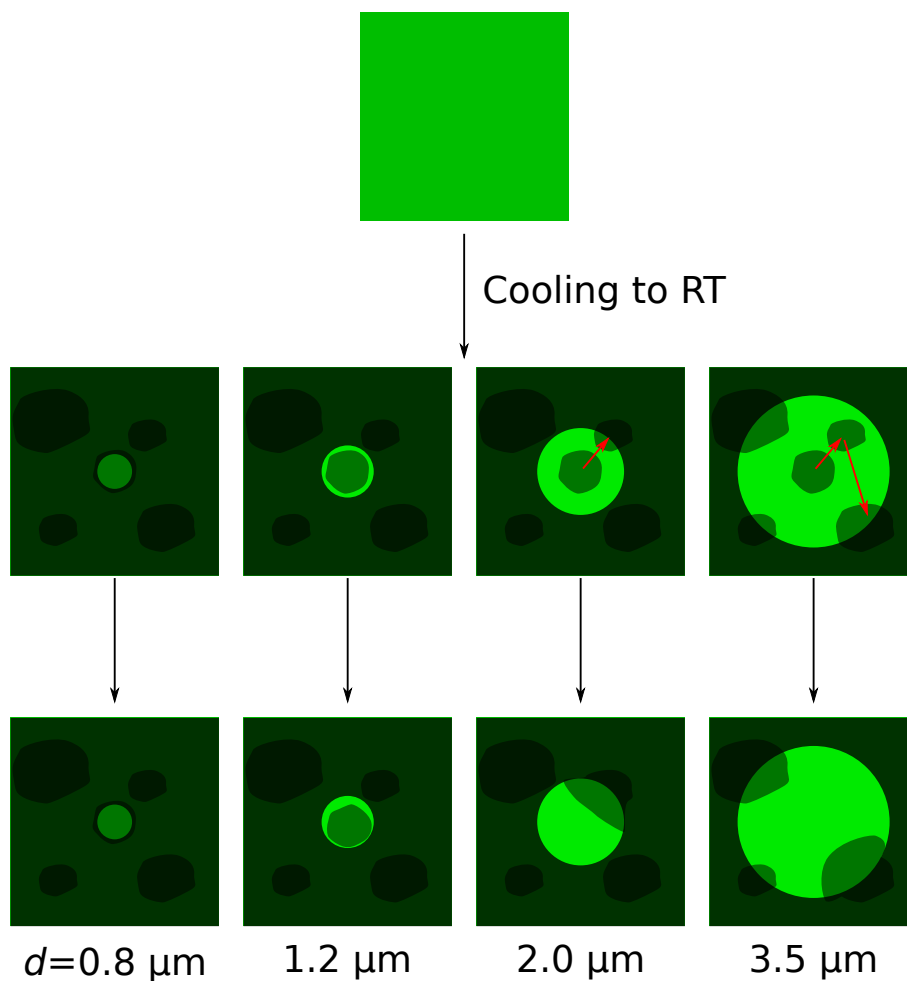
Figure 5.51: Top view on the domain formation in membranes prepared on solid support. The different pore sizes are represented by the black transparent overlay. Starting from the homogeneous membrane (top), dark l_o domains form in the membrane. Depending on the pore size, the probability to observe simultaneous phase separation in one pore increases with pore diameter. The percentage of domains in the center of the pore-spanning membranes does not increase with pore size because the domains will readily condense (red arrows) to domains at the rim. The probability to find these domains at the rim increases as the circumference of the pores increases.

On substrates with pores with diameters of 1.2 μm and 2.0 μm a higher fraction of pore-spanning membranes with domains in the center was found ($\approx 10\%$, Table 5.2). A domain that forms in the center of a PSM is trapped and will not move to the rim (see discussion in Section 5.4.4). The two intermediate pore sizes allow this to happen. Naively one would expect to also find an increase of domains in the center of larger pore-spanning membranes with a diameter of 3.5 μm or even multiple moving domains, because the area of the PSM grows quadratically

with increasing radius. However, as the circumference of the pore increases, the probability to find a domain at the interface between the solid support and the freestanding membrane area also increases. Relatively fast diffusion of the domains in the pore center will lead to a condensation of domains in the PSM to domains at the rim (see Figures 5.26 and 5.27). Once this merging happens, the diffusion of the domain is stopped and it will be frozen in this position.

These considerations assume that the geometry and topography of the membranes formed on porous support do not strongly influence the domain formation upon cooling to room temperature, but the observed morphologies are created by the condensation of moving domains and the immobilization of rim based domains.

A fully random distribution of the domains in the membrane on porous support is unlikely because Yoon *et al.* and Parthasarathy *et al.* could show that surface roughness and membrane curvature can spatially control the formation of lipid domains. The stiffer l_o domains are not positioned in curved membrane regions.[215, 217] The curvature at the border or the PSM will attenuate the domain formation directly at the interface between rim and freestanding membrane area. This lower amount of l_o area in the curved region is indeed observed in the radial density profile shown in Figure 5.22A. The extent of the effect is similar for all pore geometries because the topography at the pore rims will induce a curvature which is always high enough to inhibit the formation of l_o domains.[216, 217]

The induction of small domains by contact to the support predicted theoretically by Fischer *et al.* can only take place on the solid supported regions on the pore rim, indicating that less domains should form on the freestanding membranes areas. Depending on whether the support induces the formation of l_o or l_d domains this will change the areas occupied by the phases as a function of the substrate porosity. A detailed insight into this effect in given in Section 5.4.3.

The observed morphologies and the possible explanation presented above raise an important consideration on the capability of pore-spanning membranes to mimic the effect of the cytoskeleton on the plasma membrane. PSLBs are capable to entrap domains in a fence like manner (see Section 5.3.4 and 5.4.4). Domains in contact to the rim are pinned. Which of these effects is observed in the single pore-spanning membrane solely depends on the probability to find a domain at the pore rim, because moving domains will readily condense.

Selective induction of moving domains

To selectively induce only a fence-like effect to trap l_o domains in the pore center one would need to inhibit the formation of l_o domains at the pore border. Examples for spatially directed formation of specific lipid domains are sparsely reported in literature. The approaches are based on micro lithographic orthogonal surface functionalization.[212,213] Figure 5.52A shows the work of Roder *et al.*.[212] They attached saturated (red) and unsaturated (green) fatty acids to polymer cushions atop a solid support to induce the formation of l_o and l_d areas in these regions by vesicle spreading. The (*Z*) unsaturation of the fatty acid forms a kink in the hydrocarbon chain which generates a large area demand and disturbs the lipid order in the bottom leaflet of the membrane obtained from vesicle spreading.[235]
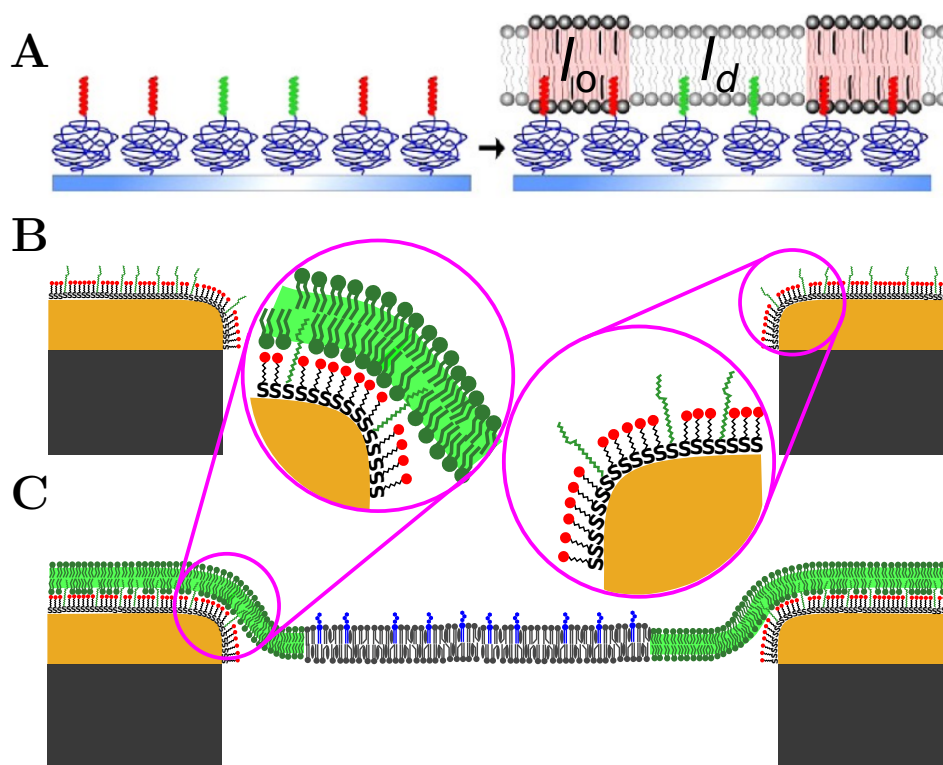
Figure 5.52: Proposed mechanism to induce l_d domain formation on the pore rims. **A** Roder *et al.* used polymer cushions covalently functionalized with saturated (red) and unsaturated (green) fatty acids to control the localization of lipid domains.[212] **B** The surface functionalization can be tuned by mixing mercaptohexanol (red/black) with a thiol bearing an (*Z*) unsaturated fatty acid. **C** The fatty acid inserts into the bottom leaflet of the membrane and (*Z*) unsaturation favors the formation of disordered domains in these regions. Panel **A** modified from Roder *et al.*.[212]

In principle this approach can be transfered to the surface functionalization of pore-spanning membranes by using a (Z) unsaturated or sterically demanding thiol. To avoid the formation of a full hybrid bilayer in which the bottom layer is fully composed of the thiol, one would need to produce mixed self assembled monolayer of the bulky component and e.g. a hydroxy terminated thiol. (Figure 5.52B/C).[236] This approach would enable to selectively induce l_d domains at the pore rim, effectively trapping any l_o domain in the pore-spanning membrane region. However, this type of hydrophobic surface functionalization has several drawbacks.[237] Simon *et al.* reported the risk of air inclusion in the pore cavities[200] and the strong contact to the surface induces high membrane tension.[43,45] This increased tension reduces the membrane stability[45] and destabilizes the phase separation.[38,238]

Influence of STxB binding on the domain structure

Figure 5.53 shows a scheme of the membrane and protein organization after STxB binding. Data obtained from fluorescence microscopy of membranes composed of DOPC/SM/Chol/Gb$_3$-Porc 40:35:20:5 incubated with $60\,\mathrm{nM}$ STxB unambiguously shows that Shiga toxin only binds to areas assigned to the l_o phase. The lipid compaction induced by the multivalent binding of STxB increases the line tension between the lipid domains and hence might lead to changes in their morphology.[72] Two major aspects were found: i) nearly all l_o domains are in contact to the pore rim, ii) isolated STxB-Gb$_3$ clusters were observed on the l_o phase. Shiga toxin binding to Gb$_3$ is known to induce membrane order.[39,71,132] Using confocal fluorescence microscopy and tether pullings experiments the protein was also found to sense and induce negative curvature in GUVs.[39,71] This indicates that binding of STxB might preferentially take place in the negatively curved regions at the pore border (left rim in Figure 5.53). The presence of l_o phase in these regions would anchor all domains to the pore rim, explaining the lack of freely moving domains after STxB binding. This is also reflected in the radial density profiles obtained for the density of l_o area in the freestanding membranes (Figure 5.22). After STxB binding l_o domains are found at the pore border to a higher extent compared to the protein free case.
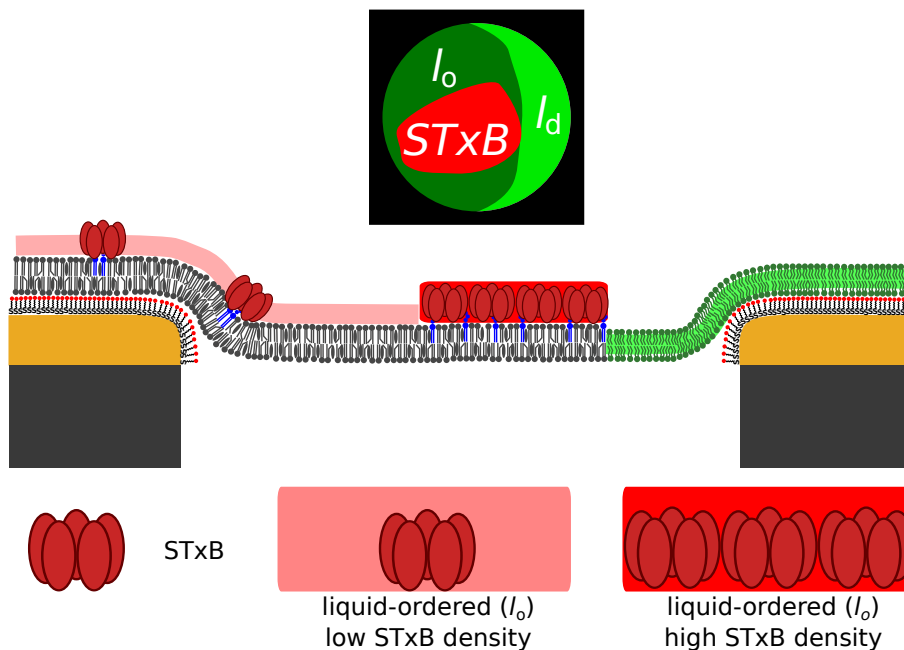
Figure 5.53: Shiga Toxin binding to phase-separated pore-spanning lipid membranes. The protein (red) selectively binds to its receptor Gb_3 which is located in the l_o phase. The density of the protein on the l_o areas might differ. STxB can form clusters (dark red).

Inhomogeneous protein coverage of the l_o phase with protein was observed. Some regions showed bright red protein fluorescence whereas others were depleted in STxB and presumably the Gb_3 receptor. This effect could be visualized in membranes prepared on substrates with a pore diameter of $3.5\,\mu m$. Using solid supported membranes (Chapter 4) different intensities of STxB-Cy3 fluorescence could be attributed to the formation of high density STxB clusters by determining the height of the protein structure by AFM. It seems reasonable to attribute the increased STxB-Cy3 fluorescence intensities observed on pore-spanning membranes to a similar STxB clustering. This is further supported by the finding that artificially reducing the l_o area by cholesterol extraction with mβCD,[52,91] leads to a compaction of the protein on the l_o phase (Figure 5.17).

Lateral movement of STxB on the membrane is required for cluster formation. The movement of STxB clusters in the l_o phase of pore-spanning membranes was observed (Figure 5.20). During the time series the clusters did not cross the border of the pore indicating an energetic barrier.

The data obtained on the movement of l_o domains in pore-spanning membranes showed that they are also not able to diffuse out of the pore (Section 5.3.4). SICM revealed the presence of a curved membrane region at the pore border which hinders the localization of the stiffer objects in these regions. Using force spectroscopy and micropipette aspiration of GUVs Dielutweit *et al.* found that a bound protein layer increases the bending rigidity.[239]

Figure 5.54: Scheme of the STxB cluster movement.

The STxB-Gb$_3$ cluster has a higher bending rigidity than the surrounding membrane, inhibiting the free movement of the STxB cluster.

It remains unclear why the formation of STxB clusters was preferably observed on large pore-spanning membranes. The theoretical considerations on STxB endocytosis developed by Ewers, Römer *et al.*, presented in detail in Section 4.2.4,[72] predict that even at relatively low surface coverages of 30 % the formation of STxB clusters should be fast and the critical nucleation size is well below 10 proteins. The size of the formed cluster might grow with an increasing area of the PSLB. This finite cluster size indicates that the diffusion of Gb$_3$ bound STxB from the rim to freestanding membrane is hindered and the growth of the STxB cluster stops when the PSLB is depleted of Gb$_3$ that can bind further protein. The large area of pore-spanning membranes prepared on substrates with pore diameters of 3.5 µm allows to visualize the clusters because they can grow larger compared to clusters formed in smaller pore-spanning membranes, explaining why the clusters were only frequently observed in membranes formed on pores with a diameter of 3.5 µm.

Using single particle tracking of labeled STxB pentamers would offer interesting insights into the clustering of the protein and the interplay with the diffusion between rim areas and the pore.

5.4.3 Percentage of lipid phases

Apart from the structure of the domains formed, the interplay between a solid supported membrane area and freestanding regions might play an important role in the overall localization of the l_o phase. l_o domains might preferentially locate on the solid support, lowering the observed l_o percentage in the freestanding membrane

areas. The interpretation of the data obtained is difficult, because no information on the organization on the pore rim is available and the size of the pores has a major influence on the shape of the domains and might also influence the area percentages.[240]

Percentage of ordered phase in GUVs

Bhatia *et al.* used confocal microscopy to quantify the amount of l_o phase in GUVs composed of DOPC/DPPC/Chol and found a clear dependence of the area fraction on the composition.[115] Bezlyepkina *et al.* used DOPC/eggSM/Chol mixtures to determine the tie lines in the ternary phase diagram.[37] For a molar ratio of 40:40:20, close to the one used in this thesis, they determined the percentage of l_o phase to be approx. 35 %, which is in excellent agreement with the value determined in this work (Table 5.1). Similar to the data obtained by Bezlyepkina *et al.* the values found for the l_o percentage scatter rather strongly, due to the heterogeneous composition of the vesicles caused by electroformation.[241]

Percentage of ordered phase in PSLBs prior to protein incubation

Spreading the GUVs on porous substrate brings the membrane into contact with the solid support of the pore rims. Lipowsky and Weikl theoretically predicted that domains and lipids preferentially localize between two types of adhesive surfaces (e.g. a freestanding membrane and a solid supported membrane),[240,242] which would influence the percentage of ordered phase observed in the freestanding membrane regions. Using porous substrates with different porosities, meaning a different ratio between the freestanding and solid support membrane areas, allows to study the distribution between rim and pore. Figure 5.55 shows the determined l_o percentages in the freestanding membranes plotted as a function of the substrate porosity. Additionally the area percentages of the GUVs used for spreading are plotted.
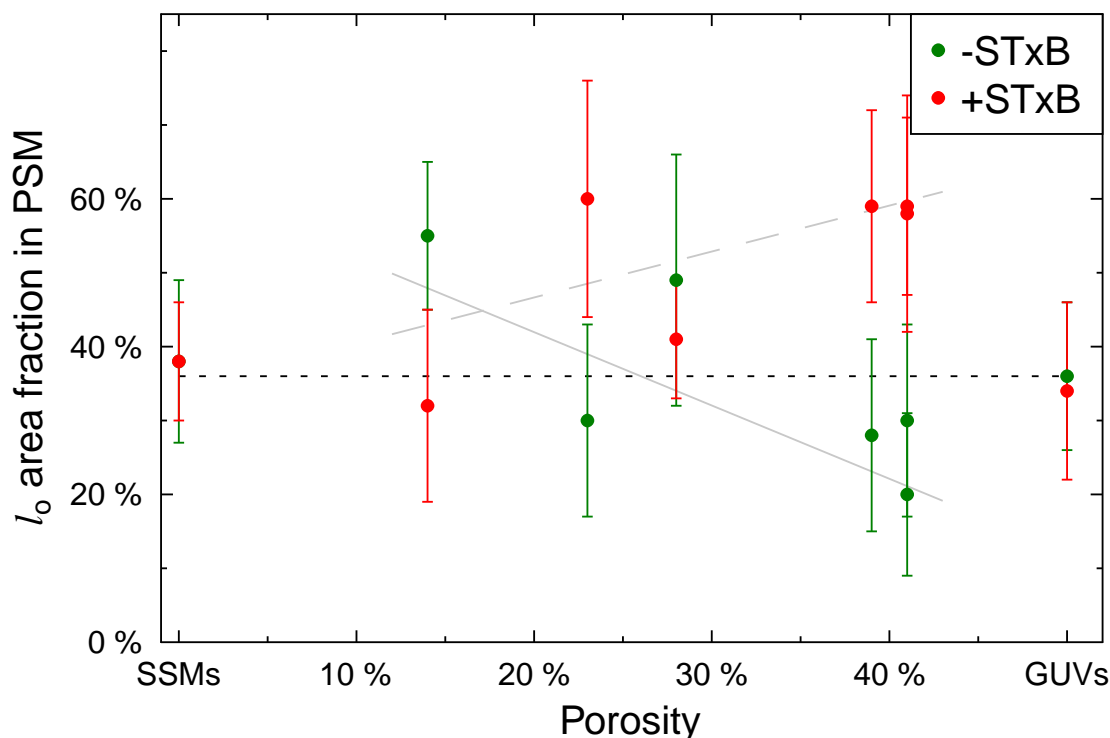
Figure 5.55: Plot showing the l_o area percentage in absence and presence of bound STxB as a function of the substrate porosity. Values prior to protein binding are shown in green; percentages after protein binding in red. The gray lines are the weighted fit of the percentages in absence (solid) and presence of STxB (dashed). The black dotted line represents the l_o percentage found in the GUVs used for spreading. Percentages for SSMs refer to the results obtained for spreading of the GUVs on silicon wafers. The values plotted can be found in Tables 5.1, 5.2 and 5.3.

In absence of bound STxB (green dots) one observes a drop of l_o area in the freestanding membrane parts with increasing porosity. The weighted fit (solid gray line) shows the trend. Similar to the l_o percentages in GUVs, the values scatter heavily between different membrane patches which is caused by the heterogeneity of the GUVs.[241] Even though a slight trend is visible, the large errors make comparison of porous substrates difficult. It is more feasible to compare the results obtained on porous substrates with the value found in GUVs both in absence and presence of bound STxB. The results in Section 5.3.1 show that spreading of the GUVs on solid support just transfers the area percentage found in GUVs to the substrate. Deviations from this behavior can be attributed to the effect of the porous support.

For pore-spanning membranes with diameters of 0.8, 2.0 and 3.5 μm prepared on substrates with porosities of 23, 41 and 39 %, respectively, l_o area percentages close to 35 % were found. These values are similar to the one of GUVs (Tables 5.1 and 5.2), indicating that the porous support has no major influence on the percentage of the ordered phase in the freestanding membrane region. Similar to the results of Bhatia *et al.* it indicates that spreading the GUVs above the phase separation temperature just transfers the l_o area present in the GUV to the porous surface and no preferential localization of the l_o area is occurring.[115] Given the uncharged lipid mixture used in this work, the main interaction force between the membrane and the support will be van-der-Waals interactions.[243] Kollmitzer found that the Hamaker constants for l_o and l_d phases are surprisingly similar, leading to the conclusion that no preferential adhesion is induced by this interaction. It has to be noted that the Hamaker constants for the substrate material (Si_3N_4 and SiO_2) differ quite strongly.[244] However, similar l_o area percentages are found for membranes prepared on substrates with similar porosity composed of Si_3N_4 with 2.0 μm pores and those composed of SiO_2 with 3.5 μm pores.

One can compare the determined l_o area percentages to examples published in literature. Using phase-separated membranes prepared on hydrophobically functionalized porous substrates, Orth *et al.* found similar values for the l_o area percentage on substrates with pore diameters of 0.8, 1.2 and 2.0 μm and porosities of 23, 41 and 41 %, respectively. This shows that despite the large experimental error induced by the heterogeneity of the GUVs, the determined values are reliable. Using confocal fluorescence microscopy Gordon *et al.* visualized that upon cooling of GUVs below the phase separation temperature, ordered domains first form in a region where two GUVs are in contact with each other. They linked this phenomenon to the suppression of thermal shape fluctuations in these areas.[245] In membranes prepared on porous support, both the solid support and the membrane tension hamper thermal shape changes,[246, 247] indicating that this effect might not lead to a strong affinity of the l_o domains to one of the membrane compartments. Lipowsky and Weikl theoretically constructed phase diagrams for a membrane with freestanding parts and areas in contact to a solid support.[240] Under the assumption that the components of the membrane show a different affinity to the surface, they found that in thermodynamic equilibrium phase separation can only occur in one of the two membrane compartments.

In this work the phase behavior on the pore rims could not be imaged due to quenching by the gold functionalization. However, the dynamics of lipids and domains in contact to the solid support were found to be slow (Section 5.4.4). This indicates a possible experimental bias. l_o domains might form on the solid support and the low diffusivity hinders them from translocating to a freestanding membrane area (Figure 5.50). The reversed process of a l_o domain leaving the pore is obstructed by the curved border region. The membrane organization observed on pore-spanning membranes might be caused by this kinetic effect. To overcome it, the membranes were slowly cooled to room temperature but due to the lack of information on the organization of the membrane on the rims, a kinetic trapping cannot be fully ruled out. To certainly reach thermodynamic equilibrium it would be beneficial to bring the membrane close to the phase transition for a longer time span or use heat-cool-cyles. The theory of Lipowski and Weikl also treats this potential bias. Contact to a surface that induces small domains by the mechanism of quenched disorder might lead to a pinning of domains suppressing their coarsening.[229,240] The phase separation in the membrane in contact to the support remains incomplete. The authors reason that this effect can be overcome using lipid mixture close to the critical point.

Under the assumption that the membranes are in equilibrium, the l_o percentages found in the pore-spanning membranes prepared on substrate with pore diameters of 3.5 µm and porosities of 14 and 28 % indicate a preferential sorting of lipid components between the rim and the pore because the observed l_o percentage in the freestanding membrane is higher than in the GUV. The precise physical reason for a sorting is unknown. Yoon *et al.* reported that l_o domains do not form on rough surfaces.[215] The freestanding membrane part of PSMs are mostly flat and do not undulate due to the membrane tension, indicating that l_o domains might rather preferentially localize here, compared to the pore rims where the surface rougher due to the gold functionalization. This also indicates a potential bias comparing the different porous substrates used. Small differences in surface roughness and the geometry of the pore border might have large influences on the membrane organization, especially given the fact that the substrates were produced using different materials (see Section 3.2.3). It is however still feasible to compare the effect of STxB binding on the membrane organization. Of note, the percentages of ordered phase observed in the PSM is only an

indirect measure for the lipid sorting predicted by Lipowsky and Weikl, because the area occupied by l_o does not strictly vary linearly with the membrane composition.[37]

l_o area percentage after STxB binding

The percentage of ordered membrane phase was reexamined after binding of STxB to the membrane. The values are plotted as a function of the substrate porosity in Figure 5.55. One observes a slight trend to find more l_o area in the freestanding membrane areas in preparations on substrates with higher porosity, but the large errors prohibit an interpretation in greater depth. To understand the effect of STxB binding it is helpful to look at the change of the l_o area percentage upon STxB binding observed in membranes on the individual porous substrates. Four of the six membrane systems investigated show a near doubling of l_o percentage in the freestanding membrane from ≈ 30 to $\approx 60\%$. No increase of l_o area was observed in GUVs (Table 5.1) and only to lower[86] or even reversed[70] extends in solid supported membranes. This indicates that the increase is not only caused by an induction of additional l_o area by STxB driven lipid compaction,[71,132] but by a translocation of l_o lipids from the pore rim to the freestanding membrane area.

Figure 5.56 shows the process. l_o area that was localized on the pore rim is transfered into the freestanding membrane area. For GUVs, Safouane *et al.* reported that STxB binding can lead to a spatial relocalization of membrane components.[134] Binding led to the formation of membrane tubes which were not only enriched in STxB and Gb$_3$ but also in the l_o domain component sphingomyelin. These results show that the binding of STxB to Gb$_3$ might induce a relocalization of l_o phase. The effect reported by Safouane and coworkers is caused by the formation of membrane invaginations. The fluorescence microscopy and SICM experiments performed in this thesis exclude the possibility of a major change in 3D structure of the pore-spanning membranes. However, the first step of the toxin's endocytosis is formation of protein-lipid clusters.[72] These clusters were observed in the freestanding membrane areas, indicating that STxB can indeed lead to a relocalization of l_o lipids.
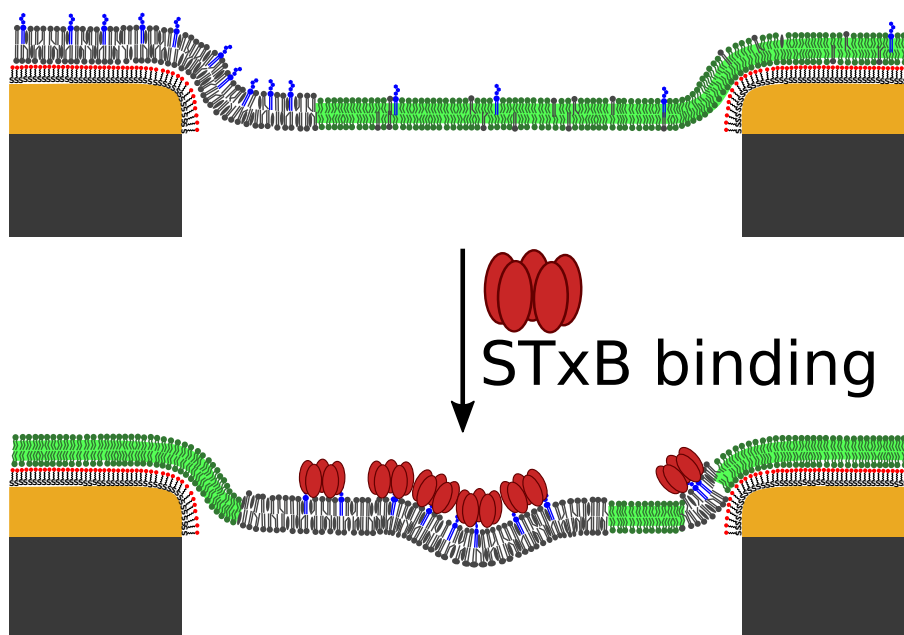
Figure 5.56: STxB binding to PSLBs increasing the l_o area percentage. STxB binding can occur in the curved membrane area (left). STxB is capable of inducing negative curvature in the membrane possibly leading to the formation of dimpled membranes.

Using the same lipid mixture as in this work, Windschiegl *et al.* reported that STxB binding to phase-separated GUVs leads to the formation of dimpled membrane regions.[70] Similar, shallow membrane structures were found by Bacia *et al.* in GUVs composed of different lipid compositions. They attributed the formation of the dimples to small changes in membrane curvature. STxB binding to Gb_3 containing PSLBs can have a similar effect, which is only possible in the freestanding areas of the membranes and not on the solid support (Figure 5.56).

A second mechanism responsible for the relocalization of l_o phase is based on the multivalent binding of STxB to Gb_3. Using STxB mutants, Soltyk *et al.* found that the occupancy of less binding sites of the protein lowers its affinity towards the membrane.[64, 65, 69] The formation of multiple Gb_3-STxB bonds is faster when the diffusion of the Gb_3 lipid in the membrane is fast. One could envision that STxB binds to Gb_3 in the freestanding membrane areas and a clustering of the lipids and proteins occurs. The same process is slower on the pore rim because the diffusion coefficient of lipids on solid support is slowed by at least a factor of ten.[195, 203, 204, 206] The off-rate of the STxB-Gb_3 interaction was determined to be in the range of seconds, indicating that unbinding of STxB on the pore rims is frequently happening. A STxB-Gb_3 cluster formed in the PSM cannot leave the pore due to the curvature

at the pore rim. Individual Gb_3 lipids are free to diffuse into the pore-spanning membrane where they have higher probability to engage in stable bonds to STxB to form protein lipid clusters. Of note, even though the STxB-Gb_3 bond is formed reversibly, with increasing cluster size the probability of Gb_3 disengaging from the cluster drops, because Gb_3 located inside the cluster will always be in spatial proximity to a bound STxB. The kinetic trapping of the STxB-Gb_3 aggregates in the pore shifts the distribution of l_o area towards the freestanding membrane area.

The values determined for the l_o percentages scatter heavily. However, Orth *et al.* found a similar increase in l_o percentage on the freestanding membrane areas of PSMs using hydrophobically functionalized pore-spanning lipid membranes, indicating that there is indeed a redistribution of l_o lipids from the rim to the pore. Pore-spanning membranes prepared on substrates with pores of $3.5\,\mu m$ in diameter and porosities of 14 and $28\,\%$ show a decrease in l_o area percentage upon STxB binding, contradicting the reasoning presented above, but the l_o percentage is still increased or in the range of the values found in GUVs, indicating that STxB binding induces a preferential localization of l_o area on the freestanding membrane parts. The lower amount of l_o recruitment to the PSM can be explained by the increased area percentage prior to protein binding. The higher amount of l_o phase slows diffusion in the PSM, lowering the difference in diffusion coefficients between freestanding and solid supported membrane areas. This favors the formation of STxB clusters on the solid support.

A full explanation of the effects observed would require knowledge on the phase separation on the pore rims. Omitting the use of gold/thiol chemistry is difficult as an orthogonal surface functionalization is required to avoid the membrane lining the pore interior.[201, 234] Commercially available hydroxy terminated thiols can increase the distance of the membrane to the gold to less than $2\,nm$ (11-hydroxy-1-undecanthiol) which is not sufficient to avoid gold quenching. Using gold nanoparticles Acuna *et al.* determined a distance of roughly $15\,nm$ to recover $50\,\%$ of the fluorescence intensity.[202] Such a large distance would require the use of polymer based surface functionalization.

An approach not based on the fluorescence of a l_d marker dye in the membrane would be single-particle tracking. Following the movement of a single cholesterol molecule for example would not only yield the diffusion coefficient on the

freestanding and solid supported parts of the membrane, but also allows for a direct determination of a partition coefficient between the two different membrane compartments. In combination with the considerations developed here for lipid domains, the experiments could help to understand how STxB binding to Gb_3 in cells is capable of achieving the large scale lipid rearrangement prerequisite for the formation of membrane invaginations.[39, 71, 134]

Influence of membrane tension

Membranes on porous support are composed of two distinct membrane environments. Membranes on the solid support exhibit a strong interaction with the surface but the membrane is tension free.[43] The freestanding membrane areas have high membrane tension induced by the strong interaction of the membrane with the pore rim which leads to a 'stretching' of the spanning membrane. One can imagine that tension might disrupt the tight packing of lipids, lowering the amount of l_o area in the pore. Theoretical work by Szleifer,[238] backed up by experimental data using micropipette aspiration of phase-separated vesicles performed in the Keller group,[38] show that the phase transition temperature of 'raft-like' lipid mixtures is decreased with tension by $\approx 1.0\,\mathrm{K}\,(\mathrm{mN}\,\mathrm{m}^{-1})^{-1}$. Membranes on hydrophilically functionalized substrates used in this thesis have a tension of $\approx 1\,\mathrm{mN}\,\mathrm{m}^{-1}$;[44, 45] as the tension of the PSLBs is low, it has no major influence on the phase separation.

The data obtained from static images of phase-separated membranes on porous support shows that the membrane structure is governed by a complex interplay between porosity and pore size. They act as a minimal model of the actin cell cortex and the immobilization of domains mimics the picket like effect of the actin cytoskeleton.

5.4.4 Domain dynamics

l_o domains that are localized in the center of a pore-spanning membrane composed of DOPC/SM/Chol/Gb_3-Porc 40:35:20:5 (Section 5.3.4) show different types of dynamic movement. Shrinking and growing of the l_o domains as presented in Figure 5.25 shows that lipids dynamically associate with the domain in the freestanding membrane area. Fluorescence recovery after photobleaching experiments revealed a diffusion coefficient of $D = 0.2 \pm 0.1\,\mu\mathrm{m}^2\,\mathrm{s}^{-1}$, which includes diffusion on the solid

supported areas of the pore rim where diffusion is expected to be slowed down by the contact to the substrate and the tight lipid packing in the l_o phase.[195, 203, 204, 206, 207] The growing of domains, demonstrates that lipids diffuse from the pore rims into the freestanding membrane area and associate with the lipid domain. The domain itself is trapped in the freestanding membrane area. This shows that the porous support reproduces the fence-like effect of the cytoskeleton.[16] Figure 5.57 depicts a schematic representation of the diffusion of a l_o domain in the freestanding membrane area.
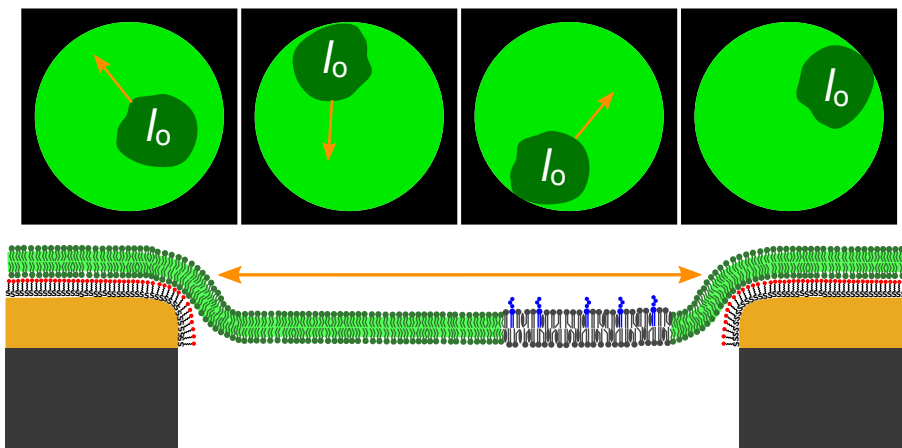
Figure 5.57: Scheme of the diffusion of a l_o domain in a PSLB. The l_o domain is moving until it comes in close proximity to the pore border.

The l_o domain (dark green) moves in the pore-spanning membrane (light green). However, contact of the domain with the pore border effectively repels it. This unique feature of PSLBs distinguishes PSLBs from other approaches to mimic the cytoskeleton *in vitro* e.g. using an artificial actin cytoskeleton where the membrane gets compartmentalized but no movement of the domains is observed.[196, 214]

The diffusion model developed in Section 5.3.4.1 is the analytical solution to the problem of a disc shaped domain diffusing in a circular membrane. It allows to determine the diffusion coefficient of the large lipid domains (see Figure 5.34). Diffusion of large objects in biological membranes can be described using the Petrov-Schwille approximation of the HPW model (see page 187).[199]
The coefficients determined for the diffusion of l_o domains in pore-spanning membranes (Figure 5.34) are lower than expected from the Petrov-Schwille approximation and lie between $2 \cdot 10^{-4}$ to $2 \cdot 10^{-1} \, \mu m^2 \, s^{-1}$.[199] However, the data obtained by SICM and fluorescence microscopy allow to rationalize this finding.

Comparing the shape of the curve of the Petrov-Schwille approximation in Figure 5.34 with the experimentally determined diffusion coefficients for the individual sizes of the PSMs, one observes a drastic drop of the diffusion coefficient as a function of the area fraction occupied by the l_o domain. Analysis of the trajectories of the domains (Figure 5.29A) showed that the domains are repelled from the pore border even if they are not in hard contact with the surface (Figure 5.58). This indicates that there is an energetic barrier at the rim.
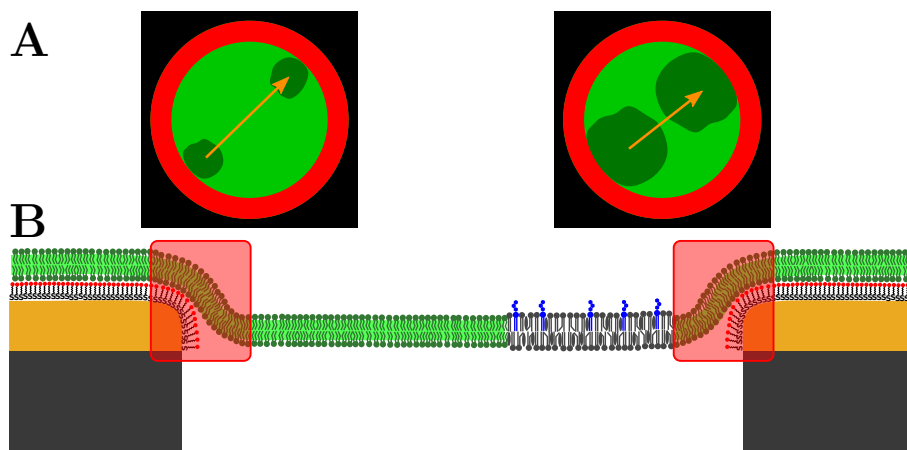
Figure 5.58: Scheme showing that curvature at the pore rime can inhibit domain movement (yellow arrow). The domain does not sample to full area of the PSLBs but avoids the curved regions at the pore border shown in **B**. The effect is more pronounced if the domain covers a larger fraction of the pore (**A**).

The data obtained from SICM show that the pore-spanning membranes are not fully flat but are located slightly lower in the pore center. This requires the membrane to bend at the pore border. This bending is afflicted with an energetic penalty as described by Equation 5.14. Displacing soft l_d area at the pore border by a stiff l_o domain requires an energy, dependent on the arc length of the contact zone between the domain and the curved membrane region, which is roughly $1\,k_B T\,\mathrm{nm}^{-1}$. Böcker[100] *et al.* predicted that the width of the curved region at the border is the curvature radius of $r_c \approx 10\,\mathrm{nm}$. The length of the contact zone between the curved region and the domain is therefore most likely below the resolution limit of the microscope and cannot be observed directly.

Movement of the stiff l_o domain in the direction of the pore border will stop due to this energetic penalty resulting in two effects: i) the area the domain is sampling in the trajectory is smaller than the actual area of the pore. The domain will only

sparsely move into the red region in Figure 5.58A, where a part of the domain is in contact to the curved border. According to Equation 5.9 this leads to an overestimation of the domain size using the developed diffusion model. Compared to the domain radius obtained from thresholding the individual images, this overestimation of about 70 % is indeed found (Figure 5.36). ii) Additionally, the energy barrier will inhibit free displacement even further, slowing the movement of the domain, leading to a lower diffusion coefficient.

This effect is more pronounced if the domain is large compared to the pore. A large domain is more often in contact to the curved membrane region, generating a smaller energetic plateau of unhindered diffusion in the pore center (Figure 5.58A). Interestingly the domain sizes are overestimated by several dozens to hundreds of nanometers. This would indicate that the curved region at the pore border is wider than predicted by Böcker *et al.*. A second mechanism for the repulsion from the pore border involving hydrodynamics is possible. Approach of the large l_o domain displaces lipids close to the border of the pore. Presumably the crossing of the pore border is associated with an energetic barrier because of the membrane curvature and the slower diffusion on the solid support. Lipids might have to move around the domain in the freestanding membrane area, effectively creating an apparently larger membrane viscosity which slows the domain movement. To get an estimate on the energetics of this process one would have to solve the Navier-Stokes equations for a cylinder moving in a round confinement.

Apart from the simple energetic penalty at the pore rim a second type of energy profile was found for large pores (Figure 5.38D). It includes a second energetic maximum in the pore center. The data obtained in SICM support this finding of a more complex 3D structures of these large pore-spanning lipid bilayers.

Experimental approaches to use curvature to control the organization of phase-separated artificial membranes are based on micropatterned substrates that force a solid support membrane into defined curvature radii. Yoon *et al.* and Parthasarathy *et al.* found that l_o domains are not formed in curved membrane regions. In these works the use of solid supported membranes inhibited fast dynamics of the domains and no lateral diffusion of the domains was found.[215–217]

Diffusion of lipid domains has been studied *in vitro* using lipid monolayers and GUVs.[194, 208, 248–251] Wilke *et al.* tracked the movement of ceramide containing domains in lipid monolayers at the air water interface and found diffusion

coefficients of $D \approx 0.1\,\mu\text{m}^2\,\text{s}^{-1}$ for domains with radii of 1 to $3\,\mu\text{m}$.[248, 250] On short time scales a linear relation of the mean square displacement and the time interval used for its calculation was found, showing that the diffusion in this system is free and unhindered. However, at larger time intervals and high domains densities they found a different behavior. Domains in lipid monolayers show a repulsive behavior due to dipole repulsion of the oriented molecules.[252] This hinders the movement of domains and leads to an apparent change in the surface viscosity of the membrane.[248] Varying the surface pressure and the membrane compositions the authors could dissect the viscosity into the contributions of the membrane and the domain-domain repulsion. This exemplifies a similar trend as found in PSLBs. Domains that are small compared to the area of the pore-spanning membrane are freely diffusing, but at higher l_o coverages the repulsion by the pore rim slows the domain's movement.

Cicuta *et al.* used GUVs and determined the diffusion coefficients of l_o domains in membranes of different lipid compositions. Petrov used membranes exhibiting gel-liquid phase separation and extracted the translational and rotational diffusion coefficients of diamond-shaped gel domains in a fluid matrix.[251] Both studies were conducted in true bilayer membranes and can be compared to the results of this work. The values found for the diffusion coefficients of the lipid domains are in excellent agreement with the prediction of the Petrov-Schwille approximation.[199, 208] However, the mean square displacement also shows a complex behavior. Cicuta *et al.* used short time frames to extract the movement. They found that at larger time separations a repulsive interaction between multiple domains in one GUV slowed the diffusion, leading to an apparent higher membrane viscosity. Aliaskarisohi *et al.* used 3D tracking of domains on giant vesicles to further study the influence of domain repulsion on the diffusion coefficient. Using vesicles with one or two domains they studied the rheology and extracted the shear viscosities of the membrane in more detail than Cicuta *et al.*.[249]

An explanation for the domain repulsion is given in the work of Yanagisawa *et al.*.[253] They studied the coalescence of lipid domains in giant vesicles and found two different mechanisms. In the simple case domains condense to form larger aggregates to minimize line tension. However, some of the vesicles studied showed that domain coalescence stops at a certain domain size. Using multiple fluorescent dyes, the authors found the process only occurs if the vesicle has excess membrane area, which

results in a budding of the domains. This budding minimizes line tension, but induces a repulsive bending of the surrounding matrix membrane which inhibits domain coalescence.[254, 255] Figure 5.59 depicts the curvature driven repulsion of domains as published by Ursell *et al.*.[254] Panel A shows a confocal slice of two domains budding from a giant vesicles. Both domains (red line) have positive curvature. Panel B illustrates that the approach of two domain with the same sign of curvature. The domains are tilted by ϕ that minimizes the deformation energy and leads to a repulsive potential.
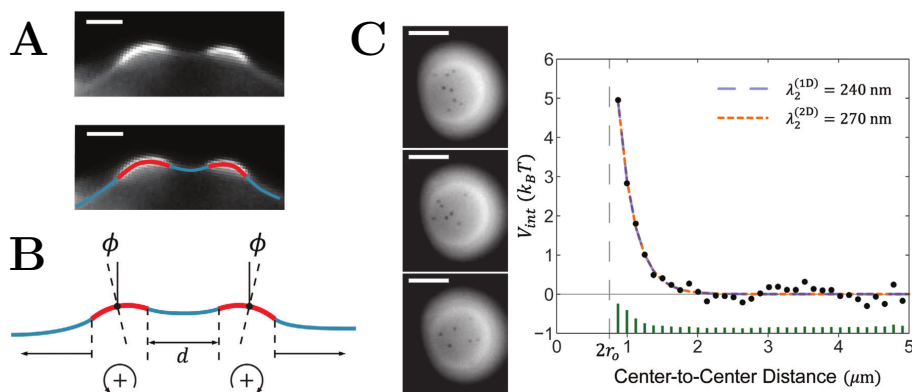
Figure 5.59: A Shape of dimpled domains imaged by fluorescence microscopy. Scale bars: 3 µm. **B** One dimensional model of the dimples shown in **A**. **C** Measured domain interactions. The inset shows GUVs with small dark domains. Scale bars: 10 µm. Tracking their movement allowed to extract the interaction potential. Image modified from Ursell *et al.*.[254]

The potential was measured for small domains on a GUV (dark areas in the inset) and is shown in panel C. The potential can be modeled using a simple one dimensional approximation taking into account the bending modulus of the membrane. Occurrence of membranes dimples in pore-spanning membranes is unlikely due to the high membrane tension but the curved geometry at the pore border will repulse the stiff l_o domains,[43] leading to a similar energy profile as observed by Ursell *et al.* (Figures 5.39A and 5.59C).[254]

These examples show that high domain surface coverage and local mechanical properties of the membrane can influence the movement of lipid domains. In PSLBs both of these effects can be monitored in a controlled way. The three dimensional structure of the membrane at the pore rim induces curvature constricting the movement. This constriction is more pronounced for large domains that cover a

high area fraction of the pore-spanning membrane. The picket-fence model of the lateral organization of the plasma membrane developed by Kusumi, predicts that the cytoskeleton can control the movement of lipids and domains. The exact nature of the interaction is still under debate. Results and discussion shown in this Section clearly prove that local membrane curvature can induce this effect.

5.5 Conclusion

From the results and considerations summarized in this chapter it becomes clear that phase-separated pore-spanning lipid membranes mimic several aspects of the interaction between the cytoskeleton and the plasma membrane. The porous mesh used as the substrate for spreading GUVs disperses the lipid domains leading to the formation of smaller domains. In the freestanding membrane areas the domains adopt the thermodynamically favored round shape, showing the high lipid dynamics in these regions. Topographic analysis of the PSLBs revealed the presence of curvature at the pore rim which acts as an energetic barrier trapping domains in the pore. The movement of the domains can be described using a model taking into account this fence-like effect of the pores.

Incubation with Shiga toxin leads to no alteration of the membrane topography. STxB only binds to the liquid-ordered phase indicating that the Shiga toxin receptor Gb$_3$ is located there. The binding leads to an alteration of the area percentage of the ordered phase in the PSLBs indicating a complex interplay between substrate porosity, pore geometry and the binding of the protein.

6 Conclusion

Processes occurring at the plasma are governed by a complex interplay of the lateral membrane organization and the active influence of the underlying cytoskeleton. The outer leaflet of the mammalian plasma membrane is enriched in sphingomyelin (SM) and cholesterol (Chol). Recently developed techniques show that the membrane segregates into lipid domains of specific composition and protein affinity.

In this thesis phase-separated artificial lipid membranes composed of DOPC/SM/Chol 40:40:20 were doped with the Shiga toxin B-subunit (STxB) receptor lipid globotriaosylceramide (Gb$_3$). The membranes show phase separation into liquid-ordered (l_o) and liquid-disordered (l_d) domains and the lateral structure, dynamics of the membrane and the binding of the toxin were studied.

Different cells lines show varying vulnerability towards STxB. They contain Gb$_3$ species with different fatty acids bound to the ceramide backbone, indicative of different functional roles. The influence of the fatty acid was investigated using solid supported membranes. Five Gb$_3$ derivatives were synthesized by the group of Prof. Dr. Daniel B. Werz. A saturated, an unsaturated, a α-hydroxylated and both 2-hydroxy enantiomers of the biologically most relevant α-hydroxylated and unsaturated fatty acid were covalently bound to Gb$_3$. Including $5\,\text{mol}\%$ of one Gb$_3$ derivative into the membrane allowed to study their impact on the lateral membrane organization by fluorescence and atomic force microscopy. Comparing to the saturated Gb$_3$ species, it was found that α-hydroxylated derivatives showed lower area percentages of l_o phase, indicative of lipid compaction excluding unsaturated lipids from the l_o phase. Using unsaturated Gb$_3$, the l_o phase was found to further segregate into two phases of different molecular composition. Applying SPR spectroscopy nanomolar affinities of STxB towards membranes containing the Gb$_3$ derivatives were found. In all cases STxB binds to the l_o phase of phase-separated membranes, indicating that the Gb$_3$ is localized in this phase independent of the fatty acid attached. Binding to the Gb$_3$ derivative with a saturated fatty acid did not change the l_o area percentage. After STxB binding, localized clusters of the toxin were visualized on the l_o phase with most of the residual l_o phase area being depleted in Gb$_3$. The same intraphase lipid reorganization caused by the multivalent binding of STxB was found for the (R) α-hydroxylated saturated and (R) α-hydroxylated unsaturated derivative.

Additionally, membranes containing the hydroxylated species show an increase of l_o area, indicative of an interphase lipid reorganization. Binding of STxB to the unsaturated Gb_3 leads to no further lipid reorganization. Both diastereomers of the biologically most relevant α-hydroxylated and unsaturated Gb_3 derivative were investigated using reflectometric interference spectroscopy (RIfS) and confocal fluorescence microscopy. Both derivatives facilitate the formation of membrane invaginations, which are believed to be the toxin's mechanism of endocytosis. Membranes containing the unnatural (S) derivative have a higher protein binding capacity and form invaginations to a greater extent. The results show that the fatty acid bound to Gb_3 strongly affects the membrane organization and the derivatives can have different functions regarding the toxin's endocytosis.

The actin cytoskeleton divides the plasma membrane into distinct lateral compartments. To mimic this effect, pore-spanning lipid bilayers (PSLBs) were prepared to create a membrane with freestanding and solid supported areas. Giant unilamellar vesicles were spread on porous substrates with pore diameters between 0.8 and 5.5 µm and porosities between 14 and 41 %, resulting in the formation of small l_o domains. Contact of a domain to the solid support immobilizes it, but l_o domains fully located in the freestanding membrane area show a broad variety of dynamics. They shrink, grow and condense but are not able to cross the pore border, trapping the domains in compartments. A model was developed to describe domain diffusion, assuming the movement of a point-like particle in a circular membrane. Analysis revealed an energetic barrier for domains to get close to the pore border. Using scanning ion-conductance microscopy (SICM) the topography of the pores was found to be mostly flat, with curved regions at the pore border. This curvature influences the movement of the stiffer l_o domains. Incubation of the Gb_3 containing PSLBs with STxB led to the formation of moving STxB-Gb_3 clusters on the l_o phase. Additionally, STxB binding led to a redistribution of lipids between the solid supported and the freestanding membrane regions which was found to be dependent on both porosity and pore size. High membrane tension inhibited STxB induced topography changes. The results show that PSLBs are a suitable model system to study the dynamics of lipids and bound proteins in a spatially confined geometry mimicking the interaction of the plasma membrane with the cytoskeleton.

7 Appendix

7.1 Amino acid sequence of STxB

The amino acid sequence of the native B-subunit isolated from *Shigella dysenteriae* is identical to the one of Verotoxin 1 isolated from *E.coli.*[60,61,256] Cysteine 4 and 57 form a disulfide bridge.[257]

```
              10          20          30          40          50
STxB  TPDCVTGKVEYTKYNDDDTFTVKVGDKELFTNRWNLQSLLLSAQITGMTV

              60
STxB  TIKTNACHNGGGFSEVIFR
```

7.2 Geometry of a domain condensing to the rim

The scheme shown in Figure 5.47 does not reproduce the exact change in line tension upon condensation of a domain of constant area to a rim based domain. Figure 7.1 shows a more precise calculation.
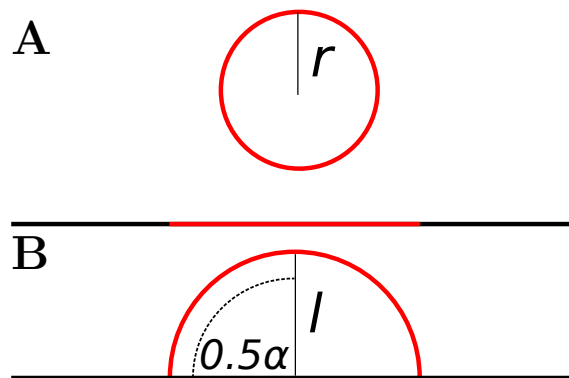
Figure 7.1: Geometry of a domain condensing to the pore rim. **A** Domain prior to condensation. The domain with radius r is not in contact to a domain on the rim (horizontal line). Lines contribunting to the line tension are shown in red. **B** Domain of the same area after condensation.

The domain has an area of $A = \pi r^2$ and a circumference of $U = 2\pi r$. Additionally the l_o domain on the rim contributes an area of line tension with length $b = 2l$. After condensation to the rim the area of the l_o domains is constant. Assuming a large pore radius and the condensed domain adopting a half circular shape, the lengths of the lines relevant for line tension can be calculated. The area of the half circle is $A = \frac{1}{2}\pi l^2$, its arc length $g = l\alpha = l\pi$. Assuming constant area gives $l = \sqrt{\dfrac{2A}{\pi}} = \sqrt{2}r$

The total length of the red line prior to condensation is $2\pi r + 2l = 2r\left(\pi + \sqrt{2}\right)$. The total length of the red line after the condensation is $\pi l = \pi\sqrt{2}r$. The ratio is independent of r and shows that upon condensation the energy of line tension will be reduced by roughly $50\,\%$.

7.3 Correction for area growth of annuli

The area of a single annuli is given by the inner radius of the annuli b and the thickness of the annuli d:

$$A = \pi(b + d)^2 - \pi b^2 = \pi(2bd + d^2). \tag{7.1}$$

Using the mean radius of an annuli $r = b + \frac{1}{2}d$ to correct for the growth in area of the annuli yields the correct proportionality and is sufficient if the resulting histogram's area is subsequently normalized to an area of one.

7.4 List of Figures

7.5 List of Schemes

7.6 List of Tables

7.7 List of symbols and abbreviations

AFM	atomic force microscope
ATP	adenosine triphosphate
bov	bovine
BSA	bovine serum albumin
c	concentration
Chol	cholesterol
CLSM	confocal laser scanning microscope

Cy3	Cyanine3
D	diffusion coefficient
DHPE	1,2-dihexadecanoyl-*sn*-glycero-3-phosphoethanolamine
DOPC	1,2-dioleoyl-*sn*-glycero-3-phosphocholine
DPPC	1,2-dipalmitoyl-*sn*-glycero-3-phosphocholine
E. Coli	*Escherichia coli*
F	force
F-actin	filamentous actin
FCS	fluorescence correlation spectroscopy
FRAP	fluorescence recovery after photobleaching
FWHM	full width half maximum
Gal	galactose
Gb_3	globotriaosylceramide
Gb_3-Porc	globotriaosylceramide from porcine erythrocytes
Glu	glucose
G_{M1}	monosialotetrahexosylganglioside
GPMV	giant plasma membrane vesicle
GPI	glycosylphosphatidylinositol
GSL	glycosphingolipid
GUI	graphical user interface
GUV	giant unilamellar vesicle
h	hour
h	height
HEPES	2-[4-(2-hydroxyethyl)piperazin-1-yl]ethanesulfonic acid
Δh	height difference
ITO	indium tin oxide
k	spring constant
l_d	liquid-disordered
l_i	liquid-intermediate
l_o	liquid-ordered
LUV	large unilamellar vesicle
λ	wave length

M	molar mass
M	molar
min	minute
pdf	probability density function
NMR	nuclear magnetic resonace
POPC	1-palmitoyl-2-oleoyl-*sn*-glycero-3-phosphocholine
porc	porcine
PSLB	pore-spanning lipid bilayer
PSM	pore-spanning membrane
PTFE	polytetrafluoroethylene
RGB	red, green, blue
RIfS	Reflectometric interference spectroscopy
ROI	region of interest
rRNA	ribosomal ribonucleic acid
s	second
SDCLM	Spinning disk confocal laser microscopy
SEM	scanning electron microscope
siRNA	small interfering ribonucleic acid
SM	sphingomyelin
SPR	surface plasmon resonance
SSM	solid supported membrane
STED	stimulated-emission-depletion
STxA	Shiga Toxin subunit A
STxB	Shiga Toxin subunit B
SUV	small unilamellar vesicle
T_m	phase transition temperature
t	time
Tris	tris(hydroxymethyl)aminomethane

7.8 List of chemicals and consumables

ammonia solution	Sigma-Aldrich (Taufkirchen, Germany)
argon	Air Liquide Deutschland GmbH (Düsseldorf, Germany)

β-Bodipy C12-HPC	Life Technologies (Darmstadt, Germany)
BSA	Carl Roth GmbH (Karlsruhe, Germany)
cantilever CSC38	Mikromasch (Tallinn, Estonia)
cholesterol	Sigma-Aldrich (Taufkirchen, Germany)
chloroform	VWR International (Darmstadt, Germany)
DOPC	Avanti Polar Lipids (Alabaster, USA)
Disodium hydrogen phosphate	Merck KGaA (Darmstadt, Germany)
Gb_3 (porcine)	Matreya LLC (Pleasant GAP, USA)
Gb_3-C24:0	Provided by Prof. Dr. Daniel B. Werz
Gb_3-C24:1	Provided by Prof. Dr. Daniel B. Werz
Gb_3-C24:0 2-OH	Provided by Prof. Dr. Daniel B. Werz
Gb_3-C24:1 2(R/S)-OH	Provided by Prof. Dr. Daniel B. Werz
Gb_3-C24:1 2(R)-OH	Provided by Prof. Dr. Daniel B. Werz
Gb_3-C24:1 2(S)-OH	Provided by Prof. Dr. Daniel B. Werz
Ethanol	Carl Roth GmbH (Karlsruhe, Germany)
HEPES	Carl Roth GmbH (Karlsruhe, Germany)
hydrochloric acid	Merck KGaA (Darmstadt, Germany)
ITO slides	Präzisions Glas & Optik GmbH (Iserlohn, Germany)
mercaptohexanol	Sigma-Aldrich (Taufkirchen, Germany)
hydrogen peroxide solution	Carl Roth GmbH (Karlsruhe, Germany)
methanol	Carl Roth GmbH (Karlsruhe, Germany)
mica	Plango GmbH (Wetzlar, Germany)
Polycarbonate membranes	Avestin (Ottawa, Canada)
Porous Si_3N_4 substrates	fluXXion (Eindhoven, Netherlands)
Porous SiO_2 substrates	Provided by Dr. Siegfried Steltenkamp, CEASAR (Bonn, Germany)
Oregon Green DHPE	Life Technologies (Darmstadt, Germany)
Perylen	Sigma-Aldrich (Taufkirchen, Germany)
potassium dihydrogen phosphate	Merck KGaA (Darmstadt, Germany)
n-propanol	Carl Roth GmbH (Karlsruhe, Germany)
silicon wafers	Crystec (Berlin, Germany)
sphingomyelin (porcine)	Avanti Polar Lipids (Alabaster, USA)
sphingomyelin (bovine)	Sigma-Aldrich (Taufkirchen, Germany)

SPR sensor chips (bare gold)	XanTec bioanalytics GmbH (Düsseldorf, Germany)
STxB	Provided by Prof. Dr. Winfried Römer
sucrose	Carl Roth GmbH (Karlsruhe, Germany)
TexasRed DHPE	Santa Cruz Biotechnology Inc. (Heidelberg, Germany)
Tris	Carl Roth GmbH (Karlsruhe, Germany)

7.9 List of devices and software

atomic force microscopy

Nano Wizard I	JPK Instruments (Berlin, Germany)
AxioVision 4.8 LE	Carl Zeiss (Jena, Germany)

Confocal laser scanning microscopy

Examiner Z1	Carl Zeiss (Jena, Germany)
LSM 710	Carl Zeiss (Jena, Germany)
WPlan-Apochromat 63x, NA 1.0	Carl Zeiss (Jena, Germany)

Fiji	http://www.fiji.sc/
Graphics Layout Engine	http://www.gle-graphics.org/
Gwyddion 2.34	http://gwyddion.net/[98]

fluorescence microscopy

Axiotech Vario	Carl Zeiss (Jena, Germany)
Achroplan 40x/0.8 W	Carl Zeiss (Jena, Germany)
Achroplan 63x/0.95 W	Carl Zeiss (Jena, Germany)
HXP 120 C lamp	Carl Zeiss (Jena, Germany)
green filter set 44	Carl Zeiss (Jena, Germany)
red filter set 45	Carl Zeiss (Jena, Germany)
blue filter set 47	Carl Zeiss (Jena, Germany)

Olymypus BX51	Olympus (Tokyo, Japan)
LumPlan FLN 40x/0.80 W	Olympus (Tokyo, Japan)
LumPlan FLN 100x/1.00 W	Olympus (Tokyo, Japan)
XCite Series 120 Q	Olympus (Tokyo, Japan)
green filter set U-MNB2	Olympus (Tokyo, Japan)

red filter set U-MNG2	Olympus (Tokyo, Japan)
blue filter set U-MNUA2	Olympus (Tokyo, Japan)
spinning disc confocal	custom build
custom stand based on ix73	Olympus (Tokyo, Japan)
spinning disc Yokogawa CSU-X	Rota Yokogawa (Wehr, Germany)
camera iXON 897Ultra	Andor Technology (Belfast, UK)
piezo P-721-CDQ	Physik Instrumente (Karlsruhe, Germany)
filter ZET405/488/561/640m	AHF Analysentechnik (Tübingen, Germany)
filter ET650/60	AHF Analysentechnik (Tübingen, Germany)
filter ET525/50	AHF Analysentechnik (Tübingen, Germany)
objective CFI Plan 100XW 100×/1.1	Nikon (Düsseldorf, Germany)
objective UPlanSApo 60x 1.20 W	Olympus (Tokyo, Japan)
ImageJ 1.49b	Wayne Rasband/NIH[258]
zen2012	Carl Zeiss (Jena, Germany)
matlab2011a	MathWorks (Natick, USA)
matlab2012b	MathWorks (Natick, USA)
matlab2014a	MathWorks (Natick, USA)
Osmometer 030	Gonotec (Berlin, Germany)
plasma cleaner PDC 32 G-2	Harrick Plasma (Ithaca, USA)
plasma cleaner zepto	diener electronic (Ebhausen, Germany)

reflectometric interference spectroscopy

Spectrometer NanoCalc-2000	OceanOptics Germany GmbH (Ostfildern, Germany)
Pump Ismatec 795C	IDEX Health & Science, Wertheim

scanning ion-conductance microscopy

puller P1000	Sutter Instruments (Novato, USA)
stand IX71	Olympus (Tokyo, Japan)
ICNano2000	Ionscope (Melbourn, UK)
oscilloscope TDS1001B	Tektronix UK Ltd. (Bracknell, UK)
amplifier Axopatch 200B	Axon Instruments (Union City, USA)
piezo controller E500K	Physik Intrumente (Karlsruhe, Germany)
software ICNano	Ionscope (Melbourn, UK)

surface plasmon resonance

spectrometer SR7000DC	Reichert Technologies Life Sciences (Buffalo, USA)
pump SR7500	Reichert Technologies Life Sciences (Buffalo, USA)
injection valve SR8300	Reichert Technologies Life Sciences (Buffalo, USA)
diverter SR8600	Reichert Technologies Life Sciences (Buffalo, USA)
degasser DEG100	XanTec bioanalytics GmbH (Düsseldorf, Germany)

vesicle formation

Sonopuls HD2070 resonator cup	Bandelin (Hagen, Germany)
frequency generator Agilent 33220A	Agilent Technology (Santa Clara, USA)
VesiclePrep Pro	Nanion Technologies (München, Germany)
evaporation device Bal-Tec Med020	oerlikon (Balzer, Liechtenstein)

8 Bibliography

[1] B. Alberts, A. Johnson, P. Walter, J. Lewis, M. Raff, K. Roberts, *Molecular Biology of the Cell*, Taylor & Francis Ltd, **2007**, 5th edition.

[2] S. J. Singer, G. L. Nicolson, The fluid mosaic model of the structure of cell membranes, *Science* **1972**, *175*, 720–731.

[3] K. Simons, M. J. Gerl, Revitalizing membrane rafts: new tools and insights, *Nat. Rev. Mol. Cell Biol.* **2010**, *11*(10), 688–699.

[4] D. Schwudke, K. Schuhmann, R. Herzog, S. R. Bornstein, A. Shevchenko, Shotgun lipidomics on high resolution mass spectrometers, *Cold Spring Harb. Perspect. Biol.* **2011**, *3*(9), a004614.

[5] M. D. Bazzi, G. L. Nelsestuen, Interaction of annexin VI with membranes: highly restricted dissipation of clustered phospholipids in membranes containing phosphatidylethanolamine, *Biochemistry* **1992**, *31*(42), 10406–10413.

[6] A. Honigmann, G. van den Bogaart, E. Iraheta, H. J. Risselada, D. Milovanovic, V. Mueller, S. Müllar, U. Diederichsen, D. Fasshauer, H. Grubmüller, S. W. Hell, C. Eggeling, K. Kühnel, R. Jahn, Phosphatidylinositol 4, 5-bisphosphate clusters act as molecular beacons for vesicle recruitment, *Nat. Struct. Mol. Biol.* **2013**, *20*(6), 679–686.

[7] M. Whitman, C. P. Downes, M. Keeler, T. Keller, L. Cantley, Type I phosphatidylinositol kinase makes a novel inositol phospholipid, phosphatidylinositol-3-phosphate, *Nature* **1988**, *332*(6165), 644–646.

[8] K. Simons, E. Ikonen, Functional rafts in cell membranes, *Nature* **1997**, *387*(6633), 569–572.

[9] J. R. Silvius, Role of cholesterol in lipid raft formation: lessons from lipid model systems, *Biochim. Biophys. Acta.* **2003**, *1610*(2), 174–183.

[10] M. Hensel, J. Klingauf, J. Piehler, Imaging the invisible: resolving cellular microcompartments by superresolution microscopy techniques, *Biol. Chem.* **2013**, *394*(9), 1097–1113.

[11] D. Lingwood, K. Simons, Lipid rafts as a membrane-organizing principle, *Science* **2010**, *327*(5961), 46–50.

[12] E. Sezgin, S. J. Davis, C. Eggeling, Membrane Nanoclusters—Tails of the Unexpected, *Cell* **2015**, *161*(3), 433–434.

[13] S. W. Hell, J. Wichmann, Breaking the diffraction resolution limit by stimulated emission: stimulated-emission-depletion fluorescence microscopy, *Opt. Lett.* **1994**, *19*(11), 780–782.

[14] C. Eggeling, C. Ringemann, R. Medda, G. Schwarzmann, K. Sandhoff, S. Polyakova, V. N. Belov, B. Hein, C. von Middendorff, A. Schönle, S. W. Hell, Direct observation of the nanoscale dynamics of membrane lipids in a living cell, *Nature* **2009**, *457*(7233), 1159–1162.

[15] V. Mueller, C. Ringemann, A. Honigmann, G. Schwarzmann, R. Medda, M. Leutenegger, S. Polyakova, V. Belov, S. W. Hell, C. Eggeling, STED nanoscopy reveals molecular details of cholesterol-and cytoskeleton-modulated lipid interactions in living cells, *Biophys. J.* **2011**, *101*(7), 1651–1660.

[16] A. Kusumi, C. Nakada, K. Ritchie, K. Murase, K. Suzuki, H. Murakoshi, R. S. Kasai, J. Kondo, T. Fujiwara, Paradigm shift of the plasma membrane concept from the two-dimensional continuum fluid to the partitioned fluid: high-speed single-molecule tracking of membrane molecules, *Annu. Rev. Biophys. Biomol. Struct.* **2005**, *34*, 351–378.

[17] A. Kusumi, Y. M. Shirai, I. Koyama-Honda, K. G. Suzuki, T. K. Fujiwara, Hierarchical organization of the plasma membrane: investigations by single-molecule tracking vs. fluorescence correlation spectroscopy, *FEBS Lett.* **2010**, *584*(9), 1814–1823.

[18] R. G. Fehon, A. I. McClatchey, A. Bretscher, Organizing the cell cortex: the role of ERM proteins, *Nat. Rev. Mol. Cell Biol.* **2010**, *11*(4), 276–287.

[19] P.-F. Lenne, L. Wawrezinieck, F. Conchonaud, O. Wurtz, A. Boned, X.-J. Guo, H. Rigneault, H.-T. He, D. Marguet, Dynamic molecular confinement in the plasma membrane by microdomains and the cytoskeleton meshwork, *EMBO J.* **2006**, *25*(14), 3245–3256.

[20] N. Morone, T. Fujiwara, K. Murase, R. S. Kasai, H. Ike, S. Yuasa, J. Usukura, A. Kusumi, Three-dimensional reconstruction of the membrane skeleton at the plasma membrane interface by electron tomography, *J. Cell Biol.* **2006**, *174*(6), 851–862.

[21] H. Heerklotz, Triton promotes domain formation in lipid raft mixtures, *Biophys. J.* **2002**, *83*(5), 2693–2701.

[22] I. Levental, M. Grzybek, K. Simons, Raft domains of variable properties and compositions in plasma membrane vesicles, *Proc. Natl. Acad. Sci. U.S.A.* **2011**, *108*(28), 11411–11416.

[23] B. B. Machta, S. Papanikolaou, J. P. Sethna, S. L. Veatch, Minimal model of plasma membrane heterogeneity requires coupling cortical actin to criticality, *Biophys. J.* **2011**, *100*(7), 1668–1677.

[24] P. Sengupta, B. Baird, D. Holowka, Lipid rafts, fluid/fluid phase separation, and their relevance to plasma membrane structure and function, *Semin. Cell Dev. Biol.* **2007**, *18*(5), 583–590.

[25] I. Levental, F. Byfield, P. Chowdhury, F. Gai, T. Baumgart, P. Janmey, Cholesterol-dependent phase separation in cell-derived giant plasma-membrane vesicles, *Biochem. J.* **2009**, *424*, 163–167.

[26] H.-J. Kaiser, D. Lingwood, I. Levental, J. L. Sampaio, L. Kalvodova, L. Rajendran, K. Simons, Order of lipid phases in model and plasma membranes, *Proc. Natl. Acad. Sci. U.S.A.* **2009**, *106*(39), 16645–16650.

[27] E. Sezgin, H.-J. Kaiser, T. Baumgart, P. Schwille, K. Simons, I. Levental, Elucidating membrane structure and protein behavior using giant plasma membrane vesicles, *Nat. Protoc.* **2012**, *7*(6), 1042–1051.

[28] M. Eeman, M. Deleu, From biological membranes to biomimetic model membranes, *Biotechnol. Agron. Soc. Envir.* **2010**, *14*, 719–736.

[29] S. L. Veatch, S. L. Keller, Seeing spots: Complex phase behavior in simple membranes, *Biochim. Biophys. Acta* **2005**, *1746*(3), 172–185.

[30] S. Veatch, S. Keller, Miscibility Phase Diagrams of Giant Vesicles Containing Sphingomyelin, *Phys. Rev. Lett.* **2005**, *94*, 148101.

[31] D. Marsh, Cholesterol-induced fluid membrane domains: a compendium of lipid-raft ternary phase diagrams, *Biochim. Biophys. Acta* **2009**, *1788*, 2114–2123.

[32] D. Marsh, *Handbook of Lipid Bilayers*, CRC Press, **2013**, 2nd edition.

[33] M. R. Vist, J. H. Davis, Phase equilibria of cholesterol/dipalmitoylphosphatidylcholine mixtures: deuterium nuclear magnetic resonance and differential scanning calorimetry, *Biochemistry* **1990**, *29*(2), 451–464.

[34] B. Kollmitzer, P. Heftberger, R. Podgornik, J. F. Nagle, G. Pabst, Bending rigidities and interdomain forces in membranes with coexisting lipid domains, *Biophys. J.* **2015**, *108*(12), 2833–2842.

[35] T. Baumgart, G. Hunt, E. R. Farkas, W. W. Webb, G. W. Feigenson, Fluorescence probe partitioning between Lo/Ld phases in lipid membranes, *Biochim. Biophys. Acta* **2007**, *1768*(9), 2182–2194.

[36] E. Sezgin, I. Levental, M. Grzybek, G. Schwarzmann, V. Mueller, A. Honig-mann, V. N. Belov, C. Eggeling, Ü. Coskun, K. Simons, P. Schwille, Partition-ing, diffusion, and ligand binding of raft lipid analogs in model and cellular plasma membranes, *Biochim. Biophys. Acta* **2012**, *1818*(7), 1777–1784.

[37] N. Bezlyepkina, R. S. Gracià, P. Shchelokovskyy, R. Lipowsky, R. Di-mova, Phase Diagram and Tie-Line Determination for the Ternary Mixture DOPC/eSM/Cholesterol, *Biophys. J.* **2013**, *104*, 1456–1464.

[38] T. Portet, S. E. Gordon, S. L. Keller, Increasing membrane tension decreases miscibility temperatures; an experimental demonstration via micropipette aspiration, *Biophys. J.* **2012**, *103*(8), L35–L37.

[39] W. Römer, L.-L. Pontani, B. Sorre, C. Rentero, L. Berland, V. Chambon, C. Lamaze, P. Bassereau, C. Sykes, K. Gaus, L. Johannes, Actin Dynamics Drive Membrane Reorganization and Scission in Clathrin-Independent Endo-cytosis, *Cell* **2010**, *140*(4), 540–553.

[40] C. Dietrich, L. Bagatolli, Z. Volovyk, N. Thompson, M. Levi, K. Jacobson, E. Gratton, Lipid rafts reconstituted in model membranes, *Biophys. J.* **2001**, *80*(3), 1417–1428.

[41] P. I. Kuzmin, S. A. Akimov, Y. A. Chizmadzhev, J. Zimmerberg, F. S. Cohen, Line Tension and Interaction Energies of Membrane Rafts Calculated from Lipid Splay and Tilt, *Biophys. J.* **2005**, *88*(2), 1120–1133.

[42] A. J. García-Sáez, S. Chiantia, P. Schwille, Effect of line tension on the lateral organization of lipid membranes, *J. Biol. Chem.* **2007**, *282*, 33537–33544.

[43] I. Mey, M. Stephan, E. K. Schmitt, M. M. Müller, M. Ben Amar, C. Steinem, A. Janshoff, Local membrane mechanics of pore-spanning bilayers, *J. Am. Chem. Soc.* **2009**, *131*(20), 7031–7039.

[44] M. Kocun, T. D. Lazzara, C. Steinem, A. Janshoff, Preparation of solvent-free, pore-spanning lipid bilayers: Modeling the low tension of plasma membranes, *Langmuir* **2011**, *27*(12), 7672–7680.

[45] J. W. Kuhlmann, I. P. Mey, C. Steinem, Modulating the Lateral Tension of Solvent-Free Pore-Spanning Membranes, *Langmuir* **2014**, *30*(27), 8186–8192.

[46] M. Gleisner, I. Mey, M. Barbot, C. Dreker, M. Meinecke, C. Steinem, Driving a planar model system into the 3rd dimension: generation and control of curved pore-spanning membrane arrays, *Soft Matter* **2014**, *10*(33), 6228–6236.

[47] L. L. G. Schwenen, R. Hubrich, D. Milovanovic, B. Geil, J. Yang, A. Kros, R. Jahn, C. Steinem, Resolving single membrane fusion events on planar pore-spanning membranes, *Sci. Rep.* **2015**, *5*, 12006.

[48] L. L. G. Schwenen, Untersuchung einzelner SNARE-vermittelter Membranfusionsereignisse auf planaren porenüberspannenden Membranen, PhD thesis, Georg-August-Universität Göttingen, **2015**.

[49] I. Kusters, A. M. Van Oijen, A. J. Driessen, Membrane-on-a-Chip: Microstructured Silicon/Silicon-Dioxide Chips for High-Throughput Screening of Membrane Transport and Viral Membrane Fusion, *ACS Nano* **2014**, *8*(4), 3380–3392.

[50] I. Höfer, C. Steinem, A membrane fusion assay based on pore-spanning lipid bilayers, *Soft Matter* **2011**, *7*(5), 1644–1647.

[51] A. Orth, L. Johannes, W. Römer, C. Steinem, Creating and Modulating Microdomains in Pore-Spanning Membranes, *ChemPhysChem* **2012**, *13*, 108–114.

[52] A. Orth, Einfluss des Zellkortex auf die Plasmamembran: Modulation von Mikrodomänen in Modellmembranen, PhD thesis, Georg-August-Universität Göttingen, **2012**.

[53] D. Frese, S. Steltenkamp, S. Schmitz, C. Steinem, In situ generation of electrochemical gradients across pore-spanning membranes, *RSC Adv.* **2013**, *3*(36), 15752–15761.

[54] L. Johannes, D. Tenza, C. Antony, B. Goud, Retrograde Transport of KDEL-bearing B-fragment of Shiga Toxin, *J. Biol. Chem.* **1997**, *272*(31), 19554–19561.

[55] L. Johannes, S. Mayor, Induced domain formation in endocytic invagination, lipid sorting, and scission, *Cell* **2010**, *142*, 507–510.

[56] J. Manitz, T. Kneib, M. Schlather, D. Helbing, D. Brockmann, Origin Detection during food-borne Disease Outbreaks-A case study of the 2011 EHEC/HUS Outbreak in Germany, *PLoS Currents* **2014**, *6*.

[57] H. Karch, EHEC O104: H4 und die Folgen, *BIOspektrum* **2011**, *17*(6), 616–620.

[58] S. S. Karve, A. A. Weiss, Glycolipid Binding Preferences of Shiga Toxin Variants, *PLoS One* **2014**, *9*(7), e101173.

[59] L. Johannes, W. Römer, Shiga toxins—from cell biology to biomedical applications, *Nat. Rev. Microbiol.* **2010**, *8*(2), 105–116.

[60] H. Ling, A. Boodhoo, B. Hazes, M. D. Cummings, G. D. Armstrong, J. L. Brunton, R. J. Read, Structure of the shiga-like toxin I B-pentamer complexed with an analogue of its receptor Gb3, *Biochemistry* **1998**, *37*(7), 1777–1788.

[61] M. E. Fraser, M. M. Chernaia, Y. V. Kozlov, M. N. James, Crystal structure of the holotoxino from shigella dysenteriae at 2.5 Å resolution, *Nat. Struct. Mol. Biol.* **1994**, *1*(1), 59–64.

[62] D. C. Smith, J. M. Lord, L. M. Roberts, L. Johannes, Glycosphingolipids as toxin receptors, *Semin. Cell Dev. Biol.* **2004**, *15*(4), 397–408.

[63] H. Shimizu, R. Field, S. Homans, A. Donohue-Rolfe, Solution structure of the complex between the B-subunit homopentamer of verotoxin VT-1 from Escherichia coli and the trisaccharide moiety of globotriaosylceramide, *Biochemistry* **1998**, *37*(31), 11078–11082.

[64] D. Pina, L. Johannes, M. Castanho, Shiga toxin B-subunit sequential binding to its natural receptor in lipid membranes, *Biochim. Biophys. Acta* **2007**, *1768*(3), 628–636.

[65] P. M. St. Hilaire, M. K. Boyd, E. J. Toone, Interaction of the Shiga-like toxin type 1 B-subunit with its carbohydrate receptor, *Biochemistry* **1994**, *33*(48), 14452–14463.

[66] R. Mahfoud, M. Mylvaganam, C. A. Lingwood, J. Fantini, A novel soluble analog of the HIV-1 fusion cofactor, globotriaosylceramide (Gb3), eliminates the cholesterol requirement for high affinity gp120/Gb3 interaction, *J. Lipid Res.* **2002**, *43*, 1670–1679.

[67] M. Watanabe, K. Igai, K. Matsuoka, A. Miyagawa, T. Watanabe, R. Yanoshita, Y. Samejima, D. Terunuma, Y. Natori, K. Nishikawa, Structural analysis of the interaction between Shiga toxin B subunits and linear polymers bearing clustered globotriose residues, *Infect. Immun.* **2006**, *74*(3), 1984–1988.

[68] V. M. Wolski, A. M. Soltyk, J. L. Brunton, Mouse toxicity and cytokine release by verotoxin 1 B subunit mutants, *Infect. Immun.* **2001**, *69*(1), 579–583.

[69] A. M. Soltyk, C. R. MacKenzie, V. M. Wolski, T. Hirama, P. I. Kitov, D. R. Bundle, J. L. Brunton, A mutational analysis of the globotriaosylceramide-binding sites of verotoxin VT1, *J. Biol. Chem.* **2002**, *277*(7), 5351–5359.

[70] B. Windschiegl, A. Orth, W. Römer, L. Berland, B. Stechmann, P. Bassereau, L. Johannes, C. Steinem, Lipid Reorganization Induced by Shiga Toxin Clustering on Planar Membranes, *PLoS One* **2009**, *4*(7), e6238.

[71] W. Römer, L. Berland, V. Chambon, K. Gaus, B. Windschiegl, D. Tenza, Aly, M. R. E., V. Fraisier, J.-C. Florent, D. Perrais, C. Lamaze, G. Raposo, C. Steinem, P. Sens, P. Bassereau, L. Johannes, Shiga toxin induces tubular membrane invaginations for its uptake into cells, *Nature* **2007**, *450*, 670–675.

[72] H. Ewers, W. Römer, A. E. Smith, K. Bacia, S. Dmitrieff, W. Chai, R. Mancini, J. Kartenbeck, V. Chambon, L. Berland, A. Oppenheim, G. Schwarzmann, T. Feizi, P. Schwille, P. Sens, A. Helenius, L. Johannes, GM1 structure determines SV40-induced membrane invagination and infection, *Nat. Cell Biol.* **2009**, *12*(1), 11–18.

[73] A. Kiarash, B. Boyd, C. A. Lingwood, Glycosphingolipid receptor function is modified by fatty acid content. Verotoxin 1 and verotoxin 2c preferentially recognize different globotriaosyl ceramide fatty acid homologues, *J. Biol. Chem.* **1994**, *269*, 11138–11146.

[74] B. Binnington, D. Lingwood, A. Nutikka, C. A. Lingwood, Effect of Globotriaosyl Ceramide Fatty Acid α-Hydroxylation on the Binding by Verotoxin 1 and Verotoxin 2, *Neurochem. Res.* **2002**, *27*(7/8), 807–813.

[75] D. Lingwood, B. Binnington, T. Róg, I. Vattulainen, M. Grzybek, Ü. Coskun, C. A. Lingwood, K. Simons, Cholesterol modulates glycolipid conformation and receptor activity, *Nat. Chem. Biol.* **2011**, *7*, 260–262.

[76] K.-P. Janssen, D. Vignjevic, R. Boisgard, T. Falguières, G. Bousquet, D. Decaudin, F. Dollé, D. Louvard, B. Tavitian, S. Robine, et al., In vivo tumor targeting using a novel intestinal pathogen-based delivery approach, *Cancer Res.* **2006**, *66*(14), 7230–7236.

[77] G. W. Feigenson, Phase diagrams and lipid domains in multicomponent lipid bilayer mixtures, *Biochim. Biophys. Acta* **2009**, *1788*, 47–52.

[78] G. van Meer, D. R. Voelker, G. W. Feigenson, Membrane lipids: where they are and how they behave, *Nat. Rev. Mol. Cell Biol.* **2008**, *9*(2), 112–124.

[79] K. P. Shaw, N. J. Brooks, J. A. Clarke, O. Ces, J. M. Seddon, R. V. Law, Pressure–temperature phase behaviour of natural sphingomyelin extracts, *Soft Matter* **2012**, *8*, 1070.

[80] B. Ramstedt, P. Leppimäki, M. Axberg, J. P. Slotte, Analysis of natural and synthetic sphingomyelins using high-performance thin-layer chromatography, *Eur. J. Biochem.* **1999**, *266*(3), 997–1002.

[81] Avanti Polar Lipids, Sphingomyelin (Brain, Porcine, 86062), accessed March 2, 2015.

[82] Life Technologies, Fluorescence Spectra Viewer, accessed March 4, 2015.

[83] AttoTec, Atto488 product page, accessed March 4, 2015.

[84] Oregon Medical Laser Center, `http://omlc.org/spectra/PhotochemCAD/html/023.html`, accessed March 4, 2015.

[85] T. Okuda, N. Tokuda, S.-i. Numata, M. Ito, M. Ohta, K. Kawamura, J. Wiels, T. Urano, O. Tajima, K. Furukawa, et al., Targeted disruption of Gb3/CD77 synthase gene resulted in the complete deletion of globo-series glycosphingolipids and loss of sensitivity to verotoxins, *J. Biol. Chem.* **2006**, *281*(15), 10230–10235.

[86] O. M. Schütte, A. Ries, A. Orth, L. J. Patalag, W. Römer, C. Steinem, D. B. Werz, Influence of Gb$_3$ glycosphingolipids differing in their fatty acid chain on the phase behaviour of solid supported membranes: chemical syntheses and impact of Shiga toxin binding, *Chem. Sci.* **2014**, *5*(8), 3104–3114.

[87] O. M. Schütte, L. J. Patalag, L. M. C. Weber, A. Ries, W. Römer, D. B. Werz, C. Steinem, 2-Hydroxy Fatty Acid Enantiomers of Gb$_3$ Impact Shiga Toxin Binding and Membrane Organization, *Biophys. J.* **2015**, *108*(12), 2775–2778.

[88] M. Pawliczek, J. Wallbaum, D. B. Werz, Synthesis of Enantiomerically Pure α-Hydroxylated Nervonic Acid – A Chiral Pool Approach to α-Hydroxylated Unsaturated Fatty Acids, *Synlett* **2014**, *25*(10), 1435–1437.

[89] R. P. Richter, R. Bérat, A. R. Brisson, Formation of solid-supported lipid bilayers: an integrated view, *Langmuir* **2006**, *22*(8), 3497–3505.

[90] M. I. Angelova, D. S. Dimitrov, Liposome electroformation, *Farad. Discuss.* **1986**, *81*, 303–311.

[91] R. Zidovetzki, I. Levitan, Use of cyclodextrins to manipulate plasma membrane cholesterol content: evidence, misconceptions and control strategies, *Biochim. Biophys. Acta* **2007**, *1768*(6), 1311–1324.

[92] S. Wilhelm, Confocal Laser Scanning Microscopy (`http://zeiss-campus.magnet.fsu.edu/referencelibrary/pdfs/ZeissConfocalPrinciples.pdf`), accessed May, 2015.

[93] D. K. Toomre, M. F. Langhorst, D. M. W., Introduction to Spinning Disk Confocal Microscopy (`http://zeiss-campus.magnet.fsu.edu/articles/spinningdisk/introduction.html`), accessed May, 2015.

[94] C. Gerber, H. P. Lang, How the doors to the nanoworld were opened, *Nat. Nanotechnol.* **2006**, *1*(1), 3–5.

[95] B. Huang, M. Bates, X. Zhuang, Super resolution fluorescence microscopy, *Annu. Rev. Biochem.* **2009**, *78*, 993.

[96] T. Ando, T. Uchihashi, S. Scheuring, Filming biomolecular processes by high-speed atomic force microscopy, *Chem. Rev.* **2014**, *114*(6), 3120–3188.

[97] Sullan, Ruby May A, J. K. Li, C. Hao, G. C. Walker, S. Zou, Cholesterol-dependent nanomechanical stability of phase-segregated multicomponent lipid bilayers, *Biophys. J.* **2010**, *99*, 507–516.

[98] D. Nečas, P. Klapetek, Gwyddion: an open-source software for SPM data analysis, *Cent. Eur. J. Phys.* **2012**, *10*(1), 181–188.

[99] P. Hansma, B. Drake, O. Marti, S. Gould, C. Prater, The scanning ion-conductance microscope, *Science* **1989**, *243*(4891), 641–643.

[100] M. Böcker, S. Muschter, E. K. Schmitt, C. Steinem, T. E. Schäffer, Imaging and patterning of pore-suspending membranes with scanning ion conductance microscopy, *Langmuir* **2009**, *25*(5), 3022–3028.

[101] D. Thatenhorst, J. Rheinlaender, T. E. Schäffer, I. D. Dietzel, P. Happel, Effect of Sample Slope on Image Formation in Scanning Ion Conductance Microscopy, *Anal. Chem.* **2014**, *86*(19), 9838–9845.

[102] H. Nitz, J. Kamp, H. Fuchs, A combined scanning ion-conductance and shear-force microscope, *Probe Microsc.* **1998**, *1*, 187–200.

[103] C. L. Baird, D. G. Myszka, Current and emerging commercial optical biosensors, *J. Mol. Recognit.* **2001**, *14*(5), 261–268.

[104] X. Fan, I. M. White, S. I. Shopova, H. Zhu, J. D. Suter, Y. Sun, Sensitive optical biosensors for unlabeled targets: A review, *Anal. Chim. Acta* **2008**, *620*(1), 8–26.

[105] A. V. Zayats, I. I. Smolyaninov, A. A. Maradudin, Nano-optics of surface plasmon polaritons, *Phys. Rep.* **2005**, *408*(3), 131–314.

[106] Standard Flow Cell (`http://www.reichertspr.com/flow-cells/standard-flow-cell/`), accessed January, 2015.

[107] H. Nakajima, N. Kiyokawa, Y. U. Katagiri, T. Taguchi, T. Suzuki, T. Sekino, K. Mimori, T. Ebata, M. Saito, H. Nakao, et al., Kinetic analysis of binding between Shiga toxin and receptor glycolipid Gb3Cer by surface plasmon resonance, *J. Biol. Chem.* **2001**, *276*(46), 42915–42922.

[108] G. Gauglitz, Direct optical sensors: principles and selected applications, *Anal. Bioanal. Chem.* **2005**, *381*(1), 141–155.

[109] D. Meschede, *Optik, Licht und Laser*, Springer-Verlag, **2009**.

[110] M. Polyanskiy, Refractive Index database (`http://refractiveindex.info/`), accessed May, 2015.

[111] R. Krick, R. A. Busse, A. Scacioc, M. Stephan, A. Janshoff, M. Thumm, K. Kuhnel, Structural and functional characterization of the two phosphoinositide binding sites of PROPPINs, a -propeller protein family, *Proc. Natl. Acad. Sci. U.S.A.* **2012**, *109*(30), E2042–E2049.

[112] K. Tawa, K. Morigaki, Substrate-Supported Phospholipid Membranes Studied by Surface Plasmon Resonance and Surface Plasmon Fluorescence Spectroscopy, *Biophys. J.* **2005**, *89*(4), 2750–2758.

[113] J. Vörös, The Density and Refractive Index of Adsorbing Protein Layers, *Biophys. J.* **2004**, *87*(1), 553–561.

[114] P. Husen, M. Fidorra, S. Härtel, L. A. Bagatolli, J. H. Ipsen, A method for analysis of lipid vesicle domain structure from confocal image data, *Eur. Biophys. J.* **2012**, *41*(2), 161–175.

[115] T. Bhatia, P. Husen, J. H. Ipsen, L. A. Bagatolli, A. C. Simonsen, Fluid domain patterns in free-standing membranes captured on a solid support, *Biochim. Biophys. Acta* **2014**, *1838*(10), 2503–2510.

[116] J. P. Snyder, *Map projections–A working manual*, 1395, USGPO, **1987**.

[117] M. Shahedi, imshow3D (`http://www.mathworks.com/matlabcentral/fileexchange/41334`), accessed June, 2014.

[118] I. Bucher, circfit (`http://www.mathworks.com/matlabcentral/fileexchange/5557`), accessed June, 2014.

[119] R. Bemis, thresh_tool (`http://www.mathworks.com/matlabcentral/fileexchange/6770`), accessed October, 2012.

[120] P. Li, LSM File Toolbox (`https://www.mathworks.com/matlabcentral/fileexchange/8412`), accessed October, 2012.

[121] J. Lundgren, zerobess (`https://www.mathworks.com/matlabcentral/fileexchange/26639`), accessed October, 2014.

[122] A. Römer, Untersuchung der Shiga-Toxin Gb_3 Interaktion mittels oberflächensensitiver Methoden, bachelor thesis, Georg-August-Universität Göttingen, **2013**.

[123] J. Arnaud, K. Tröndle, J. Claudinon, A. Audfray, A. Varrot, W. Römer, A. Imberty, Membrane Deformation by Neolectins with Engineered Glycolipid Binding Sites, *Angew. Chem. Int .Ed.* **2014**, *53*(35), 9267–9270.

[124] B. Tsai, J. M. Gilbert, T. Stehle, W. Lencer, T. L. Benjamin, T. A. Rapoport, Gangliosides are receptors for murine polyoma virus and SV40, *EMBO J.* **2003**, *22*(17), 4346–4355.

[125] T. Waddell, A. Cohen, C. A. Lingwood, Induction of verotoxin sensitivity in receptor-deficient cell lines using the receptor glycolipid globotriosylceramide, *Proc. Natl. Acad. Sci. U.S.A.* **1990**, *87*, 7898–7901.

[126] M. S. Jacewicz, M. Mobassaleh, S. K. Gross, K. A. Balasubramanian, P. F. Daniel, S. Raghavan, R. H. McCluer, G. T. Keusch, Pathogenesis of Shigella diarrhea: XVII. A mammalian cell membrane glycolipid, Gb3, is required but not sufficient to confer sensitivity to Shiga toxin, *J. Infect. Dis.* **1994**, *169*, 538–546.

[127] F. Mallard, C. Antony, D. Tenza, J. Salamero, B. Goud, L. Johannes, Direct pathway from early/recycling endosomes to the Golgi apparatus revealed through the study of shiga toxin B-fragment transport, *J. Cell Biol.* **1998**, *143*, 973–990.

[128] K. Sandvig, B. van Deurs, Transport of protein toxins into cells: pathways used by ricin, cholera toxin and Shiga toxin, *FEBS Lett.* **2002**, *529*(1), 49–53.

[129] O. Kovbasnjuk, M. Edidin, M. Donowitz, Role of lipid rafts in Shiga toxin 1 interaction with the apical surface of Caco-2 cells, *J. Cell Sci.* **2001**, *114*, 4025–4031.

[130] T. Hanashima, M. Miyake, K. Yahiro, Y. Iwamaru, A. Ando, N. Morinaga, M. Noda, Effect of Gb3 in lipid rafts in resistance to Shiga-like toxin of mutant Vero cells, *Microb. Pathog.* **2008**, *45*, 124–133.

[131] A. Pellizzari, H. Pang, C. A. Lingwood, Binding of verocytotoxin 1 to its receptor is influenced by differences in receptor fatty acid content, *Biochemistry* **1992**, *31*, 1363–1370.

[132] V. Solovyeva, L. Johannes, A. C. Simonsen, Shiga toxin induces membrane reorganization and formation of long range lipid order, *Soft Matter* **2014**, *11*(1), 186–192.

[133] X. Hagnerelle, C. Plisson, O. Lambert, S. Marco, J. Louis Rigaud, L. Johannes, D. Lévy, Two-dimensional structures of the Shiga toxin B-subunit and of a chimera bound to the glycolipid receptor Gb3, *J. Struct. Biol.* **2002**, *139*, 113–121.

[134] M. Safouane, L. Berland, A. Callan-Jones, B. Sorre, W. Römer, L. Johannes, Toombes, Gilman E. S., P. Bassereau, Lipid Cosorting Mediated by Shiga Toxin Induced Tubulation, *Traffic* **2010**, *11*(12), 1519–1529.

[135] R. Mahfoud, A. Manis, C. A. Lingwood, Fatty acid-dependent globotriaosyl ceramide receptor function in detergent resistant model membranes, *J. Lipid Res.* **2009**, *50*(9), 1744–1755.

[136] A. J. García-Sáez, P. Schwille, Stability of lipid domains, *FEBS Lett.* **2010**, *584*, 1653–1658.

[137] S. Faiss, S. Schuy, D. Weiskopf, C. Steinem, A. Janshoff, Phase Transition of Individually Addressable Microstructured Membranes Visualized by Imaging Ellipsometry, *J. Phys. Chem. B* **2007**, *111*, 13979–13986.

[138] A. E. Garner, D. Alastair Smith, N. M. Hooper, Sphingomyelin chain length influences the distribution of GPI-anchored proteins in rafts in supported lipid bilayers, *Mol. Membr. Biol.* **2007**, *24*(3), 233–242.

[139] O. Ekholm, S. Jaikishan, M. Lönnfors, T. K. Nyholm, J. P. Slotte, Membrane bilayer properties of sphingomyelins with amide-linked 2- or 3-hydroxylated fatty acids, *Biochim. Biophys. Acta* **2011**, *1808*, 727–732.

[140] B. Windschiegl, C. Steinem, Influence of α-hydroxylation of glycolipids on domain formation in lipid monolayers, *Langmuir* **2006**, *22*(18), 7454–7457.

[141] H. Löfgren, I. Pascher, Molecular arrangements of sphingolipids. The monolayer behaviour of ceramides, *Chem. Phys. Lipids* **1977**, *20*(4), 273–284.

[142] I. Pascher, Molecular arrangements in sphingolipids. Conformation and hydrogen bonding of ceramide and their implication on membrane stability and permeability, *Biochim. Biophys. Acta* **1976**, *455*(2), 433–451.

[143] N. Yahi, A. Aulas, J. Fantini, T. Ikezu, How Cholesterol Constrains Glycolipid Conformation for Optimal Recognition of Alzheimer's β Amyloid Peptide (Aβ1-40), *PLoS One* **2010**, *5*(2), e9079.

[144] J. Angström, S. Teneberg, M. A. Milh, T. Larsson, I. Leonardsson, B. Olsson, M. O. Halvarsson, D. Danielsson, I. Näslund, A. Ljungh, et al., The lactosylceramide binding specificity of Helicobacter pylori., *Glycobiology* **1998**, *8*(4), 297–309.

[145] H. Raa, S. Grimmer, D. Schwudke, J. Bergan, S. Wälchli, T. Skotland, A. Shevchenko, K. Sandvig, Glycosphingolipid Requirements for Endosome-to-Golgi Transport of Shiga Toxin, *Traffic* **2009**, *10*, 868–882.

[146] D. C. Smith, D. J. Sillence, T. Falguières, R. M. Jarvis, L. Johannes, J. M. Lord, F. M. Platt, L. M. Roberts, The association of Shiga-like toxin with detergent-resistant membranes is modulated by glucosylceramide and is an essential requirement in the endoplasmic reticulum for a cytotoxic effect, *Mol. Biol. Cell* **2006**, *17*(3), 1375–1387.

[147] Ramirez, Daniel M. Carter, W. W. Ogilvie, L. J. Johnston, NBD-cholesterol probes to track cholesterol distribution in model membranes, *Biochim. Biophys. Acta* **2010**, *1798*(3), 558–568.

[148] T. Baumgart, S. T. Hess, W. W. Webb, Imaging coexisting fluid domains in biomembrane models coupling curvature and line tension, *Nature* **2003**, *425*(6960), 821–824.

[149] L. Guo, X. Zhang, D. Zhou, A. L. Okunade, X. Su, Stereospecificity of fatty acid 2-hydroxylase and differential functions of 2-hydroxy fatty acid enantiomers, *J. Lipid Res.* **2012**, *53*(7), 1327–1335.

[150] H. Hama, Fatty acid 2-Hydroxylation in mammalian sphingolipid biology, *Biochim. Biophys. Acta* **2010**, *1801*(4), 405–414.

[151] E. B. Watkins, H. Gao, A. J. Dennison, N. Chopin, B. Struth, T. Arnold, J.-C. Florent, L. Johannes, Carbohydrate Conformation and Lipid Condensation in Monolayers Containing Glycosphingolipid Gb3: Influence of Acyl Chain Structure, *Biophys. J.* **2014**, *107*(5), 1146–1155.

[152] D. Singh, H. C. Jarrell, E. Florio, D. B. Fenske, C. W. Grant, Effects of fatty acid alpha-hydroxylation on glycosphingolipid properties in phosphatidyl-choline bilayers, *Biochim. Biophys. Acta* **1992**, *1103*(2), 268–274.

[153] C. A. Lingwood, Glycolipid receptors for verotoxin and Helicobacter pylori: role in pathology, *Biochim. Biophys. Acta.* **1999**, *1455*(2), 375–386.

[154] R. Šachl, M. Amaro, G. Aydogan, A. Koukalová, I. I. Mikhalyov, I. A. Boldyrev, J. Humpolíčková, M. Hof, On multivalent receptor activity of GM1 in cholesterol containing membranes, *Biochim. Biophys. Acta* **2015**, *1853*(4), 850–857.

[155] J. Shi, T. Yang, S. Kataoka, Y. Zhang, A. J. Diaz, P. S. Cremer, GM 1 Clustering Inhibits Cholera Toxin Binding in Supported Phospholipid Membranes, *J. Am. Chem. Soc.* **2007**, *129*, 5954–5961.

[156] T. Mori, T. Ohtsuka, Y. Okahata, Kinetic analyses of bindings of Shiga-like toxin to clustered and dispersed Gb3 glyco-arrays on a quartz-crystal microbalance, *Langmuir* **2010**, *26*(17), 14118–14125.

[157] R. A. Dick, S. L. Goh, G. W. Feigenson, V. M. Vogt, HIV-1 Gag protein can sense the cholesterol and acyl chain environment in model membranes, *Proc. Natl. Acad. Sci. U.S.A.* **2012**, *109*(46), 18761–18766.

[158] G. Margheri, R. D'Agostino, L. Becucci, R. Guidelli, B. Tiribilli, M. Del Rosso, Surface plasmon resonance as detection tool for lipids lateral mobility in biomimetic membranes, *Biomed. Opt. Express* **2012**, *3*(12), 3119–3126.

[159] G. Margheri, R. D'Agostino, S. Trigari, S. Sottini, M. Del Rosso, The β-subunit of cholera toxin has a high affinity for ganglioside GM1 embedded into solid supported lipid membranes with a lipid raft-like composition, *Lipids* **2014**, *49*(2), 203–206.

[160] B. Palmieri, S. A. Safran, Hybrid lipids increase the probability of fluctuating nanodomains in mixed membranes, *Langmuir* **2013**, *29*(17), 5246–5261.

[161] F. A. Heberle, M. Doktorova, S. L. Goh, R. F. Standaert, J. Katsaras, G. W. Feigenson, Hybrid and Non-Hybrid Lipids Exert Common Effects on Membrane Raft Size and Morphology, *J. Am. Chem. Soc.* **2013**, *135*, 14932–14935.

[162] B. L. Stottrup, S. L. Veatch, S. L. Keller, Nonequilibrium behavior in supported lipid membranes containing cholesterol, *Biophys. J.* **2004**, *86*, 2942–2950.

[163] C. Yuan, J. Furlong, P. Burgos, L. J. Johnston, The size of lipid rafts: an atomic force microscopy study of ganglioside GM1 domains in sphingomyelin/-DOPC/cholesterol membranes, *Biophys. J.* **2002**, *82*(5), 2526–2535.

[164] V. Vie, N. Van Mau, E. Lesniewska, J. Goudonnet, F. Heitz, C. Le Grimellec, Distribution of ganglioside GM1 between two-component, two-phase phosphatidylcholine monolayers, *Langmuir* **1998**, *14*(16), 4574–4583.

[165] A. R. Burns, Domain structure in model membrane bilayers investigated by simultaneous atomic force microscopy and fluorescence imaging, *Langmuir* **2003**, *19*(20), 8358–8363.

[166] P. E. Milhiet, V. Vié, M.-C. Giocondi, C. Le Grimellec, AFM characterization of model rafts in supported bilayers, *Single Mol.* **2001**, *2*(2), 109–112.

[167] M. M. Lozano, Z. Liu, E. Sunnick, A. Janshoff, K. Kumar, S. G. Boxer, Colocalization of the ganglioside GM1 and cholesterol detected by secondary ion mass spectrometry, *J. Am. Chem. Soc.* **2013**, *135*(15), 5620–5630.

[168] S. Chiantia, E. London, Acyl chain length and saturation modulate interleaflet coupling in asymmetric bilayers: effects on dynamics and structural order, *Biophys. J.* **2012**, *103*(11), 2311–2319.

[169] H. M. Seeger, A. D. Cerbo, A. Alessandrini, P. Facci, Supported lipid bilayers on mica and silicon oxide: comparison of the main phase transition behavior, *J. Phys. Chem. B* **2010**, *114*(27), 8926–8933.

[170] A. J. Sodt, M. L. Sandar, K. Gawrisch, R. W. Pastor, E. Lyman, The molecular structure of the liquid-ordered phase of lipid bilayers, *J. Am. Chem. Soc.* **2014**, *136*, 725–732.

[171] J. Ando, M. Kinoshita, J. Cui, H. Yamakoshi, K. Dodo, K. Fujita, M. Murata, M. Sodeoka, Sphingomyelin distribution in lipid rafts of artificial monolayer membranes visualized by Raman microscopy, *Proc. Natl. Acad. Sci. U.S.A.* **2015**, *112*(15), 4558–4563.

[172] J. Prades, S. S. Funari, M. Gomez-Florit, O. Vögler, F. Barceló, Effect of a 2-hydroxylated fatty acid on Cholesterol-rich membrane domains, *Mol. Membr. Biol.* **2012**, *29*(8), 333–343.

[173] C. S. Scheve, P. A. Gonzales, N. Momin, J. C. Stachowiak, Steric Pressure between Membrane-Bound Proteins Opposes Lipid Phase Separation, *J. Am. Chem. Soc.* **2013**, *135*, 1185–1188.

[174] T. Schilling, S. Pronk, B. Mulder, D. Frenkel, Monte Carlo study of hard pentagons, *Phys. Rev. E Stat. Nonlin. Soft Matter Phys.* **2005**, *71*, 036138–1.

[175] J.-S. Wang, A fast algorithm for random sequential adsorption of discs, *Int. J. Mod. Phys. C* **1994**, *05*, 707–715.

[176] D. E. Saslowsky, Welscher, Y. M. t., D. J.-F. Chinnapen, J. S. Wagner, J. Wan, E. Kern, W. I. Lencer, Ganglioside GM1-mediated Transcytosis of Cholera Toxin Bypasses the Retrograde Pathway and Depends on the Structure of the Ceramide Domain, *J. Biol. Chem.* **2013**.

[177] W. Pezeshkian, V. V. Chaban, L. Johannes, J. Shillcock, J. H. Ipsen, H. Khandelia, The effects of globotriaosylceramide tail saturation level on bilayer phases, *Soft Matter* **2015**, *11*(7), 1352–1361.

[178] B. Kollmitzer, P. Heftberger, M. Rappolt, G. Pabst, Monolayer spontaneous curvature of raft-forming membrane lipids, *Soft Matter* **2013**, *9*(45), 10877–10884.

[179] R. S. Gracià, N. Bezlyepkina, R. L. Knorr, R. Lipowsky, R. Dimova, Effect of cholesterol on the rigidity of saturated and unsaturated membranes: fluctuation and electrodeformation analysis of giant vesicles, *Soft Matter* **2010**, *6*(7), 1472–1482.

[180] L. M. C. Weber, Einfluss des ungesättigten, hydroxylierten Glycosphingolipids Gb3 und der Binding von Shiga Toxin auf die laterale Organisation von artifiziellen Lipidmembranen, bachelor thesis, Georg-August-Universität Göttingen, **2014**.

[181] R. Mahfoud, A. Manis, B. Binnington, C. Ackerley, C. A. Lingwood, A major fraction of glycosphingolipids in model and cellular cholesterol-containing membranes is undetectable by their binding proteins, *J. Biol. Chem.* **2010**, *285*, 36049–36059.

[182] M. R. Morrow, D. M. Singh, C. W. Grant, Glycosphingolipid headgroup orientation in fluid phospholipid/cholesterol membranes: similarity for a range of glycolipid fatty acids, *Biophys. J.* **1995**, *69*(3), 955–964.

[183] D. Singh, H. C. Jarrell, K. R. Barber, C. W. Grant, Glycosphingolipids: 2H NMR study of the influence of ceramide fatty acid characteristics on the carbohydrate headgroup in phospholipid bilayers, *Biochemistry* **1992**, *31*(10), 2662–2669.

[184] J. Hu, R. Lipowsky, T. R. Weikl, Binding constants of membrane-anchored receptors and ligands depend strongly on the nanoscale roughness of membranes, *Proc. Natl. Acad. Sci. U.S.A.* **2013**, *110*(38), 15283–15288.

[185] J. A. Braunger, C. Kramer, D. Morick, C. Steinem, Solid supported membranes doped with PIP2: influence of ionic strength and pH on bilayer formation and membrane organization, *Langmuir* **2013**, *29*(46), 14204–14213.

[186] J. Pan, S. Tristram-Nagle, J. F. Nagle, Effect of cholesterol on structural and mechanical properties of membranes depends on lipid chain saturation, *Phys. Rev. E Stat. Nonlin. Soft Matter Phys.* **2009**, *80*(2 Pt 1), 021931.

[187] J. M. Boggs, Lipid intermolecular hydrogen bonding: influence on structural organization and membrane function, *Biochim. Biophys. Acta* **1987**, *906*(3), 353–404.

[188] C. Yuan, L. J. Johnston, Atomic Force Microscopy Studies of Ganglioside GM1 Domains in Phosphatidylcholine and Phosphatidylcholine/Cholesterol Bilayers, *Biophys. J.* **2001**, *81*(2), 1059–1069.

[189] L. V. Schäfer, S. J. Marrink, Partitioning of lipids at domain boundaries in model membranes, *Biophys. J.* **2010**, *99*(12), L91–L93.

[190] J. Arnaud, J. Claudinon, K. Tröndle, M. Trovaslet, G. Larson, A. Thomas, A. Varrot, W. Römer, A. Imberty, A. Audfray, Reduction of lectin valency drastically changes glycolipid dynamics in membranes but not surface avidity, *ACS Chem. Biol.* **2013**, *8*(9), 1918–1924.

[191] I. Basu, C. Mukhopadhyay, Insights into binding of Cholera toxin to GM1 containing membrane, *Langmuir* **2014**, *30*(50), 15244–15252.

[192] K. R. Levental, I. Levental, Giant Plasma Membrane Vesicles: Models for Understanding Membrane Organization, *Curr. Top. Membr.* **2015**, *75*, 25–27.

[193] E. Sezgin, T. Gutmann, T. Buhl, R. Dirkx, M. Grzybek, Ü. Coskun, M. Solimena, K. Simons, I. Levental, P. Schwille, Adaptive Lipid Packing and Bioactivity in Membrane Domains, *PLoS One* **2015**, *10*(4), e0123930.

[194] A. R. Honerkamp-Smith, P. Cicuta, M. D. Collins, S. L. Veatch, M. den Nijs, M. Schick, S. L. Keller, Line tensions, correlation lengths, and critical exponents in lipid membranes near critical points, *Biophys. J.* **2008**, *95*(1), 236–246.

[195] K. Weiß, A. Neef, Q. Van, S. Kramer, I. Gregor, J. Enderlein, Quantifying the diffusion of membrane proteins and peptides in black lipid membranes with 2-focus fluorescence correlation spectroscopy, *Biophys. J.* **2013**, *105*(2), 455–462.

[196] S. Arumugam, E. P. Petrov, P. Schwille, Cytoskeletal Pinning Controls Phase Separation in Multicomponent Lipid Membranes, *Biophys. J.* **2015**, *108*(5), 1104–1113.

[197] P. Saffman, M. Delbrück, Brownian motion in biological membranes, *Proc. Natl. Acad. Sci. U.S.A.* **1975**, *72*(8), 3111–3113.

[198] B. Hughes, B. Pailthorpe, L. White, The translational and rotational drag on a cylinder moving in a membrane, *J. Fluid Mech.* **1981**, *110*, 349–372.

[199] E. P. Petrov, P. Schwille, Translational diffusion in lipid membranes beyond the Saffman-Delbrück approximation, *Biophys. J.* **2008**, *94*(5), L41–L43.

[200] A. Simon, C. Gounou, S. Tan, L. Tiefenauer, M. Di Berardino, A. R. Brisson, Free-standing lipid films stabilized by Annexin-A5, *Biochim. Biophys. Acta* **2013**, *1828*(11), 2739–2744.

[201] T. D. Lazzara, C. Carnarius, M. Kocun, A. Janshoff, C. Steinem, Separating attoliter-sized compartments using fluid pore-spanning lipid bilayers, *ACS Nano* **2011**, *5*(9), 6935–6944.

[202] G. P. Acuna, M. Bucher, I. H. Stein, C. Steinhauer, A. Kuzyk, P. Holzmeister, R. Schreiber, A. Moroz, F. D. Stefani, T. Liedl, et al., Distance dependence of single-fluorophore quenching by gold nanoparticles studied on DNA origami, *ACS Nano* **2012**, *6*(4), 3189–3195.

[203] K. Bacia, P. Schwille, T. Kurzchalia, Sterol structure determines the separation of phases and the curvature of the liquid-ordered phase in model membranes, *Proc. Natl. Acad. Sci. U.S.A.* **2005**, *102*(9), 3272–3277.

[204] F. Heinemann, S. K. Vogel, P. Schwille, Lateral membrane diffusion modulated by a minimal actin cortex, *Biophys. J.* **2013**, *104*(7), 1465–1475.

[205] A. Sonnleitner, G. Schütz, T. Schmidt, Free Brownian motion of individual lipid molecules in biomembranes, *Biophys. J.* **1999**, *77*(5), 2638–2642.

[206] S. Chiantia, N. Kahya, J. Ries, P. Schwille, Effects of ceramide on liquid-ordered domains investigated by simultaneous AFM and FCS, *Biophys. J.* **2006**, *90*(12), 4500–4508.

[207] M. Tanaka, E. Sackmann, Polymer-supported membranes as models of the cell surface, *Nature* **2005**, *437*(7059), 656–663.

[208] P. Cicuta, S. L. Keller, S. L. Veatch, Diffusion of liquid domains in lipid bilayer membranes, *J. Phys. Chem. B* **2007**, *111*(13), 3328–3331.

[209] J. Kestin, M. Sokolov, W. A. Wakeham, Viscosity of liquid water in the range −8 °C to 150 °C, *J. Phys. Chem. Ref. Data* **1978**, *7*(3), 941–948.

[210] A. Honigmann, V. Mueller, H. Ta, A. Schoenle, E. Sezgin, S. W. Hell, C. Eggeling, Scanning STED-FCS reveals spatiotemporal heterogeneity of lipid interaction in the plasma membrane of living cells, *Nat. Commun.* **2014**, *5*, 5412.

[211] F. Okada, K. Morigaki, Micropatterned model membrane with quantitatively controlled separation of lipid phases, *RSC Adv.* **2015**, *5*(2), 1507–1513.

[212] F. Roder, O. Birkholz, O. Beutel, D. Paterok, J. Piehler, Spatial organization of lipid phases in micropatterned polymer-supported membranes, *J. Am. Chem. Soc.* **2013**, *135*(4), 1189–1192.

[213] E. L. Kendall, V. N. Ngassam, S. F. Gilmore, C. J. Brinker, A. N. Parikh, Lithographically defined macroscale modulation of lateral fluidity and phase separation realized via patterned nanoporous silica-supported phospholipid bilayers, *J. Am. Chem. Soc.* **2013**, *135*(42), 15718–15721.

[214] A. Honigmann, S. Sadeghi, J. Keller, S. W. Hell, C. Eggeling, R. Vink, A lipid bound actin meshwork organizes liquid phase separation in model membranes, *Elife* **2014**, *3*, e01671.

[215] T.-Y. Yoon, C. Jeong, S.-W. Lee, J. H. Kim, M. C. Choi, S.-J. Kim, M. W. Kim, S.-D. Lee, Topographic control of lipid-raft reconstitution in model membranes, *Nat. Mat.* **2006**, *5*(4), 281–285.

[216] R. Parthasarathy, J. T. Groves, Curvature and spatial organization in biological membranes, *Soft Matter* **2006**, *3*(1), 24–33.

[217] R. Parthasarathy, C.-h. Yu, J. T. Groves, Curvature-modulated phase separation in lipid bilayer membranes, *Langmuir* **2006**, *22*(11), 5095–5099.

[218] C. Saßen, A scanning ion conductance microscopy assay to investigate interactions between cell penetrating peptides and pore-suspending lipid membranes, PhD thesis, Georg-August-Universität Göttingen, **2013**.

[219] A. Finkelstein, A. Cass, Permeability and electrical properties of thin lipid membranes, *J. Gen. Physiol.* **1968**, *52*(1), 145–172.

[220] C. Farre, S. Stoelzle, C. Haarmann, M. George, A. Brüggemann, N. Fertig, Automated ion channel screening: patch clamping made easy, *Expert Opin. Ther. Targets* **2007**, *11*(4), 557–565.

[221] J. Rheinlaender, T. E. Schäffer, Image formation, resolution, and height measurement in scanning ion conductance microscopy, *J. Appl. Phys.* **2009**, *105*(9), 094905.

[222] R. F. Epand, J.-C. Martinou, M. Fornallaz-Mulhauser, D. W. Hughes, R. M. Epand, The apoptotic protein tBid promotes leakage by altering membrane curvature, *J. Biol. Chem.* **2002**, *277*(36), 32632–32639.

[223] R. W. Clarke, A. Zhukov, O. Richards, N. Johnson, V. Ostanin, D. Klenerman, Pipette–Surface Interaction: Current Enhancement and Intrinsic Force, *J. Am. Chem. Soc.* **2012**, *135*(1), 322–329.

[224] J. Rheinlaender, T. E. Schäffer, Mapping the mechanical stiffness of live cells with the scanning ion conductance microscope, *Soft Matter* **2013**, *9*(12), 3230–3236.

[225] R. Lipowsky, Budding of membranes induced by intramembrane domains, *J. Phys. II France* **1992**, *2*(10), 1825–1840.

[226] J. Pan, S. Tristram-Nagle, J. F. Nagle, Effect of cholesterol on structural and mechanical properties of membranes depends on lipid chain saturation, *Phys. Rev. E Stat. Nonlin. Soft Matter Phys.* **2009**, *80*(2 Pt 1), 021931.

[227] A. Tian, B. R. Capraro, C. Esposito, T. Baumgart, Bending stiffness depends on curvature of ternary lipid mixture tubular membranes, *Biophys. J.* **2009**, *97*(6), 1636–1646.

[228] M. Böcker, Entwicklungen in der Rasterionenleitfahigkeitsmikroskopie und Untersuchungen von porenüberspannenden Lipidmembranen, PhD thesis, Friedrich-Alexander-Universität Erlangen-Nürnberg, **2007**.

[229] T. Fischer, H. J. Risselada, R. L. Vink, Membrane lateral structure: the influence of immobilized particles on domain size, *Phys. Chem. Chem. Phys.* **2012**, *14*(42), 14500–14508.

[230] M. H. Jensen, E. J. Morris, A. C. Simonsen, Domain shapes, coarsening, and random patterns in ternary membranes, *Langmuir* **2007**, *23*(15), 8135–8141.

[231] J. Ehrig, E. P. Petrov, P. Schwille, Near-critical fluctuations and cytoskeleton-assisted phase separation lead to subdiffusion in cell membranes, *Biophys. J.* **2011**, *100*(1), 80–89.

[232] A. Sharonov, R. Bandichhor, K. Burgess, A. D. Petrescu, F. Schroeder, A. B. Kier, R. M. Hochstrasser, Lipid diffusion from single molecules of a labeled protein undergoing dynamic association with giant unilamellar vesicles and supported bilayers, *Langmuir* **2008**, *24*(3), 844–850.

[233] A. P. Dabkowska, C. S. Niman, G. Piret, H. Persson, H. P. Wacklin, H. Linke, C. N. Prinz, T. Nylander, Fluid and highly curved model membranes on vertical nanowire arrays, *Nano Lett.* **2014**, *14*(8), 4286–4292.

[234] T. D. Lazzara, D. Behn, T.-T. Kliesch, A. Janshoff, C. Steinem, Phospholipids as an alternative to direct covalent coupling: Surface functionalization of nanoporous alumina for protein recognition and purification, *J. Colloid Interface Sci.* **2012**, *366*(1), 57–63.

[235] B. Brüning, M. Rheinstädter, A. Hiess, B. Weinhausen, T. Reusch, S. Aeffner, T. Salditt, Influence of cholesterol on the collective dynamics of the phospholipid acyl chains in model membranes, *Eur. Phys. J. E Soft Matter* **2010**, *31*(4), 419–428.

[236] H. Basit, A. Van der Heyden, C. Gondran, B. Nysten, P. Dumy, P. Labbé, Tethered bilayer lipid membranes on mixed self-assembled monolayers of a novel anchoring thiol: impact of the anchoring thiol density on bilayer formation, *Langmuir* **2011**, *27*(23), 14317–14328.

[237] J. Kozuch, C. Weichbrodt, D. Millo, K. Giller, S. Becker, P. Hildebrandt, C. Steinem, Voltage-dependent structural changes of the membrane-bound anion channel hVDAC1 probed by SEIRA and electrochemical impedance spectroscopy, *Phys. Chem. Chem. Phys.* **2014**, *16*(20), 9546–9555.

[238] M. J. Uline, M. Schick, I. Szleifer, Phase behavior of lipid bilayers under tension, *Biophys. J.* **2012**, *102*(3), 517–522.

[239] S. Dieluweit, A. Csiszár, W. Rubner, J. Fleischhauer, S. Houben, R. Merkel, Mechanical properties of bare and protein-coated giant unilamellar phospholipid vesicles. A comparative study of micropipet aspiration and atomic force microscopy, *Langmuir* **2010**, *26*(13), 11041–11049.

[240] R. Lipowsky, T. Rouhiparkouhi, D. E. Discher, T. R. Weikl, Domain formation in cholesterol–phospholipid membranes exposed to adhesive surfaces or environments, *Soft Matter* **2013**, *9*(35), 8438–8453.

[241] N. F. Morales-Penningston, J. Wu, E. R. Farkas, S. L. Goh, T. M. Konyakhina, J. Y. Zheng, W. W. Webb, G. W. Feigenson, GUV preparation and imaging: minimizing artifacts, *Biochim. Biophys. Acta.* **2010**, *1798*(7), 1324–1332.

[242] T. R. Weikl, R. Lipowsky, Membrane adhesion and domain formation, *Advances in Planar Lipid Bilayers and Liposomes* **2006**, *5*, 63–127.

[243] U. Seifert, R. Lipowsky, Adhesion of vesicles, *Phys. Rev. A* **1990**, *42*(8), 4768.

[244] L. Bergström, Hamaker constants of inorganic materials, *Adv. Colloid Interface Sci.* **1997**, *70*, 125–169.

[245] V. D. Gordon, M. Deserno, C. Andrew, S. Egelhaaf, W. Poon, Adhesion promotes phase separation in mixed-lipid membranes, *Europhys. Lett.* **2008**, *84* (4), 48003.

[246] E. Evans, W. Rawicz, Entropy-driven tension and bending elasticity in condensed-fluid membranes, *Phys. Rev. Lett.* **1990**, *64* (17), 2094.

[247] R. Lipowsky, U. Seifert, Adhesion of vesicles and membranes, *Mol. Cryst. Liq. Cryst.* **1991**, *202* (1), 17–25.

[248] N. Wilke, B. Maggio, The influence of domain crowding on the lateral diffusion of ceramide-enriched domains in a sphingomyelin monolayer, *J. Phys. Chem. B* **2009**, *113* (38), 12844–12851.

[249] S. Aliaskarisohi, P. Tierno, P. Dhar, Z. Khattari, M. Blaszczynski, T. M. Fischer, On the diffusion of circular domains on a spherical vesicle, *J. Fluid Mech.* **2010**, *654*, 417–451.

[250] N. Wilke, F. Vega Mercado, B. Maggio, Rheological properties of a two phase lipid monolayer at the air/water interface: effect of the composition of the mixture, *Langmuir* **2010**, *26* (13), 11050–11059.

[251] E. P. Petrov, R. Petrosyan, P. Schwille, Translational and rotational diffusion of micrometer-sized solid domains in lipid membranes, *Soft Matter* **2012**, *8* (29), 7552–7555.

[252] H. M. McConnell, Structures and transitions in lipid monolayers at the air-water interface, *Annu. Rev. Phys. Chem.* **1991**, *42* (1), 171–195.

[253] M. Yanagisawa, M. Imai, T. Masui, S. Komura, T. Ohta, Growth dynamics of domains in ternary fluid vesicles, *Biophys. J.* **2007**, *92* (1), 115–125.

[254] T. S. Ursell, W. S. Klug, R. Phillips, Morphology and interaction between lipid domains, *Proc. Natl. Acad. Sci. U.S.A.* **2009**, *106* (32), 13301–13306.

[255] S. Semrau, T. Idema, T. Schmidt, C. Storm, Membrane-mediated interactions measured using membrane domains, *Biophys. J.* **2009**, *96* (12), 4906–4915.

[256] S. B. Calderwood, F. Auclair, A. Donohue-Rolfe, G. T. Keusch, J. J. Mekalanos, Nucleotide sequence of the Shiga-like toxin genes of Escherichia coli, *Proc. Natl. Acad. Sci. U.S.A.* **1987**, *84* (13), 4364–4368.

[257] N. G. Seidah, A. Donohue-Rolfe, C. Lazure, F. Auclair, G. Keusch, M. Chretien, Complete amino acid sequence of Shigella toxin B-chain. A novel polypeptide containing 69 amino acids and one disulfide bridge., *J. Biol. Chem.* **1986**, *261* (30), 13928–13931.

[258] C. A. Schneider, W. S. Rasband, K. W. Eliceiri, NIH Image to ImageJ: 25 years of image analysis, *Nat. Methods* **2012**, *9* (7), 671–675.

Curriculum vitae

Personal data

Name:	Ole Mathis Schütte
Date of birth:	07.10.1985
Place of birth:	Bremen, Germany
Citizenship:	German

Carreer

2012-2015	**Ph.D. thesis** at the Georg-August University, Göttingen (Prof. Dr. C. Steinem), title of the thesis: *Structure and dynamics of artificial lipid membranes containing the glycosphingolipid Gb$_3$*
2009-2011	**graduate studies** in chemistry at the Georg-August University, Göttingen, degree: Master of Science with honours, grade: 1.0, title of the master thesis: *Investigation of the membrane-peptide-interaction in case of modified gramicidin A derivatives*, grade: 1.0
2010-2011	**Erasmus stay** at The University of Manchester, UK
2006-2009	**undergraduate studies** in chemistry at the Georg-August University, Göttingen, degree: Bachelor of Science with honours, grade: 1.3, title of the bachelor thesis: *Investigation of the temperature dependent Shiga Toxin binding to model membranes containing Gb$_3$*, grade: 1.0
2005-2006	**civilian service** at the Senator for construction, traffic and environmental issues, federal state of Bremen, Germany
2002-2005	**Allgemeine Hochschulreife** at Schulzentrum Neustadt, Bremen, degree: Abitur, grade: 1.0

Awards

2012	Excellence stipend of the state of Lower Saxony within the International Max Planck Research School Physics of Biological and Complex Systems of the Göttingen Graduate School for Neurosciences, Biophysics, and Molecular Biosciences
2011	Gustav-Tammann award, Georg-August University, Göttingen, Germany

2009	Otto-Wallach award, Georg-August University, Göttingen, Germany

Scientific contributions

Peer-reviewed publications

2015	O. M. Schütte, L. J. Patalag, L. M. C. Weber, A. Ries, W. Römer, D. B. Werz, C. Steinem, 2-Hydroxy Fatty Acid Enantiomers of Gb_3 Impact Shiga Toxin Binding and Membrane Organization, *Biophys. J.* **2015**
2015	R. N. Das, Y. P. Kumar, O. M. Schütte, C. Steinem, J. Dash, A DNA-Inspired Synthetic Ion Channel Based on G-C Base Pairing, *J. Am. Chem. Soc.* **2015**, *137*, 34-37.
2014	O. M. Schütte, A. Ries, A. Orth, L. J. Patalag, W. Römer, C. Steinem, D. B. Werz, Influence of Gb_3 glycosphingolipids differing in their fatty acid chain on the phase behavior of solid supported membranes: Chemical syntheses and impact of Shiga toxin binding, *Chem. Sci.* **2014**, *5*, 3104-3114.
2014	N. Hafi, M. Grunwald, L. S. van den Heuvel, T. Aspelmeier, J.-H. Chen, M. Zagrebelsky, O. M. Schütte, C. Steinem, M. Korte, A. Munk, P. J. Walla, Fluorescence nanoscopy by polarization modulation and polarization angle narrowing, *Nat. Methods* **2014**, *11*, 579-584.
2014	Y. P. Kumar, R. N. Das, S. Kumar, O. M. Schütte, C. Steinem, J. Dash, Triazole tailored guanosine dinucleosides as biomimetic ion channels to modulate transmembrane potential, *Chem. Eur. J.* **2014**, *20*, 3023-3028.
2013	T. Hotz, O. M. Schütte, H. Sieling, T. Polupanow, U. Diederichsen, C. Steinem, A. Munk, Idealizing ion channel recordings by a jump segmentation multiresolution filter, *IEEE Transact. NanoBiosci.* **2013**, *12*, 376-386.

Oral presentations

2014	GDCh Weihnachtskolloqium Göttingen, The globoside Gb_3: how subtle differences change membrane morphology and protein binding
2014	CRC803 winterschool, Mühlhausen
	Phase-separation of Gb_3-containing membranes
2013	IMPRS PBCS renewal, Göttingen
	Mimicking the plasma membrane -
	Chemical and physical tools to rearrange artificial membrane

2012	CRC803 winterschool, Brotterode
	Tailor-made glycosphingolipids in artificial membranes
	Posters
2014	CRC 803 Symposium 2014, Göttingen
	Influence of Gb_3 glycosphingolipids differing in their fatty acid chain on the phase behaviour of solid supported membranes: chemical syntheses and impact of Shiga toxin binding
2014	Retreat of PBCS graduate school within the GGNB, Bad Salzdetfurth
	Lipid Phase Separation: Molecular to Micron Scale
2014	International Workshop "Molecular Membrane Biophysics, Hünfeld
	Rebuilding the Plasma Membrane: Linking Chemical Tools to Pore-Spanning Lipid Bilayers
2014	Labex CelTisPhyBio Workshop on Cell Membranes 2014, Paris
	Pore-spanning lipid bilayers to study lipid domains
2013	GGNB Science Day 2013, Göttingen
	Lipid domains in artificial pore-spanning lipid bilayers
2013	GZMB Symposium, Göttingen
	Influencing lipid domains in pore-spanning lipid bilayers
2013	9th European Biophysics Congress, Lisbon
	Modulating the phase separation in pore-spanning lipid bilayers
2013	IMPRS PBCS renewal, Göttingen
	Artificial Membranes as Plasma Membrane mimics
2013	Chemieforum Göttingen, Göttingen
	Tweaking the phase behavior of lipid membranes
2012	CRC803 grant renewal, Göttingen
	Tailor-made glycosphingolipids as a toolkit to visualize domain formation and lipid-protein interactions
2012	Annual Meeting of the DGfB, Göttingen
	Modulating Membrane Microdomains: Influences of Substrate Functionalization and Chemical Structure

Danksagung